Experimental investigations in spheromaks: injection into a tokamak and formation in an unbounded environment

Thesis by

Jimmy Yee

In Partial Fulfillment of the Requirements
for the Degree of
Doctor of Philosophy

California Institute of Technology
Pasadena, California

2000
(Submitted September 13, 1999)

Acknowledgements

I would like to thank my advisor, Dr. Paul Bellan, for his support, guidance, and patience through my long career as a graduate student. I have learned much from him, and will continue to value his advice and friendship. This manuscript also benefitted greatly from his careful reading and insightful comments.

I am grateful to Peter Loewenhardt and Michael Brown, who both made major contributions toward the development of the CT Injector. Many thanks go to Bill Rowan and the staff and students at the Fusion Research Center in UT Austin for their hospitable treatment during my stay there. I am indebted to Frank Cosso for providing his technical expertise in building and repairing much of the equipment I have used. Thanks to Freddy Hansen and Steve Pracko, who supplied very useful feedback in the preparation of this text.

Last, but certainly not least, I wish to thank my family for their love and support through my many years away from home.

I will look back at my stay at Caltech as a time of learning, personal growth, new friendships, and rich experiences. I feel very grateful toward the institution for having afforded me this opportunity. I will cherish the memories.

This work was supported by DOE Grants DE-FG03-86ER53232 and DE-FG03-98ER54461.

Abstract

Spheromaks are investigated in two separate experiments. In the first, the CT Injector experiment, spheromaks are accelerated by a coaxial rail gun for injection into a medium-sized tokamak (B_T=10 kG). Speeds of 3×10^5 m/s and densities in the high 10^{21} m^{-3} range are achieved upon implementation of impurity reduction techniques and high bias flux. Tokamak injection experiments indicate anomalous stopping of the spheromak within the injector at toroidal field (TF) levels well below previous theoretical predictions. Modifications of the electrode geometry were found to substantially improve performance.

An extension of the previously accepted theory is proposed which takes into account the effect of TF flux trapping within the electrodes. A 2-D magnetostatic analysis indicates that this phenomenon increases the spheromak kinetic energy density required for penetration by a factor dependent on spheromak size. A numerical analysis extends these results to finite length spheromaks. These calculations also show that the spheromak shape has an effect on penetration levels. The proposed theory indicates that a realistic assessment of spheromak injection requirements must take into account magnetic field interaction with the injector walls as well as the spheromak itself.

The second part of this thesis describes an experiment examining the formation and decay of spheromaks in unbounded environments; i.e., without the influence of flux-conserving walls. A coaxial gun is discharged into a much larger vacuum chamber and the subsequent evolution of the plasma is observed, mainly using high speed cameras and a magnetic probe array. Photographic results suggest four distinct regimes of operation, labeled I-IV, each possessing qualitatively different dynamics, with the parameter $\lambda_{gun} = \mu_0 I_{gun}/\Phi_{stuff}$ determining the operative regime.

Plasmas produced in Regime II are identified as detached spheromak configurations. Images depict a roughly donut-like shape, while magnetic data, when interpreted using a propagation inference method, suggest that a closed toroidal flux-surface topology is present. Poloidal flux amplification shows that Taylor relaxation mechanisms are at work. Calculations of the spatial and temporal variation of λ ($\equiv \mu_0 \mathbf{J}/\mathbf{B}$) indicate that the spheromak is decaying and expanding in a manner consistent with the self-similar expansion model proposed for magnetic clouds. This implies that magnetic heating may be operative.

Regime III is associated with stuffed coaxial gun operation. Images show several complex helical and twisted features, which are shown to be magnetic in nature through field line tracing of the magnetic data. Toroidal and poloidal flux and λ calculations clearly demonstrate the stuffed nature of this regime.

Contents

List of Figures

List of Tables

Chapter 1 Introduction

Magnetized plasmas comprise a large proportion of the material in the known universe. Observers have long noted the curious feature that in many plasmas, both astrophysical and earth-bound, the magnetic field structure assumes a twisted, helical form. The ground breaking work by Woltjer [1] and Taylor [2] has contributed much to the understanding of the mechanisms which lead to these types of structures. The central concept is that, under certain circumstances, plasmas self-organize into magnetically force-free equilibrium configurations, often called Taylor states. This thesis presents experimental results from two projects involving the formation of a specific type of Taylor state, the spheromak.

Chapter 2 provides some background information which is relevant to this thesis; the ideas of magnetic helicity and relaxation. In Section 2.2, helicity is defined and the appropriate conservation law is presented, with gauge issues addressed. Helicity is then interpreted in terms of linkage, knottedness, and twist. The Taylor conjecture is explained and spheromaks are defined; two particular equilibria, the spherical and cylindrical spheromak, are derived. Finally, the methods of helicity injection are outlined.

The experimental portion of this thesis work is divided into two parts. Part I, comprising Chapters 3-5, describes work performed on the Caltech CT Injector experiment, whereas Part II comprises Chapters 6-11, and details results from an experiment forming an unbounded expanding spheromak. The two projects had distinctly different motivations and objectives, although the same magnetized coaxial gun was employed in both. The magnetized coaxial gun technique was pioneered by Alfven[3] as a method of producing and ejecting plasmoids. Subsequent to Taylor's conjecture of relaxation to minimum energy states, it was realized that the plasmoids so formed possess magnetic helicity and quickly evolve into Taylor states; i.e., spheromaks.

Chapter 3 describes the apparatus used in the CT Injector experiment. This experiment involved the acceleration of spheromaks to extremely high speeds, with the aim of injection into a tokamak reactor for refueling purposes. Spheromaks are particularly suitable for this application because they are robust, dense, and long-lived plasmoids, which can withstand high accelerations. The earliest work in this field involved unaccelerated spheromaks injected into the small ENCORE tokamak at Caltech [4]. This has been followed by acceleration, employing a coaxial rail-gun technique pioneered by Hammer, Hartman, et al. at the RACE device [5], and injection into mid-sized tokamaks [6].

Chapter 4 outlines the methods which were implemented in order to improve and optimize injector performance, as measured by the kinetic energy density of the spheromak produced. Section 4.2 reviews the efforts made by Brown, Loewenhardt, and Bellan [7] to reduce impurity levels in the device. Section 4.3 outlines the parameter space optimization scan undertaken by Loewenhardt, Brown, Yee, and Bellan [8]. A high λ, i.e., partially stuffed regime was found in which the spheromak achieved especially high kinetic energy densities. The performance thus attained was predicted [9] to be sufficient for penetrating tokamak fields of 1 Tesla, a prescribed goal of the experiment. The CT Injector was subsequently shipped to the Fusion Research Center in Austin, Texas, to begin injection experiments in conjunction with the Texas Experimental Tokamak-Upgrade (TEXT-U). However, initial experiments found that the particle inventory injected by the spheromak exceeded the tokamak density limit [33] and quenched the discharge. In fact, it was found that the gas puff needed to be reduced by 90% in order to avoid injection-induced disruption of the tokamak. Section 4.4 details the steps which were taken to recover the high performance regime after this drastic gas reduction was implemented.

Theories [9] predicted that the kinetic energy requirement involved in spheromak penetration into a tokamak is dependent solely on the toroidal field (TF) of the tokamak. As the spheromak travels into the strong TF, it behaves as a perfect conductor and diamagnetically excludes the field; the energy expended in this displacement of magnetic field is drawn from the spheromak's kinetic energy, thus retarding its forward momentum. Chapter 5 presents results from experiments in which spheromaks, accelerated up to energies which had been expected to be sufficient for penetration of the 1 Tesla fields of TEXT-U, nevertheless failed to achieve injection. Several electrode geometries were tested with differing levels of success, but all efforts fell short of theoretical models.

In order to explain the anomalously poor penetration levels, Section 5.3 presents a modification of the previously accepted theory. Increased deceleration is caused by trapping of flux within the accelerator electrodes, thus enhancing the retarding effect produced by diamagnetic exclusion. For an idealized case of an infinitely long spheromak, the enhancement factor α is calculated analytically. This is compared with spheromaks modeled as finite length cylinders, for which α is computed using an SOR algorithm. The modified theory is consistent with our observations of the relative performance of different electrode geometries. Further examination of the theory indicates that the value of α does not, as expected, converge to unity (i.e., no enhancement) in the limit of a very small spheromak, in which case the proposed flux trapping phenomenon should be negligible. This surprising result has a simple explanation: the standard diamagnetic exclusion model does not take into account the shape of the spheromak in boundary conditions. Various shapes and orientations of spheromaks are analyzed in order to determine the effect that this has on penetration; calculated limiting values of α range from 1 to 2. The theory proposed in this chapter has serious implications for the design of future injection devices. This material is published in Ref. [10].

Chapter 6 introduces the apparatus used in the second part of this thesis work, the unbounded spheromak experiment. In Taylor's theory, plasma is assumed to be confined within a fixed container with flux-conserving walls, and relaxes to a minimum-energy force-free state. However, there is abundant evidence of force-free states in nature (e.g., solar and space plasmas) which do not satisfy this boundary constraint [11][12][13]. For this reason, it is natural to suspect that the Taylor relaxation principle can be extended to include these situations. However, no generally accepted theory exists currently, although the relaxation conjecture has been applied in modeling several types of astrophysical plasmas [14][15] with some success. The unbounded spheromak experiment described here critically tests, in a laboratory setting, the validity of some basic concepts in a space-like environment: helicity conservation, rapid magnetic energy dissipation, and reconnection.

The unbounded spheromak experiment employs the same coaxial gun assembly previously used as the formation stage of the CT Injector described above. This gun is mated to a very large vacuum vessel so that no interaction with the boundaries can take place. Section 6.3 describes the two main diagnostics employed: high speed imaging cameras and a magnetic pickup-loop probe array. The cameras are ICCD-based, and provide a means of ascertaining the global structure and topology of the plasma in a non-perturbing manner. The magnetic probe array consists of a linear array of twelve 3-axis pickup-loops which can be positioned to diagnose a 3D volume of space within the vacuum chamber. Construction details and an analysis of sources of measurement error are provided.

By varying the point in time at which the camera photographs the plasma, a movie sequence of plasma evolution can be obtained. Several such image sequences are presented in Chapter 7, for different settings of the gun parameters. It is found that four distinct regimes of operation exist, which we enumerate as I-IV, with qualitatively distinct plasma dynamics observed. Not surprisingly, the ratio of the gun current to stuffing flux λ_{gun} is found to be the single parameter which determines the operative regime. Regimes II and III are deemed to be the more interesting cases, corresponding to unstuffed and stuffed, respectively. These two regimes are studied in the following chapters.

Chapters 8 and 9 outline evidence that the plasma produced in Regime II is indeed in a spheromak-like force-free state. Section 8.1 presents pictures viewing the plasma end-on, which depict a roughly donut-shaped bright region of the plasma. Although these images are suggestive, they do not constitute definitive proof that the signature closed magnetic flux surface topology is formed. For this, direct magnetic diagnosis of the plasma is needed. However, lack of high shot-to-shot reproducibility prevents compiling a 3D record of the volume.

In order to help overcome this problem, a novel technique was developed to aid in data analysis. The Single Shot Propagation Inferred (SSPI) method assumes that the magnetic field structure in the plasma is fixed and merely convects along with the plasma, which travels at a constant rate. With this assumption, it becomes possible to reconstruct an entire plane of magnetic data (typically the gun's poloidal plane) from a single plasma discharge. The poloidal plots generated in this manner clearly show the vortical magnetic field structure characteristic of a spheromak. Further analysis of this data in Chapter 9 indicates that poloidal flux amplification is occurring, suggesting that Taylor relaxation processes are operative here. The 100% increase in poloidal flux observed coincides with a drop in toroidal flux, as expected. This process occurs over a time of 3.5-4 μsec, which may be associated with the relaxation time, and the fluxes remain relatively constant thereafter.

Chapter 10 presents calculations of the plasma λ ($\equiv \mu_0 \mathbf{J}/\mathbf{B}$) spatial profiles and time dependence in Regime II, again based on the SSPI principle. Contour plots of λ presented in Section 10.3 are indicative of a decaying spheromak, with λ falling monotonically from a central peak near the magnetic axis. The broadening of this profile with time reflects growth in the minor radius of the spheromak, whereas the fall-off in peak values appears to be highly consistent with a self-similar expansion model in which total helicity is conserved. Section 10.5 discusses a close connection between the assumptions used in a model for magnetic clouds given by Kumar and Rust [16] and the observed characteristics of the spheromak generated in the present experiment. By applying the model to our experiment, a prediction is made suggesting that self-similar expansion may drive magnetic heating within the plasma, as appears to occur in magnetic clouds. This hypothesis is yet untested and is presented as an intriguing area for further study. The measurements presented in Chapters 8-10 constitute the most comprehensive study yet undertaken investigating the evolution of the magnetic structure during the formation, relaxation, and decay of an unbounded, expanding spheromak configuration.

In Chapter 11, an analysis of plasma generated by the stuffed gun, Regime III, is presented. Side-view pictures exhibit several complex dynamical features, including helical arms, a twisted central column, and a propagating mushroom head shape.

By comparing images taken with positive and negative helicity injection, it is found that the helical and twisted structures have chirality (handedness) which is directly associated with the polarity of helicity injection, suggesting that structures have a magnetic origin. Data from a magnetic probe scan is analyzed and correlated with the pictures by performing field line tracing and flux tube reconstruction. These comparisons are indicative of a direct correspondence between bright filaments of plasma observed in the pictures and magnetic flux tubes. This relationship is consistent with the interpretations which solar astronomers use for filaments observed in H_α images of the solar corona [12]. Also using the magnetic data, poloidal and toroidal flux is calculated, but do not exhibit the characteristic flux amplification which Taylor relaxation would predict. Calculations of λ distributions also give no evidence of the signature of a decaying isolated spheromak observed in Chapter 10. These flux and λ measurements definitively demonstrate the stuffed nature of discharges in this Regime.

Chapter 2 Magnetic helicity and spheromaks

2.1 Introduction

In plasma physics, the behavioral dynamics of the plasma is often influenced to a large extent by the magnetic field in which it is immersed. For instance, in the conventional thermonuclear fusion plasma confinement concept of the tokamak, a strong toroidal magnetic field is produced by a set of electrical coils in order to stabilize the plasma against kink instabilities which would otherwise occur. In addition to these vacuum fields created by sources external to the plasma, currents flowing within the plasma also generate a magnetic field. In the tokamak example, toroidal current induced in the plasma produces poloidal field which provides the primary confinement mechanism.

Because magnetic fields play such an important role in plasma physics, it is illuminating to analyze the dynamics of plasmas solely by considering the magnetic field structure. From Maxwell's equations, the magnetic field is ultimately just a divergence-free vector field, and hence can be represented by field lines which are everywhere parallel to the vector field and eventually return to their starting positions (although they may be infinitely long in the special case of ergodic fields). Researchers have found that examining the topological information contained within these field lines uncovers a particularly powerful yet simple way to predict plasma behavior. The most basic topological quantity characterizing a magnetic field is called the *magnetic helicity*, and is the unifying theme of this thesis. In this chapter we will define magnetic helicity, explain its physical interpretation, and relate its importance. The topics of spheromaks and helicity injection will also be discussed. These ideas comprise the theoretical underpinnings of this research work.

2.2 Basic concepts

We begin with a few definitions. A magnetic *field line* is a curve in three-dimensional space whose tangent is everywhere parallel to the local magnetic field vector. Due to the divergence free nature of the magnetic field, no field lines have beginning or ending points, as these would constitute sources or sinks in the vector field. This property implies that all field lines are closed curves, if ergodic situations are neglected. (For ergodic cases, complications arise but the results below remain valid.)

A *flux surface* is defined as a surface through which no magnetic field lines penetrate; i.e., $B \cdot \hat{n}|_S = 0$ where $\hat{n}$ is unit surface normal on surface S. Hence, the flux surface will generally contain within it a continuum of field lines. A *flux tube* is a topological tube which is bounded by a flux surface. As long as the field contained within the flux tube does not exhibit any complex (e.g., bifurcation) behavior, the flux tube will generally resemble a thick field line which closes upon itself, and with varying cross-sectional area along its length. The net magnetic flux Φ through a cross-sectional area of the flux tube will remain invariant along its length.

Consider a volume V which is bounded by a flux surface. We may define the net magnetic helicity K contained within the volume as a scalar quantity given by

$$K = \int_V \mathbf{A} \cdot \mathbf{B} \, dV \tag{2.1}$$

where $\mathbf{A}$ is the vector potential of the magnetic field $\mathbf{B}$.

Since the magnetic vector potential can in principle be constructed for any magnetic field, given the appropriate boundary conditions and gauge constraint, it is clear that the magnetic helicity is fundamentally related to the magnetic field within the volume. Its importance as a meaningful physical concept in plasmas stems from its conservation properties. In particular, by straightforwardly applying vector calculus relations and Maxwell's relations, the conservation equation for the helicity density

$H = \mathbf{A} \cdot \mathbf{B}$ can be written as

$$\frac{\partial H}{\partial t} + \nabla \cdot (\mathbf{E} \times \mathbf{A} + \Phi \mathbf{B}) = -2\mathbf{E} \cdot \mathbf{B} \tag{2.2}$$

or

$$\frac{\partial H}{\partial t} + \nabla \cdot \mathbf{Q} = \mathbf{D} \tag{2.3}$$

where

$$\begin{aligned} \mathbf{Q} &= \mathbf{E} \times \mathbf{A} + \Phi \mathbf{B} \\ \mathbf{D} &= -2\mathbf{E} \cdot \mathbf{B} \end{aligned} \tag{2.4}$$

give explicit expressions for the helicity flux $\mathbf{Q}$ and dissipation $\mathbf{D}$.

For a plasma which is governed by the magnetohydrodynamic (MHD) laws, the electric and magnetic fields obey Ohm's law

$$\mathbf{E} + \mathbf{U} \times \mathbf{B} = \eta \mathbf{J} \tag{2.5}$$

where $\mathbf{U}$ is the convective fluid velocity, $\mathbf{J}$ is the volume current density, and η is the very small electrical resistivity. Thus the dissipation term in the conservation equation is linearly related to the resistivity, $\mathbf{E} \cdot \mathbf{B} = \eta \mathbf{J} \cdot \mathbf{B}$. For ideal MHD plasmas where resistivity is vanishingly small, helicity dissipation is identically zero. Furthermore, if the volume V is bounded by a perfectly conducting container, the electric field

$$\mathbf{E} = -\nabla \Phi_{\mathbf{E}} - \frac{\partial \mathbf{A}}{\partial t} \tag{2.6}$$

vanishes at the boundary and the electrostatic potential $\Phi_{\mathbf{E}}$ is a constant (with the appropriate choice of gauge for $\mathbf{A}$), so that the integral of the helicity flux $\mathbf{Q}$ also vanishes at the surface. Under these circumstances, it is clear that the net magnetic helicity is a well conserved quantity.

$$\frac{\partial K}{\partial t} = \int_V \frac{\partial H}{\partial t}\, dV = 0 \tag{2.7}$$

The concept of helicity conservation in plasmas was first demonstrated by Elsasser [17], and has been applied in a wide variety of contexts. In most laboratory plasmas, highly conductive plasmas are produced within metallic vacuum vessels. Thus, for timescales shorter than the timescale of magnetic diffusion through the vessel walls, the net magnetic helicity can be regarded as a constant. For astrophysical plasmas, where no such conducting boundary is present, the situation is a bit more problematic. However, even in these cases, appropriate choice of boundary conditions admit applicability of the helicity concept.

An apparent difficulty in the use of helicity as a physical invariant lies in the gauge dependence of the vector potential. The vector potential is not unique, as an arbitrary change of gauge $\mathbf{A}' = \mathbf{A} + \nabla\chi$ leaves the magnetic field unchanged $\mathbf{B} = \nabla \times \mathbf{A} = \nabla \times \mathbf{A}'$. However, it can be demonstrated straightforwardly that this difficulty vanishes for simple systems, in which $\mathbf{B}$ does not penetrate the bounding surface; i.e., homogeneous boundary conditions. Consider a simply connected volume V. The gauge change produces the primed helicity

$$\begin{aligned} K' &= \int \mathbf{A}' \cdot \mathbf{B}\, dV \\ &= K + \int \nabla\chi \cdot \mathbf{B}\, dV \\ &= K. \end{aligned} \tag{2.8}$$

Thus, the net helicity of the system is gauge invariant despite the fact that the local helicity density within the volume is not. This property can be extended to the more general inhomogeneous case by defining a relative helicity [18][19][20] rather than the conventional helicity defined above.

2.3 Links, knots, and twist

In the previous section, the net magnetic helicity of a plasma system was shown to exhibit the mathematical properties required of a well behaved physical invariant. However, belying its exceedingly simple definition, the physical meaning of magnetic helicity is not immediately intuitively obvious. In this section, it will be demonstrated that the net magnetic helicity within a volume can be associated with the degree of linkedness, knottedness, and twistedness of field lines within the volume.

As an example, consider the following situation in which two simple untwisted flux tubes are interlinked (see Figure 2.1) [21]. The surfaces of the flux tubes are by definition flux surfaces, and by "untwisted," we mean that field lines within each tube run parallel to its axis, and do not helically wrap around this axis.

The net helicity of this system can be calculated as follows:

$$\begin{aligned} K &= \int\limits_{V1} \mathbf{A}\cdot\mathbf{B}\,dV + \int\limits_{V2} \mathbf{A}\cdot\mathbf{B}\,dV \\ &= \int_{C1} \mathbf{A}\cdot\mathbf{dl} \int_{S1} \mathbf{B}\cdot\mathbf{dS} + \int_{C2} \mathbf{A}\cdot\mathbf{dl} \int_{S2} \mathbf{B}\cdot\mathbf{dS} \\ &= \Phi_1 \int_{C1} \mathbf{A}\cdot\mathbf{dl} + \Phi_2 \int_{C2} \mathbf{A}\cdot\mathbf{dl} \\ &= \Phi_1 \int_{S2} \mathbf{B}\cdot\mathbf{dS} + \Phi_2 \int_{S1} \mathbf{B}\cdot\mathbf{dS} \\ &= 2\Phi_1\Phi_2 \end{aligned} \tag{2.9}$$

or twice the product of the magnetic fluxes through the two flux tubes. On the other hand, if the two flux tubes had not been interlinked, the net helicity would then have vanished. (In the above calculation, note that we have made use of the collinearity of the vectors **B**, **dl**, and **dS**.)

The calculation above demonstrates that helicity is a topological concept closely related to linkage of flux tubes or field lines. Knottedness of flux tubes also contributes to the magnetic helicity, as a similar exercise involving a single flux tube containing a knot would show. This configuration would possess a magnetic helicity in the amount of $\pm\Phi^2$, with polarity determined by the sense of the knot. The correspondence

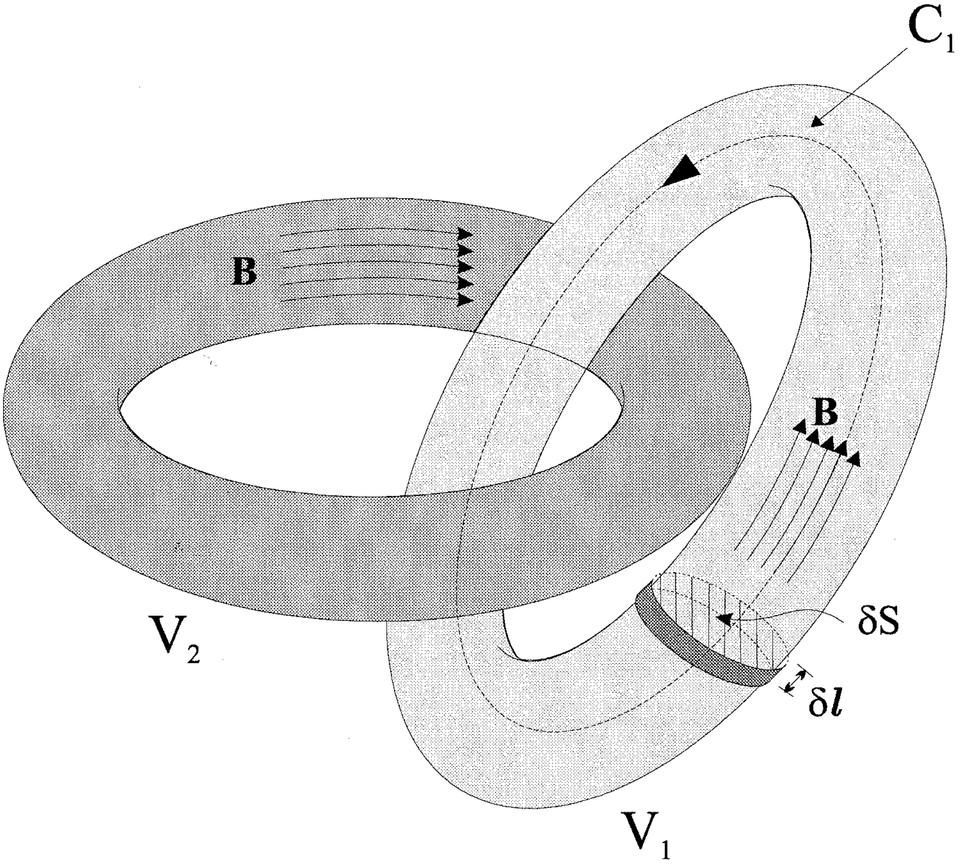

Figure 2.1: Two interlinked untwisted flux tubes. The integration regions and paths discussed in the text are labeled.

between magnetic helicity and flux tube linkage and knotting can be shown formally (see Moffatt [22]) by establishing the equivalence between the definition of helicity and the Gauss linkage integral [23] from knot theory. The linkage integral quantifies the amount of linkage or knotting in closed curves.

In the treatment above, it has been assumed that the flux tubes with which we are dealing are without twist. This constraint may be removed if the contribution to helicity due to twistedness is taken into consideration. An originally untwisted flux tube which is cut and then twisted by $2\pi n$ will acquire a helicity of $n\Phi^2$. This type of helicity is often termed *internal* helicity (i.e., internal to flux tubes) in contrast to the linking and knotting forms of *external* helicity (see, e.g., Berger and Field [20]).

In general the total magnetic helicity can be found by totalling all forms of internal and external helicity.

The physical invariance of helicity in ideal MHD plasmas can hence be interpreted as a statement of the fact that the various types of helicity, including linkedness, knottedness, and twistedness, can be transformed from one form to another but cannot be destroyed. This is perhaps not surprising, as the well known frozen in flux idea implies that field lines must be convected along with the plasma fluid, so that topological relationships between these lines clearly must be preserved throughout the dynamical evolution of the plasma. These topological relationships may only be modified when a small amount of dissipation is introduced into the system, in the form of resistivity. This finite resistivity allows for diffusion of magnetic field lines through the fluid and, for example, admits the possibility that two field lines which had previously been linked can become unlinked. The implications of finite resistivity on magnetic helicity is an important subject which will be considered in the next section.

2.4 Taylor states

In 1959, Woltjer [1] examined the problem of characterizing those states of minimum magnetic energy subject to the constraint of specified constant magnetic helicity. Minimization of the total magnetic energy corresponds, in the language of variational calculus, to $\delta \int_V |\nabla \times \mathbf{A}|^2 \, dV = 0$ while the imposition of the helicity constraint requires the addition of a Lagrangian multiplier [24] λ so that the variational problem can be stated as

$$\delta \int_V \left(|\nabla \times \mathbf{A}|^2 - \lambda \mathbf{A} \cdot (\nabla \times \mathbf{A}) \right) dV = 0 \tag{2.10}$$

and leads to the criterion

$$\nabla \times \mathbf{B} = \lambda \mathbf{B}. \tag{2.11}$$

Invoking Maxwell's equations and noting that the displacement current is neglected in the low frequency MHD approximation, we have $\nabla \times \mathbf{B} = \mu_0 \mathbf{J}$, and Equation 2.11 is simply a statement of the force free condition (i.e., the magnetic force term $\mathbf{J} \times \mathbf{B}$ in the equation of motion vanishes), but with the additional proviso that the Lagrange multiplier λ must be uniform throughout the volume. Thus, neglecting thermal pressure forces, a plasma satisfying this criterion would be in equilibrium. The prediction of a tendency of plasmas toward force-free equilibria agreed well with astrophysical observations which suggested that these force-free states were ubiquitous in nature.

Taylor later expanded upon these results by postulating that in non-ideal MHD plasmas, dissipative effects such as magnetic turbulent reconnection would preserve magnetic helicity while providing a mechanism of destroying magnetic energy [2]. Thus, helicity is better conserved than the energy and such a system would naturally approach this *Taylor state* of minimum magnetic energy, with magnetic helicity invariant. This process of magnetic energy decaying through magnetic reconnection in the approach toward the Taylor state is referred to as *relaxation*.

Taylor applied these ideas to the reversed field pinch (RFP), and suggested that they could be used to explain the magnetic profiles in these laboratory plasmas, with remarkable success. In the time period since the Taylor conjecture was first put forth, it has also been applied in numerous situations and plasma devices. In laboratory plasmas, a Taylor state configuration called the spheromak (which will be described in detail below) has been created and observed to have magnetic field profiles closely matching those predicted by the Taylor theory. Some features of tokamak behavior, such as magnetic islands, also draw upon the Taylor ideas. Many astrophysical and solar plasmas have also been observed to exhibit near force-free behavior, suggesting that some relaxation phenomena are operative in these environments as well.

The most notable advantage inherent in the Taylor approach is a discarding of the usual requirement of knowledge about the initial conditions of the plasma in order to fully determine its final state. Instead, the plasma itself seeks out its preferred magnetic field arrangement subject to the prescribed boundary conditions and helicity conservation. The system is in effect self-organizing or self-ordering and specification of its ultimate state is not dependent on understanding the complex details of the dynamical relaxation process.

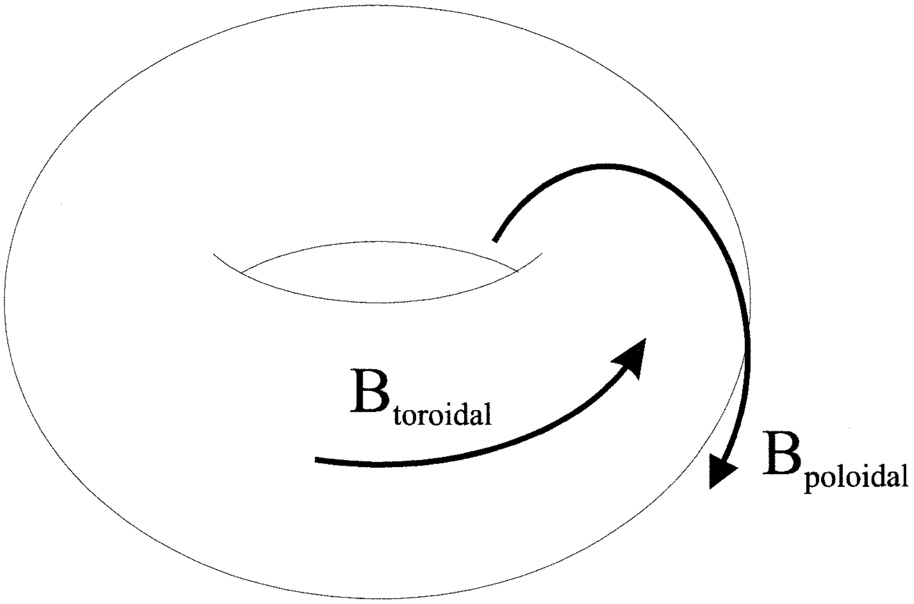

Figure 2.2: Generalized picture of a spheromak.

2.5 Spheromaks

The spheromak configuration, as defined for the purposes of this thesis, is a Taylor state plasma of roughly toroidal shape with finite helicity in which no extraneous materials thread the central hole of the torus (see Figure 2.2). The spheromak contains both toroidal and poloidal magnetic fields of similar magnitudes, the mutual linkage of which contributes to the net magnetic helicity. The volume occupied by a spheromak plasma is singly connected and the topological equivalent of a sphere, and is thus the simplest example of an isolated Taylor state. The particular magnetic field structure within the spheromak is then dependent only on the boundary conditions imposed, and is typically specified by the shape of the flux surface bounding the spheromak. For example, the derivation might proceed as follows.

The right-hand side of the force-free condition (Eq. 2.11) may be substituted into the left-hand side of the same to give

$$\nabla \times \left(\frac{\nabla \times \mathbf{B}}{\lambda} \right) = \lambda \mathbf{B} \tag{2.12}$$

$$\begin{aligned}\nabla\left(\nabla\cdot\mathbf{B}\right)-\nabla^2\mathbf{B} &= \lambda^2\mathbf{B}\\ \left(\nabla^2+\lambda^2\right)\mathbf{B} &= 0\end{aligned}$$

where the ∇^2 operator is the vector Laplacian. It is thus evident that the force-free criterion is exactly equivalent to a statement of the vector Helmholtz equation. The problem becomes fully determined once a complete set of boundary conditions is specified.

In order to simplify the analysis, we will make use of the following observation (modified from Ref. [19]). The general solution of Eq. 2.11 can be written in the form

$$\mathbf{B}=\lambda\nabla\times\left(\chi\mathbf{a}\right)+\nabla\times\nabla\times\left(\chi\mathbf{a}\right) \tag{2.13}$$

where $\mathbf{a}$ is an irrotational vector field whose divergence is constant spatially $\nabla\left(\nabla\cdot\mathbf{a}\right)=0$, and χ satisfies the scalar Helmoltz equation

$$\left(\nabla^2+\lambda^2\right)\chi=0.$$

This assertion can be shown by direct substitution into Eq. 2.11. The second term on the right-hand side of Eq. 2.13 can, with the help of vector calculus relations, be written in the form

$$\begin{aligned}\nabla\times\nabla\times\left(\chi\mathbf{a}\right) &= \nabla\times\left(\chi\nabla\times\mathbf{a}-\mathbf{a}\times\nabla\chi\right)\\ &= \left(\mathbf{a}\cdot\nabla\right)\nabla\chi-\left(\nabla\chi\cdot\nabla\right)\mathbf{a}+\nabla\chi\left(\nabla\cdot\mathbf{a}\right)-\mathbf{a}\left(\nabla^2\chi\right)\end{aligned}$$

so that taking its curl leaves only one term

$$\nabla\times\nabla\times\nabla\times\left(\chi\mathbf{a}\right)=-\nabla\times\left(\left(\nabla^2\chi\right)\mathbf{a}\right).$$

Thus, taking the curl of Eq. 2.13 gives

$$\begin{aligned}\nabla \times \mathbf{B} &= \lambda \nabla \times \nabla \times (\chi \mathbf{a}) - \nabla \times \left(\left(\nabla^2 \chi \right) \mathbf{a} \right) \\ &= \lambda \nabla \times \nabla \times (\chi \mathbf{a}) + \nabla \times \left(\lambda^2 \chi \mathbf{a} \right) \\ &= \lambda \mathbf{B}\end{aligned}$$

where the final equality holds as long as λ is a constant. QED.

In the following sections, the force-free magnetic profiles of two basic types of spheromaks will be derived: the spherical (i.e., classical) spheromak and the cylindrical spheromak.

2.5.1 Spherical spheromak

In the so-called classical spheromak, first discussed by Rosenbluth and Bussac [25], the plasma is enclosed within a spherical conducting boundary through which no magnetic field lines penetrate. In this case, spherical coordinates (r, θ, φ) are appropriate and we will apply Eq. 2.13 choosing the vector field $\mathbf{a} = \mathbf{r} = r\widehat{\mathbf{r}}$, which has the properties $\nabla \times \mathbf{a} = 0$ and $\nabla \cdot \mathbf{a} = 3$, and thus satisfies the requirements. The necessary boundary conditions for a sphere of radius R are

$$B_r|_{r=R} = 0$$

with

$$\begin{aligned}B_r &= \widehat{\mathbf{r}} \cdot \left[\lambda \nabla \times (\chi \mathbf{r}) + \nabla \times \nabla \times (\chi \mathbf{r}) \right] \qquad (2.14) \\ &= \widehat{\mathbf{r}} \cdot (\mathbf{r} \cdot \nabla) \nabla \chi - \widehat{\mathbf{r}} \cdot (\nabla \chi \cdot \nabla) \mathbf{r} + \widehat{\mathbf{r}} \cdot \nabla \chi (\nabla \cdot \mathbf{r}) - \widehat{\mathbf{r}} \cdot \mathbf{r} \left(\nabla^2 \chi \right) \\ &= (\mathbf{r} \cdot \nabla) (\widehat{\mathbf{r}} \cdot \nabla \chi) - (\nabla \chi \cdot \nabla) r + 3 \widehat{\mathbf{r}} \cdot \nabla \chi + r \left(\lambda^2 \chi \right) \\ &= r \frac{\partial^2 \chi}{\partial r^2} - \frac{\partial \chi}{\partial r} + 3 \frac{\partial \chi}{\partial r} + r \lambda^2 \chi \\ &= \frac{1}{r} \left[r^2 \frac{\partial^2 \chi}{\partial r^2} + 2r \frac{\partial \chi}{\partial r} + \lambda^2 r^2 \chi \right] .\end{aligned}$$

The general solution to the scalar Helmholtz equation can be written

$$\chi = \sum_{l,m} c_{lm} \cdot j_l\left(\lambda r\right) P_l^m\left(\cos\theta\right) e^{im\phi}$$

where $P_l^m\left(\cos\theta\right)$ are the associated Legendre polynomials and $j_l\left(\lambda r\right)$ are the spherical Bessel functions, which satisfy the differential equation

$$r^2\frac{\partial^2\chi}{\partial r^2} + 2r\frac{\partial\chi}{\partial r} + \left(\lambda^2 r^2 - l\left(l+1\right)\right)\chi = 0.$$

Thus, comparing to the bracketed term in Eq. 2.14, we have as the boundary condition $B_r|_{r=R} \propto \chi\left(\lambda R\right) = 0$ and λ must be chosen so that λR is the first zero of the Bessel function $j_l\left(\lambda r\right)$. The spheromak solution is the minimum energy equilibrium with azimuthal symmetry $\left(\partial/\partial\varphi = 0\right)$, which we identify as the $m = 0$, $l = 1$ eigenfunctions so that

$$\chi = j_l\left(kr\right)\cos\theta$$

and the resulting components of **B** are then

$$\begin{aligned}
B_r &= 2B_0\frac{j_1\left(kr\right)}{kr}\cos\theta \\
B_\theta &= -B_0\frac{1}{kr}\frac{d}{dr}\left(rj_1\left(kr\right)\right)\sin\theta \\
B_\phi &= B_0 j_1\left(kr\right)\sin\theta.
\end{aligned}$$

The classical spheromak solution flux-surfaces are shown in Figure 2.3a.

2.5.2 Cylindrical spheromak

The cylindrical spheromak configuration is perhaps a more appropriate model for the majority of laboratory spheromaks. In this situation, the flux-conserving boundary of the spheromak comprises a cylinder with circular endcaps. In cylindrical coordinates

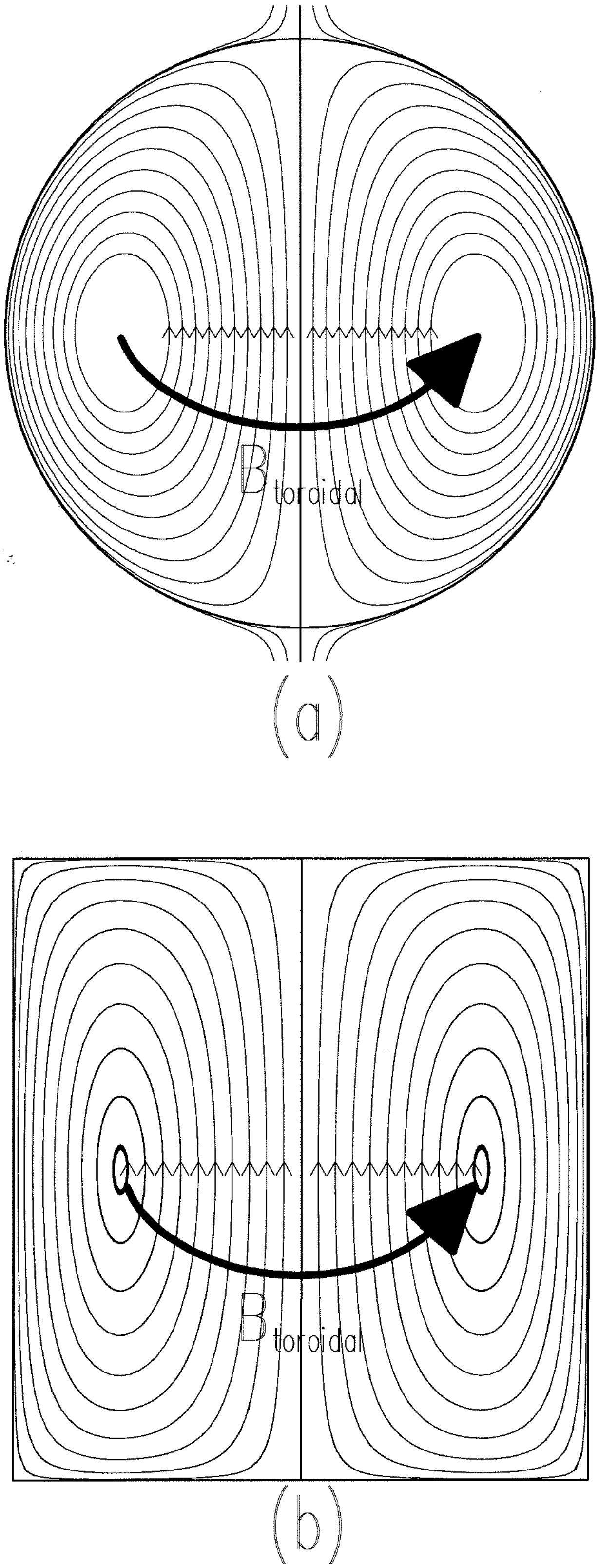

Figure 2.3: Magnetic field structure in a poloidal plane for two types of spheromaks: (a) Spherical (i.e., classical) and (b) Cylindrical.

(r, ϕ, z) the Helmholtz equation has the general solution

$$\chi = \sum_m c_m J_m \left(k' r\right) \sin kz \cdot e^{im\phi}$$

where $k' = \sqrt{\lambda^2 - k^2}$. Using Eq. 2.13 with $\mathbf{a} = \widehat{\mathbf{z}}$ gives

$$\begin{aligned} \mathbf{B} &= \lambda \nabla \times (\chi \widehat{\mathbf{z}}) + \nabla \times \nabla \times (\chi \widehat{\mathbf{z}}) \\ &= \lambda \nabla \chi \times \widehat{\mathbf{z}} + (\widehat{\mathbf{z}} \cdot \nabla) \nabla \chi - (\nabla \chi \cdot \nabla) \widehat{\mathbf{z}} + \nabla \chi (\nabla \cdot \widehat{\mathbf{z}}) - \widehat{\mathbf{z}} \left(\nabla^2 \chi\right) \\ &= \lambda \nabla \chi \times \widehat{\mathbf{z}} + (\widehat{\mathbf{z}} \cdot \nabla) \nabla \chi + \lambda^2 \chi \widehat{\mathbf{z}} \end{aligned}$$

the components of which are

$$\begin{aligned} B_r &= \lambda \frac{1}{r} \frac{\partial \chi}{\partial \phi} + \frac{\partial^2 \chi}{\partial r \partial z} \\ B_z &= \lambda^2 \chi + \frac{\partial^2 \chi}{\partial z^2} \\ B_\phi &= -\lambda \frac{\partial \chi}{\partial r} + \frac{\partial^2 \chi}{\partial \phi \partial z}. \end{aligned}$$

Restricting to the case of azimuthal symmetry ($m = 0$), the boundary conditions

$$\begin{aligned} B_r|_{r=R} &= 0 \\ B_z|_{z=0} &= B_z|_{z=L} = 0 \end{aligned}$$

are satisfied when $k' R$ is a zero of the Bessel function $J_1 \left(k' r\right)$ and $k = n\pi/L$. The minimum energy solution corresponds to $n = 1$. Thus, we have finally that the components of the magnetic field in the cylindrical spheromak are

$$\begin{aligned} B_r &= B_0 \left(\frac{\pi}{L}\right) J_1 \left(k' r\right) \cos \left(\pi z/L\right) \\ B_\phi &= -B_0 \lambda J_1 \left(k' r\right) \sin \left(\pi z/L\right) \\ B_z &= -B_0 \left(\frac{\pi}{L}\right) J_0 \left(k' r\right) \sin \left(\pi z/L\right). \end{aligned}$$

The magnetic flux surfaces of the cylindrical spheromak are shown in Figure 2.3b. Note the qualitative similarities to the spherical case.

2.6 Helicity injection

In many important situations, the net helicity within the system is not conserved because the boundary conditions imposed differ from those described above. Because of these modified boundary conditions, net helicity flux may increase or decrease the total helicity within the volume, a process called *helicity injection.* This circumstance may in fact be desirable; for example, helicity injection can provide a method of replenishing helicity lost through dissipation in a spheromak or other plasma device. Thus, it is important to understand the processes by which helicity injection may take place.

Helicity injection can be categorized into two classes: DC (or electrostatic) helicity injection and AC (or electromagnetic) helicity injection. These two classes become readily apparent once the helicity flux $\mathbf{Q}$ in Eq. 2.4 is rewritten as

$$\begin{aligned} \mathbf{Q}' &= \mathbf{Q} + \nabla\times(\Phi_{\mathbf{E}}\mathbf{A}) \\ &= 2\Phi_{\mathbf{E}}\mathbf{B} + \mathbf{A}\times\frac{\partial\mathbf{A}}{\partial t} \end{aligned} \tag{2.15}$$

where we have taken advantage of the fact that adding an arbitrary divergence-free field does not affect the conservation equation. We now identify the first term on the right-hand side of Eq. 2.15 as contributing to DC helicity injection and the second term as contributing to AC helicity injection.

The net rate of DC helicity injection can be calculated by integrating a surface integral

$$\left(\frac{dK}{dt}\right)_{DC-injection} = \int_S (2\Phi_{\mathbf{E}}\mathbf{B})\cdot dS \tag{2.16}$$

and clearly requires both that magnetic field lines intercept the boundaries of the volume and that the electrostatic potential must not be a constant in order for the injection rate to be finite. The second requirement implies that the boundary cannot

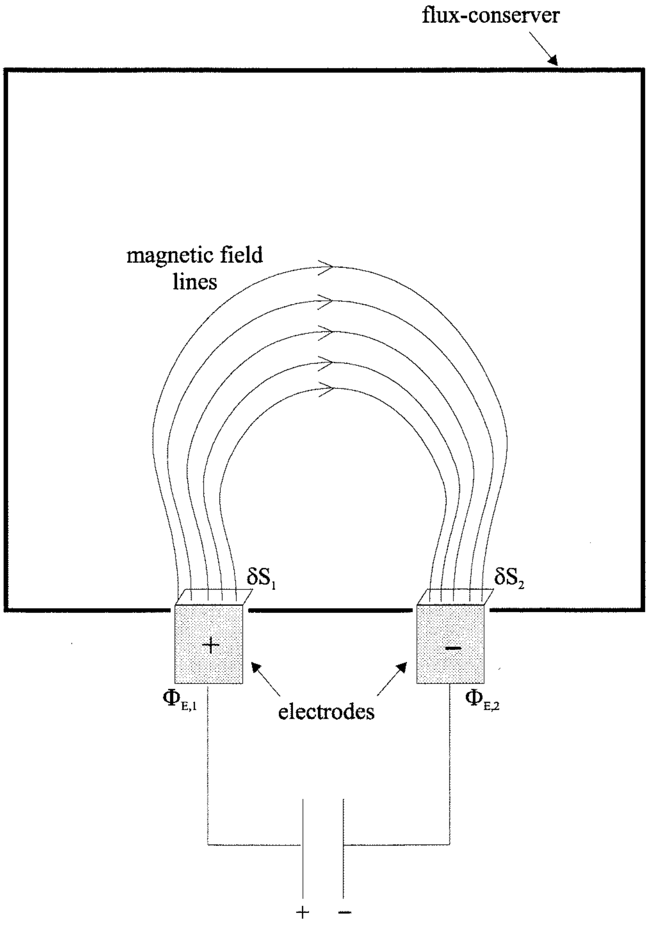

Figure 2.4: Example of DC Injection into a volume.

consist of one continuous electrical conductor, which would form an equipotential. Rather, the boundary must be made up of multiple conductors at different potentials.

A simple example of a DC injection scheme is shown in Figure 2.4. Two areas δS_1 and δS_2 of the boundary have differing electric potentials $\Phi_{\mathbf{E},1}$ and $\Phi_{\mathbf{E},2}$, and are joined by magnetic field lines (which intersect both areas) with net magnetic flux $\Phi = \int_{\delta S_1} \mathbf{B} \cdot dS = -\int_{\delta S_2} \mathbf{B} \cdot dS$. Each unit of magnetic flux which enters the volume through one area leaves the volume through the other area. The net DC injection rate is then $2V\Phi$ where $V = \Phi_{\mathbf{E},1} - \Phi_{\mathbf{E},2}$ is the voltage applied between the two areas (which may be electrodes). DC injection using this method has been verified in numerous experimental configurations (e.g., see Barnes [26]).

AC or electromagnetic helicity injection originates from the second term of Eq. 2.15. In order to evaluate the rate of AC injection, we need to evaluate the integral

$$\left(\frac{dK}{dt}\right)_{AC-injection} = \int_V \nabla \cdot \left(\mathbf{A}\times\frac{\partial \mathbf{A}}{\partial t}\right) dV = \int_S \left(\mathbf{A}\times\frac{\partial \mathbf{A}}{\partial t}\right) \cdot dS. \tag{2.17}$$

Noting that with the gauge convention that the electrostatic potential is constant on electrical conductors, Eq. 2.6 implies that $\partial \mathbf{A}/\partial t$ vanishes on the surface. Thus, AC injection is not possible for simply connected volumes. AC injection is only applicable to multiply connected volumes, in which Gauss' Law must be modified so that the second equality in Eq. 2.17 is not applicable. Essentially, one or more branch cuts must be created in **A** in order to reduce the volume to a simply connected one. The subject of electromagnetic helicity injection will not be explored at greater length here, because in the present thesis we will restrict ourselves to simply connected volumes. The interested reader is referred to Ref. [18]. It should be noted that, unlike in the case of electrostatic injection, AC injection has not been robustly verified experimentally.

Part I

Compact Toroid acceleration and injection into a tokamak

Chapter 3 CT Injector: experimental setup and diagnostics

3.1 Introduction

The first part of this thesis work describes experiments performed on a compact toroid[1] (CT) accelerator, a novel device which takes advantage of features unique to the spheromak state. The spheromak is particularly well suited as a candidate for acceleration due mainly to the fact that it is a minimum energy state. Because of this, it is a robust object which possesses the properties of stability and long lifetimes. Under the extreme forces encountered during high acceleration, a spheromak is able to survive and maintain its cohesion. Furthermore, it consists of a closed magnetic topology so that the integrity of the field lines will be maintained under translation.

The development of the spheromak acceleration concept began in the 1980s with the work of Hammer, Hartman, et al., at the Ring Accelerator Experiment (RACE) program at Lawrence Livermore National Laboratory [5]. With the RACE device, spheromaks of 20 μg were accelerated up to speeds of 140 km/s with an electrical efficiency of 30%. A two-fold radial compression of the spheromak was simultaneously achieved through tapering of the acceleration electrodes. These experiments provided the first demonstrations of the use a coaxial railgun accelerator to propel a dense spheromak plasma to extremely high speeds.

Several applications are made possible with the ability to produce high density and high velocity spheromaks. For example, x-rays can be produced by colliding a heavy ion plasma with a wall. In the tokamak physics area, injection of a high

---

[1] The term compact toroid refers to a class of plasmoids which includes but is not limited to spheromaks. It is used here in order to maintain consistency with previous published work documenting this device. This also happens to be the terminology commonly used in the injection/acceleration field.

helicity content spheromak could provide a means of helicity injection (and thus non-inductive current drive)[27]. One particularly promising concept which also motivates the present work is the injection of a high density spheromak into a tokamak for refueling purposes.

Theoretical analyses of spheromak injection into tokamaks have concluded that it may be a viable refueling technique for reactor-grade tokamak plasmas [9][28]. However, to date, empirical investigations in this area have been fairly limited. Initial experiments of unaccelerated CTs into the small ENCORE tokamak at Caltech [4] were followed by a demonstration of accelerated CT injection into the medium-sized TdeV tokamak [6].

The goal of the Caltech CT Injector project, the subject of the first part of this thesis work, is to further understanding of the issues involved in spheromak acceleration and injection into a tokamak for the purposes of refueling. In the first phase of the project, which took place at Caltech, the device was made ready and its performance was improved to the point where penetration of 1 Tesla toroidal fields was possible. In the second phase, the Injector was transported to Austin, Texas, where it was mated with the Texas Experimental Tokamak-Upgrade (TEXT-U) device and tokamak injection experiments were performed.

3.2 Coaxial spheromak formation

The CT Injector employs a magnetized Marshall gun [29] (also known as a magnetized coaxial gun) configuration for the formation stage. This formation method is one of several which have been successfully utilized by previous researchers; other methods include the flux core, Z θ-pinch, and kinked Z-pinch. However, the coaxial gun method is arguably the most well established formation scheme, having been employed to generate very high performance spheromaks with high temperatures (400 eV), helicity content (magnetic fields of 3 T), and long lifetimes (10 ms).

The coaxial gun operational sequence is summarized in Figure 3.1. The sequence involves four steps:

(a) In this initial step, a poloidally directed magnetic field is generated by energizing an electromagnet coil. This magnetic field is called the *stuffing flux* field (or alternatively, the *bias* magnetic field). Although the stuffing flux field is generally powered by a pulsed power supply, the time scale of its waveform is often much greater than the duration of the formation discharge, so that it can be considered to be a quasistatic DC field.

Four high-speed valves then puff a cloud of gas (typically hydrogen, deuterium, or helium) into the region between the inner and outer electrodes.

(b) Through the use of a high voltage pulsed power supply (usually consisting of an ignitron-switched capacitor bank), a large voltage is abruptly applied across the electrode gap. The high voltage breaks down the gas and subsequently drives current through the resulting donut-shaped plasma, creating a toroidal magnetic field imbedded ("frozen") in the plasma.

(c) MHD $\overrightarrow{J} \times \overrightarrow{B}$ forces acting on the ring of plasma push the ring out the muzzle of the gun. However, since the plasma is a flux-conserver and expels the external magnetic field, the stuffing flux field must be distended to accommodate this motion out of the gun. Furthermore, this stretching of the field lines requires energy and thus robs kinetic energy from the plasma.

(d) If the formation current is sufficiently large, the $\overrightarrow{J} \times \overrightarrow{B}$ force overcomes the resistance provided by the tension forces and is able to sufficiently distend the stuffing flux field lines so that reconnection occurs behind the plasma ring. The isolated plasmoid thus formed possesses a closed magnetic field structure containing both poloidal and toroidal field, and consequently has finite magnetic helicity. This completes the formation process, and by Taylor's conjecture the plasma relaxes to a near force-free compact torus (i.e., spheromak) configuration.

From this discussion, it is apparent that there is a threshold value for gun current which determines the coaxial gun's operational regime. For gun currents higher than this value a free spheromak is formed, whereas the plasma cannot overcome the tension forces imposed by the stuffing flux when the current is less than this value. Empirically, a sharp cutoff in operable values of $\lambda_{gun} \equiv \mu_0 I_{gun}/\Phi_{stuff}$ (with gun

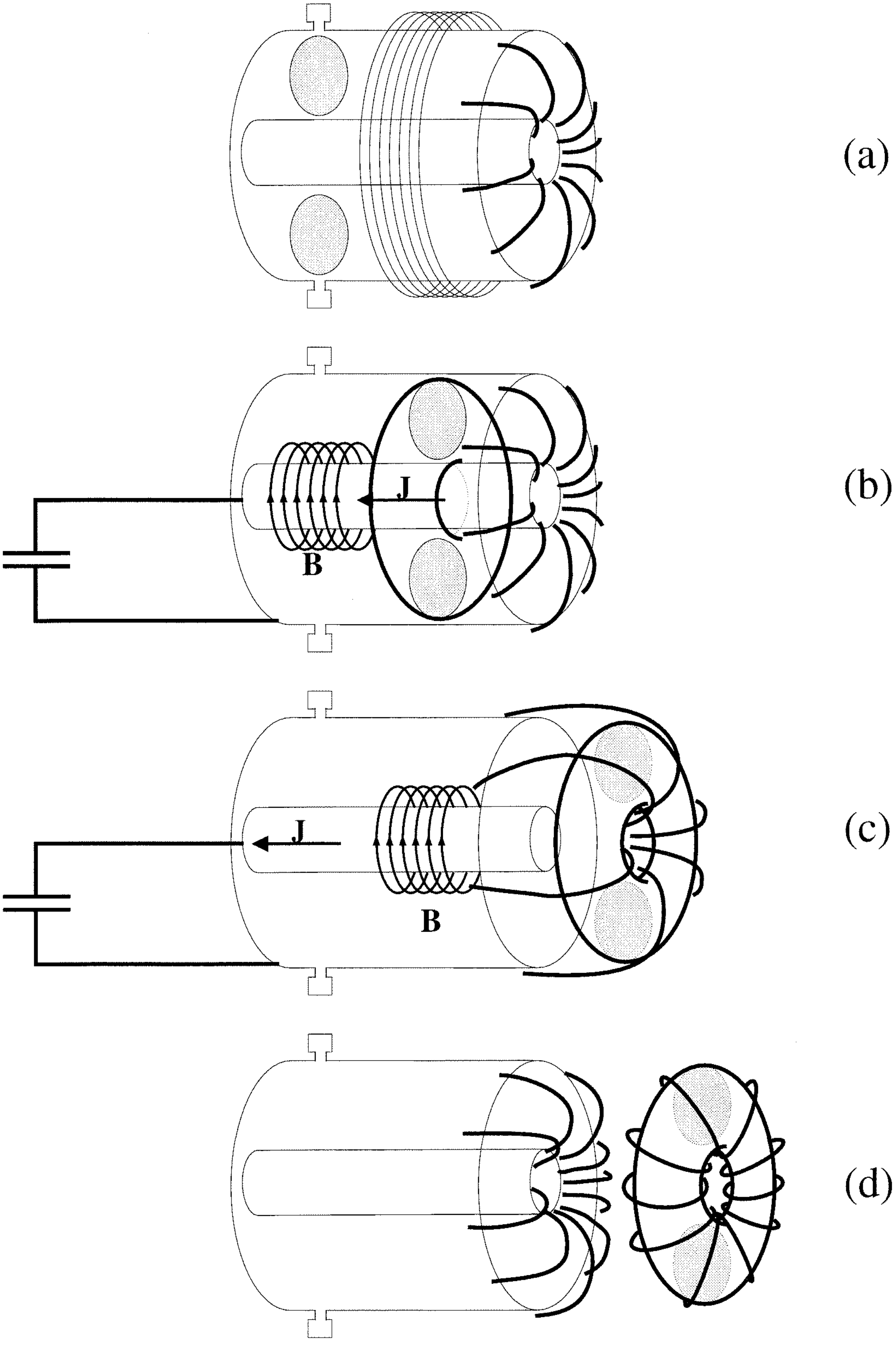

Figure 3.1: Spheromak formation sequence in the magnetized coaxial gun method. See text.

current I_{gun} and stuffing flux Φ_{stuff}) has been observed [26]. Gun behavior can be described intuitively: when λ_{gun} is below the threshold value the plasma cannot detach (i.e., is "stuffed"), while excessively high values of λ_{gun} correspond to very low stuffing flux cases, in which case spheromaks with very low helicity content are produced.

However, the precise criterion that must be met for successful spheromak formation is a subject of current debate. Nevertheless, the essential physics can be obtained by considering a simple model as follows. If the toroidal field is assumed to be of the form $B_{tor} \cong \mu_o I_{gun}/(2\pi r)$ (i.e., an infinitely long wire) and the poloidal field is $B_{pol} \cong \Phi_{stuff}/(\pi r^2)$, then the requirement that magnetic pressure exceeds tension gives $\lambda_{gun} > 2/r$ where the applicable value of r would be a characteristic radius of the system, such as the outer electrode radius r_e. For example, this naive result may be compared with the value derived by Schaffer [30] for an axisymmetric spheromak in an infinite cylinder, $\lambda_{geom} = 3.8317/r_e$. It is evident that although the numerical constant may depend on the model used and the details (e.g., shape) of the gun mouth, the critical value λ_{geom} is mainly dependent on geometric considerations.

3.3 Apparatus

3.3.1 Overview

Figure 3.2 depicts the principal elements of the Caltech compact torus injector schematically. The injector consists of a two-stage coaxial electrode system, comprised of a formation section and an acceleration section. The outer electrode (16 cm inner diameter) is copper spray-coated with tungsten in the formation region, and transitions into copper-shrouded tantalum in the acceleration region. The inner electrode is a 6.4 cm diameter tantalum sheath surrounding a copper tube. The copper ensures that both electrodes are good magnetic flux-conservers on the experimental time scale, so that the decay of the CT magnetic helicity is minimized.

The spheromak is first formed using the magnetized coaxial gun method described

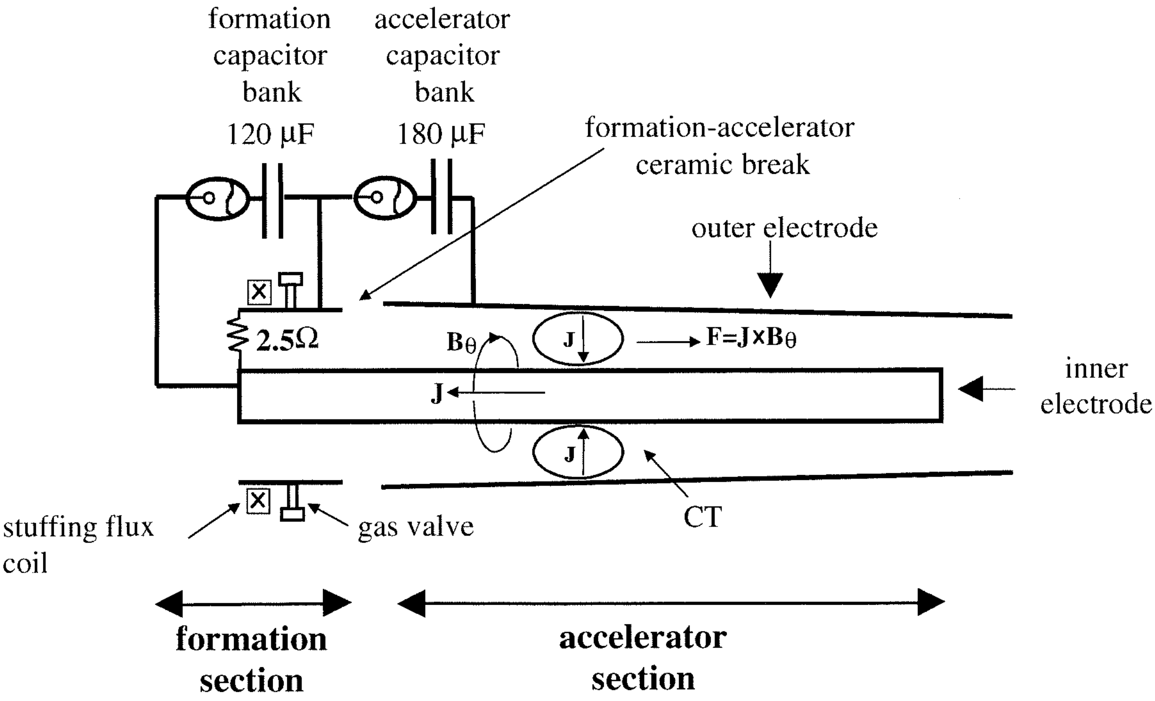

Figure 3.2: Schematic diagram of major components of the compact torus injector.

above, with an ignitron employed to discharge a capacitor bank consisting of 2×60 μF capacitors operated at 8-10 kV. After the CT is formed, acceleration is provided by the second stage of the device. Another ignitron circuit discharges the accelerator capacitor bank (3×60 μF at ≈11 kV), propelling the CT through the ≈3 meter acceleration section, again using MHD $\vec{J} \times \vec{B}$ forces. The acceleration stage is exactly equivalent to a coaxial railgun, with the CT acting as its armature.

The electrode system is housed within a stainless steel vacuum vessel with 8 inch inner diameter. A cantilevering assembly supports the inner electrode from one end (the left end in the diagram). Conflat flanges at various locations along the vacuum vessel allow for diagnostic access for the experiment. Vacuum is maintained using a Leybold Turbovac-1000 oil-free turbopump backed by a Tribodyn-100/38 roughing pump. Thus, vacuum purity is maintained through the use of oil-free pumping components throughout; this was an important performance concern, as will be discussed in the next chapter. Base pressures of approximately 10^{-7} Torr were typically attained.

3.3.2 Stuffing magnetic field subsystem

The stuffing flux, or bias magnetic field, is generated by an electromagnet coil and magnetic circuit as illustrated in Figure 3.3. A magnetic circuit consisting of an iron cage and a Permandure core inside the inner electrode concentrates the magnetic field in the interelectrode region. (The iron cage is constructed out of two annular endplates joined by 16 connecting rods.) The field is also thus shaped to produce the poloidal field as required for the CT formation process (c.f. Section 3.2).

With the associated power supply, the stuffing flux subsystem provides up to 6 milliwebers of stuffing flux. The maximum value is determined mainly by saturation of the magnetic material.

3.3.3 Gas valve subsystem

Gas is puffed into the interelectrode region using a set of four gas valves employing a design (Figure 3.4) modified from that of Thomas [31]. The valve normally has a back-pressure of 30 psi of ultra high purity hydrogen. When the driver coil is energized, the aluminum disc is repelled by virtue of the diamagnetic effect. Gas is then admitted through the valve until the combination of the spring restoring force and gas pressure forces on the disc reseat the disc over the O-ring, thus reestablishing the vacuum seal. With a fast pulsed power supply (see below) driving the coil, this arrangement produces a very sharp puff of gas due to the very fast opening time of about 160 μs.

3.3.4 Power supplies

Due to the pulsed nature and high peak power requirements of the device, the power supplies used to power the various subsystems are based on capacitors. The formation and accelerator subsystems, which demand extremely high currents, were switched

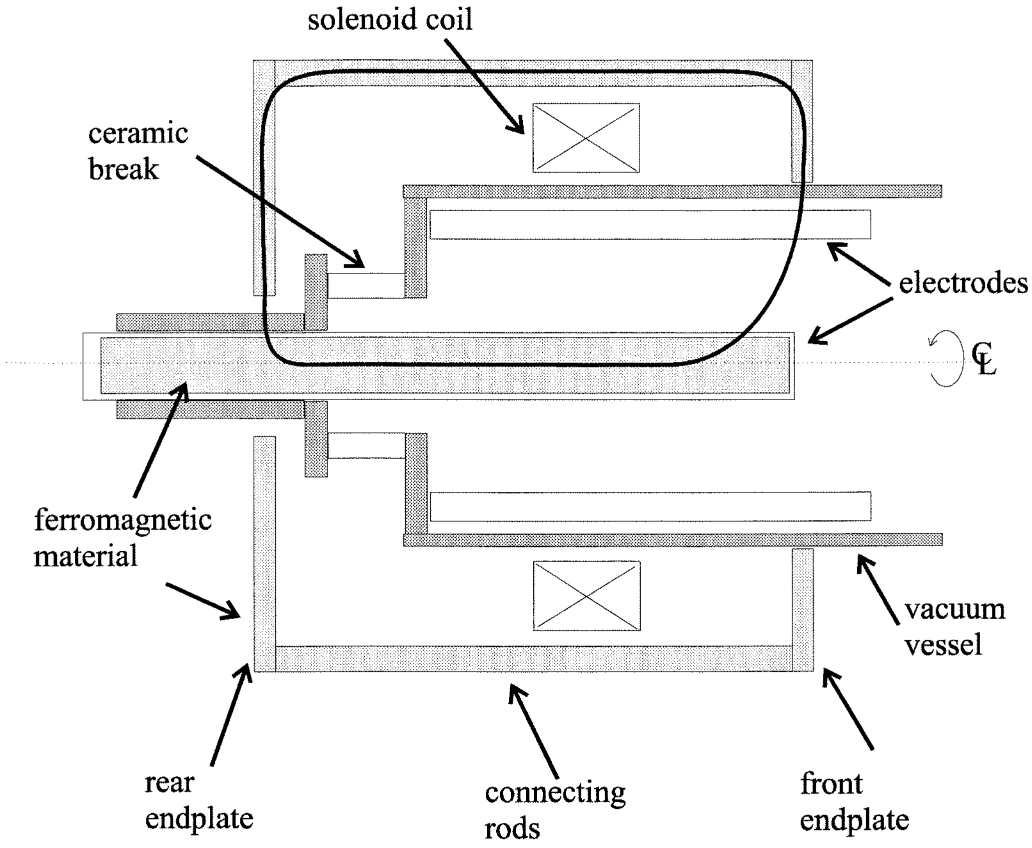

Figure 3.3: Schematic of stuffing magnetic field subsystem, including solenoid coil and magnetic circuit. The superimposed solid line is a representative magnetic field line.

using ignitron/krytron circuits, whereas the stuffing flux and gas valves required lower currents and were handled with silicon controlled rectifiers (SCR).

Triggering of both the ignitron and SCR switched capacitor banks is fiberoptic in order to provide electrical isolation and to prevent ground loops. A custom built timing sequencer (constructed by F. Cosso) generates the fiberoptic pulses which trigger the various power supplies with the appropriate time delays.

In Figure 3.5, the basic ignitron trigger circuit is shown. A krytron switch (EG&G model KN-6B) is triggered by a fiberoptical input and discharges a 2 μF trigger capacitor which is charged with about 1500 V. The resultant voltage pulse is coupled to the ignitor of the ignitron (National Electronics NL-7703) through a 1:3 step-up transformer. After a delay of less than 1 μs, the ignitron becomes fully conductive;

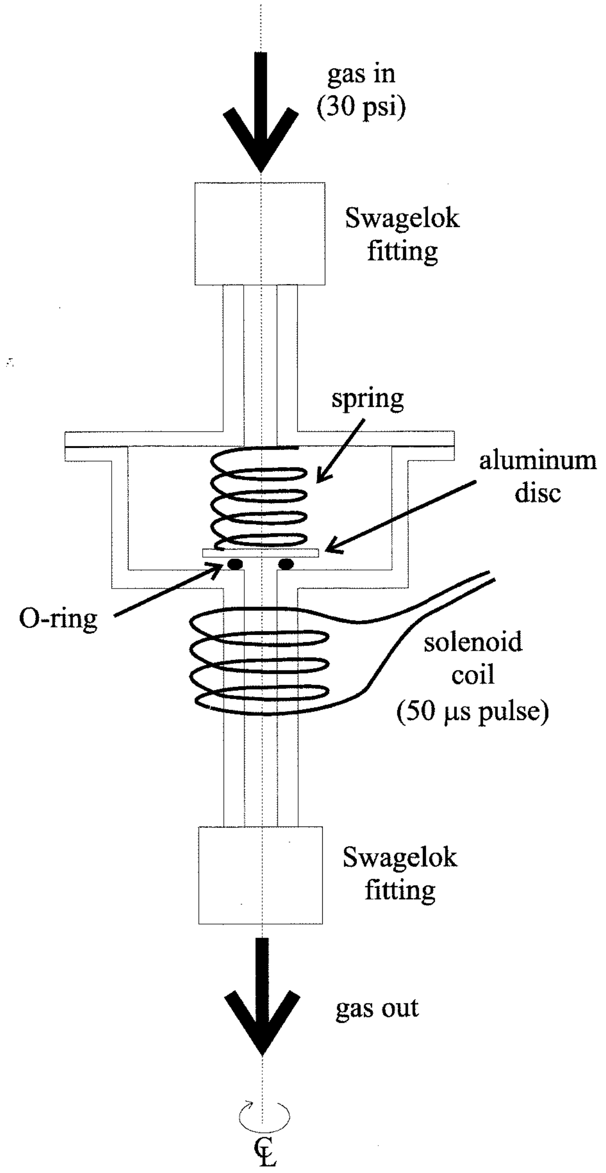

Figure 3.4: Schematic of fast gas puffing valve.

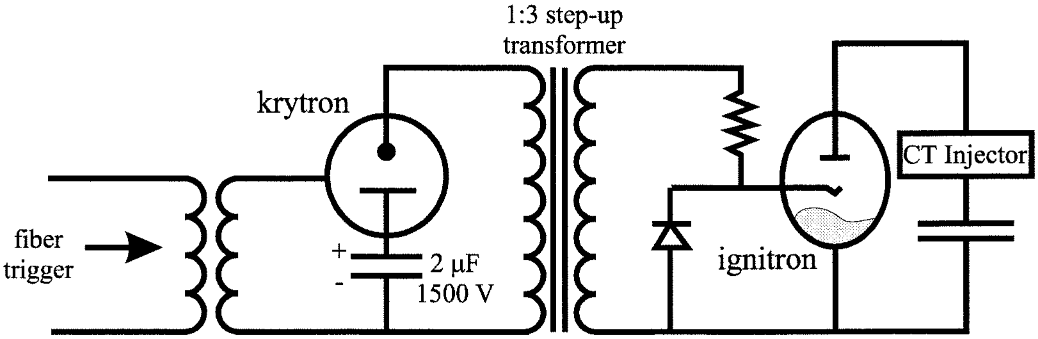

Figure 3.5: Schematic of krytron-based ignitron trigger circuit.

the risetime and peak current achieved is highly dependent on the inductance of the system. In order to increase performance and maximize efficiency, connections and busswork were accordingly designed to minimize inductance. Each ignitron was mounted onto one 60 μF capacitor along with the associated busswork and coaxial low inductance Belden YK-198 cables. Two such assemblies in parallel were used for the formation bank (120 μF total) while three were employed for the accelerator bank (180 μF). Fast charging of the capacitor banks was provided by a constant current high voltage source (Maxwell CCDS).

3.3.5 TEXT-U tokamak

Figure 3.6a shows a cross-sectional view of the TEXT-U tokamak, including one toroidal field coil and the CT injector acceleration electrodes superimposed. The CT injector was connected to the tokamak vacuum chamber with a vacuum bellows, and the entire injector assembly was mounted on rails, allowing adjustment of the longitudinal positioning of the injector relative to the tokamak plasma. TEXT-U is a medium-sized tokamak, with major radius 1.05 m and minor radius 27 cm. TEXT-U diagnostics include multichord density interferometers, soft x-ray detectors, and Mirnov MHD coils. CT injection experiments were conducted with the tokamak operating in a limiter configuration, with $\approx$10 kG toroidal fields, and $\approx$100 kA plasma currents. Some experiments were performed at lower toroidal fields by firing the

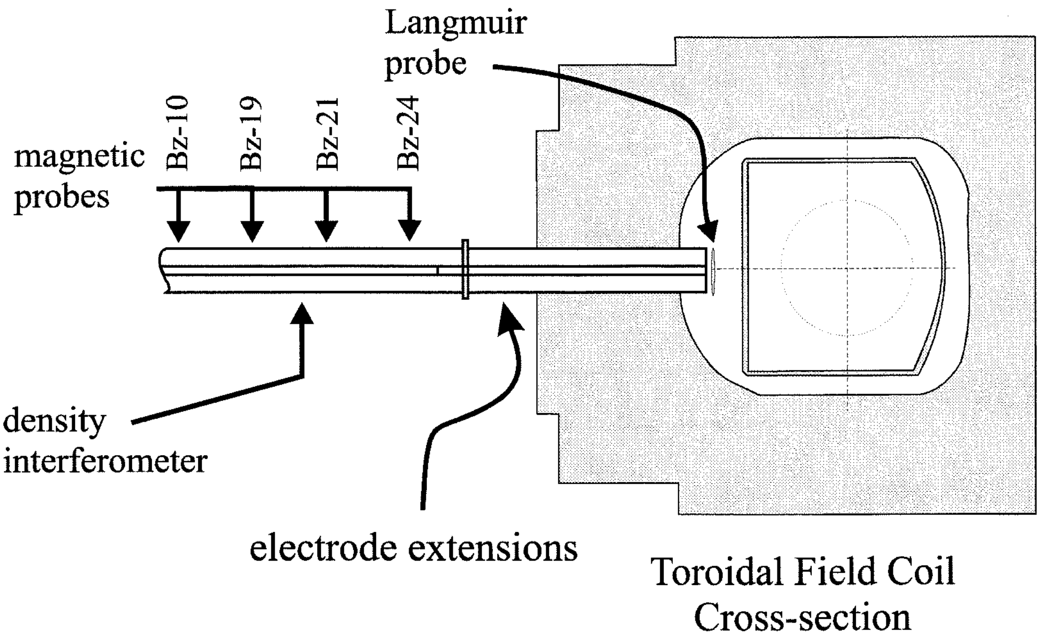

Figure 3.6: Schematic of the accelerator electrodes (with extensions) superimposed over a cross-sectional view of the TEXT-U tokamak and a toroidal field coil.

injector during the decaying portion of the TF, after the tokamak discharge.

3.4 Diagnostics

Four magnetic pickup probes spaced at 0.5 meter intervals along the outer electrode provide time of flight measurements, a helium-neon laser interferometer measures the density at a point late in the acceleration phase, and a Langmuir probe measures ion current from the plasma as it exits the injector (Figure 3.6). A sample shot is shown in Figure 3.8.

3.4.1 Magnetic probes

The magnetic probes consist of pickup loops made of magnet wire which are wound on a 0.19 inch diameter Teflon form. The probes are situated inside thin wall (10 mil) stainless steel tubes which are inserted through holes in the accelerator outer electrode. In this way, the magnetic field in the Z direction (along the axial length

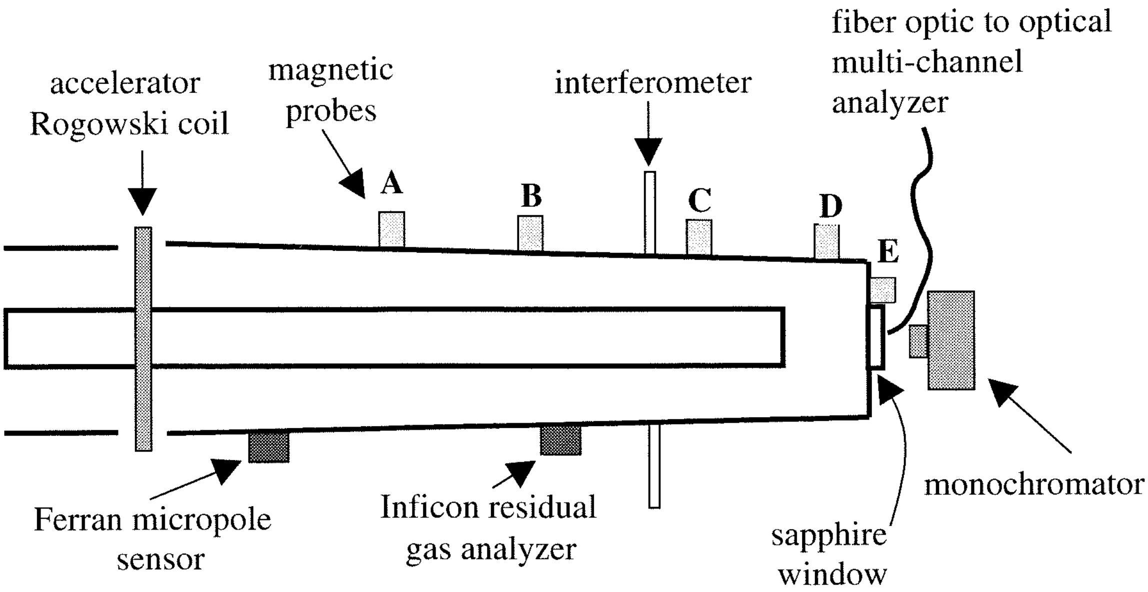

Figure 3.7: Diagnostics on the CT Injector.

of the device) is measured near the edge of the spheromak. Peak fields are typically 200-300 Gauss.

3.4.2 Quadrature interferometer

The density interferometer is of a quadrature type [32] as shown in Figure 3.9. In this method, a circularly polarized reference beam is produced with the aid of quarter and half wave plates. The circularly polarized beam interferes with the linearly polarized scene beam, and the resulting beam is passed through a Wollaston prism oriented at 45 degrees to the plane of linear polarization. By analyzing the amplitudes of the two output beams produced by the Wollaston prism, the phase difference (and hence plasma electron density) can be deduced. This technique avoids calibration difficulties and eliminates data interpretation ambiguities due to fringe skipping.

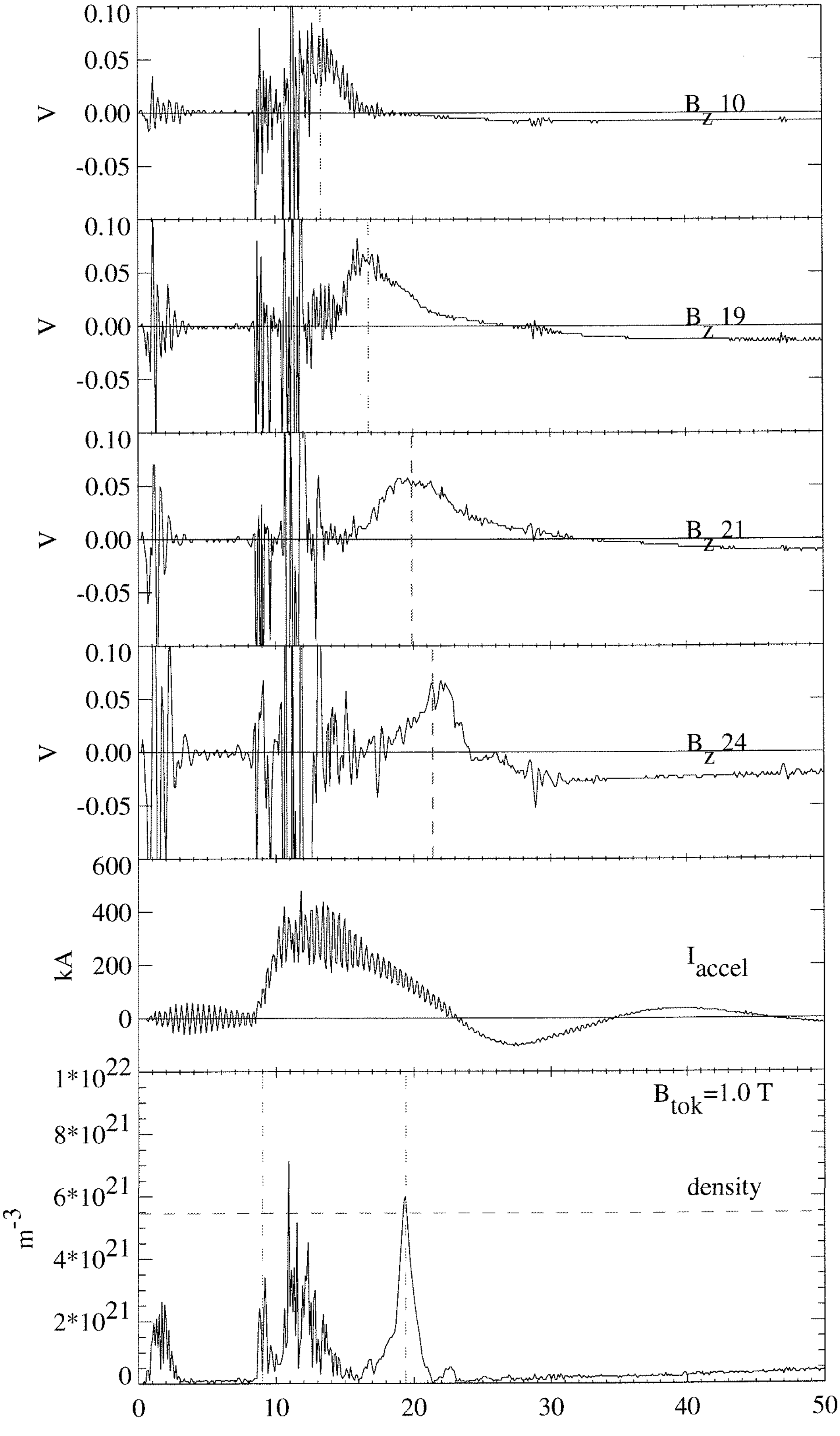

Figure 3.8: Diagnostic data from a typical CT Injector shot.

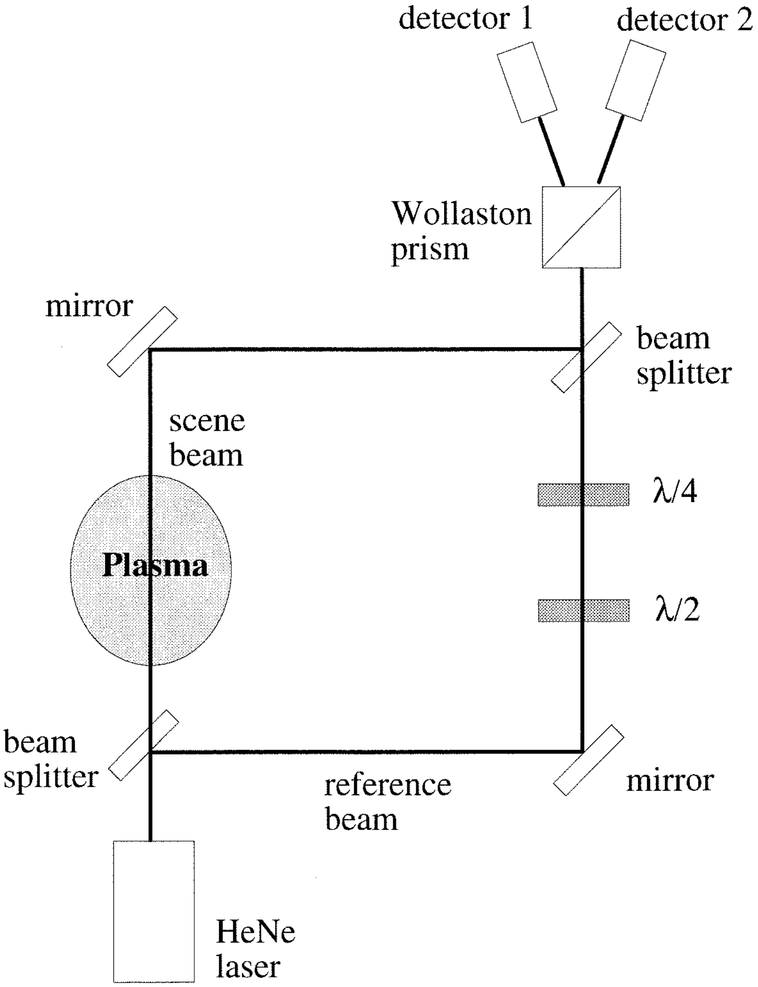

Figure 3.9: Quadrature density interferometer.

3.4.3 Data acquisition and analysis

All of the data from the diagnostics described above is acquired through Aeon (Model 3248) four channel 8-bit 10 MHz CAMAC-based digitizers. The CAMAC Crate is connected to an IBM PC compatible computer through a DSP Model PC004 interface card and DSP Model 6001 CAMAC Crate controller. Additional isolation was required during the second phase of the project, when the Injector was mated to the tokamak, in order to address safety concerns. This was accomplished by changing to a two Crate system with fiberoptic coupling. The digitizer Crate was placed near the Injector and controlled remotely using a serial highway through fiberoptic cables from a second Crate connected directly to the computer and located within the control room area.

Data acquisition control software and subsequent analysis and visualization of the data was written in the Interactive Data Language (IDL) from Research Systems. IDL is a powerful high level programming language which allows for easy manipulation and visualization of complex data structures. User-friendly Microsoft Windows based event-driven programs were written in IDL to facilitate data acquisition and archival.

3.5 CT speed and energy density calculation

As we shall see in the next chapter, one of the main requirements of a compact torus injector is that the spheromak attain sufficiently high speed to penetrate the tokamak field. As such, in order to gauge the performance of the Injector, it is important to accurately measure the exit velocity attained by the spheromak after passing through the accelerator stage. This final speed is calculated using measurements from the magnetic probe and density interferometer and employing an algorithm based on time of flight.

The time at which passage of the CT is detected by each of the four magnetic probes is determined by numerically smoothing the voltage trace and directly finding the time at which the maximum value occurs. These times, along with the time of

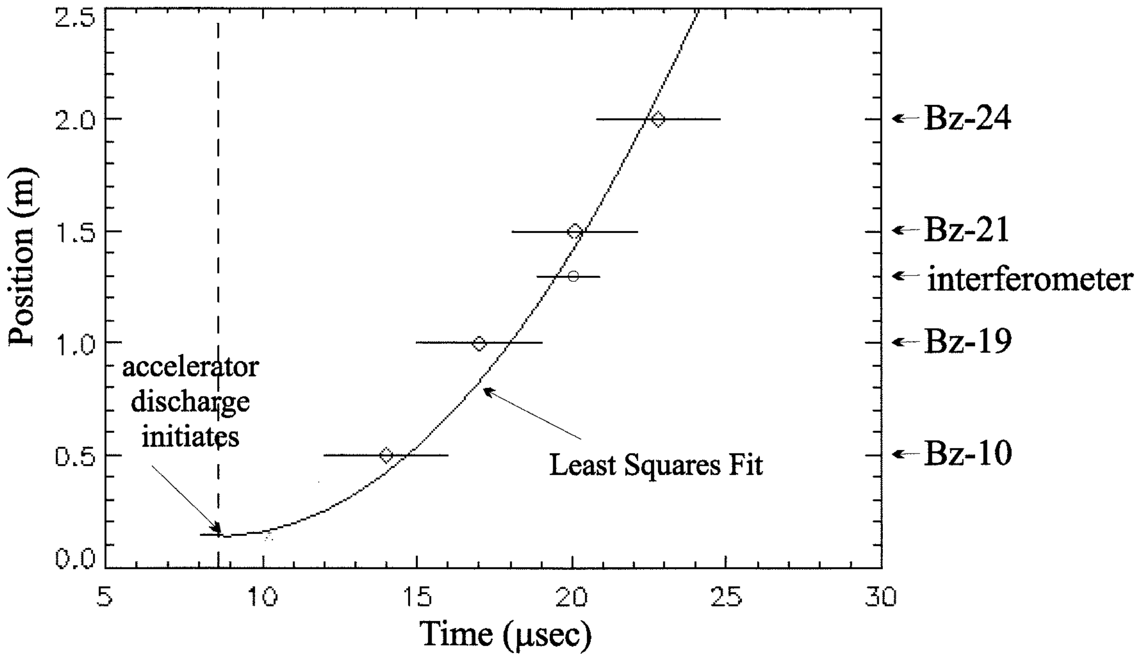

Figure 3.10: Sample Least Squares Fit (LSF) of magnetic probe and density interferometer data to a uniform acceleration model.

peak density, are least-squares fit (LSF) to a uniform acceleration model as shown in Figure 3.10, using the data from Figure 3.8. The LSF fit gives a velocity of 3×10^5 m/s at the location of the interferometer. This value, when combined with the peak density value of $6 \times 10^{21}\text{m}^{-3}$, corresponds to a kinetic energy density of 4×10^5 J/m^3. Based on the calculated velocity, the FWHM of the density pulse corresponds to a CT axial length of about 0.5 meter.

Uncertainty in the value of the kinetic energy density arises mainly from measurement uncertainties in determining the final velocity of the CT, which may be on the order of 20-30%. This relatively high uncertainty must be kept in mind in the discussions below. We may use a simple energy argument to verify that this estimate of the kinetic energy density is, at the very least, reasonable. The total kinetic energy contained in the CT is 2 kJ. Comparing this to the total gun and accelerator capacitor bank energies of 16 kJ gives a moderate energy efficiency of 12.5%.

Chapter 4 CT Injector performance issues

4.1 Introduction

For a CT Injector to successfully be used as a tokamak refueller, two major requirements must be met. The first of these can be understood on physically intuitive grounds. In order for the CT plasma to merge with the magnetically confined tokamak plasma, it must first have sufficient kinetic energy to be able to penetrate that very same magnetic field. Because the spheromak plasma is a flux conserver on these time scales, the tokamak magnetic field must be displaced. Using the simple model of an incompressible CT, this leads to the criterion

$$\frac{1}{2}\rho v^2 > B_T^2/2\mu_o \tag{4.1}$$

where ρ is the average mass density of the CT, v is the velocity of the CT after acceleration, and B_T is the tokamak toroidal field strength. This criterion will be examined more closely in the next chapter, where we will in fact show that it needs to be modified. However, for the time being, we will find it useful to establish a benchmark goal for CT kinetic energy.

The above criterion can be used to compute the required kinetic energy density for penetration (T_{CT}) given a particular tokamak magnetic field. Conversely, for a CT kinetic energy density we may define an equivalent tokamak penetration level as $B_T = \sqrt{2\mu_o T_{CT}}$. The Caltech CT Injector was commissioned to inject spheromaks into a medium-sized tokamak with 1 Tesla toroidal fields. Thus, this requirement established the major goal of the first phase of the CT Injector project ($T_{CT} \simeq 4 \times 10^5$ J/m^3), an objective which needed to be achieved before tokamak experiments could be performed.

The second main requirement for a CT injection refueller is that injection does not adversely affect tokamak operation. The most serious reaction the tokamak plasma could have is disruption, a destabilization of the plasma column which quenches the discharge and may be dangerous for the tokamak vacuum chamber. This is a very real possibility because tokamaks can only operate within a finite density range, and fresh fuel from CT injection may increase density to a level that it is outside of this range. When the so-called *density limit* is exceeded, atomic processes such as radiation, charge-exchange and ionization at the plasma edge may lead to disruption [33]. In early experiments at Caltech injecting unaccelerated spheromaks into a small tokamak, this type of disruptive effect was noted [4]. A practical injector must avoid this problem by ensuring that the particle inventory contained in the CT is relatively small compared to the tokamak plasma particle inventory.

Another adverse effect which must be avoided is injection of impurities into the tokamak. Great efforts are made to reduce impurities in tokamaks, as high-Z plasmas tend to radiatively cool and lead to poor tokamak performance [33]. Thus, to preserve tokamak cleanliness, the spheromak should also contain only a minimum of high-Z impurities. Because the spheromak is produced from a gas puff of high purity, the main source of such impurities will generally be the electrode walls. As it progresses through the injector toward the tokamak, the CT plasma may become contaminated through entraining of materials from the electrode surfaces. It is therefore imperative that the electrodes remain devoid of adsorbed materials.

In this chapter, issues relating to improving and optimizing performance of the Injector in order to satisfy the above requirements will be discussed. In Section 4.2, previous work in reducing impurity levels in the CT Injector [7] will be reviewed. Section 4.3 discusses experiments which were performed in order to optimize CT kinetic energy through adjustment of parameters such as gun current, stuffing flux, and acceleration [8]. Section 4.4 details modifications of the operation of the gas valve which were needed to reduce particle inventory generated by the Injector.

4.2 Reduction of impurities

After assembly of the device was complete, early experiments exhibited performance far short of the minimum kinetic energy benchmark. Brown, Loewenhardt, and Bellan [7] attributed the slowing of the CT mainly to the presence of an excessive amount of impurities in the Injector and undertook a campaign to increase the cleanliness of the device. This section will briefly review some of the main impurity reduction measures.

The vacuum (10^{-7} torr) was initially maintained using a Leybold turbopump paired with an oil backing pump. However, measurements taken using a Leybold Quadrex 100 residual gas analyzer (RGA) showed patterns characteristic of pump oil in the Injector. This implied that pump oil was backstreaming from the foreline through the turbopump and contaminating the vacuum. This situation is clearly undesirable as the organic molecules will be deposited onto the electrode surfaces, where they may be entrained by the passing CT. An oil-free Tribodyn-100/38 backing pump was subsequently installed and RGA measurements showed a substantial decrease of the pump oil pattern.

Concerns about other contaminants adsorbed onto the electrodes prompted the implementation of active baking of the accelerator electrodes. A power supply passes a high current (1 kA at 60 Hz) through the tantalum liner of the accelerator outer electrode, heating the liner to 200°C. This baking operation remains on whenever hydrogen shots are not being fired, and helps to liberate any volatile impurities from the electrode. However, the electrode was allowed to cool prior to firing hydrogen shots in order to avoid the embrittlement effect on hot tantalum when exposed to hydrogen gas.

In addition to pump oil adsorbed onto the electrodes, several other plasma-surface interactions may adversely affect Injector performance. For example, sputtering of the electrode surface material can result in dirty and slow CTs. However, this difficulty is minimized in the present device through the usage of refractory materials (tantalum and tungsten). Perhaps a more serious source of problems arises from hydrogen adsorbed into the accelerator electrode walls. Although hydrogen liberated by the passing spheromak does not result in contamination, the released hydrogen will slow the fast moving CT and result in reduced performance. To combat this effect, 20 helium CT shots were fired at the beginning of any day of running. This operation serves to liberate large amounts of hydrogen, as was observed using a Xybion intensified CCD camera and H_α filter.

The implementation of these techniques greatly improved overall performance of the CT Injector. In addition to higher final kinetic energy, increased magnetic activity and longer CT lifetimes were observed. Impurity radiation (such as the CIII line) measured using a monochromator was also reduced. Finally, the FWHM of the density profile of the accelerated CT was diminished, indicating a more highly localized CT. Thus, impurity control measures in the CT Injector had a twofold effect: reduction of impurities and increased kinetic energy in the generated CT.

4.3 Optimization: Gun current, stuffing flux, and accelerator parameters

The CT Injector is a complex device, with numerous independent operational parameters, including various power supply voltages and timing delays. Because of the many degrees of freedom, finding the operating point which maximizes CT performance presents a challenge. In order to build upon the rather limited body of established knowledge in this area, Loewenhardt, Brown, Yee, and Bellan [8] obtained a systematic characterization of the dependence of Injector performance on basic parameters such as gun current, stuffing flux, accelerator current and timing. This section reviews those results.

4.3.1 Gun current and stuffing flux

As was discussed in Section 3.2, the behavior of a coaxial spheromak gun is to a large extent determined by the gun current and applied stuffing flux. The spheromak λ can be calculated by taking the ratio of these two parameters $\lambda_{gun} = \mu_0 I_{gun}/\Phi_{stuff}$; values of λ_{gun} significantly less than the critical value λ_{geom} generates a stuffed plasma, while values significantly greater than λ_{geom} produce a spheromak with low helicity content. Clearly, there is an optimal value of λ_{gun} (determined by geometrical considerations) which results in a well-formed spheromak with high helicity content. This optimal value of λ_{gun} establishes a range of values of gun current and stuffing flux which may be used for operation of the coaxial gun in the optimal regime.

Because the CT Injector consists of a coaxial gun formation section coupled to an acceleration stage, one naturally expects the operation of the Injector to depend on gun current and stuffing flux in a similar manner. It is thus interesting to examine how overall performance is affected by varying these parameters (and therefore varying λ_{gun}).

Experimental data was taken in a scan of the two-dimensional parameter space spanned by gun current and stuffing flux, while holding all other parameters constant. Gun current ranged from 75 kA to 125 kA in 5 kA increments while stuffing flux ranged from 4.5 mW to 7.5 mW in 0.3 mW increments. Acceleration current was fixed at 350 kA. At each setting of gun current and stuffing flux, the final CT kinetic energy was computed as described in Section 3.5 and the equivalent tokamak TF penetration level was calculated. This data was then compiled in order to generate the contour plot shown in Figure 4.1.

The most interesting feature of this plot is a ridge of high performance which corresponds to a λ_{gun} of 24 m^{-1}. It is surprising that operation of the Injector in this regime should lead to increased CT energies as this is significantly below the calculated critical value of $\lambda_{geom} = 60\ m^{-1}$ and would be expected to produce a stuffed spheromak. Indeed, operation of the Injector in this regime with no acceleration shows evidence of magnetic activity at only the first two probe positions and thus appears to be at least partially stuffed. It appears that a unique situation is arising with these Injector parameters: the acceleration stage may be aiding in the detachment of the CT. As the distended still-attached spheromak progresses beyond the formation-accelerator break, it is unable to detach due to the stuffing flux magnetic tension.

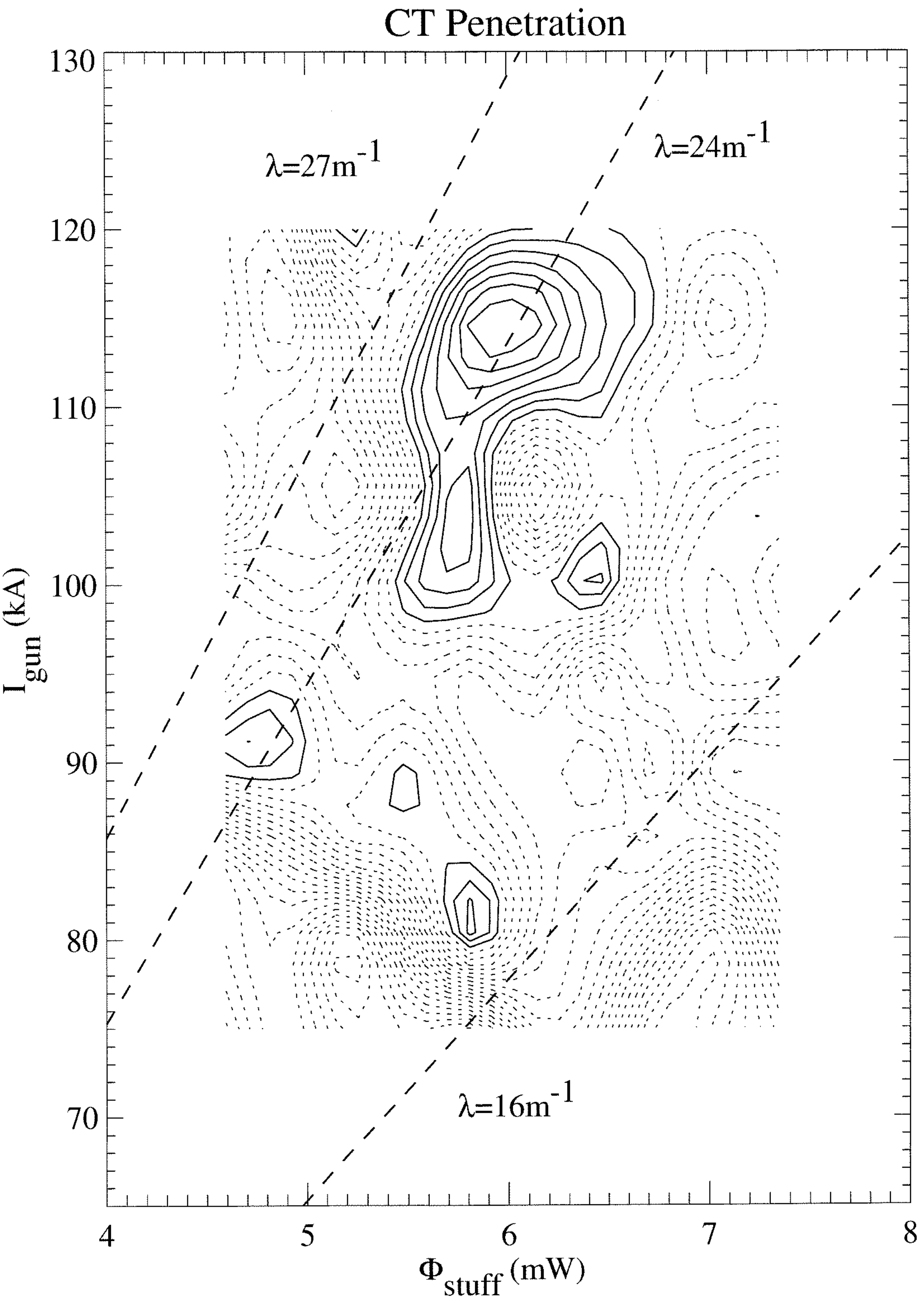

Figure 4.1: Contour plot of B_{tok} as a function of gun current and stuffing flux. Solid contour lines indicate B_{tok}>1.15 T whereas dotted contour lines indicate B_{tok}<1.15 T. Several lines of constant λ_{gun} are superimposed.

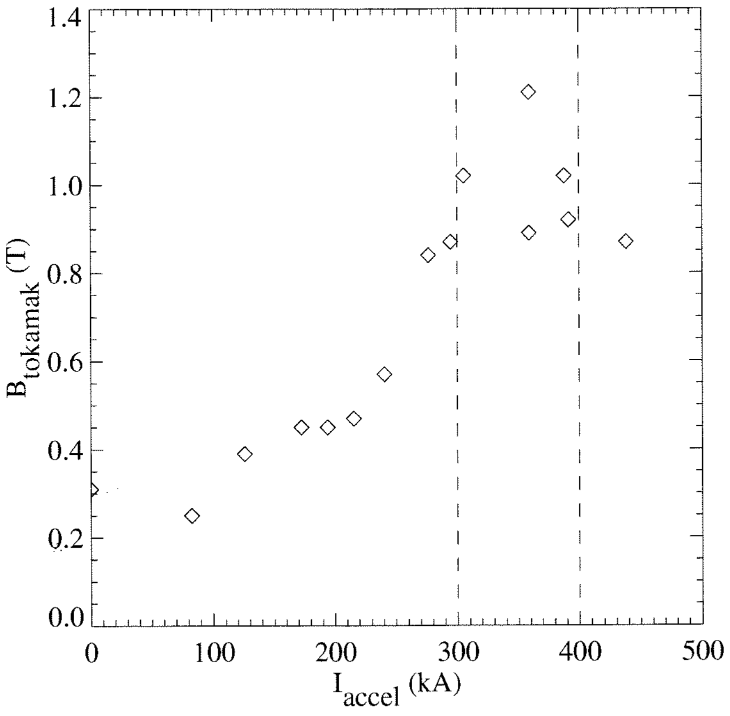

Figure 4.2: Variation of B_{tok} as I_{accel} is varied with λ_{gun} held constant at 24 m^{-1}. Dashed vertical lines bracket the optimal performance regime.

At this point, the accelerator fires and the increased **J** × **B** force is then able to overcome this magnetic tension, enabling full spheromak formation to take place. This is essentially a type of forced reconnection [34].

4.3.2 Acceleration current and timing

A simple physical model of the acceleration stage would treat the CT as an incompressible solid conducting ring which is propelled as the armature of a coaxial rail gun. The force exerted on the CT is then equal to the product of the magnetic pressure and the cross-sectional area of the device. Because this acceleration force is then proportional to the square of the rail gun (or accelerator) current, this model predicts the simple result that the kinetic energy of the CT is maximized by maximizing the acceleration current.

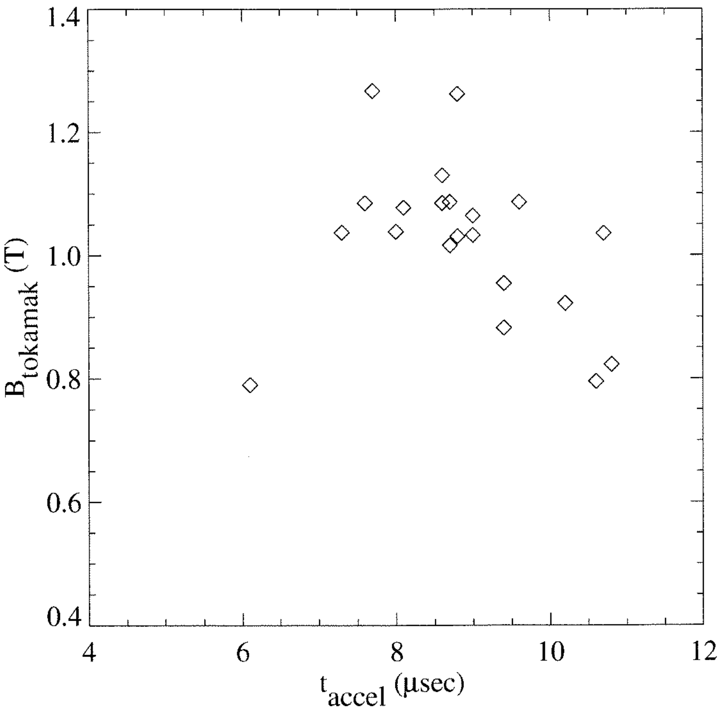

Figure 4.3: Variation of B_{tok} with timing of the accelerator discharge. λ_{gun} is held constant at 24 m^{-1}.

It is interesting to examine how well the description above agrees with actual Injector performance as accelerator current is varied. This data is presented in Figure 4.2 with the gun parameters set in the high performance ridge ($\lambda_{gun} = 24\ m^{-1}$) described in the previous section. Final CT kinetic energy is given in terms of the equivalent tokamak magnetic field penetration level, calculated as explained above. For the most part, the performance increases with acceleration current, with a particularly sharp rise at 250 kA to 300 kA. However, above 400 kA energies show no evidence of further increasing, and in fact appear to begin to degrade. At these very high acceleration levels, the CT may experience blow-by wherein the acceleration force is so large that the CT lifts from the center electrode and the accelerating flux blows by the CT. This represents a substantial departure from the idealized model given above.

Besides the magnitude of the acceleration, timing of the discharge relative to the formation stage may play a major role. As shown in Figure 4.3, the performance of the injector is fairly sensitive to the precise timing of the acceleration stage. This scan was performed in the optimized ($\lambda_{gun} = 24\ m^{-1}$) regime found in the previous section. This type of dependence is consistent with the scenario proposed earlier, wherein the accelerator stage aids in the detachment and reconnection of the spheromak, as this would require acceleration to begin precisely when the front of the spheromak has distended just past the formation-accelerator break region.

4.4 Reduction of gas levels

As described above in Sections 4.2 and 4.3, implementation of several impurity reduction techniques and operation of the device with gun, accelerator, and stuffing flux parameters in an unexpected higher performance regime resulted in CTs possessing kinetic energies in excess of the commisioned requirements. The Injector was subsequently transported to the Fusion Research Center in Austin, Texas, in order to begin tokamak experiments.

However, a serious difficulty was discovered upon initial experiments of injection into the TEXT-U tokamak. Subsequent to CT injection the tokamak particle inventory quickly rose beyond the density limit and led directly to tokamak disruption. Because the influx of material was more than could be accounted for by the calculated particle inventory in the CT (approximately 10^{20} protons), this phenomenon was attributed to an excessive amount of trailing plasma and neutral gas being emitted by the Injector. This hypothesis was verified by performing an experiment in which only the gas valves of the Injector were triggered, and resulted in a similar rise in tokamak density.

Because one of the experimental objectives was to demonstrate disruption-free CT injection, a method of decreasing the amount of gas puffing while preserving CT performance needed to be found. Control over the amount of gas emitted by the valves could be achieved by modifying the gas valve capacitor bank voltage. Reduction of this voltage results in a reduction of the current pulse which energizes the gas valve.

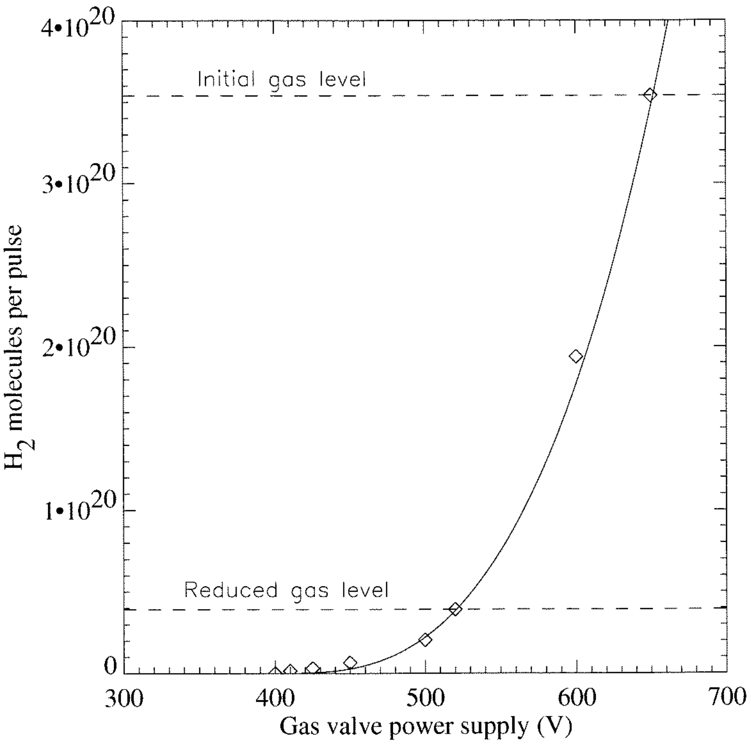

Figure 4.4: Variation of gas puff with voltage on gas valve power supply. Data points were obtained using a pressure thermocouple. Measurements are fit well by a cubic function (solid line). Dashed lines represent initial gas level and the reduced gas level required to avoid disrupting the tokamak discharge.

The dependence of the size of gas puffing on valve power supply voltage is quantified in Figure 4.4. Data was obtained by pulsing the valves multiple times and noting the rise in vacuum chamber pressure with the chamber isolated (valved off) and pumps shut down.

Further experimentation with firing only the gas valves into the tokamak discharge showed that the amount of gas needed to be reduced by roughly 90%, from about 3.6×10^{20} H_2 molecules to about 4×10^{19} H_2 molecules, in order to only modestly affect the tokamak density. Unfortunately, operation of the CT Injector with the reduced gas levels resulted in substantially degraded performance.

High performance was not recovered until operational characteristics of the gas valves were analyzed in greater detail. Experiments conducted by J.F. Hansen with

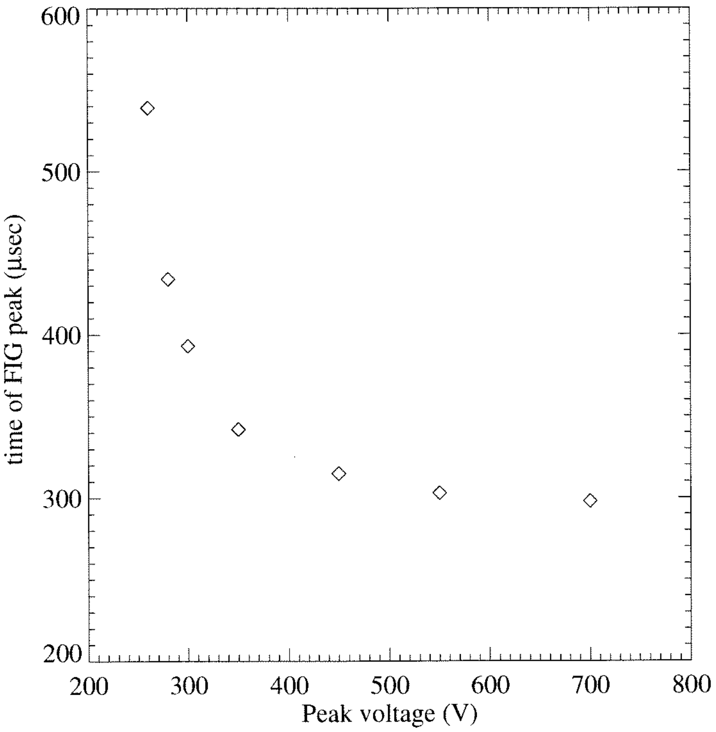

Figure 4.5: Time delay of fast ion gauge pulse for various driver coil pulse amplitudes, using a gas valve of similar design.

a similarly designed gas valve and a fast ion gauge (FIG) measured the time dependence of the gas puff propagating away from the valve. By examining the FIG data, both the amount of gas and the time at which the FIG encounters the gas can be determined. As the voltage pulse applied to the driver coil was reduced in magnitude, an unexpected behavior was observed in the FIG signal. In addition to reducing the amplitude of the signal (indicating reduced gas), the time delay of the peak also increased (see Figure 4.5). This result indicates that the gas valve requires substantially more time to open at lower voltages. Note that this behavior differs from that documented by Thomas [31], despite the similar design.

Upon modifying of the gas valve timing in the CT Injector to accommodate the delayed gas valve opening, the high performance regime was recovered (see Figure 4.6a) and tokamak injection experiments could proceed. In comparison with operation at the earlier gas settings (Figure 4.6b), at the reduced gas levels CT peak density was diminished ($6 \times 10^{21}\mathrm{m}^{-3}$) but velocities were a bit higher (3×10^5 m/s). The total particle inventory of the CT can be estimated by noting the velocity and calculating the area under the density trace. According to this calculation, the CT consists of approximately 9×10^{19} protons and electrons.

This value for CT particle inventory appears puzzling, because Figure 4.4 indicates that the gas puff consists of only 8×10^{19} protons. However, these are rough estimates, and uncertainties can easily account for the discrepancy. In addition to velocity measurement uncertainties (see Section 3.5), the measured density is averaged over a chord and does not provide information on the distribution of density radially and axially within the CT. Allowing for the uncertainties, this calculation suggests that a large proportion of the atoms comprising the gas puff eventually end up as the CT plasma, and this regime of operation is highly efficient from the standpoint of leaving little residual neutrals and trailing plasma.

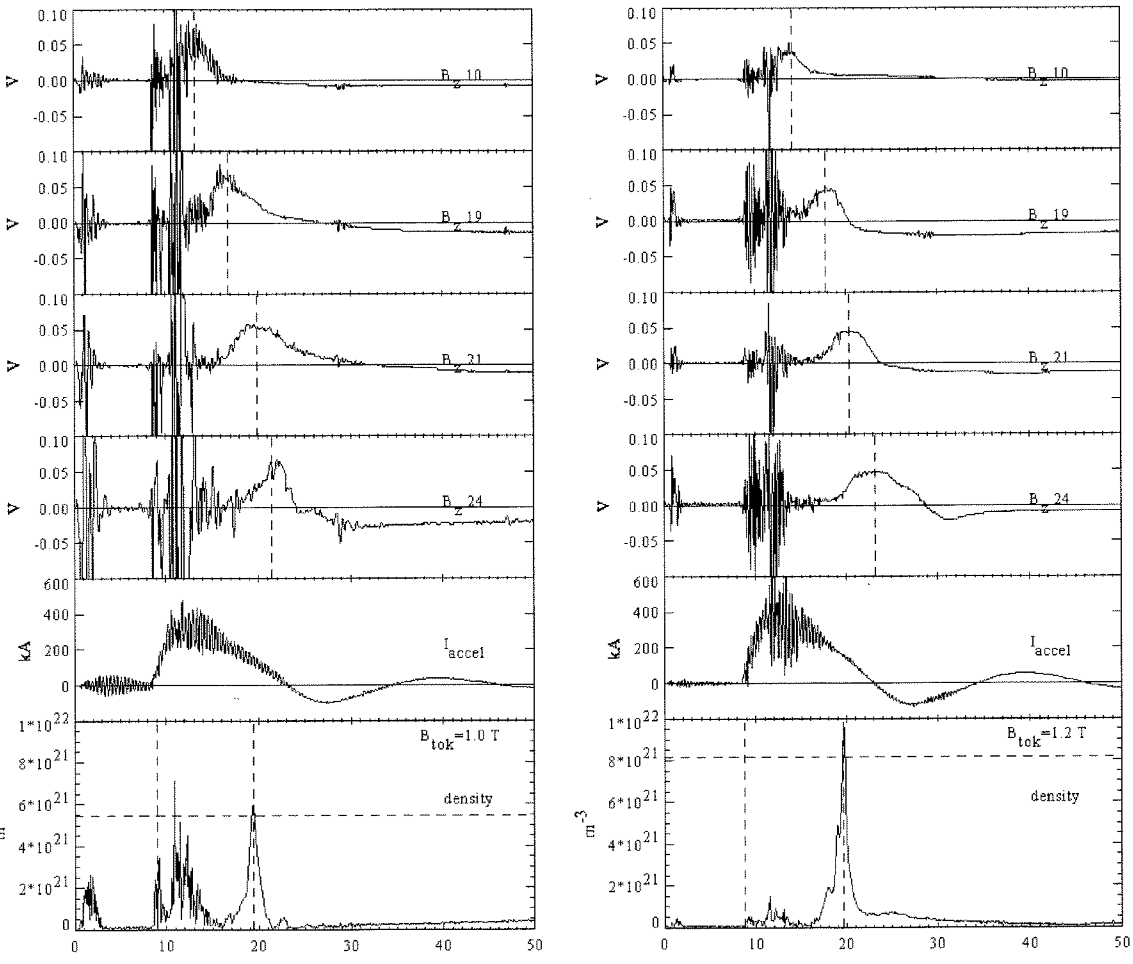

(a) (b)

Figure 4.6: (a) Magnetic and density traces from the CT Injector operated with reduced gas levels and re-optimized gas valve timing delay. (b) For comparison, operation at the original higher gas levels. In both cases, the spheromak should be able to penetrate 1 Tesla fields.

Chapter 5 Effects of accelerator electrode geometry

5.1 Introduction

According to current theories, one of the key requirements for the success of CT injection schemes is that the plasmoid must attain sufficient kinetic energy density in order to overcome the strong gradient of the tokamak toroidal field [9]. Due to the short timescales involved in the injection process, and the high electrical conductivity of the plasma, the tokamak toroidal field (TF) must be diamagnetically displaced by the travelling CT. The CT encounters a retarding force per unit volume $\overrightarrow{F}_{CT}/V = -\overrightarrow{\nabla}\left(B^2/2\mu_0\right)$ analogous to the buoyancy force an object experiences when submersed in a liquid, with magnetic pressure taking the place of hydrostatic pressure. Thus, the initial translational kinetic energy of the CT must be sufficiently high in order to penetrate a given magnetic field. Based on this argument, the kinetic energy requirement is

$$\frac{1}{2}\rho v^2 > B_T^2/2\mu_o \tag{5.1}$$

where ρ is the average mass density of the CT, v is the velocity of the CT after acceleration, and B_T is the tokamak toroidal field strength. In physical terms, the initial kinetic energy density of the CT must exceed the magnetic energy density of the tokamak toroidal field. We shall present in this chapter strong evidence that this criterion is not always accurate and may significantly underestimate the actual kinetic energy requirement for successful penetration.

In addition to toroidal magnetic field displacement, other drag mechanisms have also been predicted. In Parks' model [28], CT motion through the tokamak plasma excites a wake of Alfvén waves which drains kinetic energy from the CT. The resulting drag force on the CT is $F_{Parks} = \frac{1}{2}B_T^2 a^2(v/v_A)$, where v_A is the Alfvén speed and a is the CT's radius. Newcomb [35] included power radiated in the form of magnetoacoustic waves and arrived at an expression $F_{Newcomb} = 2\pi\rho a^2 Ivc_s$, where c_s is the sound speed, and I is a drag coefficient of order unity. These additional sources of drag would further slow the CT, increasing the kinetic energy requirement.

In this chapter, we present results from CT injection experiments using the Caltech CT Injector on the University of Texas at Austin TEXT-U tokamak operating at toroidal field strengths B_T $\approx$10 kilogauss. Various acceleration electrode configurations were examined, and it was discovered that electrode modifications had pronounced effects on penetration levels. In the discussion section, we propose a theory attempting to explain the anomalous behavior. These results form the basis of Ref. [10].

5.2 Experimental results

CT Injector experiments were conducted with three different configurations of the acceleration electrodes, as shown in Figure 5.1, and it was found that the choice of configuration profoundly affected the CT penetration into the tokamak. The key feature distinguishing the various electrode geometries is the position of the ends of the electrodes relative to the toroidal field coils of TEXT-U. The initial configuration (Figure 5.1(I)) included extension sections of both the center and outer electrodes, to provide additional acceleration, compression, and confinement of the CT into a region just outside the outermost flux surface of the tokamak plasma. The outer electrode extension is tapered from 12.7 cm diameter to 11.3 cm over its 0.74 m length. In the second configuration, shown in Figure 5.1(II), the center electrode was shortened by removing the extension section. Figure 5.1(III) shows the final configuration, in which the outer electrode extension was removed as well, terminating the acceleration electrode assembly outside of the extent of the toroidal field coils.

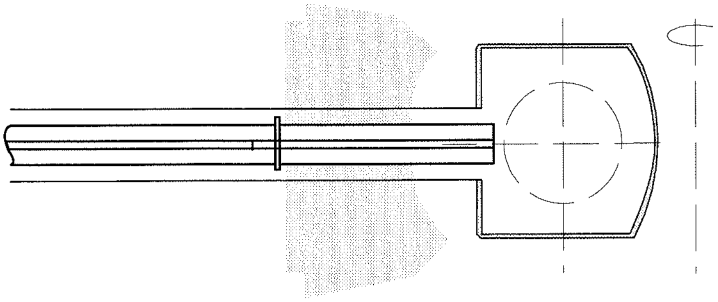

(I) Electrode Extensions On

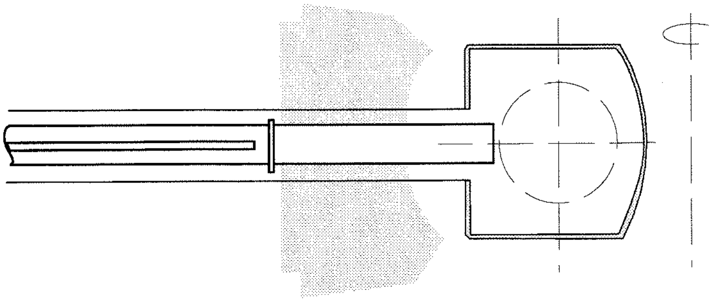

(II) Center Electrode Extension Removed

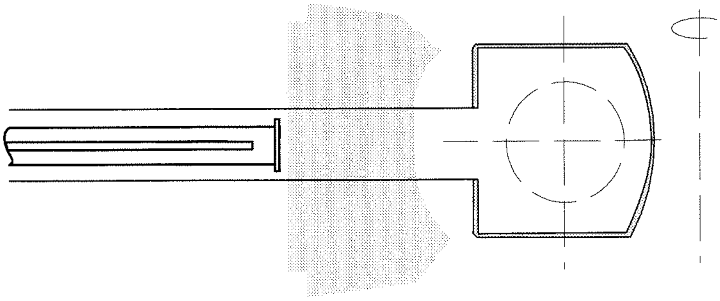

(III) Both Electrode Extensions Removed

Figure 5.1: Diagram illustrating the three electrode configurations used during the CT Injector experiments.

5.2.1 (I) Electrode extensions on

Initial experiments, with both center and outer electrode extensions attached, exhibited surprisingly poor penetration by the CT. Figure 5.2a shows tokamak interferometry data for a discharge with B_T=10 kG, with CT injection occurring at t=217 milliseconds. The lower trace on this same plot shows the tokamak density for a shot in which the CT Injector gas valves are fired, but the formation and acceleration capacitor banks are not discharged. The similarity of the two cases indicates that the density increase in the tokamak beginning at t=217 ms is due to diffusion of neutrals, and not CT injection. Magnetic probes and interferometry data on the CT Injector indicate an estimated CT kinetic energy density of 4×10^5 J/m^3, so that the standard minimum energy criterion Eq. (5.1) is satisfied.

Further direct evidence of the lack of CT penetration was provided by measurements using a Langmuir probe mounted at the end of the acceleration (outer) electrode, positioned to detect the presence of plasma leaving the end of injector. Lack of signal from this diagnostic indicates that the CT has slowed to a stop within the final section of the injector. Figure 5.3a shows the peak signal from this probe as a function of tokamak toroidal field strength. Each data point represents a CT injection shot in which the estimated kinetic energy density is 3-4 $\times$ 10^5 J/m^3, corresponding to a maximum toroidal field of 10 kG. (Toroidal field values $<$10 kG were obtained by firing the CT Injector during the decay of the toroidal field, after the tokamak discharge). The amount of plasma which exits the injector is obviously highly dependent on the toroidal field, with a threshold value of 2 kG, much less than the predicted 10 kG.

5.2.2 (II) Center electrode extension removed

In the second electrode configuration, the center electrode extension was removed, shortening this electrode. This modification reduces the length of the acceleration region, and the final section of outer electrode is converted into a "drift tube," where the CT must travel into the tokamak by virtue of its initial momentum. Despite the

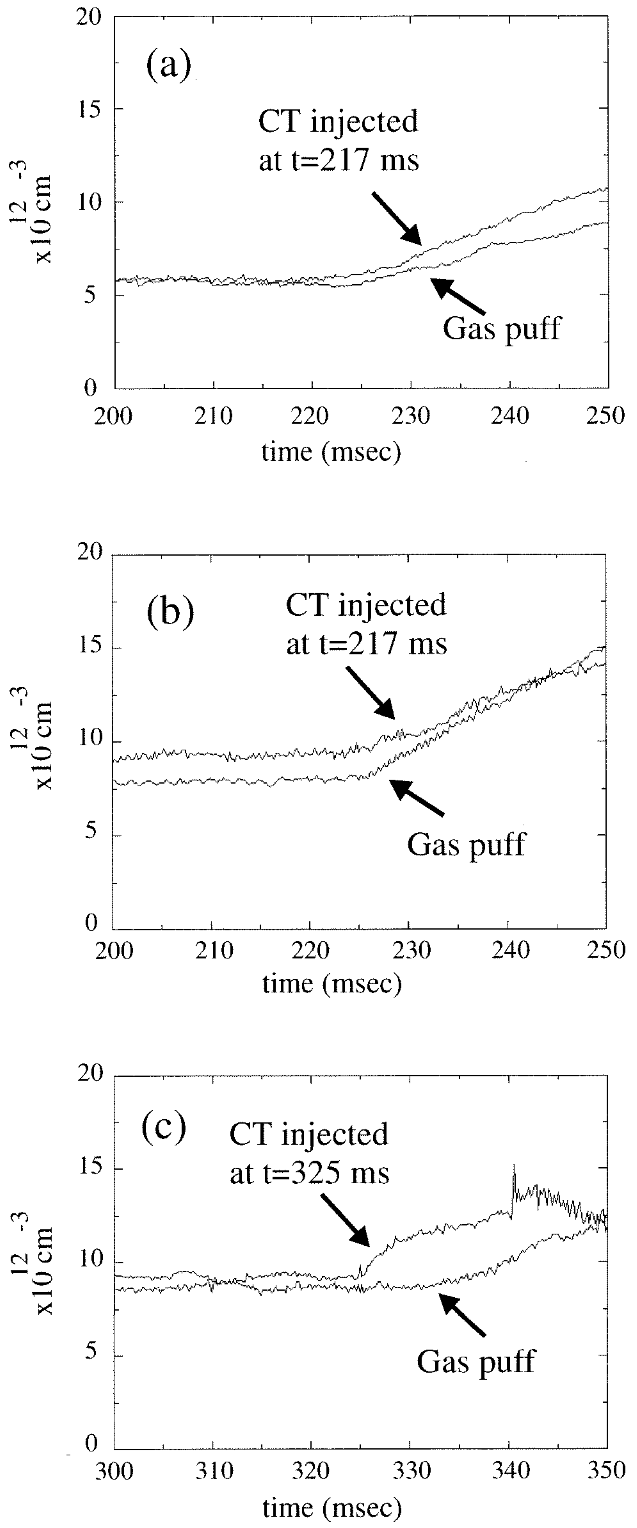

Figure 5.2: Tokamak density interferometer traces (central chord) for each electrode configuration, I, II, and III. In all cases, the tokamak TF is 10 kG and the plasma current is 100 kA. In each plot, the tokamak density upon CT injection is compared with the density following puffing of the CT injector gas valves used in CT formation.

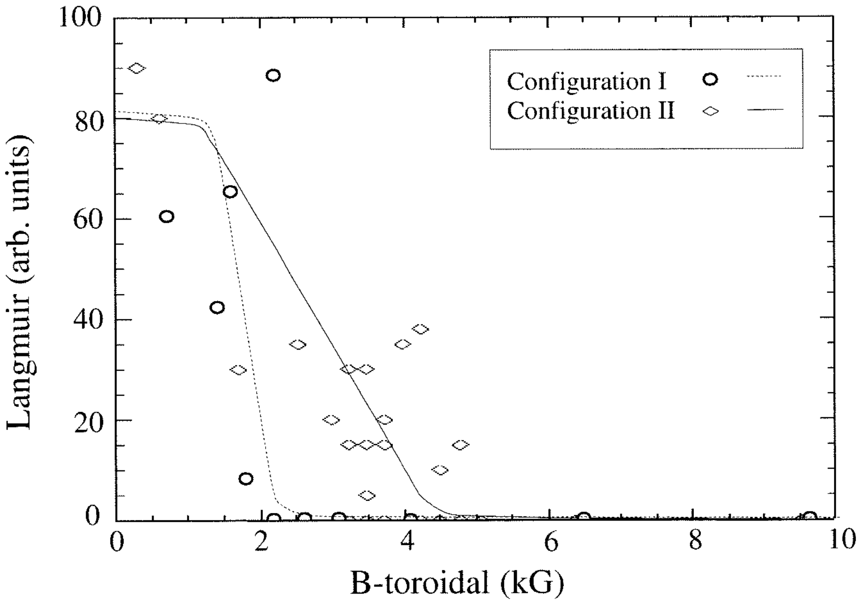

Figure 5.3: Langmuir probe measurements for the first two electrode configurations, I and II. Each point represents the maximum CT Langmuir signal detected at the end of the injector, for a particular tokamak TF strength.

reduction in the acceleration stage, injection performance was notably improved in this configuration, as compared to (I). Langmuir probe measurements and tokamak interferometry data are shown in Figures 5.2b and 5.3b, respectively. As shown in Figure 5.3b, the toroidal field magnitude above which no plasma can be detected leaving the injector increased to approximately 4.5 kG. However, at the tokamak's operating TF strength of 10 kG, there is still no plasma detected leaving the injector. Figure 5.2b shows the density trace of a 10 kG tokamak discharge, upon CT injection at t=217 ms, with an estimated CT kinetic energy density of 4×10^5 J/m^3. Comparing this to the reference gas-puffing injection, the data indicates that the bulk of the CT mass has not penetrated into the tokamak, and the density rise after the CT injection time is again due to neutral particle diffusion.

5.2.3 (III) Both electrode extensions removed

In the third configuration, the outer electrode extension was removed as well, resulting in an effective drift tube consisting of the larger stainless steel vacuum bellows cylinder ($\approx$20 cm inner diameter). Unfortunately, accessibility problems prevented a Langmuir probe from being mounted as in the previous configurations. Sample tokamak data is shown in Figure 5.4, for a 10 kilogauss tokamak discharge, with CT injection occurring at t=325 ms, and an estimated CT kinetic energy density of 4×10^5 J/m^3. Note the sharp (several millisecond timescale) rise in density upon CT injection, which is higher than can be accounted for by simple neutral gas diffusion, indicating penetration of the CT to a point nearer to the outermost flux surface of the tokamak. The x-position trace shows the horizontal location of the imaginary plasma current "filament" in a particular poloidal cross-section, measured using magnetic probes (used for active feedback stabilization of the discharge). This latter plot indicates a sharp (several millisecond) motion of the plasma column upon injection. Soft-xray, H-alpha, Mirnov and MHD-probe measurements show a great deal of MHD activity after CT injection, with a particularly strong component with 3 ms periodicity, resulting in a minor tokamak disruption at t=341 ms. These diagnostics clearly demonstrate that CT injection dramatically affects the tokamak discharge. In contrast, gas-puff reference shots exhibit none of this behavior.

A few injection shots were attempted at TF strengths of 7 kG (below the normal operating regime of TEXT-U), with the expectation of increased penetration. In these cases, results were qualitatively similar to those described for 10 kG.

5.3 Toroidal flux trapping

The results described above suggest that interaction between the CT and the toroidal field of the tokamak results in slowing down of the CT to an extent far greater than can be explained using the standard energy criterion (Eq. 5.1). Since the drag occurs in the final stage of the injector, where no stationary background plasma is present,

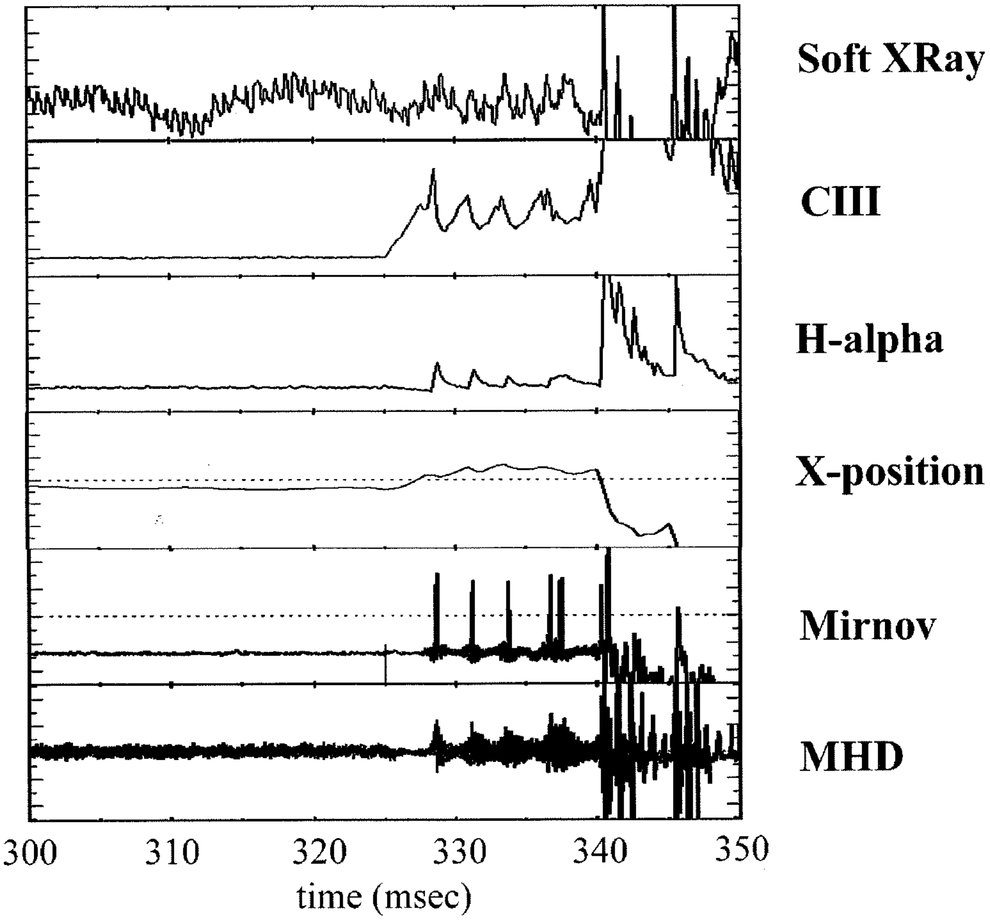

Figure 5.4: Tokamak diagnostic data for configuration III with tokamak parameters: $B_T = 10$ kG and $I_p = 100$ kA. Compact toroid injection occurs at $t = 325$ ms.

the drag mechanisms proposed by Parks and Newcomb, which involve energy loss via emission of Alfvén or acoustic waves, are not relevant. Only the force due to the gradient of the toroidal field $\nabla(B^2/2\mu_0)$ is applicable in this region. Clearly, this force does not adequately account for CT slowing, since CTs with kinetic energies which we have estimated to be sufficient to penetrate 10 kG become stalled within the injector and do not emerge, at toroidal field strengths as low as 2 kG.

In attempting to interpret these anomalous results, let us first consider the possibility that the kinetic energy of the accelerated CT has simply been overestimated.

Substantial measurement uncertainties in the final velocity, as discussed earlier, as well as possible slowing of the CT due to electrode surface effects could potentially result in significantly reduced final energies. However, it seems unlikely that these factors can account for the 80% reduction in velocity (and correspondingly greater reduction in energy) which would be required. We will therefore restrict our attention to stopping mechanisms related to the tokamak toroidal field.

We hypothesize that the anomalously poor penetration is attributable to toroidal field being trapped within the flux-conserving walls of the coaxial electrodes. Due to the finite size of the coils which generate the toroidal field, the tokamak toroidal field drops off gradually outside of the tokamak. In the case of TEXT-U, the field decays from 77% of the nominal value at the tokamak plasma edge down to 25% a distance 40 cm away from the edge. (The nominal value of the toroidal field is measured at the center of the tokamak discharge.) This residual toroidal field will then transversely permeate the CT injector electrodes, which are flux-conserving on the relevant microsecond time scales. Thus, the field lines are effectively "frozen in" or trapped within the electrode walls, impeding the progress of the CT plasma, which is also flux-conserving and must displace these field lines as it travels into the high field region.

We first examine the effect of the toroidal field on the electrode geometries (II) and (III), in which magnetic flux is trapped within the outer electrode (or drift tube). In this case, shown in Figure 5.5a, the energy required for the CT plasma to displace the toroidal field lines can be greatly increased, as compared to the case in which no electrode is present, since any field which is displaced must be compressed against the walls. The TF magnetic flux is effectively trapped inside the drift tube, resulting in an increase in the magnetic field strength in the vicinity of the CT. We first use a simple 2D magnetostatic analysis to calculate the change in magnetic field energy resulting from the flux-displacement caused by the plasmoid and then use numerical methods to investigate the full 3D case.

The axial extent of our CT greatly exceeds its radius, so that a two-dimensional analysis is appropriate. We assume that the (uniform) toroidal field has had sufficient

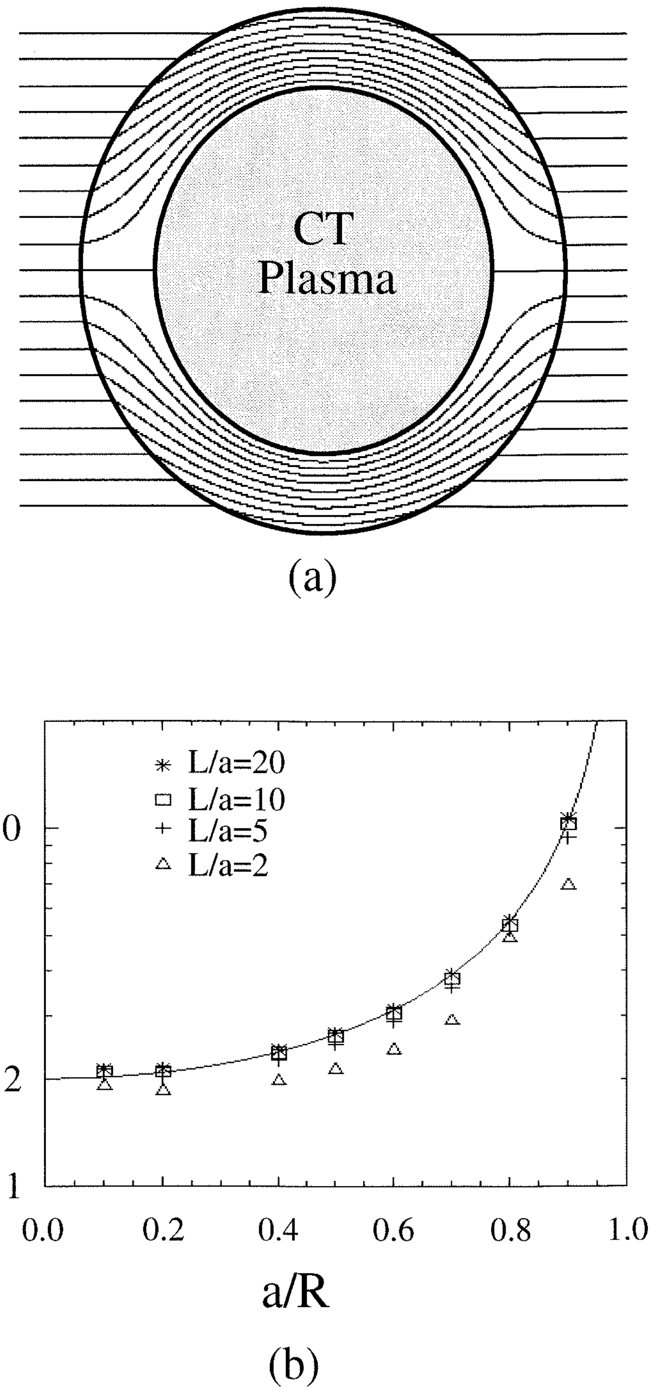

Figure 5.5: Toroidal flux trapping. (a) Cross-sectional view of magnetic field topology for the case of a circular CT plasma within a circular drift tube. (b) Magnetic energy enhancement factor α as a function of CT radius a normalized by drift tube radius R. The solid curve shows the 2D analytical expression. The data points were numercially calculated for various values of L/a.

time to fully penetrate the walls of the drift tube, and is "frozen in" on the CT time scale. Furthermore, for simplicity, we will assume an axisymmetric, incompressible CT. The cylindrical CT drifts from infinity (a field-free region) into this high toroidal field region, and must fully exclude these magnetic field lines, since the CT is itself a flux-conserver.

We thus consider a magnetically impermeable body of radius a within a larger ring of inner radius R, with a uniform magnetic field of strength B_0 frozen inside it. In a 2D polar coordinate system, the general (current free) magnetic field is $\overrightarrow{B} = \overrightarrow{\nabla}\Psi$ where the potential function Ψ is

$$\Psi(r,\theta) = \sum_m (c_{1m}r^m + c_{2m}r^{-m}) \sin m\theta. \tag{5.2}$$

Applying the boundary conditions, $[B_r]_{r=R} = B_0 \sin\theta$ and $[B_r]_{r=a} = 0$ give

$$\Psi = B_0 r(1+\frac{a^2}{r^2})\frac{R^2}{R^2-a^2}\sin\theta. \tag{5.3}$$

The total magnetic field energy within a cylindrical control volume V is given by

$$\begin{aligned} W &= \int_V \frac{1}{2\mu_o}\left|\nabla\Psi\right|^2 d^3x & (5.4)\\ &= \frac{R^2+a^2}{R^2-a^2}\frac{B_0^2}{2\mu_o}V. & (5.5)\end{aligned}$$

Before the CT enters the drift tube, the control volume is permeated by a uniform field of magnitude B_0, so the magnetic field energy is simply $W_0 = (B_0^2/2\mu_0)V$. Thus, the net change in magnetic field energy resulting from the addition of the flux-excluding body in a section of length L is

$$\Delta W = W - W_0 = \frac{2R^2}{R^2-a^2}\frac{B_0^2}{2\mu_o}(\pi a^2 L). \tag{5.6}$$

If we now identify $V_{CT} = \pi a^2 L$ as the volume of the CT, and apply conservation of energy, $\Delta W + \Delta K = 0$, the change in kinetic energy of a CT as it enters a flux conserving drift tube is then

$$\Delta K = -\frac{2R^2}{R^2 - a^2}\left[\left(\frac{B_0^2}{2\mu_o}\right)(V_{CT})\right]. \tag{5.7}$$

This requires the CT to have a minimum initial kinetic energy $K_0 \geq \alpha\,(B_0^2/2\mu_o)\,V_{CT}$ in order to displace the magnetic field trapped inside the drift tube, where

$$\alpha \equiv \frac{2R^2}{R^2 - a^2}. \tag{5.8}$$

In order to arrive at a form analogous to the standard criterion, the CT's total kinetic energy must be rewritten in terms of its average kinetic energy density, $K_0 = \frac{1}{2}\rho v^2 V_{CT}$, where ρ and v are the CT's average density and initial velocity, respectively. The criterion for required CT kinetic energy density becomes

$$\frac{1}{2}\rho v^2 \geq \alpha\frac{B_0^2}{2\mu_o}. \tag{5.9}$$

This modified energy criterion differs from the standard expression only in the multiplicative factor α, which may be interpreted as a measure of the enhancement of the retarding force on the CT as it displaces field lines in a flux-trapped region. Note that α is proportional to the ratio between the cross-sectional area of drift-tube πR^2 and the area between the CT and the drift tube $\pi(R^2 - a^2)$. Also, α depends strongly on the ratio between the radius a of the CT plasma and the drift tube inner radius R (c.f. Figure 5.5b); this ratio is determined by magnetic and thermal pressure balance, as well as the dynamics of the deceleration process. Furthermore, α can be quite large, and even in the most energetically favorable case, which is the limit of an infinitely thin CT, approaches a minimum value of 2. This implies that deceleration of the CT may frequently be dominated by this mechanism, so that the critical CT kinetic energy required for penetration is determined by Eq. (5.9), rather than the commonly used Eq. (5.1).

One may, at first, be surprised by the limiting value of $\alpha_{\text{min}}=2$ derived for the case of a drift tube with infinitely large diameter. In this situation, the walls of the drift tube have no effect upon the magnetic field around the CT, and thus flux-trapping cannot be an issue. Instead, the value of 2 stems entirely from the boundary conditions on the surface of the CT (and hence, on the shape of the CT). These surface boundary effects on the magnetic field were incorrectly neglected in the earlier argument (leading to Eq. 5.1). Unlike the case of an object submersed in a liquid, in which the fluid pressure simply increases linearly with depth, the magnetic field (and thus the magnetic pressure) around a flux-excluding CT is influenced by the object's shape. As a result, the deceleration force which the CT experiences is inherently dependent upon its shape and this is quantitatively reflected in the value of α_{min} . Note that this issue is entirely separate from the flux-trapping effect resulting from the confining influence of the drift tube.

The value of α_{min} appropriate for any particular CT shape can be calculated using a magnetostatic analysis. In addition to the value of 2 calculated above for a long cylindrical CT which is oriented perpendicular to the magnetic field, it is illuminating to examine two other cases which may be solved analytically. Straightforward calculations show that $\alpha_{\text{min}}=3/2$ would be applicable for a spherical CT (i.e., the "classical" spheromak), and $\alpha_{\text{min}}=1$ for a long thin cylinder oriented parallel to the magnetic field (c.f. Appendix). These latter results reflect the fact that there is an energy preference for thin objects with a small profile perpendicular to the magnetic field, because this results in the least distortion of field lines; the minimum value of $\alpha_{\text{min}}=1$ may be regarded as an absolute lower bound for α. A general consequence of this observation is that any diamagnetic object in a magnetic field will tend toward a shape or orientation which reduces its transverse dimensions (i.e., cross-section).

In order to ascertain the effect of including finite CT axial length in this model, a numerical calculation was also performed. In the computational model, the CT is a cylinder of radius a and length $2L$ located within a larger cylinder of radius R and length $5L$. (The length of the outer cylinder was chosen so that it did not significantly affect the result). By assuming $\Psi \propto \sin\theta$, as is required by the boundary conditions, the azimuthal coordinate is eliminated, transforming the problem into a two-dimensional one (in r and z). The region is discretized into 400 intervals in the radial direction and 100 intervals in the axial direction. The finite elements differential

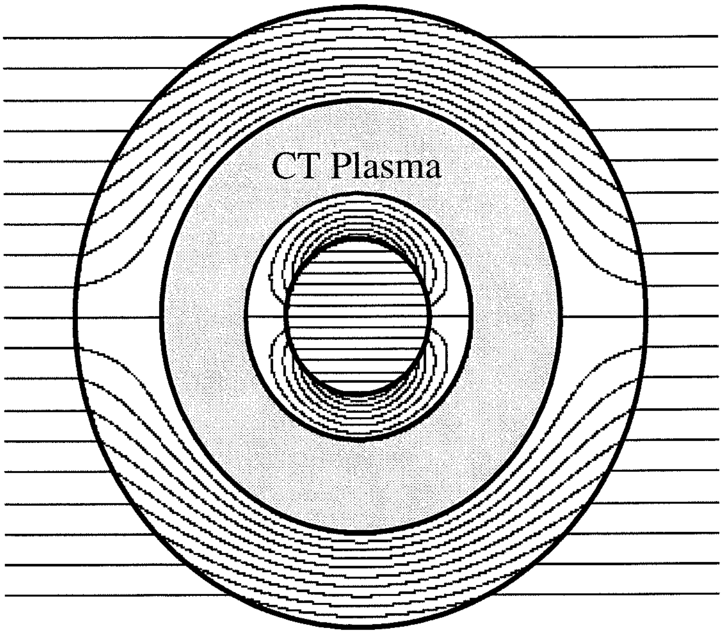

Figure 5.6: Toroidal flux trapping. Cross-sectional view of the magnetic field for the case of an annular CT plasma, with both inner and outer electrodes present.

equation $\nabla^2\Psi = 0$, along with the appropriate boundary conditions, was then solved using a successive over-relaxation (SOR) algorithm, performing 10000 iterations. The total magnetic energy in the volume could then be calculated numerically, and the kinetic energy criterion could be evaluated in a manner identical to that used in the analytical model above. In Figure 5.5b, the calculated values for α are shown for several CT aspect ratios (L/a). The numerical values closely approach those predicted by the previous 2D analytical model for aspect ratios of about 10 and higher. This implies that the analytical model should be a good approximation for the present case, where the measured aspect ratio is $L/a \approx 5$. For smaller aspect ratios, the analytical model may modestly overestimate the required CT kinetic energy.

A similar calculation can also be performed for configuration (I), in which a transverse dc magnetic field is trapped within both the center and outer electrodes. The resulting magnetic field structure is shown in Figure 5.6, with an annular CT cross-section. In this case, the amplification factor α depends on two additional quantities: the inner radius of the CT and the radius of the center electrode. The essential physics remains the same, and the required kinetic energy is increased by an amount which is sensitive to the dimensions of the CT. The notable difference, however, lies in the decreased cross-sectional area which the CT is permitted to occupy. As discussed above, increased drag is caused when the magnetic field strength is magnified by toroidal flux-trapping within the limited area between the CT and the electrode walls. Thus, if we assume an incompressible CT, removal of the center electrode in this region would increase the space available for the magnetic field and reduce the effects of toroidal flux-trapping.

The influence on injector performance of toroidal flux-trapping, with and without the center electrode, can be quantified by comparing the results obtained with electrode configurations (I) and (II). In the latter geometry, removal of the center electrode converts the region into a simple drift tube, with a 30% increase in cross-sectional area. As described above, the Langmuir probe results indicate an increase of the magnetic field threshold value from 2 to 4.5 kilogauss, as compared to configuration (I). Thus, the presence of the center electrode within the toroidal field region does appear to have a detrimental effect on performance, with an approximately five-fold reduction in CT energy in our experiment.

Our results are also consistent with this analysis of flux-trapping within a drift tube. Both configurations (II) and (III) involve final drift tube sections, with differing diameters. In the latter case, the 20 cm ID stainless steel vacuum bellows comprises the drift tube. (Although stainless steel is a relatively poor electrical conductor, it is still a magnetic flux-conserver for the time scales of interest). The improved performance of geometry (III) is due to the increased drift tube diameter R, reducing the critical ratio a/R, and hence reducing the decelerating effect of flux-trapping.

5.4 Calculation of limiting values for α

In the above analysis of a cylindrical CT displacing magnetic field, it was shown that the retarding force is enhanced by a factor α, which approaches a minimum value of 2 in the limit of infinitely distant confining walls, so that no flux-trapping occurs. In this section, we will analyze $\alpha_{\min}$ for two other CT geometries. In each case, the flux-excluding CT is first placed within an enclosure of finite dimensions with flux conserving walls. The magnetic field energy is then calculated to determine α, and finally the size of the enclosure is allowed to grow to infinity.

5.4.1 Spherical CT

We first consider the case of a spherical CT, using a spherical coordinate system in which the azimuthal axis is aligned with the direction of the uniform external magnetic field B_0. The CT is represented by a sphere of radius a within a larger sphere of inner radius R, with magnetic field trapped within its walls. The configuration is similar to that shown in Figure 5.5a, and we will use the same approach as in the earlier analysis.

The general azimuthally symmetric (current free) magnetic field is $\overrightarrow{B} = \overrightarrow{\nabla}\Psi$ where

$$\Psi = \sum_m (c_{1m}r^m + c_{2m}r^{-(m+1)}) \cos m\theta. \tag{5.10}$$

Applying the boundary conditions $[B_r]_{r=R} = B_0 \cos\theta$ and $[B_r]_{r=a} = 0$ give

$$\Psi = B_0 a \frac{R^3}{R^3 - a^3}(\frac{r}{a} + \frac{a^2}{2r^2}) \sin\theta. \tag{5.11}$$

The total magnetic field energy within the volume between the two concentric spheres is given by

$$W = 2\pi \int_a^R dr \cdot r^2 \int_0^\pi d\theta \cdot \sin\theta \cdot \frac{1}{2\mu_o} (\nabla\Psi)^2 . \tag{5.12}$$

Before the CT enters the region and perturbs the field, the sphere of radius R is permeated by a uniform field of magnitude B_0, so the magnetic field energy is simply $W_0 = (B_0^2/2\mu_0)(4\pi R^3/3)$. Thus, the net change in magnetic field energy resulting from the addition of the flux-excluding body in a section of length L is

$$\Delta W = W - W_0 = \frac{3}{2}\frac{R^3}{R^3 - a^3}\frac{B_0^2}{2\mu_o}(\frac{4}{3}\pi a^3). \tag{5.13}$$

The volume of the CT is $V_{CT} = 4\pi a^3/3$ and by inspection $\alpha = (3/2)R^3/(R^3 - a^3)$ so that the desired limit is $\alpha_{\text{min}} = 3/2$.

5.4.2 Cylindrical CT aligned with magnetic field

The second case we consider is that of a long thin cylinder oriented parallel to the magnetic field. Suppose the CT is represented by a cylinder of radius a and length L, and is located within a larger cylinder of radius R and length L'. The appropriate boundary conditions are then simply that $B_\perp = 0$ for all surfaces except the end caps ($z = \pm L'/2$) of the larger cylinder, where $B_\perp = \pm B_0$. By integrating over a cylindrical volume, $\overrightarrow{\nabla} \cdot \overrightarrow{B} = 0$ leads immediately to the condition that the magnetic flux Φ through any cross-section of the outer cylinder must be a constant. Using this result at an end-cap ($z = L'/2$) and at the center ($z = 0$) gives

$$B_0 \pi R^2 = \int_a^R 2\pi r \, B_z|_{z=0} \, dr. \tag{5.14}$$

Let us now consider only the region defined by $-L/2 \leq z \leq L/2$ around the inner cylinder. In the limit of large L (and L'), edge effects can be ignored, and the magnetic field is spatially uniform and purely axial in this region. Thus, $\overrightarrow{B} = B_z|_{z=0}\,\hat{z}$ can be obtained directly from Eq. 5.14, and the total magnetic field energy is simply

$$\begin{aligned} W &= \frac{B^2}{2\mu_o}\pi(R^2 - a^2)L \\ &= \left(\frac{B_0 R^2}{R^2 - a^2}\right)^2 (\frac{1}{2\mu_o})\pi(R^2 - a^2)L \end{aligned} \tag{5.15}$$

$$= \left(\frac{B_0^2}{2\mu_o}\right)\pi\frac{R^4}{R^2-a^2}L.$$

In this case, the initial energy is $W_0 = (B_0^2/2\mu_0)(\pi R^2 L)$, and the net change in energy is then

$$\Delta W = W - W_0 = \frac{R^2}{R^2-a^2}\frac{B_0^2}{2\mu_o}(\pi a^2 L). \tag{5.16}$$

Thus, $\alpha = R^2/(R^2-a^2)$ and the corresponding limit is $\alpha_{\min} = 1$.

5.5 Discussion and concluding remarks

Clearly, in the final configuration (III), increased effects on tokamak diagnostics such as density and radiation measurements are indicative of greatly improved CT penetration through the drift-tube, as compared to earlier configurations. Despite this improvement, an analysis of diagnostic data indicates that the CT has still not been successfully injected into the tokamak at the operational toroidal field strength of 10 kG. Injection of the CT occurs on the timescale of several microseconds, followed by a period of disintegration, which should require less than 100 microseconds, applying either of the two dissassembly mechanisms proposed by Parks [28]. Rapid (<0.5 ms) density increase accompanied by a similarly fast soft-xray drop, upon CT injection, was reported by Raman et al., in an experiment with similar CT and tokamak parameters [6]. The several millisecond risetime in tokamak density measured in this experiment is much longer than can be accounted for by CT decay, and suggests that the CT has not fully penetrated into the tokamak plasma.

The reasons for the lack of CT penetration are unclear, since the details of CT behavior and dynamics within the drift tube are not understood. We present here two possible scenarios which would lead to failure of the CT to penetrate. First, the CT may stop towards the end of the drift tube, in spite of our electrode modifications. For example, stopping may occur as a result of the toroidal flux-trapping mechanism proposed above, combined with an expansion of the CT within the drift-tube (and a corresponding decrease in kinetic energy density). The CT subsequently decays and recombines, resulting in a high density of particles near the edge of the tokamak discharge, which then feeds the tokamak density through particle diffusion. Another possible stopping mechanism is contact with the drift tube walls, which were not baked to improve vacuum cleanliness, resulting in rapid decay of the CT and deposition of its fuel at the tokamak edge. During earlier development of the CT injector, electrode surface impurities were linked to dramatic degradation in performance [7].

A second possibility which is consistent with the data is that the CT arrives at the tokamak plasma edge, but is subsequently stopped upon interaction with the plasma. One would expect a small cohesive plasmoid body to be able to penetrate the tokamak discharge, but as it travels within the drift tube, the CT may expand both horizontally or vertically, and may be unable to maintain its structural integrity. A large and/or ill-formed CT which strikes the tokamak plasma would likely be unable to penetrate to the interior, due to the gross displacement and rearrangement of tokamak flux tubes which would be required. In fact, this agrees rather well with observed MHD behavior of the tokamak upon injection. In particular, we have noted a shift in the tokamak plasma column beginning immediately after CT injection, which may be ascribed to the impulsive transfer of momentum from the CT. This shock impulse generates MHD modes which quickly grow unstable and often lead to disruption. The sharp pulses in carbon impurity may be produced by motion of the plasma column resulting in contact with the limiter. This pattern of effects was observed both in 10 kG discharges and in several 7 kG shots.

At this point, it is interesting to compare the present results with those reported by Raman on TdeV. In the latter experiment, the electrode configuration most closely resembles our configuration (III), with the end of the injector extending just slightly into the extent of the toroidal magnetic field [36]. That the TdeV results differ so strikingly from those reported here is most likely due to two factors. First, due to a thinner, close-fitting TF coil on the TdeV tokamak, the CT needs to travel only 17 cm within a drift tube in order to reach the entry port of the tokamak, as compared to 70 cm for the present experiment on the TEXT-U tokamak. The much shorter drift region reduces the effects of flux-trapping and avoids expansion of the CT. Secondly, the CT kinetic energies reported by Raman were based on average velocities, taken using time of flight measurements between two magnetic probes during the acceleration phase. Thus, the final velocities may have been significantly higher than reported, with correspondingly higher kinetic energies. Higher CT energies are also consistent with the much larger acceleration stage power supplies used in the latter experiment.

In light of the present results, we can make a few comments about the performance of CT injection systems. Clearly, close attention must be paid to the shape of acceleration electrodes in the toroidal field region. Focusing (or compression) of the CT through tapering of the electrodes should ideally occur just outside of the influence of the TF coils, followed by a larger-diameter drift tube section which directs the CT into the tokamak. However, care must be taken in minimizing the length of the drift tube region, and avoiding excessive drift-tube diameter, to provide some confinement of the CT so that expansion does not occur to an unacceptable degree. The length and maximum diameter of the drift region will, in many practical cases, be constrained by the dimensions of the toroidal field coil system and entry port of the tokamak.

Part II

Investigations of an unbounded expanding spheromak

Chapter 6 Unbounded spheromaks: experimental setup, diagnostics, and methods

6.1 Introduction

In the 25 years since Taylor's original helicity conjecture [2] was proposed, the minimum energy spheromak state has been studied in laboratory experiments rather extensively, with particular emphasis devoted to fusion-related applications. The original theory has been expanded upon and applied with remarkable success to plasma devices including tokamaks, reverse field pinches (RFPs), as well as expressly designed spheromak experiments (see, e.g., Ref. [37]).

However, there is substantial evidence which suggests that the applicability of these ideas extends well beyond the bounds of the fusion arena. Numerous solar, space, and astrophysical plasmas exhibit helical force-free magnetic fields which are suggestive of minimum energy Taylor equilibria; i.e., magnetic clouds [11][38], solar prominences [12], the earth's magnetotail [13], and astrophysical jets [15]. Indeed, it was the prevalence of force-free states which provided the motivation for the original work by Woltjer [1].

The second part of this thesis work comprising Chapters 6-11, deals with a laboratory experiment which employs a standard coaxial spheromak gun to generate plasma in a much larger vacuum vessel. The size of the vessel effectively removes the flux-conserving boundary which is common to all previous spheromak experiments. This situation closely simulates the vacuum boundary one often encounters in space plasmas. The experiment is thus a hybrid of sorts, employing established spheromak technology to investigate plasma in the relatively unfamiliar space environment.

The aim of this project is to characterize the formation and evolution of an unconfined spheromak produced by a coaxial gun. Details of the formation and reconnection process will be examined in order to determine the extent to which Taylor relaxation occurs. Departures from the minimum energy state will also be quantified. Laboratory spheromak ideas such as helicity conservation, flow, and injection threshold will be tested.

As a historical note, it should be remarked that the present experiment closely resembles in principle an experiment performed nearly four decades ago by Alfven and Lindbergh [3]. In the latter work, plasma generated by a coaxial gun was examined and found to exhibit interesting helical features and flux amplification. However, this early effort was undertaken without the benefit of modern diagnostic techniques, computational analysis tools, and, most importantly, insight which can be drawn from the now well-developed Taylor theory. In addition, the Alfven device was fired into an insulating (glass) container which was only moderately larger than the gun and thus the plasma was not permitted to freely expand without interacting with boundaries. Nevertheless, the present project may be viewed as a continuation of, and expansion upon, the Alfven experiment.

This Chapter is organized as follows. Section 6.2 details the experimental setup employed. In Section 6.3, the various diagnostics are described. Some estimates for plasma properties are given in Section 6.4. Finally, Section 6.5 explains details regarding the methods used in operating the device and acquiring data.

6.2 Apparatus

The experiments described in this part of this thesis work were performed on the apparatus shown in Figure 6.1. A magnetized Marshall gun is mounted so as to fire spheromaks into a much larger, roughly cylindrical vacuum chamber. A mechanical drawing of the chamber is presented in Figure 6.2. The size of the vacuum chamber provides generous optical access to view the plasma dynamics and also avoids plasma-wall interactions, so that boundary conditions appropriate for a true freely expanding

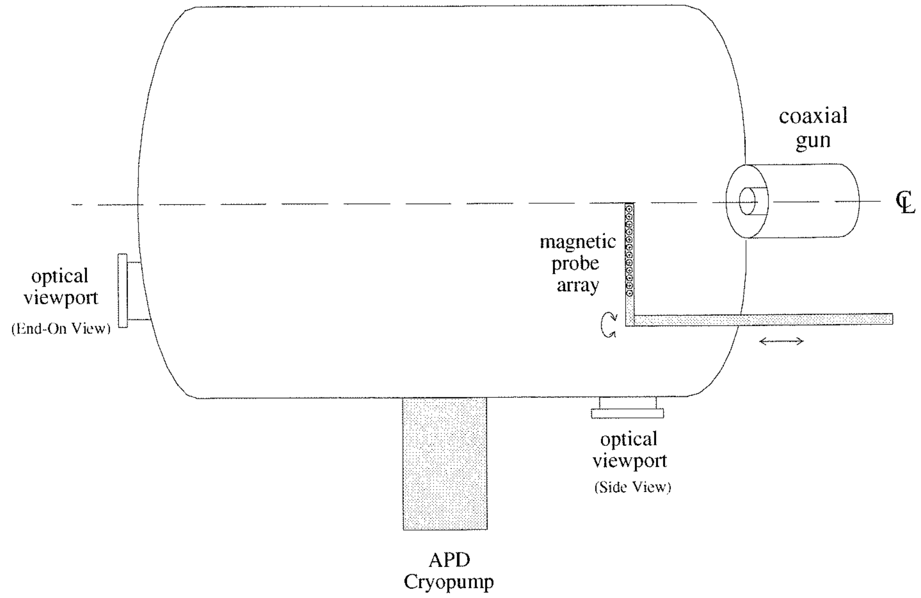

Figure 6.1: Diagram showing top view of coaxial gun, vacuum chamber, and magnetic probe diagnostic.

spheromak are achieved.

The coaxial gun and its power supply is identical to that used in the formation section of the CT Injector project described in the first part of this thesis work. The inner electrode is a 6.4 cm diameter copper tube sheathed with tantalum. The outer electrode consists of a 16 cm inner diameter copper tube spray-coated with tungsten. The gun is powered by a 120 μF ignitron-switched capacitor bank which was operated in a range of 4-8 kilovolts. Stuffing fluxes of up to 7 mWb are produced by a solenoid coil.

Vacuum is maintained by an APD Cryogenics cryopump, providing typical base pressures of approximately 2×10^{-7} Torr. A Varian sorption pump system is used for rough pumping of the chamber from atmosphere. This oil-free vacuum system ensures a high level of cleanliness, a consideration which was found to be of great importance for the CT Injector in Section 4.2.

All timing trigger signals are provided by a programmable, fully fiberoptic, CAMAC-

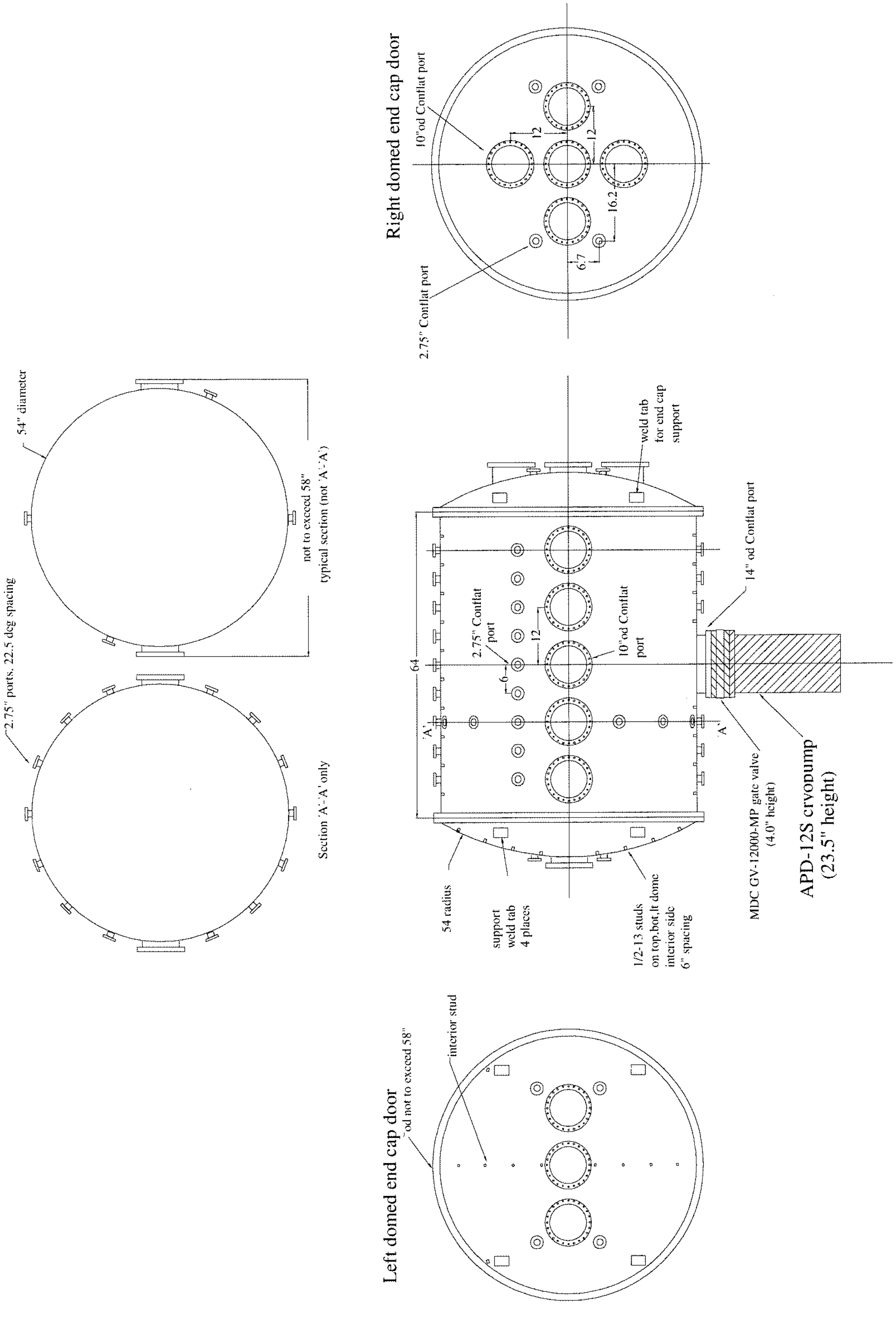

Figure 6.2: Mechanical drawing of vacuum chamber. The coaxial gun is mounted on the right domed end cap.

based timing module custom built by F. Cosso. The operation sequence of a plasma discharge generally proceeds as follows. The gas valve power supply is triggered 23 ms after the stuffing flux bank. With hydrogen gas, the main gun capacitor bank is fired 400 μsec afterwards. Simultaneously, digitization of the various diagnostic waveforms is initiated. Finally, after an adjustable time delay (typically 4-25 μsec), the camera is triggered.

6.3 Diagnostics

6.3.1 Electrical

Figure 6.3 shows a closeup of the electrode system and stuffing flux magnetic circuit. Also shown are two diagnostics which probe the electrical characteristics of the discharge.

A high voltage probe (Tektronix P6105) measures the voltage of the central electrode (which is the high potential side). The output of this probe is fed into a battery-powered 50Ω line-driver, which carries the signal to the digitizers. Due to electrical noise, it was necessary to heavily shield the line-driver enclosure and route its output through triaxial cable. With these measures implemented, output noise was dramatically reduced.

The ceramic break which isolates the two electrodes is encircled by a Rogowski coil to measure the total current carried by the plasma. The signal from the Rogowski coil is fed into a passive RC integrator, whose output is then digitized. Early tests of this diagnostic found a large degree of electrical ringing present in the output. This ringing was generated by LC oscillation between the inductance of the coil and stray capacitance in the cable to the integrator. This problem was ultimately resolved by adding a small series resistance near the Rogowski coil in order to absorb reflections from the transmission line.

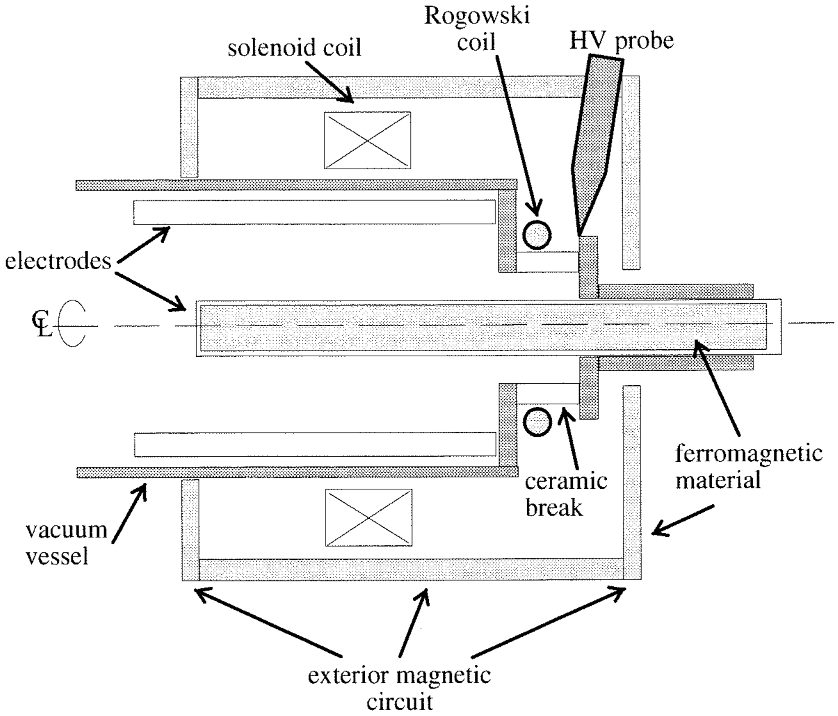

Figure 6.3: Closeup of gun, stuffing flux system, and electrical diagnostics.

6.3.2 Intensified CCD camera(s)

This experiment was expressly designed for excellent viewing access, and photography is one of the most important diagnostics employed. Two Princeton Instruments (Model ICCD-576) cameras can be positioned to image the plasma through either of two glass viewport windows. One window is located on the side and the other, at the opposite end of the vacuum vessel as shown in Figure 6.1.

These cameras use image intensified charge-coupled device (ICCD) technology to achieve high sensitivity and ultra-fast gating times. The image is focused by a lens onto a microchannel plate (MCP) image intensifier which is fiber-optically coupled to the CCD array, containing 576×384 elements. The image pixel data is subsequently digitized at a resolution of 14 bits by a Princeton Instruments model ST-138 camera controller and can then be transferred into the PC through a PCI-based interface card to be stored, displayed, and analyzed. By switching the image intensifier rapidly on and off with a Berkeley Nucleonics high voltage pulse generator (model 6040 with module 310H), an extremely short exposure time can be achieved (down to 10 ns).

Several precautions needed to be followed in operating the cameras. The CCD array is cooled using a Peltier device and water must be circulated during operation in order to carry away waste heat. Dry nitrogen also must be continuously flushed to avoid condensation of atmospheric water vapor onto the array.

Various commercial zoom lenses can be mounted on the camera housing on a standard Nikon F-mount. These lenses allow a range of fields of view to be achieved. In addition, a concave lens attachment was constructed in order to enable ultrawide angle (fisheye) pictures to be acquired. Exposure can be adjusted through the lens aperture ring, camera intensifier gain, and exposure time.

In some cases, three-dimensional information about the plasma was desirable, and the two cameras were set up for stereoscopic imaging as shown in Figure 6.4. Because the two cameras could not be physically located sufficiently close together in order to simultaneously image through the same viewport, an apparatus was designed by J.F. Hansen to support the cameras at right angles to each other. A mirror at 45^o effectively moves the cameras closer together.

6.3.3 Magnetic probe array

General principles

The second main diagnostic used in this project was a magnetic probe array, which enables measurements of the local magnetic field within the plasma. The probe array consists of a linear array of small magnetic pickup loops. This type of detector takes advantage of Faraday's Law: a voltage is induced which is proportional to the time rate of change of the magnetic flux through the loop.

$$V_{loop} = \int_C E \cdot dl = -\int_S \frac{\partial B}{\partial t} \cdot dA = -\frac{\partial \Phi}{\partial t}$$

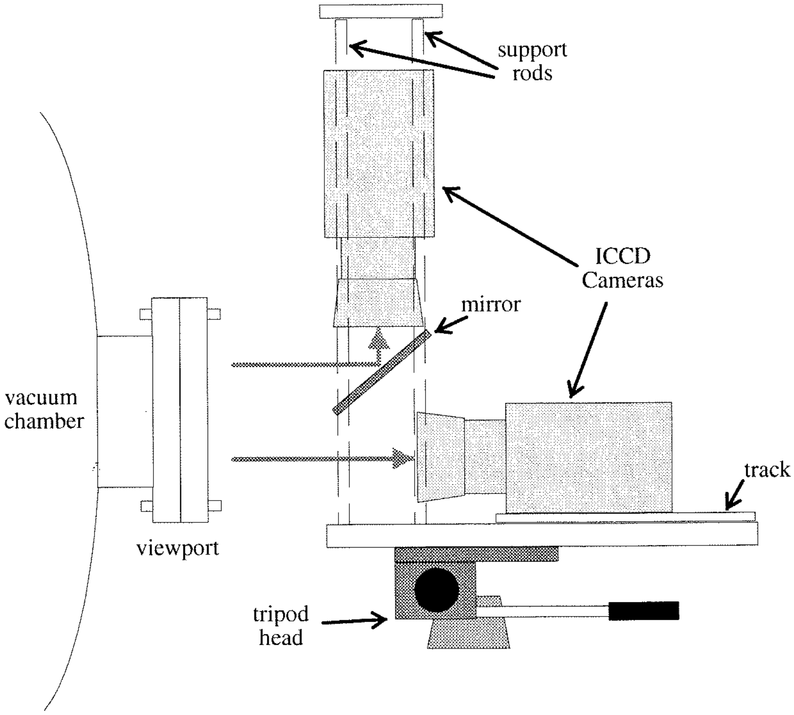

Figure 6.4: Diagram of stereoscopic camera support assembly.

Specifically, for an N-turn loop of area A, the average magnetic field threading the loop can be calculated using

$$B = \frac{1}{NA}\int_0^t V_{loop} \cdot dt$$

A practical consideration which limits the time response of this device relates to the self-inductance L of the loop. If the loop's output is connected to an instrument with input impedance R, the fundamental response time of this system is $\tau = L/R$ and corresponds to a frequency cutoff at $\omega_{cutoff} = R/L$. Frequency components much higher than this threshold value are filtered out of the output. The relative importance of this effect will be discussed below.

Overview

A schematic view of the magnetic probe array assembly is shown in Figure 6.5. The probe array is located on a Teflon form, which is threaded into a 0.25 inch outer diameter thin-walled (.010") stainless steel tube which is in turn sheathed in a 8 mm outer diameter protective, insulating ceramic tube. The SS tube is capped on its end, and serves the dual purposes of maintaining vacuum and providing some electrostatic shielding.

As shown in the figure, various Swagelok fittings connect the 0.25 inch tubing at right angles to a section of 0.5 inch stainless steel tubing, which then passes through a Cajon Ultra-Torr vacuum seal mounted on a 2.75 inch Conflat flange. The Cajon fitting allows for translation in the axial direction and rotation azimuthally. A three-dimensional volume of space can thus be probed by the array. Note that the axial travel of the probe is restricted so that the probe array cannot be positioned any closer than 10 cm from the mouth of the gun. This inaccessible region will be referred to as the *entrance region.*

Outputs from the probe are fed through the 0.5 inch tubing to a RF shielded BNC breakout box. From the box, RG-58 50Ω coaxial cables carry the signal to a set of 9 modules of Aeon (Model 3248) CAMAC based 8-bit digitizers, each with 4 input channels sampling at a 10 MHz rate. The time dependent waveforms are subsequently stored in an IBM-compatible Personal Computer (PC), where they can be integrated digitally and analyzed. Each of the cables is 50Ω terminated, and has inline 6, 10, or 20 dB attenuators as required to reduce the signal amplitudes to within the maximum allowable range of the digitizers (± 2.5 V).

Coordinate systems

Throughout the remainder of this text, two coordinate systems will be referred to in describing locations within the vacuum chamber. The first is (r,ϕ,z), the natural cylindrical coordinate system of the coaxial gun electrodes. The axis of this system

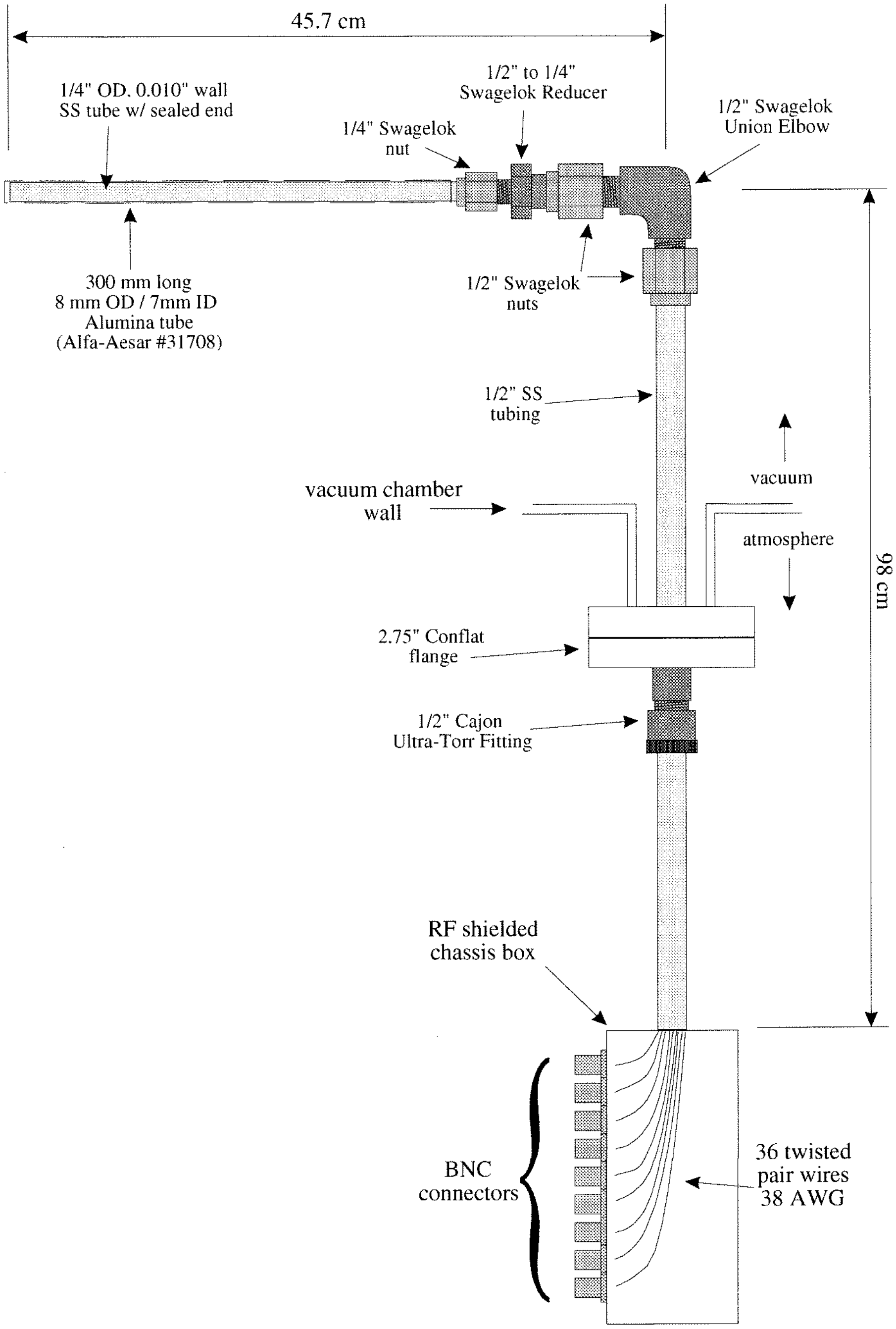

Figure 6.5: Components of the magnetic probe assembly.

is coincident with the geometrical axis of the gun and z is measured from the muzzle of the gun (end of outer electrode). The second system is (r^1, ϕ^1, z^1), the natural cylindrical coordinate system of the magnetic probe array. The axis is the rotational axis of the probe array, parallel to the axis of the unprimed system but offset from it. The axial coordinate z^1 is also measured from the same origin as the unprimed system, so that $z^1 = z$. (For example, the inaccessible entrance region is located at $0 < z^1 < 10$ cm.) The $\phi^1 = 0$ direction is defined to point towards the gun axis, while the $\phi = 0$ direction is defined to point towards the probe axis.

Construction details

The probe array was constructed on a 0.19 inch diameter, 12.5 inch long Teflon form, as shown in Figure 6.6. At each of 12 locations, spaced 1 inch apart, 3 separate wire loops measure the three components of the magnetic field: $\widehat{\mathbf{r}^1}$, $\widehat{\boldsymbol{\phi}^1}$, and $\widehat{\mathbf{z}^1}$. The $\widehat{\mathbf{r}^1}$ loop consists of 10 windings around the circumference of the form, while the $\widehat{\boldsymbol{\phi}^1}$ and $\widehat{\mathbf{z}^1}$ loops each consist of 10 windings through pairs of 1/32" holes drilled perpendicularly through the form. The $\widehat{\mathbf{r}^1}$ loops were wound before the other two, so that the $\widehat{\boldsymbol{\phi}^1}$ and $\widehat{\mathbf{z}^1}$ loops could also function to hold the $\widehat{\mathbf{r}^1}$ loop windings in place.

The windings were made using very fine (38 AWG) magnet wire in order to allow all 36 pairs of leads sufficient room to pass in the clearance space between the Teflon form and the inner diameter of the stainless steel tubing. The fine wire proved to be quite delicate and required careful handling in order to avoid damaging, tangling or knotting it. These difficulties were exacerbated by the long (~2 meter) lead lengths needed to carry the signal out of the probe to the BNC breakout box. It was found that the most efficient means of twisting these long leads was suspending the probe about 2.5 meters above the ground, hanging small weights from the two lead wires, and then spinning the weights.

Calibration

Calibrations were performed after the probe was fully constructed, complete with stainless steel tubing. At each of the 12 probe locations, the probe was placed at the

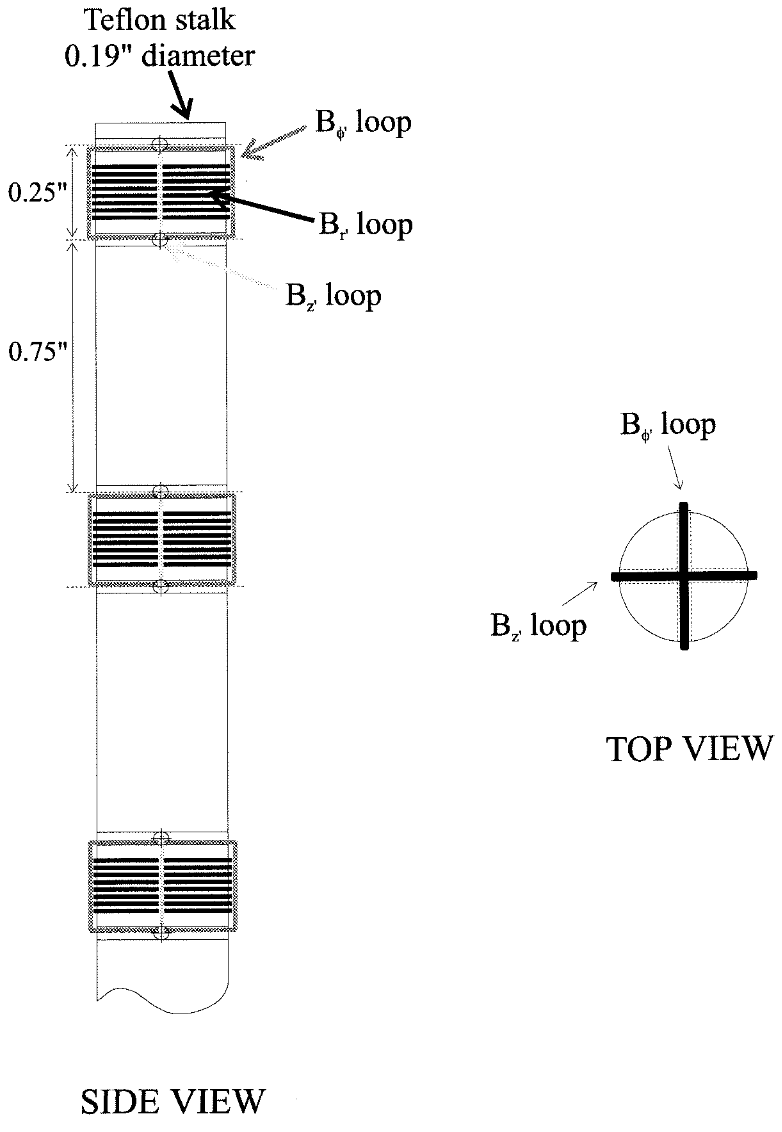

Figure 6.6: Detail sketch of magnetic probe Teflon form.

center of a Helmholtz coil set up to generate a 10 Gauss field with 30 μsec risetime. The output signals of all three probes at that location were then measured with an oscilloscope and the peak values recorded. By changing the orientation of the probe, the field was applied in each of the three orthogonal directions. In this way, the full 3×3 response matrix was obtained for each of the 12 probe locations. By inverting this matrix, the applied field can be reconstructed, given the 3 loop output signals. The matrices are not generally diagonal due to inaccuracies in the orientations of the loops.

Fundamentally, the induction loop method only measures the change in magnetic field $\Delta B = B(t) - B(t_0)$, where t_0 is the initial time of integration. Thus, it is generally necessary to measure the initial magnetic field $B(t_0)$ which in this case is produced by the stuffing flux field. To this end, the B_z field was measured at multiple points on a constant z plane ($z = 10$ cm) using a Hall Effect detector. Assuming axisymmetry, this information is sufficient to reconstruct the entire static vacuum field. Note that the magnitudes of the DC field were found to be relatively small: on the order of 40 Gauss at the $z = 10$ cm plane at high stuffing flux values, and correspondingly less at greater distances from the gun and at reduced stuffing flux.

Sources of measurement error

As with any diagnostic, it is important to be aware of the contributions to uncertainty in the quantity to be measured. Of particular concern is the frequency response of the magnetic probe due to the relatively fast time scales involved in this experiment. In order to analyze the frequency response of the probe, the frequency response of several components of the system must be considered in turn. As discussed above, the inherent frequency response of the inductive loop is determined by L/R. The inductance was directly measured to be approximately 5 μH, whereas the input impedance of the digitizer is determined by the 50Ω termination to the coaxial cabling. Thus, this criteria predicts a roll-off at about 1.6 MHz.

Also of relevance to this discussion is the electromagnetic shielding effect of the stainless steel tubing. In this situation, the $\widehat{\mathbf{r}^1}$ loops behave differently from the

Description	f_{cutoff} (MHz)
Self-inductance	1.6
Magnetic diffusion ($\widehat{\mathbf{r}^1}$)	0.6
Magnetic diffusion ($\widehat{\phi^1}$ and $\widehat{\mathbf{z}^1}$)	6
Digitization rate	5

Table 6.1: Contributions to frequency rolloff in the magnetic probe and the corresponding cutoff frequencies.

$\widehat{\phi^1}$ and $\widehat{\mathbf{z}^1}$ loops. In the former case, we must examine the behavior of an external magnetic field penetrating down the axis of a cylinder of conducting material. With the approximation of the infinitely long cylinder, it is straightforward to show that the appropriate timescale is $\tau = \mu_0 Rd/\eta$, where R is the radius of the tubing, d is its thickness, and η is the volume resistivity of the material. With the present dimensions, and a volume resistivity for stainless steel of $\eta = 3.5 \times 10^{-6}$ Ω·m, the soak time is $\tau = 0.3$ μsec, or $f_{cutoff} = 0.6$ MHz.

On the other hand, for the fields being measured by the $\widehat{\phi^1}$ and $\widehat{\mathbf{z}^1}$ loops, the magnetic field is in a direction perpendicular to the walls of the tube. For this situation, the well-known example of an electromagnetic wave incident on a plane conducting wall may be applied (see, e.g., Jackson [42]). The appropriate quantity is then $\omega = \frac{1}{d^2}\sqrt{2\eta/\mu_0}$, which corresponds to a frequency of 6 MHz.

The final frequency which needs to be considered is the 10 MHz sampling rate of the digitizer. By Nyquist's Theorem, this rate is sufficient to capture the signal's Fourier components up to a maximum of 5 MHz.

The various cutoff frequencies are tabulated in Table 6.1. From these values, we may conclude that the limiting frequencies are 0.6 MHz in the probe's radial direction and 1.6 MHz in the two orthogonal directions. These rolloff frequencies must be borne in mind in the data analysis which will be presented below, but are fairly high and unlikely to produce a major effect.

Besides the frequency response issue, several other effects may further degrade probe measurement accuracy. Crosstalk may be produced through electrostatic or inductive interaction between the leads from different probe loops. Tests were performed using the calibration Helmholtz coil, stimulating one probe location and observing the response of neighboring probe locations. In these tests, no crosstalk was observed, although all of the combinations were not attempted due to the prohibitively large number of possibilities. Electrostatic noise is minimized by the presence of the stainless steel shell. In fact, observable noise was only found at times near the ignitron discharge, and was negligible during the time periods of interest. Because no magnetic activity takes place during the several μsec following ignitron discharge, this observed noise could be removed in software without affecting the results. Another source of uncertainty is electromagnetic pickup of plasma magnetic fields in the leads emerging from the probe. This was minimized through twisting of the wire pairs. A final source of error stems from the discrete nature of digitization. For the 8-bit digitizers used, 256 levels are attainable, typically half of which are allocated to positive values and half to negative values. Thus, approximately $1/128 \approx 1$ % errors are to be expected from this effect. This is likely negligible compared to other sources of error mentioned above.

6.3.4 Fast ionization gauge

An auxiliary diagnostic found to be useful in this experiment was the fast ionization gauge. The ionization gauge is a standard piece of equipment in vacuum systems which is used to measure pressure. All ionization gauges operate on the basis of ionizing a fraction of the gas molecules present in the gauge and then collecting the gas ions. Within the gauge, a hot filament emits thermal electrons which are accelerated towards a positively biased grid. Some gas molecules within the gauge will be ionized through collisions with these electrons. The gas ions are positively charged and are attracted towards a negatively charged ion collector. The magnitude of this ion collector current indicates the amount of pressure. A higher pressure (density of gas molecules) will cause a larger rate of ionization, resulting in a greater rate of positive ionic charge on the collector.

Device	I_{gun}(kA)	Φ_{stuff}(mWb)	B_{sph}(T)	n_e(m^{-3})	T_e(eV)	τ_{res}(μsec)
CTX	400	11	0.3	10^{20}	100	40-100
BetaII	200-300	5-25	0.5	4×10^{20}	10	80-160
SPHEX	60	3.2	0.06	4×10^{19}	20	?
Caltech	130	2-6	0.15	?	?	?

Table 6.2: Review of typical plasma parameters for various spheromak experiments.

The fast ionization gauge simply provides a dynamic measure of the pressure, rather than the usual steady state DC measurement. To obtain this time dependence, the ion collector circuitry of a Varian ion gauge controller was bypassed while retaining the use of its filament and grid supply functionality. The ion collector pin, normally at electrical ground potential, was then connected to ground through a large resistor (200 kΩ). The voltage across this resistor, proportional to the ion collector current, was probed with an oscilloscope and provided a signal whose amplitude (typically 200 mV) was monotonically dependent on the gas pressure at the ion gauge. Because the precise value of the pressure was not needed in this case, the calibrated functional dependence of ion current on gas pressure was irrelevant. The usage of this diagnostic is described in the next section.

6.4 Plasma parameters

Unfortunately, several important and basic parameters of the plasma, such as densities and temperatures, have not been directly measured in this device. Diagnostics to address this issue are currently in development, but are not available at the time of this writing. However, estimates of these parameters can be obtained by comparison with other spheromak experiments with similar device and discharge characteristics, which have been more fully characterized.

Table 6.2 summarizes typical parameters from several previous experiments [26][34] [43][41]. It is clear that the current device falls in the middle of the spectrum in terms of currents, fluxes, and peak spheromak magnetic fields. Noting that the range in electron density values is quite narrow, we can, with a high degree of confidence, ex-

Description	**symbol**	**value**	**units**
magnetic field strength	B_{sph}	0.15	T
density	n_e	10^{20}	m^{-3}
Temperature	T_e	10	eV
characteristic length	L	20	cm
characteristic velocity	V	8×10^4	m/s
electron plasma frequency	ω_{pe}	6×10^{11}	rad/sec
electron gyrofrequency	ω_{ce}	3×10^{10}	rad/sec
ion plasma frequency	ω_{pi}	10^{10}	rad/sec
ion gyrofrequency	ω_{ci}	10^7	rad/sec
electron gyroradius	r_{Le}	5×10^{-3}	cm
Debye length	λ_D	2×10^{-4}	cm
electron thermal velocity	v_{Te}	2×10^6	m/s
ion sound velocity	c_s	3×10^4	m/s
Alfven velocity	v_A	3×10^5	m/s
e-e collision frequency	ν_{ee}	10^8	sec^{-1}
i-i collision frequency	ν_{ii}	2×10^6	sec^{-1}
mean free path	λ_{mfp}	2	cm
resistivity	η	0.01-0.1	$\Omega \cdot cm$
Beta	β	0.02	
Magnetic Reynolds	R_M	20-200	
Lundquist	Lu	80-800	
Magnetic Mach	M_M	0.25	

Table 6.3: Nominal plasma parameters.

pect values of density of $n_e \approx 10^{20}$ m^{-3}. This is also roughly consistent with the peak densities measured in the CT Injector (high 10^{21} m^{-3}), adjusted for no acceleration. Temperatures vary a bit more, but we can reasonably expect temperatures of in the low 10's of eV, implying a fully ionized plasma.

With these estimates, the plasma may be characterized by the parameters listed in Table 6.3.

6.5 Methods

6.5.1 Reproducibility considerations

For many of the diagnostics described above, measurements must be taken over multiple plasma discharges with fixed gun settings in order to form a complete data set.

Implicit in the validity of this methodology is the assumption that identical gun parameters produce identical plasma discharges; i.e., gun behavior is reproducible. In this section, the measures which were taken to maximize reproducibility will be described.

Most of the electrical power supplies to the device were eliminated as significant sources of irreproducibility. These power supplies are essentially passive electrical components such as capacitors, resistors, and inductors, and even the active components such as SCRs and ignitrons are highly repeatable. Measured electrical waveforms from these power supplies were reproducible as long as charging voltages were identical.

The chief source of variability was found to be the gas valves. Since these are mechanical devices, this is perhaps not surprising. Effects such as thermal expansion of the spring and resiliency properties in the O-ring seal are possible factors. Measurements with a fast ion-gauge showed that the amount of gas puffed gradually increased over time, rising quickly initially but plateauing after a time. The result of this increase in gas puff, as observed in camera and magnetic data, was a reduction in plasma propagation speeds.

Although this effect is subtle, it can introduce substantial errors over time, and is particularly harmful for larger data sets of 50 shots or more. To counteract this phenomenon, during data taking runs the amount of gas puff was checked using the fast ion gauge periodically. The voltage on the gas valve power supply was then gradually reduced to produce a smaller gas puff. This procedure was found to significantly improve reproducibility.

6.5.2 Magnetic probe operation

Data acquisition

Control of all data acquisition in this experiment is through an Interactive Data Language (IDL) program, which was written for this purpose. The user-friendly mouse-driven program enables the computer to archive experimental data (including magnetic signals, gun current, and voltage data), record notes on experimental parameters, and adjust digitizer range settings.

In obtaining magnetic data for a plasma discharge, it is necessary to make efficient use of the digitizers' limited dynamic range in order to maximize the signal-to-noise ratio. To this end, the voltage range of each Aeon digitizer module is adjusted through the control software to match the probe output voltage swing. This adjustment mechanism often requires some compromise due to the restriction that each module comprises 4 probe channels, but can only be set to one voltage range setting. In many cases, the adjustment range available in the digitizers is often exceeded by the signal, requiring the addition of in-line attenuators to be added to the 50Ω terminations. Calibrated BNC attenuators made by Elcom Systems of the 6, 10, and 20 dB variety were found to be well-suited to this application.

Data analysis

After digitization of the induced voltages from the magnetic probe loops, several steps are necessary to determine the magnitude of the source magnetic field. These steps are summarized in Figure 6.7.

a) The raw signal is based on the digitized values and accounts for the digitizer gain settings as well as any attenuation by in-line Elcom attenuators.

b) The data is then compensated for the calibration values (c.f. Section 6.3.3) by multiplying by the inverse 3×3 matrix. This calculation involves all 3 components (raw signal) of the magnetic field at this probe array location.

c) The calibrated data can now be integrated straightforwardly. Note that any electrical noise in the vicinity of the ignitron breakdown is removed by setting values in the range $0 < t < 7$ μsec to zero, before integration. This time period is well before magnetic activity begins. The constant of integration is chosen such that the integrated signal vanishes at $t = 40$ μsec, well after all magnetic activity ceases.

d) After step (c), there is generally a B_{offset} such that the calculated field at $t = 0$ does not vanish as would be physically expected. Generally B_{offset} was found to be fairly small, typically less than 10% of the maximum value of B. (For data in which this was not the case, the shot was repeated until this criteria was satisfied.)

(a) Raw signal compensated for attenuation

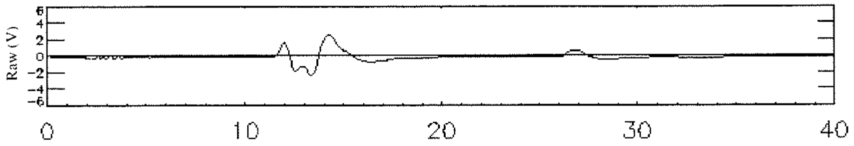

(b) Calibrated

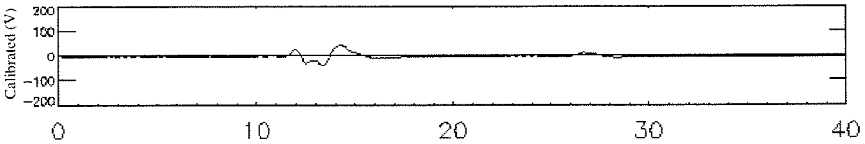

(c) Integrated

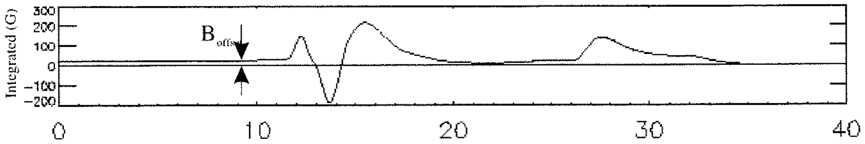

(d) Integrated and zero level adjusted

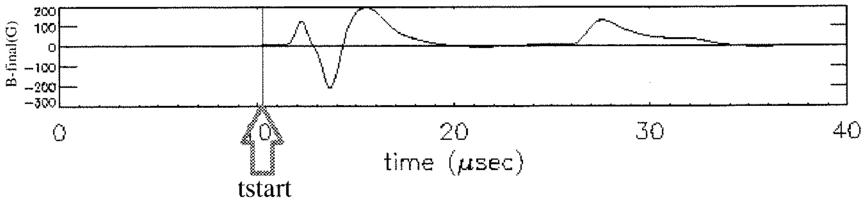

Figure 6.7: Steps involved in magnetic probe integration.

Besides an incorrect measurement of the zero level of the unintegrated signal, a second effect can produce this finite B_{offset} result. Consider any measured value V with uncertainty $\pm\sigma_V$, which must be time integrated. Discrete integration over N time intervals is equivalent to the summation $I = \sum_{i=1}^{N} V_i \cdot \Delta t$, from which the standard deviation of I can be straightforwardly computed $\sigma_I = \Delta t \cdot \sigma_V \sqrt{N}$. This is a random walk type of result and indicates that uncertainty increases with the integration interval.

In order to reduce this uncertainty, it is desireable to reduce the integration interval, and in step (d) this is achieved by identifying the time at which magnetic activity begins. The time is labeled in the figure as t_{start} and is computed as the time at which the raw signal first exceeds 2% of its maximum value. Integration is performed over the interval $t_{start} < t < 40$ μsec, and B_{offset} is reduced to zero by including a small zero level adjustment before integration.

e) In this final step (not shown) the static magnetic field, previously characterized in the calibration stage, is calculated at the probe location and simply added to the value from step (d).

6.5.3 Camera movie sequences

Movies of the plasma are compiled by firing multiple plasma shots with the same operating parameters while acquiring images at varying times within the discharge. Thus, this technique relies on a high degree of reproducibility between shots. It is also important to note that the camera exposure does not generally remain at a constant setting throughout an image sequence. As the discharge progresses, the plasma emerges from the gun and typically rapidly increases in intensity until a peak intensity is reached and then gradually decays away.

In order to take maximum advantage of the dynamic range of the CCD, the camera exposure is varied through adjustment of the lens aperture, exposure time, and intensifier gain settings. Accordingly, setting of the exposure entails some degree of compromise between competing considerations. Increased lens aperture increases the amount of light admitted at the expense of decreased depth of field. Longer exposure times also improve the signal magnitude, but may result in motion-induced blurring of the image. Higher intensifier gain settings results in further amplification of the signal, but also degrades the image from a noise standpoint. Care must also be taken to avoid fully saturating any CCD pixels due to the CCD "bleeding" effect, which causes saturated detector elements to bleed charge onto neighboring elements.

A quantitative example of the actual time dependence of plasma intensity at $I_{gun} = 130$ kA, $\Phi_{stuff} = 6$ mWb (calculated from the movie sequence shown in Figure 11.1 in Chapter 11) is presented in Figure 6.8. Each data point represents the net incident light and is found by integrating over all of the pixels in the image

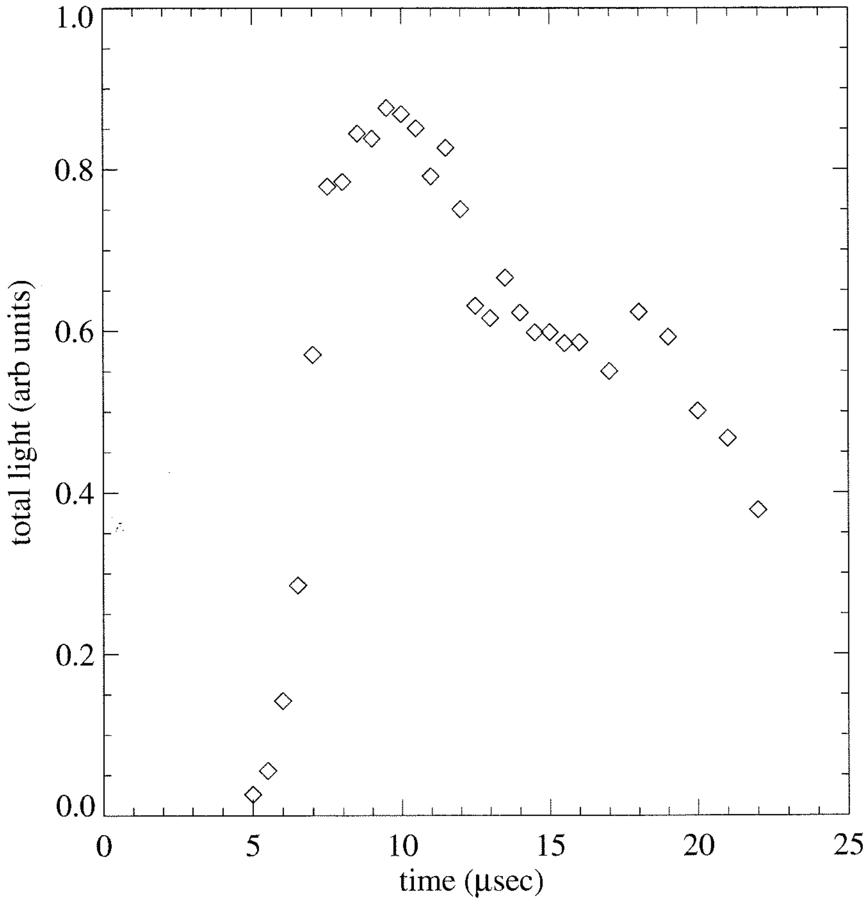

Figure 6.8: Time dependence of total light received by camera.

and then compensating for exposure settings. This summation procedure essentially provides a measure of the cumulative light received by the full CCD array and is proportional to the total amount of light emitted by the plasma. Times are given in relation to the initiation of the gun discharge. Note that the plasma is not visible until it begins to emerge from the muzzle of the gun at 5 μsec. Intensity quickly increases to a peak at approximately 10 μsec and then decays away, reaching one half of its maximum value at approximately 20 μsec.

In each image, the digitized pixel data, which initially has a range of 0 to 65535, is scaled down linearly to a range of 0 to 255. The black value (0) is chosen according to the darkest region of the background, and the brightest value (255) is associated to a bright region in the plasma. Each of these values is color-mapped as shown in Figure 6.9. The scale ranges from black to red-orange, with white denoting the brightest, fully saturated pixels (level 255).

The spectral response of the CCD camera includes mainly the visible spectrum. Furthermore, simple experiments with notch filters placed in front of the lens indicate that the bulk of the light collected is in the H_α line. Thus, strictly speaking, these images are not viewing radiation generated by the plasma itself, but are instead looking at excited neutral hydrogen emissions. Nevertheless, the pattern of this radiation is clearly linked closely with the behavior of the plasma, as evidenced by the frequent appearance of filamentary structures, often with twist. Furthermore, similar features which have also been observed in H_α images of solar prominences have been subsequently confirmed to be magnetic in nature [44]. The mechanism most likely driving this phenomenon is collisions between the energetic electrons carrying the generally field-aligned plasma current and the residual non-ionized hydrogen, resulting in the observed line radiation. Evidence for the connection between the plasma's magnetic field and the visibly observed structures will be presented in Chapter 11.

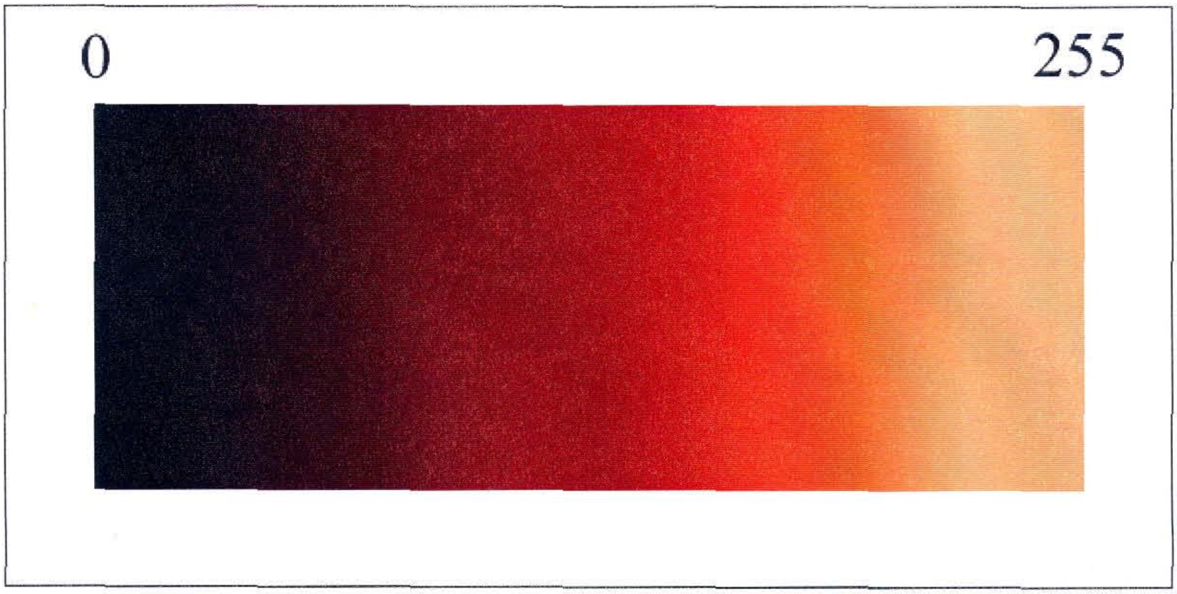

Figure 6.9: Intensity scale color mapping.

Chapter 7 Classification of operating regimes

7.1 Introduction

Photography is a largely neglected diagnostic technique in modern experimental plasma physics. Emphasis is instead often placed upon direct probing of local plasma properties, which often risks perturbation of plasma behavior. Imaging avoids this drawback by virtue of its passive and non-invasive nature, in addition to providing a means of gaining information concerning the global properties of the plasma, such as plasma morphology. Thus, it is particularly appropriate for this experiment, in which one of the main interests lies in the magnetic helicity content and associated magnetic topology structure.

In this project, generous viewing access allows the spheromak to be imaged from several locations as it emerges from the gun. By sequentially varying the instant at which the plasma discharge is photographed, time sequences of pictures could be compiled and assembled into movies documenting plasma evolution. In this chapter, observations of spheromak formation will be presented in the form of time sequence images acquired using the Princeton Instruments ICCD camera. These movies demonstrate qualitatively distinct plasma behavior as the gun parameters are varied, and suggest classification of plasma dynamics into several categories which will be examined in detail in the following chapters.

The chapter is organized as follows. Section 7.2 reviews general coaxial gun formation theory. Section 7.3 presents four representative movie sequences. In Section 7.4, the plasma dynamics regime is associated with gun parameters. Finally, Section 7.5 discusses the results and provides an outline of Chapters 8-11.

7.2 Coaxial-gun-based spheromak formation

In this section, the procedure employed in forming a spheromak by the coaxial gun method is explained. This material was previously presented in Section 3.2 in reference to the CT Injector experiment. It is repeated here for convenient reference.

The coaxial gun operational sequence is summarized in Figure 7.1. The sequence involves four steps:

(a) In this initial step, a poloidally directed magnetic field is generated by energizing an electromagnet coil. This magnetic field is called the *stuffing flux* field (or alternatively, the *bias* magnetic field). Although the stuffing flux field is generally powered by a pulsed power supply, the time scale of its waveform is often much greater than the duration of the formation discharge, so that it can be considered to be a quasistatic DC field.

High-speed valves then puff a cloud of gas (typically hydrogen, deuterium, or helium) into the region between the inner and outer electrodes.

(b) Through the use of a high voltage pulsed power supply (usually consisting of an ignitron-switched capacitor bank), a large voltage is abruptly applied across the electrode gap. The high voltage breaks down the gas and subsequently drives current through the resulting donut-shaped plasma, creating a toroidal magnetic field imbedded ("frozen") in the plasma.

(c) MHD $\overrightarrow{J} \times \overrightarrow{B}$ forces acting on the ring of plasma push the ring out the muzzle of the gun. However, since the plasma is a flux-conserver and expels the external magnetic field, the stuffing flux field must be distended to accommodate this motion out of the gun. Furthermore, this stretching of the field lines requires energy, and thus robs kinetic energy from the plasma.

(d) If the formation current is sufficiently large, the $\overrightarrow{J} \times \overrightarrow{B}$ force overcomes the resistance provided by the tension forces, and is able to sufficiently distend the stuffing flux field lines so that reconnection occurs behind the plasma ring. The isolated plasmoid thus formed possesses a closed magnetic field structure containing both poloidal and toroidal field, and consequently has finite magnetic helicity. This

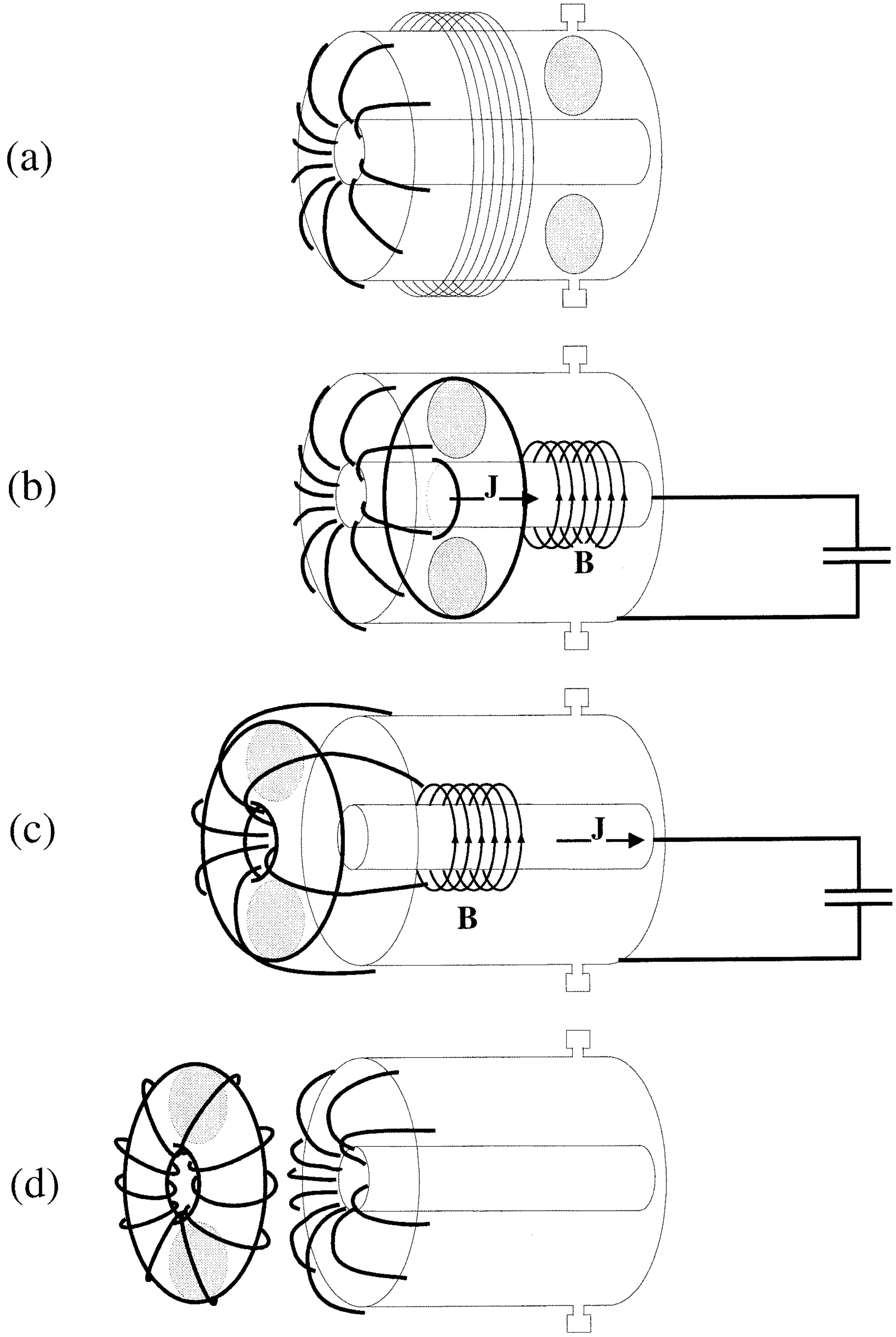

Figure 7.1: Spheromak formation sequence in the magnetized coaxial gun method. See text.

completes the formation process, and by Taylor's conjecture the plasma relaxes to a near force-free spheromak configuration.

From this discussion, it is apparent that there is a threshold value for gun current which determines the coaxial gun's operational regime. For gun currents higher than this value, a free spheromak is formed, whereas the plasma cannot overcome the tension forces imposed by the stuffing flux when the current is less than this value. Empirically, a sharp cutoff in operable values of $\lambda_{gun} \equiv \mu_0 I_{gun}/\Phi_{stuff}$ (with gun current I_{gun} and stuffing flux Φ_{stuff}) has been observed [26]. This cutoff is also referred to as a *helicity injection threshold*. Gun behavior can be described intuitively: when λ_{gun} is below the threshold value, the plasma cannot detach (i.e., it is "stuffed"), while excessively high values of λ_{gun} correspond to very low stuffing flux cases, in which case spheromaks with very low helicity content are produced.

However, the precise criterion that must be met for successful spheromak formation is a subject of current debate. Nevertheless, the essential physics can be obtained by considering a simple model as follows. If the toroidal field is assumed to be of the form $B_{tor} \cong \mu_o I_{gun}/(2\pi r)$ (i.e., an infinitely long wire) and the poloidal field is $B_{pol} \cong \Phi_{stuff}/(\pi r^2)$, then the requirement that magnetic pressure exceeds tension gives $\lambda_{gun} > 2/r$ where the applicable value of r would be a characteristic radius of the system, such as the outer electrode radius r_e. For example, this naive result may be compared with the value derived by Schaffer [30] for an axisymmetric spheromak in an infinite cylinder, $\lambda_{geom} = 3.8317/r_e$. It is evident that, although the numerical constant may depend on the model used and the details (e.g., shape) of the gun mouth, the critical value λ_{geom} is mainly dependent on geometric considerations.

7.3 Camera movies

The camera is a powerful diagnostic tool because it provides a simple means of obtaining direct information about the gross structure of the plasma, which may hint at the underlying structure of the magnetic field. As such, in order to quickly characterize gun operation in terms of general plasma behavior, it is informative to acquire image sequences with the gun operated over a wide range of parameters.

During the course of these parameter-space surveys, qualitative plasma evolution is observed to generally fall into one of four categories. These categories will be referred to as Regimes I-IV, and sample movie sequences of each are presented in Figures 7.6 and 7.7. These pictures were taken with the camera positioned to image the plasma from the Side View (see Figure 6.1). The vacuum port of the plasma gun is visible as an upright oval at the right of each image. The muzzle of the gun is located near this position, and plasma is ejected from the gun across the field of view, from right to left.

7.3.1 Regime I

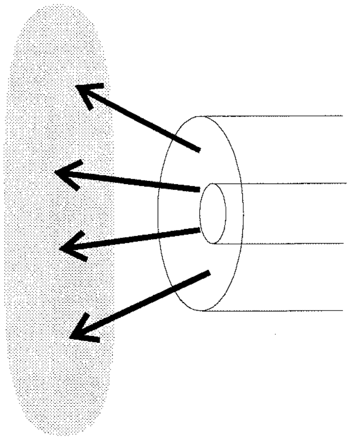

Figure 7.2: Representative sketch showing plasma appearance in Regime I.

In Regime I (Figure 7.6), the plasma remains fairly homogeneous throughout the discharge, exhibiting no fine structure. The plasma exits the gun as an essentially vertical amorphous blob, as sketched in Figure 7.2. The gun parameters are $I_{gun} = 130$ kA and $\Phi_{stuff} = 0.4$ mWb for this case, corresponding to a nearly unmagnetized Marshall gun discharge, so that little helicity content is present and the applied bias field does not impede the plasma. (In this case, the stuffing flux is provided by residual magnetization in the magnetic circuit.)

7.3.2 Regime II

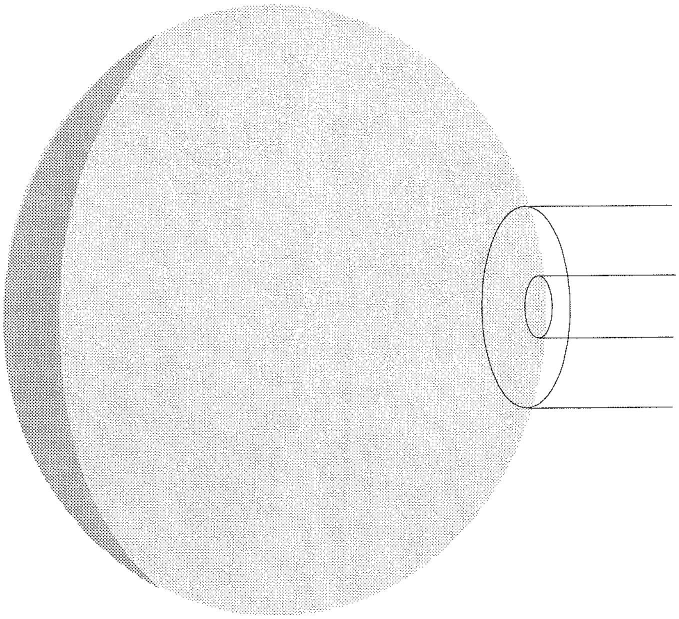

Figure 7.3: Representative sketch showing plasma appearance in Regime II.

In Regime II (Figure 7.6), on the other hand, the plasma emerges with a spherical shape which further expands over time. The well-defined left edge is especially bright and sporadically contains filamentary structure. The general appearance is shown in Figure 7.3. Here, the gun parameters are $I_{gun} = 130$ kA and $\Phi_{stuff} = 2$ mWb. Evidence will be presented in Chapters 8 and 9 showing that a spheromak-like state is generated in this case.

7.3.3 Regime III

In sharp contrast to the other Regimes, the plasma in Regime III (Figure 7.7) contains a wealth of fine structure. Of particular note are the distinct central column (twisted) and helical outer loops which appear. These features evolve through a sequence of stages, as will be described in greater detail in Chapter 11. Figure 7.4 summarizes the appearance of the plasma for this case. The gun is operated at $I_{gun} = 130$ kA and $\Phi_{stuff} = 6$ mWb for these images, and appears to be marginally stuffed, based on magnetic data which will also be presented in that chapter.

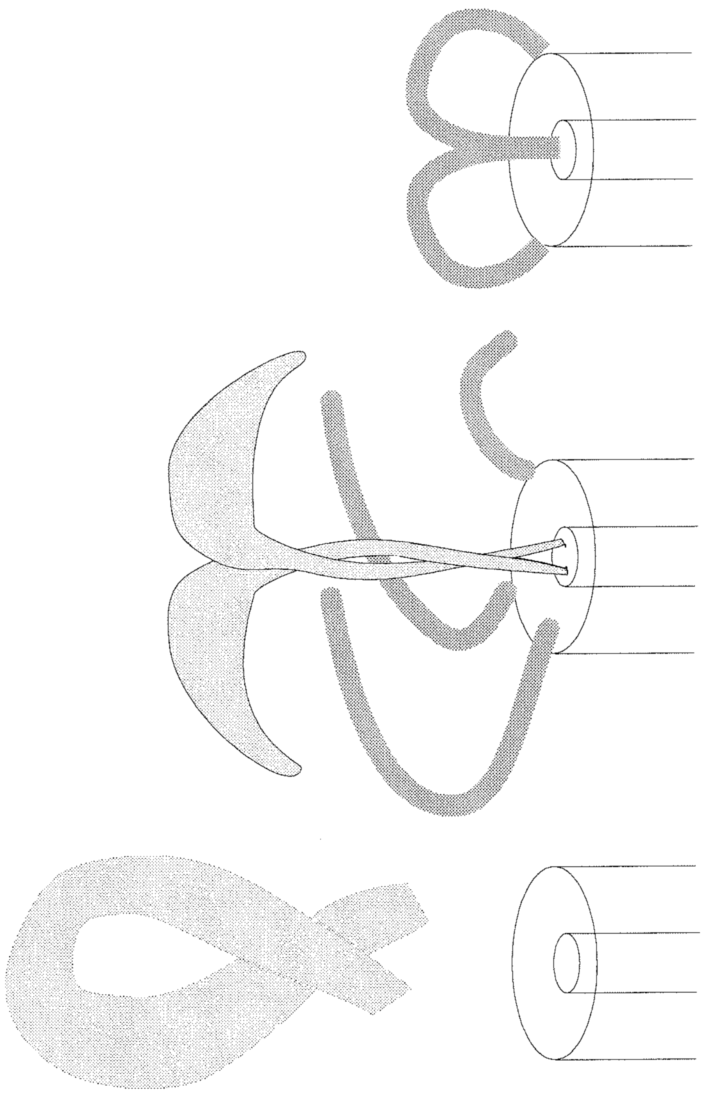

Figure 7.4: Representative sketch showing plasma appearance in Regime III.

7.3.4 Regime IV

Finally, in Regime IV (Figure 7.7), the plasma emerges very slowly from the gun and decays away at the mouth of the gun. Similar to Regime I, the plasma here is quite homogeneous in appearance. An indentation at the midplane suggests that the high stuffing flux field is successfully confining the plasma, as depicted in Figure 7.5. The gun is stuffed in this Regime, with gun parameters of $I_{gun} = 90$ kA and $\Phi_{stuff} = 6$ mWb.

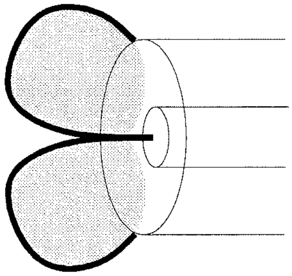

Figure 7.5: Representative sketch showing plasma appearance in Regime IV.

7.3.5 Propagation rates

The discharges in these four cases can also be distinguished by their propagation rates. For each picture, the leftmost edge of the plasma at the device midplane is calculated. This data is plotted in Figure 7.8, using the images presented in Figures 7.6 and 7.7. Linear regression fits show that propagation rates vary considerably, with a plasma speed of 10.6 cm/μsec in Regime I slowing to a speed of 2.6 cm/μsec in Regime IV. This behavior agrees with the expected notion of increasingly stuffed gun operation; i.e., plasma motion is increasingly restricted by magnetic tension at higher applied bias fields. Propagation will be found to be an important issue in Chapter 8.

7.4 Correlation with λ_{gun} values

As discussed in Section 7.2, a key parameter governing the behavior of a spheromak gun is $\lambda_{gun} = \mu_0 I_{gun}/\Phi_{stuff}$, the ratio of the gun current to the stuffing flux. Numerous experiments have demonstrated empirically that operation with λ_{gun} differing significantly from its nominal value will not produce a well-formed spheromak. (This parameter was also found to have a strong effect on CT accelerator performance in Chapter 5.) It is thus important in any comprehensive survey of gun operation to investigate how the generated plasma evolution is affected by varying this parameter.

The extent of the various Regimes was found to be associated with the gun current and stuffing flux parameters. This dependence is shown in Figure 7.9. Each point

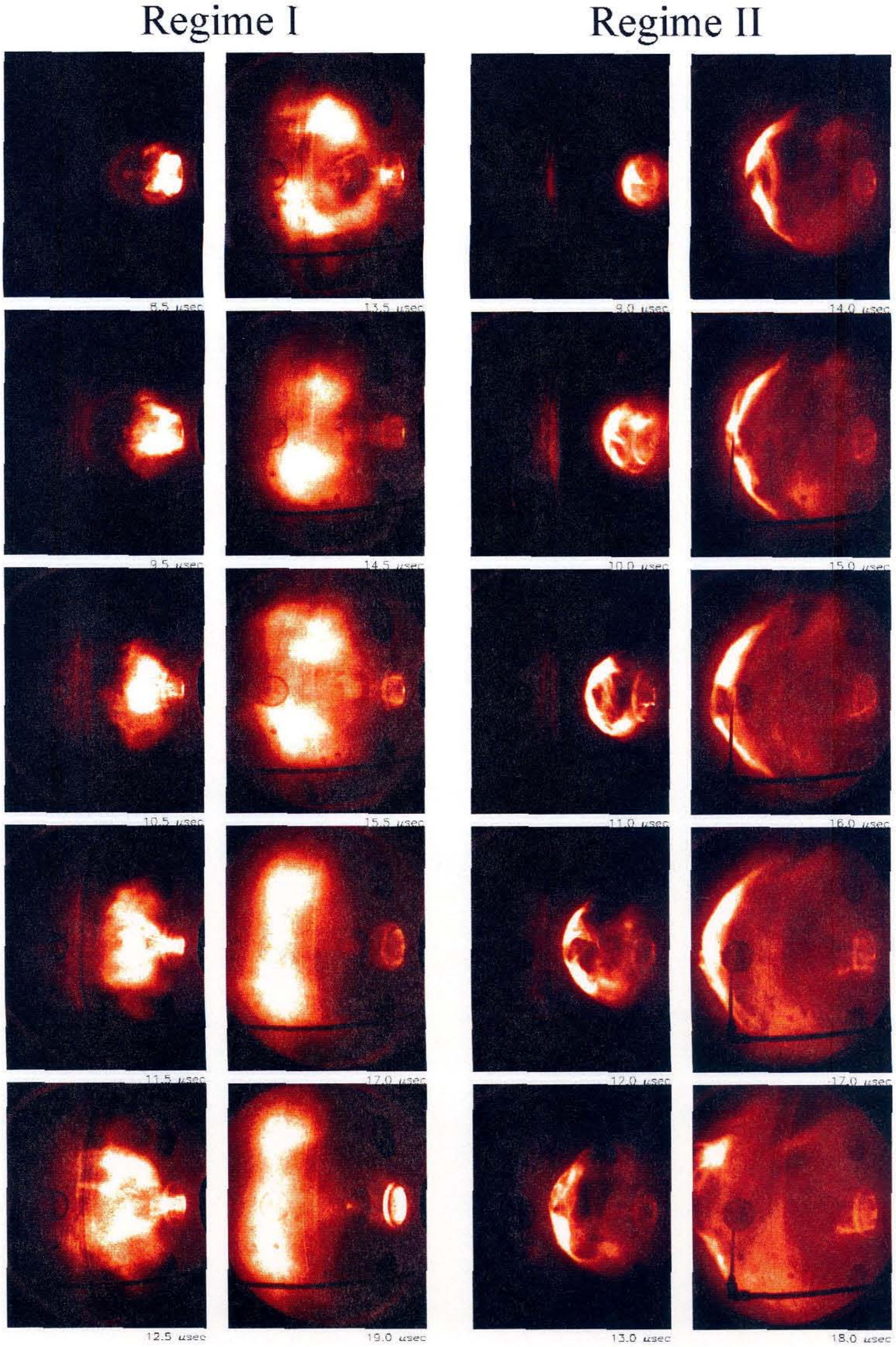

Figure 7.6: Side View image sequences with gun parameters: $I_{gun} = 130$ kA, $\Phi_{stuff} = 0.4$ mWb (Regime I) and $I_{gun} = 130$ kA, $\Phi_{stuff} = 2$ mWb (Regime II).

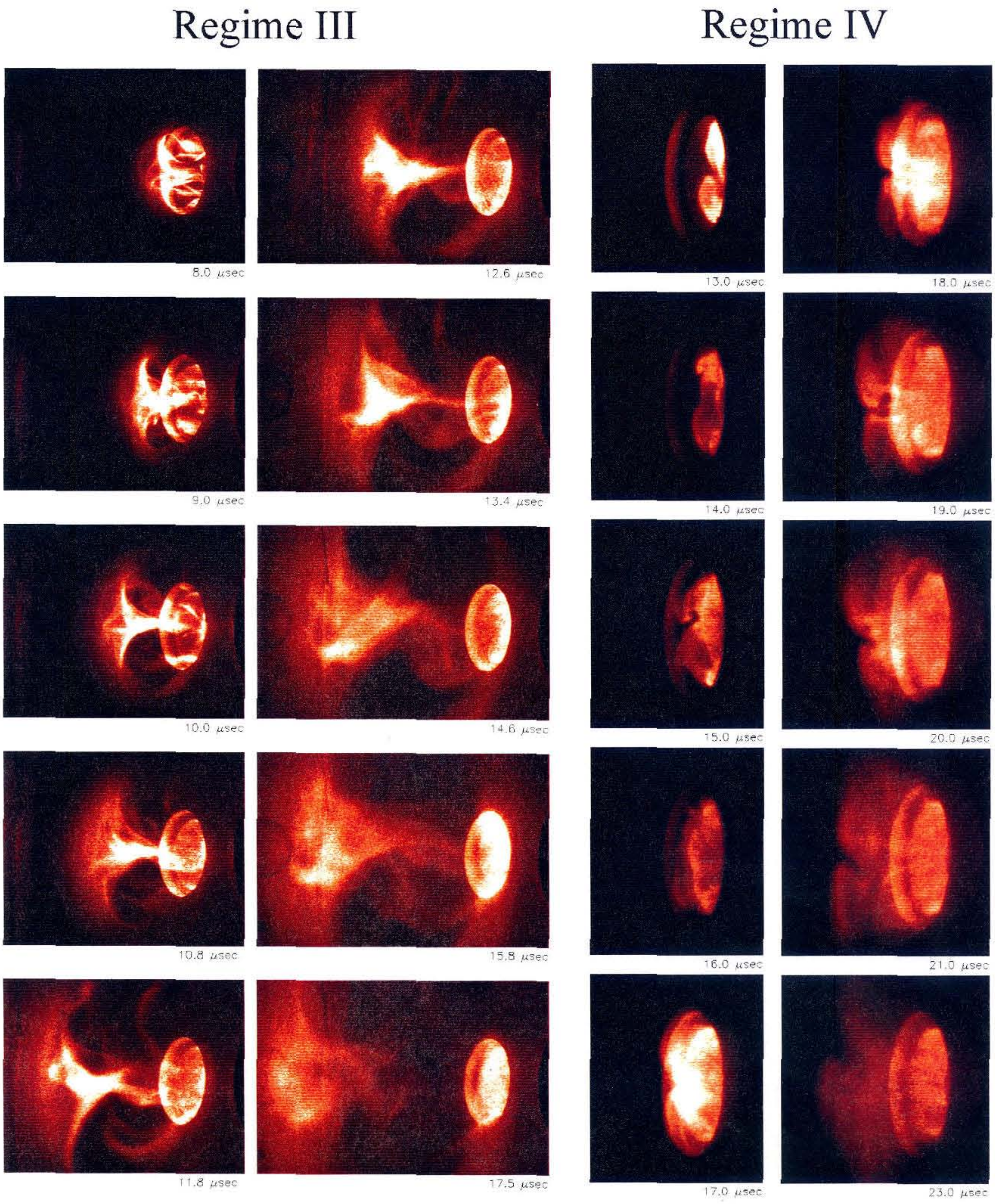

Figure 7.7: Side View image sequences with gun parameters: $I_{gun} = 130$ kA, $\Phi_{stuff} = 6$ mWb (Regime III) and $I_{gun} = 90$ kA, $\Phi_{stuff} = 6$ mWb (Regime IV).

corresponds to a series of images obtained at that gun setting, and gives a subjective determination of the appropriate Regime classification. Approximate λ_{gun} boundaries between Regimes are also superimposed.

7.5 Discussion

In this chapter, plasma dynamics were classified into four regimes, dependent on the gun parameters; plasma evolution varies substantially between different regimes. These regimes are associated with varying levels of stuffed or unstuffed gun operation, and the boundaries between adjacent regimes are found to be correlated with helicity injection thresholds; i.e., λ_{gun} values.

Regimes I and IV correspond to less interesting extreme cases in which the plasma is either unaffected by, or dominated by, the stuffing flux field. On the other hand, plasmas produced in Regimes II and III exhibit a greater level of structure which may be associated with magnetic helicity. For this reason, the remainder of this thesis work will focus on these latter two Regimes of operation. Chapters 8-10 present evidence of a spheromak state and examine the extent to which relaxation is incomplete. Chapter 11 delves into the details of plasma morphology in Regime III, the marginally stuffed case, as observed from both camera and magnetic data.

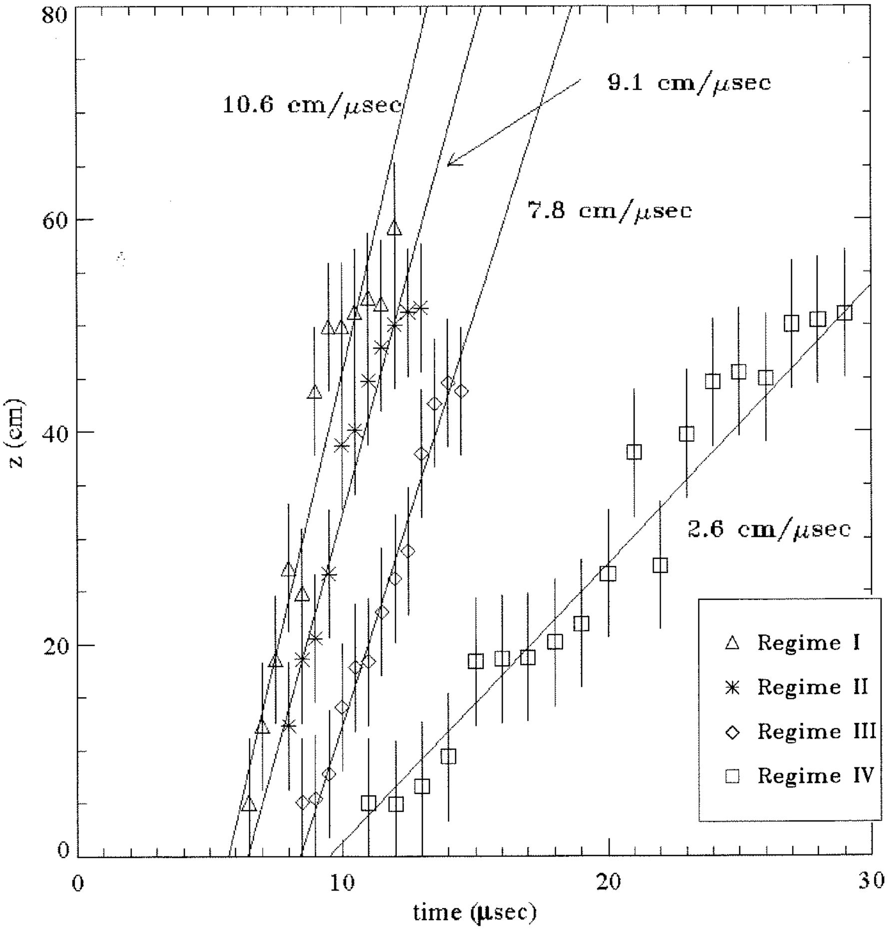

Figure 7.8: Propagation rates of the plasma front for the four Regimes, as obtained from camera data.

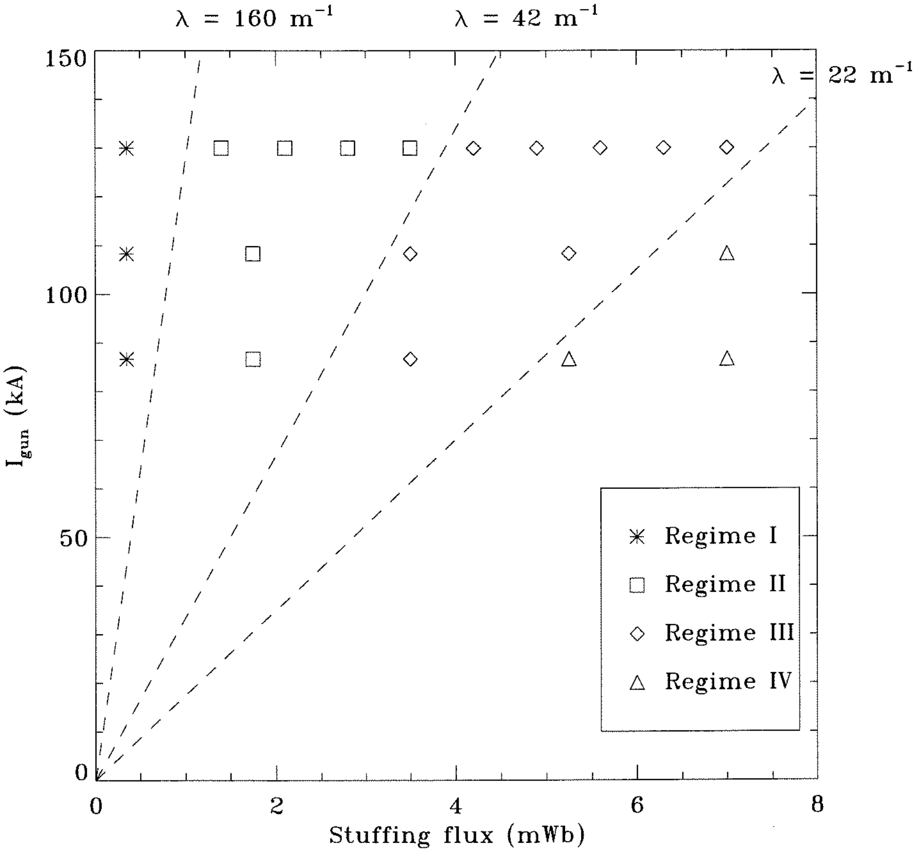

Figure 7.9: Survey of Regime classification versus gun current and stuffing flux. Dashed lines indicate λ=160, 42, and 22 m^{-1}.

Chapter 8 Regime II: Verification of a spheromak state

8.1 Introduction

As described in the discussion in Chapter 2, the basic axisymmetric spheromak configurations such as the spherical and cylindrical spheromaks have qualitatively similar magnetic topology. They are characterized by a set of concentric flux surfaces when viewed in the poloidal plane, corresponding to nested toroidal surfaces in three dimensions, as shown in Figure 8.1. Because they have this type of organization, these Taylor states may be described as donut shaped (or plasma rings). Note that the hole of the donut may be threaded by open field lines connected to the spheromak gun, in the case of incomplete detachment.

In Chapter 7, plasma evolution was classified phenomenologically into four Regimes on the basis of camera image sequences taken from the Side View. In the present chapter, diagnostic measurements in Regime II will be examined in greater detail in order to determine whether a detached spheromak configuration is in fact produced. Observations using the camera and magnetic probe array are compared with the general physical picture given in the previous paragraph.

The chapter is organized as follows. In Section 8.2, gun current, gun voltage, camera, and magnetic data are presented. Section 8.3 discusses analysis of the magnetic data based on a propagation technique. Finally, Section 8.4 examines the results of this analysis.

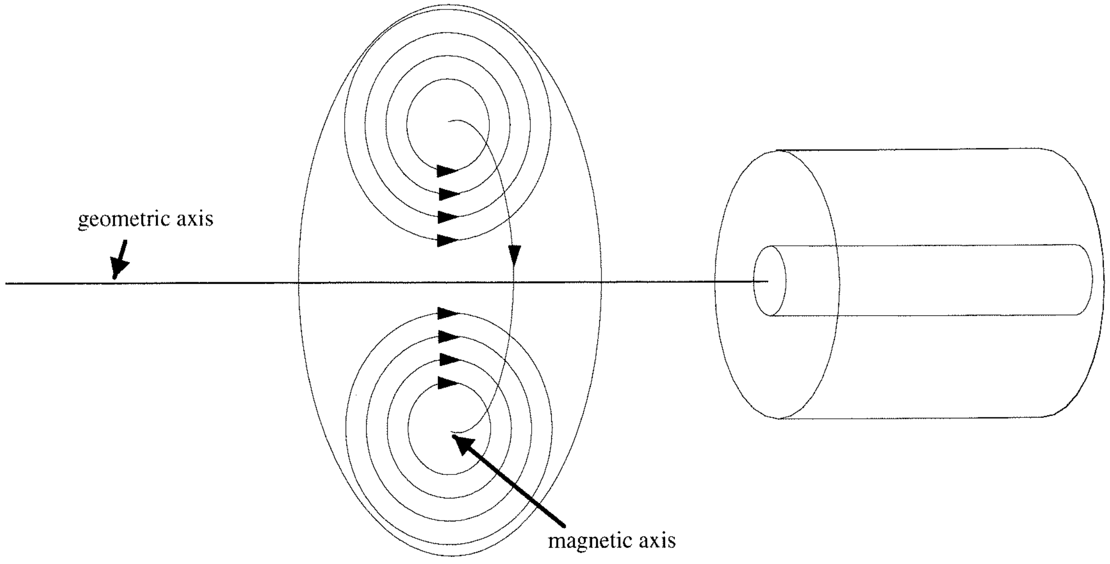

Figure 8.1: Representative sketch of typical spheromak topology: nested toroidal surfaces. The magnetic axis is defined as the point at which the poloidal field vanishes. The geometric axis is the axis of symmetry for the gun.

8.2 Experimental data

8.2.1 Current and voltage characteristics

The current and voltage waveforms with the gun operated with nominal settings in Regime II (I_{gun} = 130 kA, Φ_{stuff} = 2 mWb) are displayed in Figure 8.2. The gun bank ignitron switch breaks down and enters conduction mode at $t = 1$ μsec, followed by plasma breakdown approximately 0.3 μsec afterwards. The plasma gun behaves as a primarily reactive load so that the circuit exhibits typical underdamped oscillations. The current rises to its peak value of 130 kA at 6.5 μsec and reverses polarity at 14.5 μsec. Because the helicity injection rate is proportional to the voltage across the electrodes (c.f. Chapter 2), the process of helicity injection terminates when the voltage reverses polarity at 9.5 μsec. After this point, helicity is extracted from the plasma volume. Thus, for optimized spheromak formation with maximal injected helicity, the spheromak should be detached at approximately this point in time.

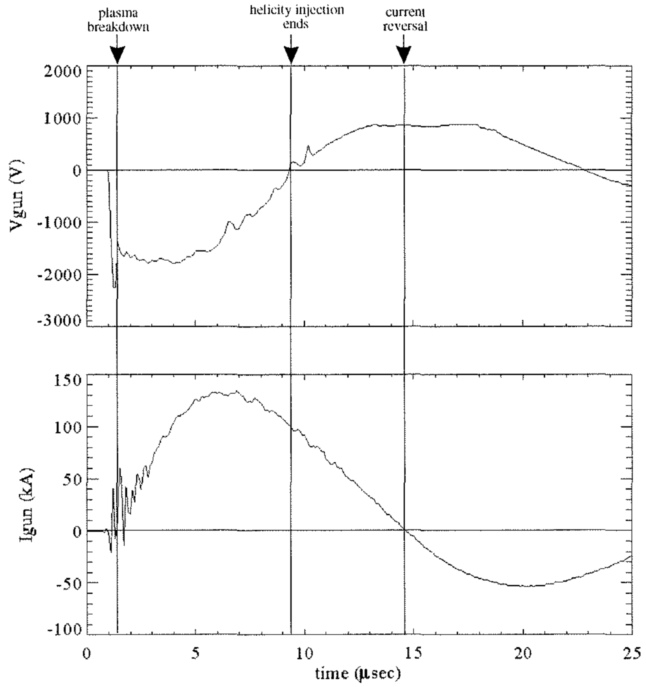

Figure 8.2: Sample gun current and voltage traces for gun operation at the nominal settings in Regime II.

8.2.2 Camera images

Figure 8.3 reviews camera data presented in Chapter 7. The figure shows an image sequence of the plasma discharge at nominal settings in Regime II taken from the Side View. The coaxial gun is located at the right edge of the field of view and fires plasma toward the left. Towards the latter stages of the discharge, the L-shaped magnetic probe is visible in silhouette in the foreground.

As mentioned in Chapter 7, plasmas obtained at these settings were classified in Regime II, and exhibit behavior qualitatively distinct from the other Regimes. Beginning at 9 μsec, the plasma emerges from the gun and expands in a relatively homogeneously luminous spherical shape. The roughly spherical expansion contin-

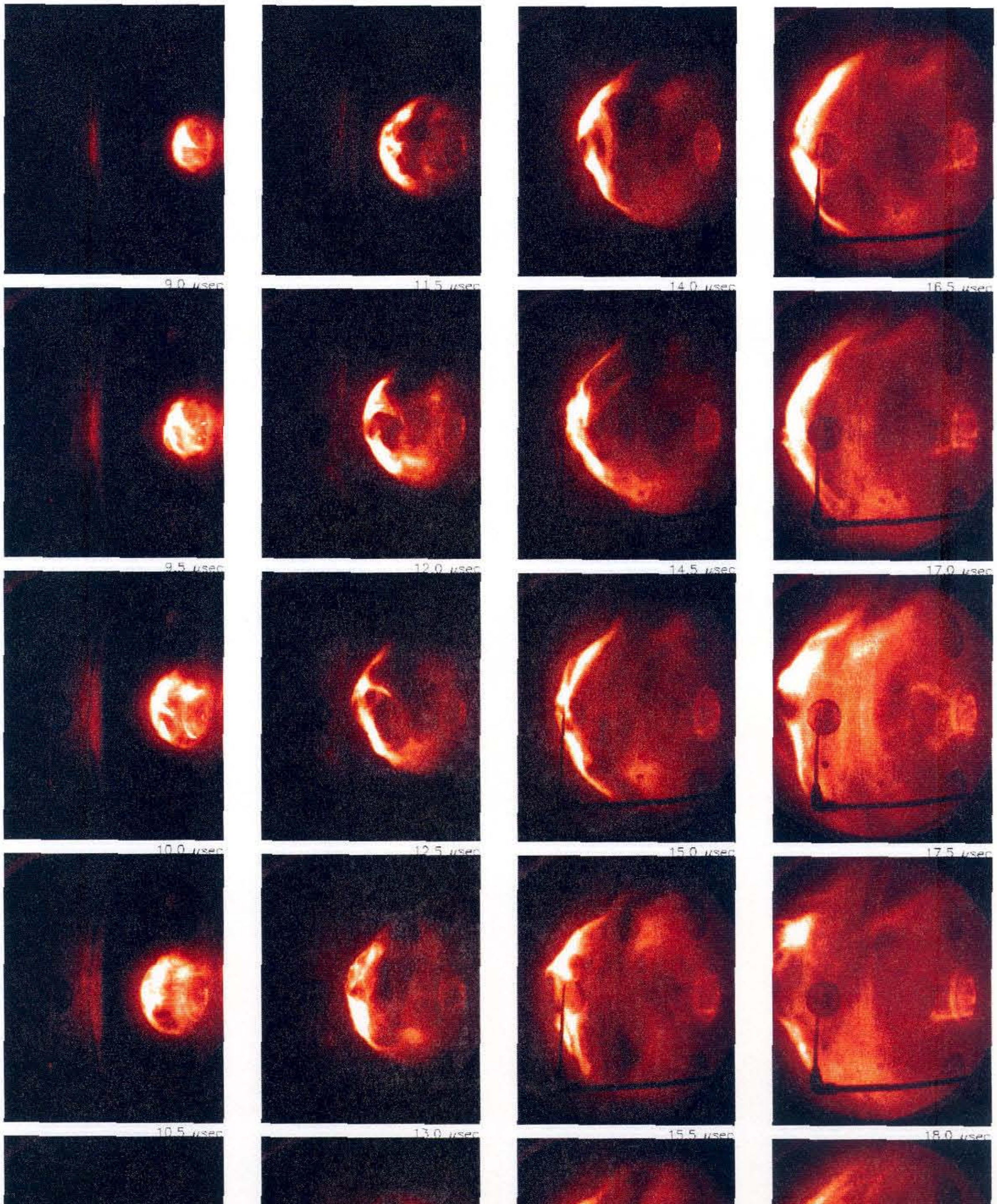

Figure 8.3: Image sequence with gun operated at nominal settings in Regime II.

ues throughout the shot. However, beginning at 11 μsec, the front (leftmost) edge becomes distinctly brighter in comparison with the remainder of the plasma. This brighter region continues to expand and propagates away to the left.

Additional information can be extracted from images of the discharge taken from the End-On View, shown in Figure 8.4. From this vantagepoint, it becomes apparent that a bright ring encircles the geometric axis of the gun. The ring first appears at 11 μsec and gradually expands in diameter.

Note that a significant amount of irreproducibility is exhibited in these pictures. In the End On Views, some images show filaments of material emerging from the central electrode and twisting counter-clockwise around the geometric axis. Some images seem to show multiple strands of material encircling the axis. In some images, the ring of material is not well centered on the axis. Nevertheless, in all these pictures a clear ring-shaped structure is visible emerging from the gun.

Correlation of the Side View and End-On View images provide evidence of material encircling the geometric axis of the gun in a roughly axisymmetric manner. However, it is not clear from these images whether a distinct spheromak possessing the characteristic nested toroidal flux surface magnetic topology is in fact ejected. In order to obtain direct and concrete information about the magnetic structure of the plasma, the magnetic probe array was used.

8.2.3 Magnetic traces

A sample of data obtained using the probe array is shown in Figures 8.5 and 8.6, for a shot taken with nominal gun parameters. For this data, the probe was positioned at $z = 30$ cm and rotated so that it lay in a gun poloidal plane ($\phi = \phi^1 = 0$). For each magnetic field direction, the time dependence of the field is shown at the 12 radial arm locations, with $r^1 = 45.7$ cm corresponding to the geometric axis ($r = 0$) and $r^1 = 17.8$ cm corresponding to $r = 27.9$ cm.

Most of the magnetic activity takes place between $t = 12$ μsec and $t = 20$ μsec. During this time period, B_ϕ is typically unipolar and positive, while B_z is negative

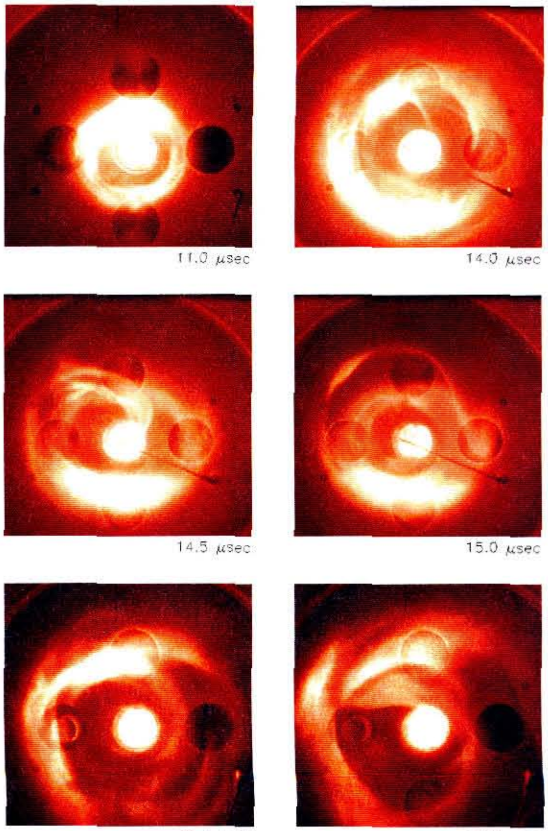

11.0 μsec

14.0 μsec

14.5 μsec

15.0 μsec

15.5 μsec

16.0 μsec

Figure 8.4: Selected End-On views with gun operated at nominal settings in Regime II.

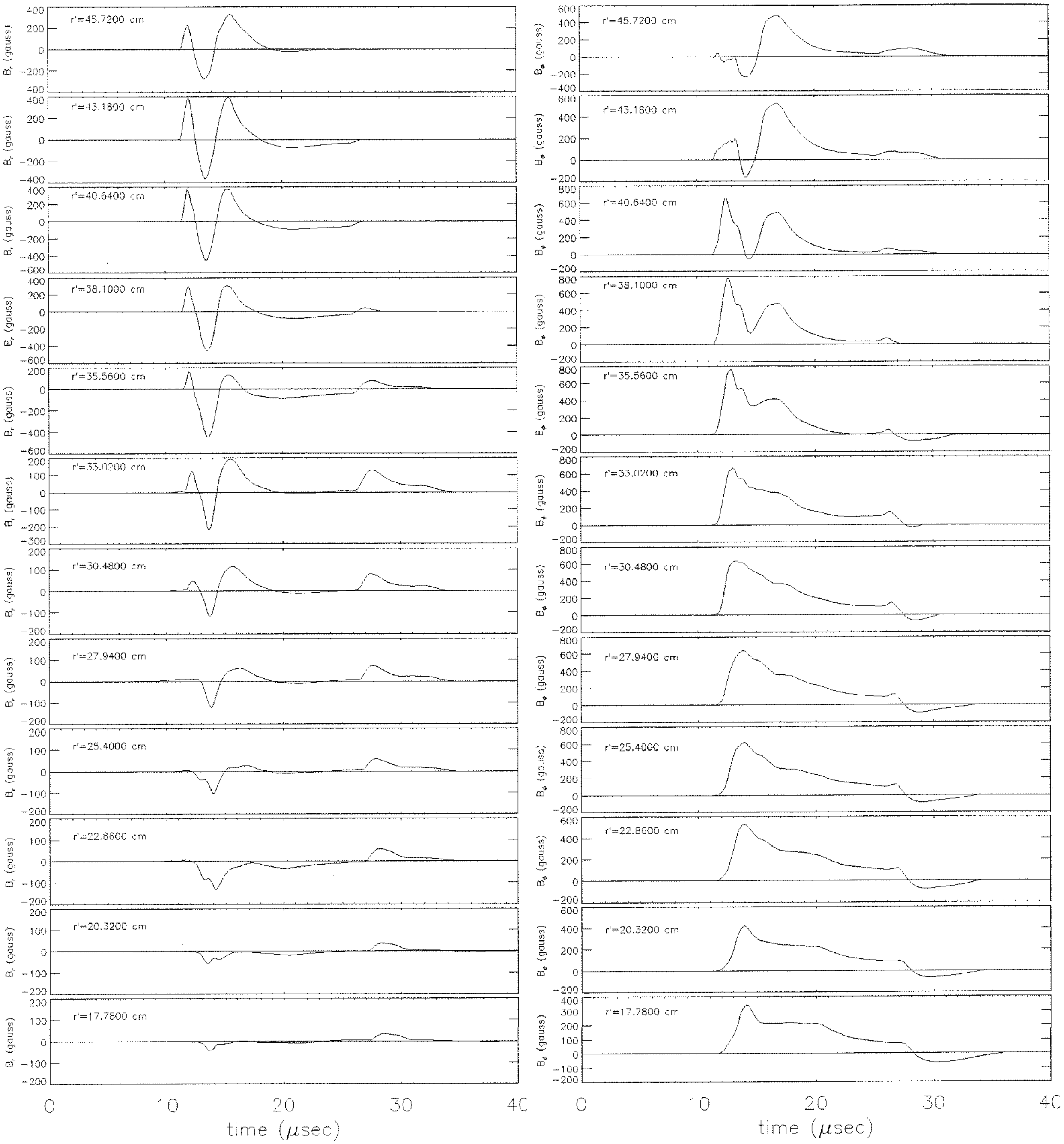

Figure 8.5: Sample magnetic probe data with gun operated at nominal settings in Regime II. Magnetic probe is positioned at z=30 cm, ϕ=0.

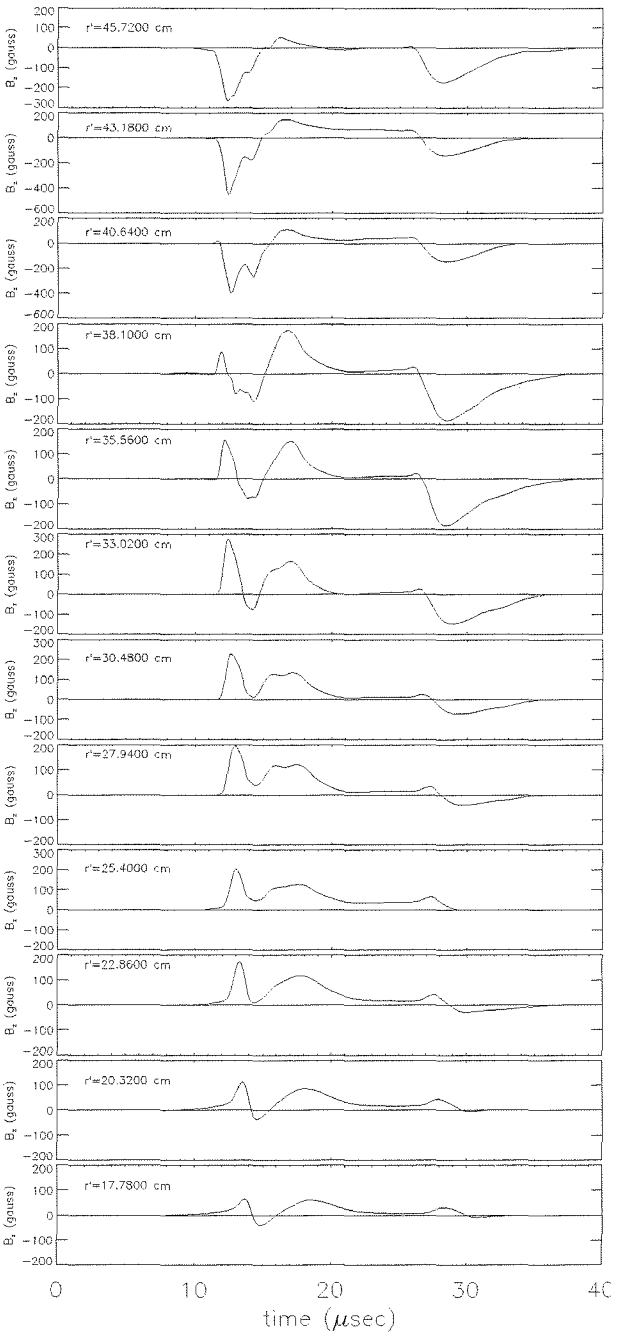

Figure 8.6: Sample magnetic probe data with gun operated at nominal settings in Regime II. Magnetic probe is positioned at z=30 cm, ϕ=0.

near the axis and positive further away from the axis. B_r oscillates through 1.5-2 cycles. This behavior will be shown below to be consistent with a spheromak magnetic signature.

It is interesting to note also that a secondary event occurs at $t = 28-35$ μsec, and is likely associated with an additional plasma ejection event produced by the negative gun current peak at approximately $t = 20.5$ μsec (see Figure 8.2). We will, however, restrict the present discussion to the primary event at $t = 12 - 20$ μsec.

Magnetic probe data was obtained at a variety of axial and azimuthal positions. However, compiling all of this data from multiple shots in order to arrive at a complete picture of magnetic configuration proved unfeasible due to shot-to-shot irreproducibility. Although shots with identical gun parameters generated similar magnetic waveforms in a qualitative sense, characteristics such as magnitudes and time offsets were often inconsistent. In order to overcome this problem, a technique based on propagation was developed to aid in data analysis. This technique is described in the next section.

8.3 Propagation inference technique

8.3.1 Propagation rate

The propagation rate of the expanding front of the ejected plasma is calculated in Figure 8.7. As the axial position of the magnetic probe is varied (with azimuthal position fixed at $\phi = 0$), the time at which magnetic field is first detected changes. In this plot, this time is determined from the instant at which the ϕ component of the field at radial position $r = 7.6$ cm exceeds an arbitrary threshold value of 100 Gauss, and is represented by an asterisk. (The arbitrary level was chosen to be significantly above the noise level, but well below the peak values of up to 1500 Gauss.) A linear regression of these data points produces a slope of 8.6 cm/μsec and fits the data remarkably well.

A second possible method of calculating the propagation rate is based on the first

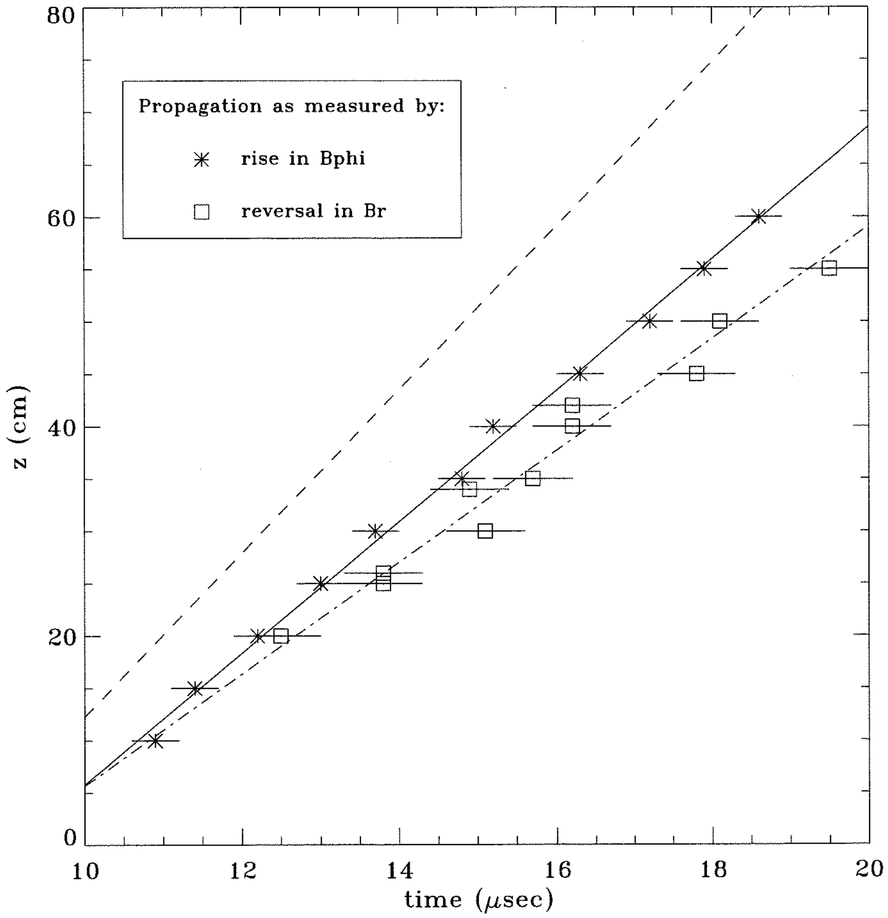

Figure 8.7: Position of the expanding plasma front versus time. Data points correspond to magnetic data (see text). Dashed line shows the optical propagation speed from Chapter 6.

positive to negative transition in B_r (c.f. Figure 8.5). As will be seen below, this reversal point can be associated with the magnetic axis of the spheromak. On the plot, the times at which the B_r probe measurement at $r = 7.6$ cm reverse sign are denoted by squares. A linear regression fit to these points yields a slope of 8 cm/μsec, but fits the data less well than the previous calculation. For reference, the camera-based propagation rate found in Chapter 7 is represented by a dashed line in the plot.

8.3.2 Propagation inferred data

In the following, we will make use of the conjecture that the magnetic field structure remains fixed in the plasma and is merely convected along at the propagation rate in the $\hat{\mathbf{z}}$ direction. This property suggests itself from the qualitative consistency of magnetic waveforms at varying axial probe positions. Taking advantage of this conjecture provides a powerful means of examining the magnetic configuration of the plasma using only one discharge. The z-dependence of the field may then be entirely inferred from the time dependence of the waveforms.

The conjecture may be applied to magnetic data as follows. The magnetic field measured by the probe at position z_{probe} is $\mathbf{B}(r, z_{probe}, t)$. If convection at a speed v_{prop} is assumed, then the field at an arbitrary point is

$$\mathbf{B}(r, z, t) = \mathbf{B}\left(r, z_{probe}, t - (z - z_{probe})/v_{prop}\right)$$

and can be directly obtained from the field measured at the probe.

The use of the Single Shot Propagation Inference (SSPI) method is schematically represented in Figure 8.8. The donut-shaped spheromak travels from right to left through the stationary magnetic probe array. The signal detected by a B_r probe at one probe position (which is aligned with the magnetic axis of the spheromak) is shown versus time. It is also evident from this plot that the positive to negative transition of B_r is associated with the passage of the magnetic axis, as mentioned in Section 8.3.1.

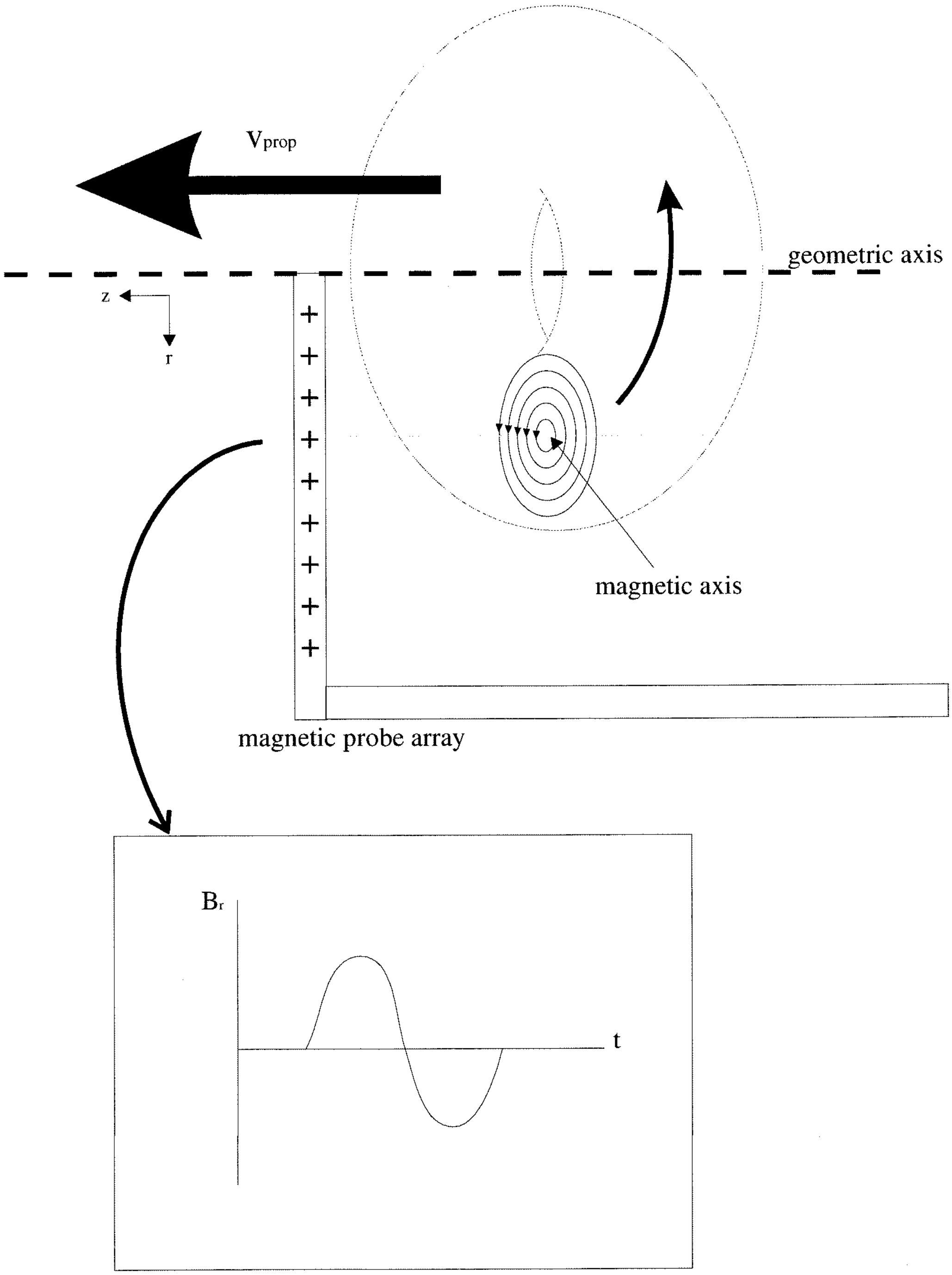

Figure 8.8: Sketch of the Single Shot Propagation Inference (SSPI) method.

Figure 8.9 shows a magnetic field plot constructed based on the above technique, to analyze the magnetic data presented earlier in Figure 8.5 (with the probe positioned at $z = 30\,\mathrm{cm}$ and $\phi = 0$). In this gun coordinate poloidal slice, the poloidal field vectors are shown in the bottom plot and the toroidal field appears as a contour plot above it. The coaxial gun electrode system is shown schematically, with the vertical (but not the horizontal) dimension to scale. The actual position of the probe is indicated by an arrow on the horizontal axis. It is important to note that the magnetic field has been measured only at this point in space. Data to the left (increasing z) of this location correspond to data taken at earlier times in the discharge (relative to $t = 12$ μsec) and data to the right correspond to data taken at later times. Thus, the data is exact at the probe location and may be expected to increasingly become an approximation away from this location. (A propagation rate of 8 cm/μsec was used in this calculation.)

Using this SSPI technique, the spheromak configuration becomes immediately obvious. The vortex-like swirl pattern in the poloidal direction combined with the peak (of negative polarity) in the toroidal field are clearly consistent with the idealized picture of the spheromak magnetic topology (c.f. cylindrical and spherical spheromaks of Chapter 2). Within the context of this propagation viewpoint, there is a close connection between the positive to negative transition in B_r and the location of the magnetic axis. Trailing behind the spheromak, an X-point is also clearly visible, indicating that the reconnection region arrives at $z = 30$ cm approximately 1.5 μsec later.

8.3.3 Consistency check

The validity of this propagation inference technique may be critically tested by comparing the fields inferred from several different shots fired with the probe located at substantially different axial positions. This self-consistency check is shown in Figures 8.10 and 8.11 for two different points in time. Ideally, the inferred field structure would be identical regardless of probe location. Instead, the plots are qualitatively

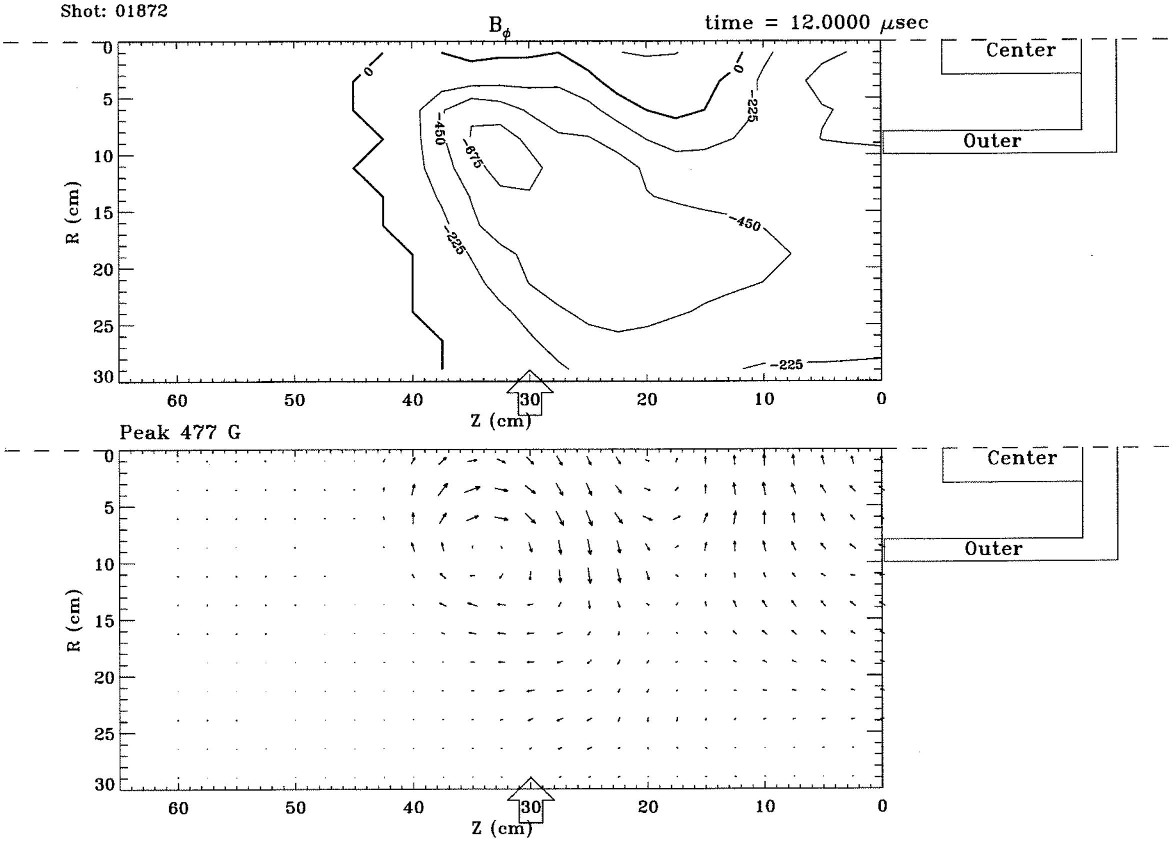

Figure 8.9: Single Shot Propagation Inferred (SSPI) magnetic data. Top plot is contour plot of B_ϕ. Bottom plot is a vector field plot of B_r, B_z. Maximum vector length corresponds to the peak value (477 Gauss). The arrow on the horizontal axis (30 cm) indicates the actual position of the magnetic probe.

similar, but exhibit a few distinguishing characteristics. At the earlier ($t = 12$ μsec) time, the vortex pattern detected at $z = 10$ cm seems to be less well-formed and smaller than that detected at $z = 40$ cm. This behavior is consistent with expansion and possible relaxation of the spheromak. The X-point reconnection region also seems to disappear for $z > 20$ cm, indicating that this region does not propagate beyond this point. Also evident from the two figures is a gradual reduction in the peak field magnitude at increasing distances from the gun. With these caveats then, it is clear that this technique provides an accurate picture of field structure. This test also supports the calculated value for the propagation rate (8 cm/μsec).

8.3.4 Reproducibility

It is interesting to examine the manifestations of shot irreproducibility within the context of the propagation inferred viewpoint. In Figure 8.12, several different shots are shown using the same gun parameters and probe position. Comparing the various vector field plots, it is apparent that the magnetic fields are qualitatively similar, with each exhibiting a clear spheromak poloidal vortex pattern. However, the field magnitude, uniformity, radial position, and axial position (the latter corresponding to a time offset) vary from shot to shot. Of these characteristics, the peak field magnitude and radial position are the most consistent, varying by 5-10% typically. The axial position exhibits an uncertainty of approximately 5 cm (or 0.6 μsec). Lastly, the uniformity of the field across the spheromak appears to vary significantly from shot to shot, particularly in the radial direction. The radial field is in some cases higher in amplitude at the leading or trailing edges of the spheromak, whereas in other cases it is more uniformly distributed across the spheromak. In the former cases, this may be an indication of incomplete relaxation.

Reproducibility is also a factor with regards to the reconnection region. Although the X-point is always visible with data taken at probe positions of $z_{probe} \leq 20$ cm, reconnection is intermittent at $z_{probe} = 30$ cm. For example, this variability is apparent in comparing the vector field plots in Figure 8.9 with the corresponding plot in

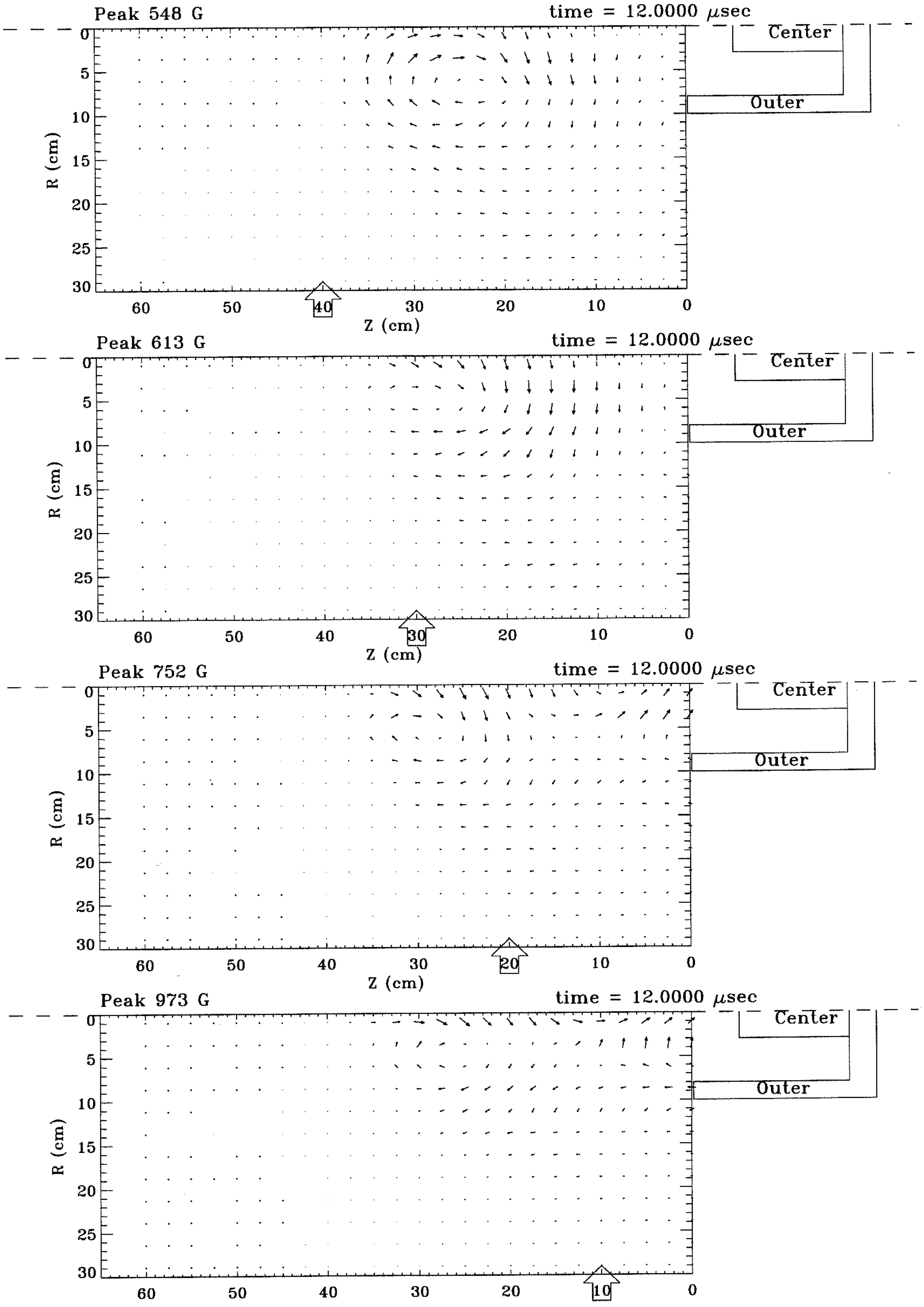

Figure 8.10: Consistency check. Several SSPI vector field plots generated from data taken at different magnetic probe locations. t=12 μsec

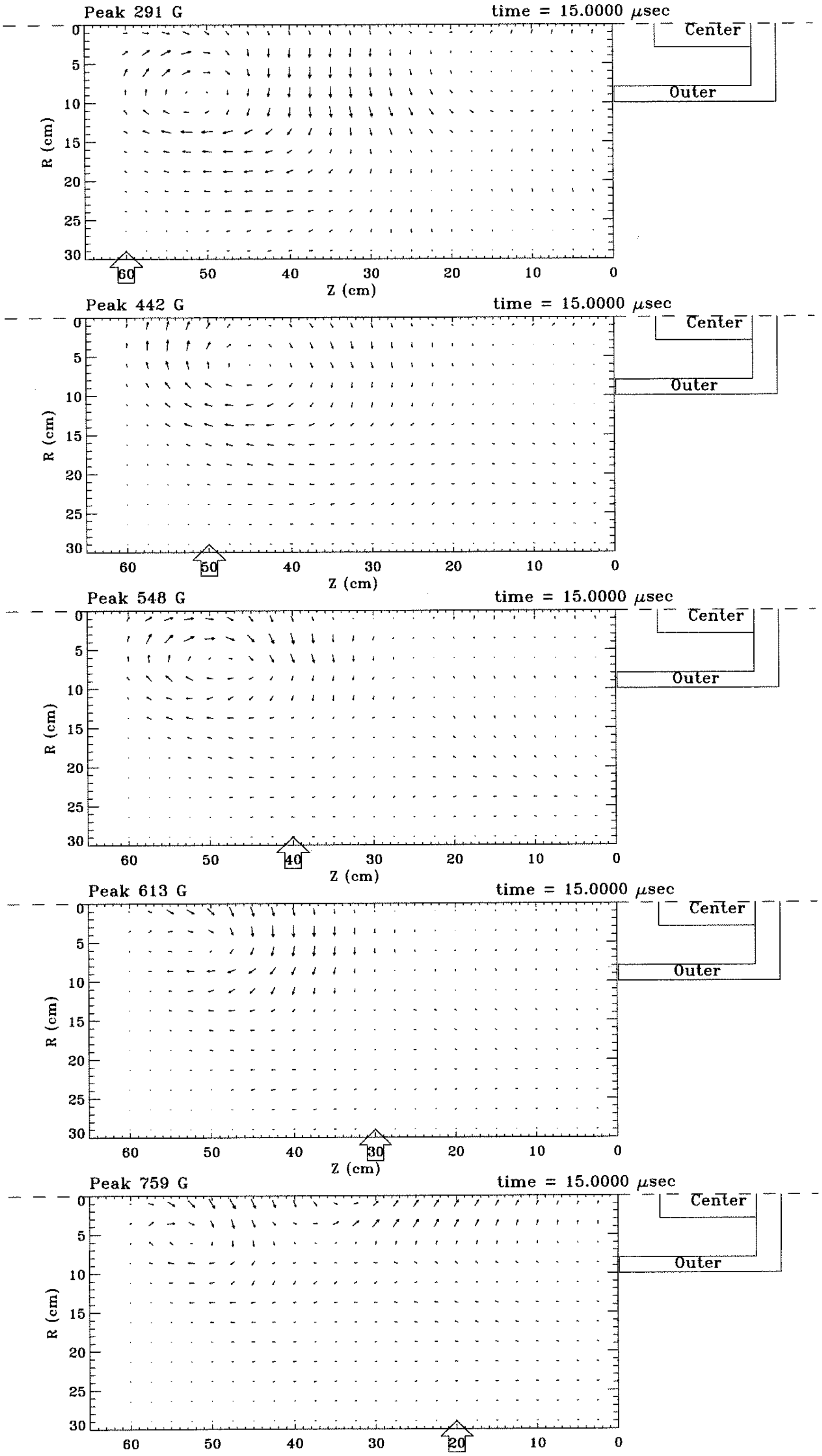

Figure 8.11: Consistency check. Several SSPI vector field plots generated from data taken at different magnetic probe locations. t=15 μsec

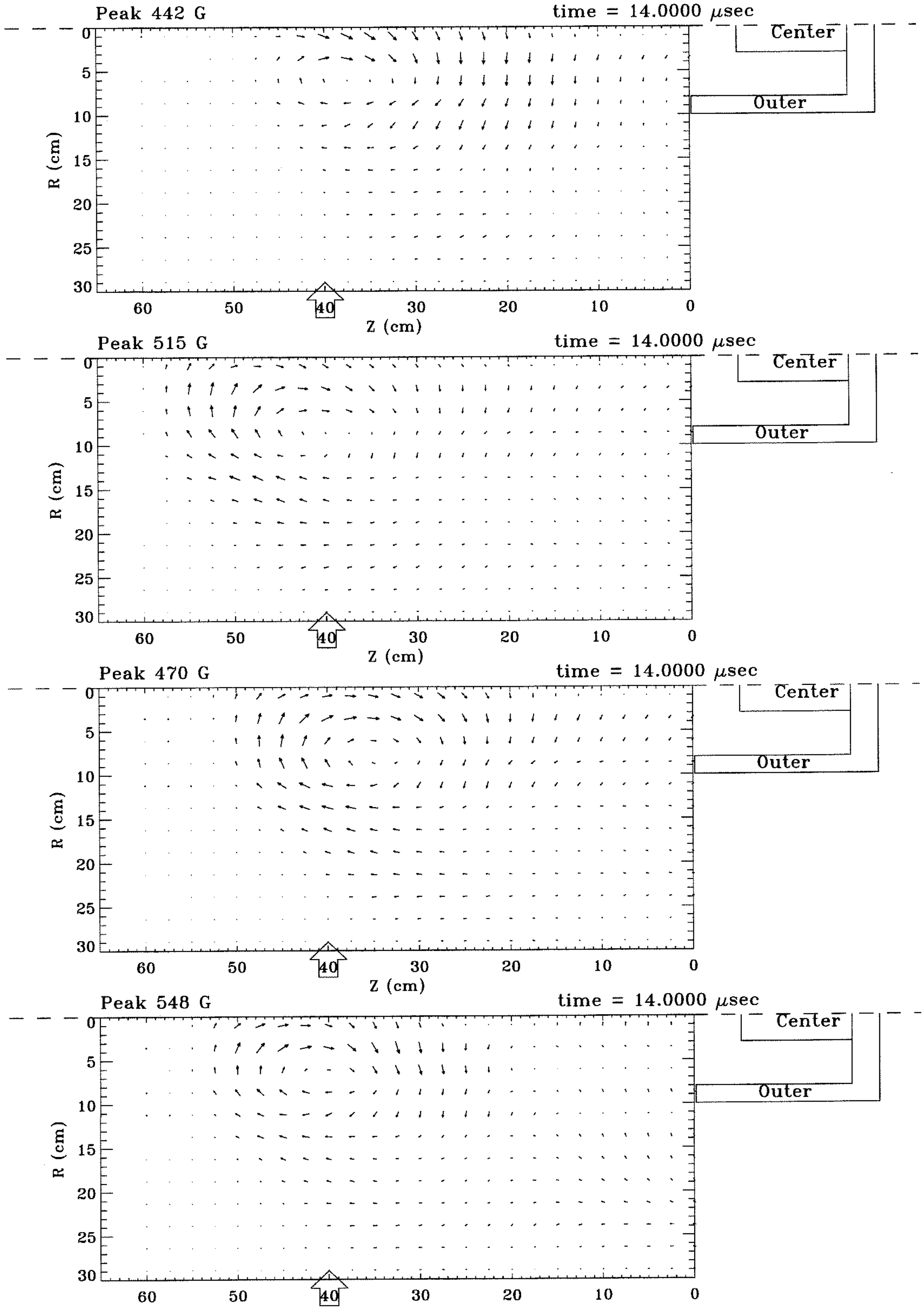

Figure 8.12: Reproducibility: Several SSPI vector field plots of plasma discharges with identical parameters.

Figure 8.11 (also at $z_{probe} = 30$ cm). The substantial irreproducibility observed in the details of reconnection is not surprising and is likely due to the complex nature of the tearing process. In the vector field poloidal plots, probe measurements at a position nearest to the gun ($z = 10$ cm) typically observe the first signs of reconnection at approximately 11 μsec. However, the initial reconnection point in fact likely occurs in the inaccessible entrance region ($0 < z < 10$ cm), which would correspond to an initial reconnection time of 10-11 μsec, based on the propagation argument. Spheromak detachment thus begins soon after the end of helicity injection at 9.5 μsec. Reconnection typically persists over a range of 10-25 cm in the axial direction, corresponding to a time interval of approximately 1-3 μsec. In contrast, the region is generally more narrow in the radial direction, with a width of 2.5-5 cm. The rectangular nature of the reconnection region is suggestive of a reconnection current sheet (e.g., [39]).

8.4 Discussion

The plasma generated by the coaxial gun in this experiment may be expected to be inherently more complex than in other spheromak setups due to the lack of a confining flux-conserver which would serve to guide the Taylor relaxation process. Verification of Taylor states in these latter cases is typically obtained by measuring the magnetic field with a linear probe in the device midplane and assuming axisymmetry [34][40]. In the present device, a midplane does not exist. Furthermore, the plasma dynamics will generally involve both propagation and expansion, in addition to any relaxation dynamics. Thus, without a high degree of reproducibility, one might expect that a complex 2-D probe array would be required. The SSPI method described in this chapter avoids this problem.

The SSPI method relies on three properties of the plasma behavior. First, a uniform propagation speed is assumed in order to provide axial dependence of the magnetic field. Secondly, the plasma is taken to be nearly force-free, so that dramatic changes in field structure are not expected. Lastly, the general expansion of the plasma is taken to be a small effect for short time periods. By taking advantage of these properties, the SSPI provides a useful and powerful means of gaining information about the magnetic topology from a single discharge.

It should be noted that the SSPI method resembles a technique which has been used previously in measuring force-free magnetic fields of space plasmas. Burlaga [11] analyzed data from an earth orbiting spacecraft in order to characterize the field of magnetic clouds. In this case, the single 3-axis magnetic probe is located on the spacecraft, which is effectively stationary as the magnetic cloud propagates through it. Burlaga was able to successfully fit the data to a simple Lundquist [45] Taylor state model (constant λ and axially independent). The key difference in this experiment is the availability of measurements at 12 positions transverse to the direction of motion of the plasma, allowing reconstruction of a plane of magnetic data rather than simply a single line.

To summarize, in this chapter data obtained with the gun operating in Regime II was presented which supports the hypothesis of Taylor relaxation into an axisymmetric spheromak state. Camera pictures from the Side View and End-On View generally depict ring-like structures which encircle the geometric axis being emitted from the gun.

Magnetic data, when interpreted using a plausible assumption of simple propagation away from the gun, shows a striking vortex-like magnetic pattern in vector field plots in a poloidal plane. This suggests that the plasma possesses the closed flux surface topology characteristic of standard models of axisymmetric spheromaks. Rough quantitative information about the extent and duration of the reconnection process is also obtainable from the magnetics.

In light of the results from the magnetic data, it is interesting at this point to attempt to directly identify in close-up camera images the structures which correspond to the spheromak. This can be achieved by acquiring both camera and magnetic data simultaneously. The results are shown in Figure 8.13. In this figure, the picture is scaled so that the horizontal axis is roughly aligned with the magnetic vector and contour plots; i.e., the locations of the mouth of the gun and the locations of the magnetic probe (the arrow on the horizontal axis) are each aligned. The image is

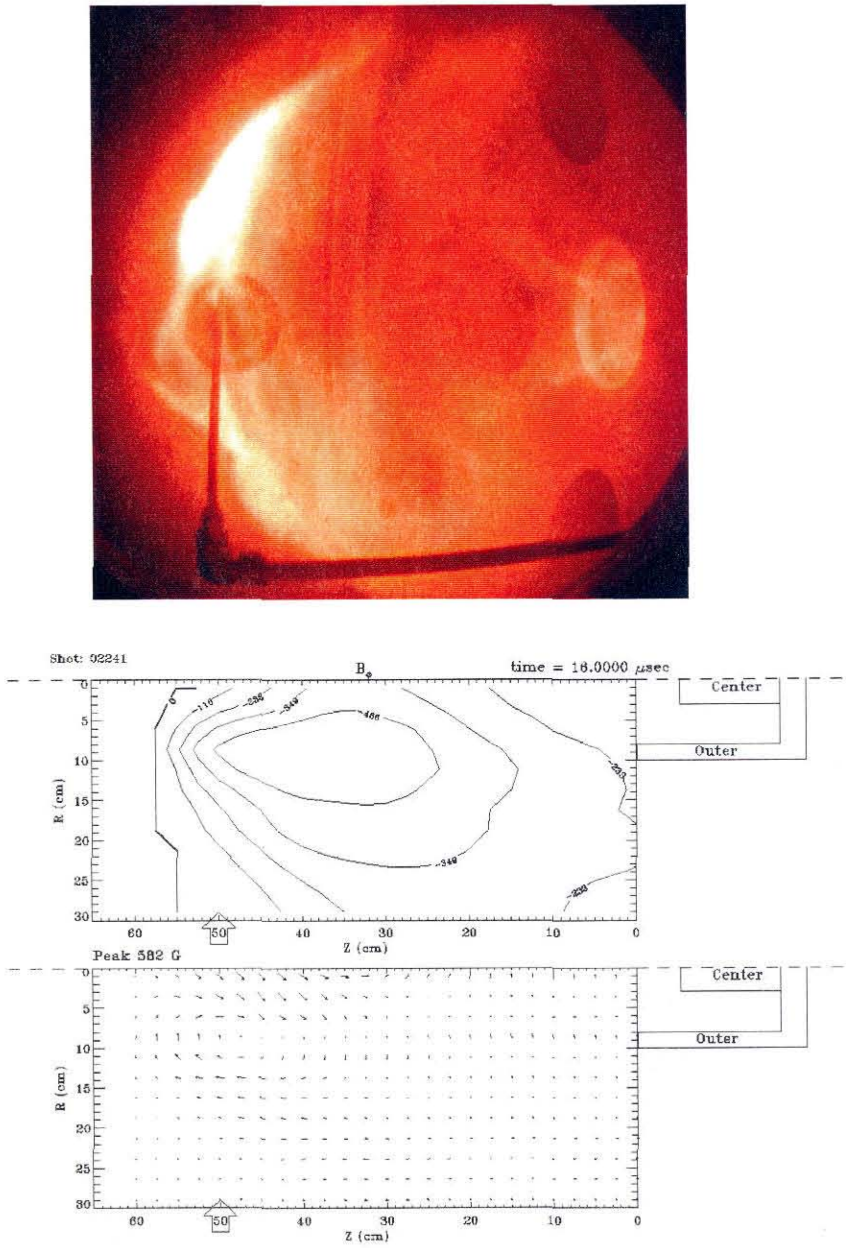

Figure 8.13: Simultaneous camera and magnetic probe data.

acquired at the same time (t=16 μsec) as the magnetic probe observes the passing of the magnetic axis.

From the figure, it is apparent that the leading (bright) edge of the plasma coincides with the leading edge of magnetic activity, both toroidal and poloidal. The magnetic vortex appears to be located within the bright region. Some filament structures are visible in the vicinity of the probe. However, no twist is observable.

In the next chapter, magnetic data analyzed using the SSPI method will be examined for further evidence of spheromak formation: poloidal flux amplification.

Chapter 9 Regime II: Taylor relaxation and poloidal flux amplification

9.1 Introduction

In the coaxial gun formation method, helicity injection is achieved by driving poloidal current through the plasma; alternatively, this process can be viewed as injection of toroidal flux to link the existing applied poloidal flux. This high helicity-content plasma should then relax into a Taylor equilibrium. An interesting fact, however, is that in practice the total injected toroidal flux is typically substantially greater than the poloidal flux [46], whereas spheromak states contain comparable toroidal and poloidal fluxes. Thus, Taylor relaxation entails some type of flux conversion; i.e., poloidal flux amplification, presumably accompanied by toroidal flux depletion. Indeed, this feature was first noted by Lindberg and Alfven [55] and provides evidence of the relaxation process occurring.

Flux amplification presents an apparent paradox in that two well known rules appear to be broken. Cowling's theorem [47] states that MHD does not allow for steady-state axisymmetric sustainment of toroidal current in a dissipative system. This would seem to preclude the generation of poloidal flux. Furthermore, MHD flux-conservation in this simple axisymmetric system would appear to require separate conservation of poloidal and toroidal fluxes, since no means of coupling the two is available. The resolution of these difficulties can be found by relaxing the axisymmetry constraint. In fact, the preceding arguments show that flux amplification must involve non-axisymmetric processes.

There is good experimental evidence that flux amplification involves mechanisms with mode structure higher than $m = 0$ (where m is the mode number). Knox [48], Janos [51], Nagata [52], and al-Karkhy [53] all observed non-axisymmetric fluctuations associated with the relaxation process in spheromak devices. These fluctuations appear to be the dynamo mechanism which drives and sustains the current involved in Taylor relaxation, and are a topic of current theoretical investigation (e.g., see Ref. [54] and [56]).

In Chapter 8, camera and magnetic data showed that the plasma in Regime II is qualitatively consistent with a spheromak configuration. In this chapter, evidence is presented demonstrating that poloidal flux amplification, and thus Taylor relaxation, is taking place. That flux amplification is expected to occur in the present experiment can be shown as follows. With the gun operated under nominal settings in Regime II, the net toroidal injected flux can be found by time integrating the gun voltage (c.f. Figure 8.2) $\Phi_{tor} = \int_0^t V_{gun} \cdot dt$. This calculation produces a net injected toroidal flux of 11 mWb at the end of helicity injection (9.5 μsec), in comparison to the applied poloidal stuffing flux of 2 mWb.

This chapter is organized as follows. Section 9.2 describes the details involved in calculating the poloidal flux. In Section 9.3, the time dependence of the toroidal flux is determined. Finally, in Section 9.4, these results are discussed.

9.2 Poloidal flux calculation

For an axisymmetric system, the poloidal flux function Ψ is commonly defined as the net amount of flux which penetrates a circle of radius r, centered on the geometric axis, at axial position z.

$$\Psi(r,z) = \int_0^r 2\pi r' \cdot B_z(r',z)dr' \tag{9.1}$$

Note that this definition implies that the two conditions

$$\begin{aligned} \Psi(r &= 0,z) = 0 \text{ and} && (9.2) \\ \Psi(r &\rightarrow \infty,z) = 0 && (9.3) \end{aligned}$$

must be satisfied due to the divergence-free nature of the magnetic field.

The integration given in Eq. 9.1 can straightforwardly be applied to the magnetic data if the Single Shot Propagation Inference (SSPI) technique detailed in the previous chapter is used to convert the time coordinate into z dependence. A sample calculation of the estimated poloidal flux function is presented in Figure 9.1, corresponding to the magnetic data from the plasma discharge shown earlier in Figure 8.5. In this calculation, it was found that the two conditions 9.2 were *not* met, likely due to imprecise knowledge of the location of the axis of symmetry. The second condition is deemed more robust in this regard; thus, a constant is added to the integral in order to ensure that $\Psi(r = r_{\text{max}}, z) = 0$. From the plot, it can be seen that $\Psi(r, z)$ does not vanish at the geometric axis $(r = 0)$ as would be expected. This departure from theory is likely due to an offset in the actual symmetry axis relative to the geometric axis, or it may be that the configuration is simply not truly axisymmetric. Nevertheless, this calculation should give at least a rough estimate for the poloidal flux.

The maximum poloidal flux should be found at the magnetic axis of the spheromak. In this example, the peak value is approximately 4 mWb, or about 2 times the applied stuffing flux poloidal flux of 2 mWb. This degree of flux amplification is beyond what can be accounted for by uncertainties in the measurements or flux calculations, and constitutes strong evidence for Taylor relaxation in the form of reconnection. At axial locations 10-20 cm in front of or behind the magnetic axis (or equivalently, the peak of the poloidal flux), it can be seen that the flux function drops off dramatically. This is an indication of magnetic detachment from the gun.

It is also interesting to consider the poloidal flux time dependence. By calculating the maximum poloidal flux at various probe positions, the time evolution of a spheromak's poloidal flux can be examined. The result of such an analysis is shown in Figure 9.2. Each point corresponds to 3-5 plasma shots taken with the magnetic probe located at a fixed axial position. The mean value of the maximum poloidal flux is shown, and the standard deviation of each calculation is indicated by the error bars. From this plot, it is evident that the poloidal flux rises from 2 mWb up to 4 mWb in the region $0 < z < 30$ cm, at which point it reaches a plateau. This region

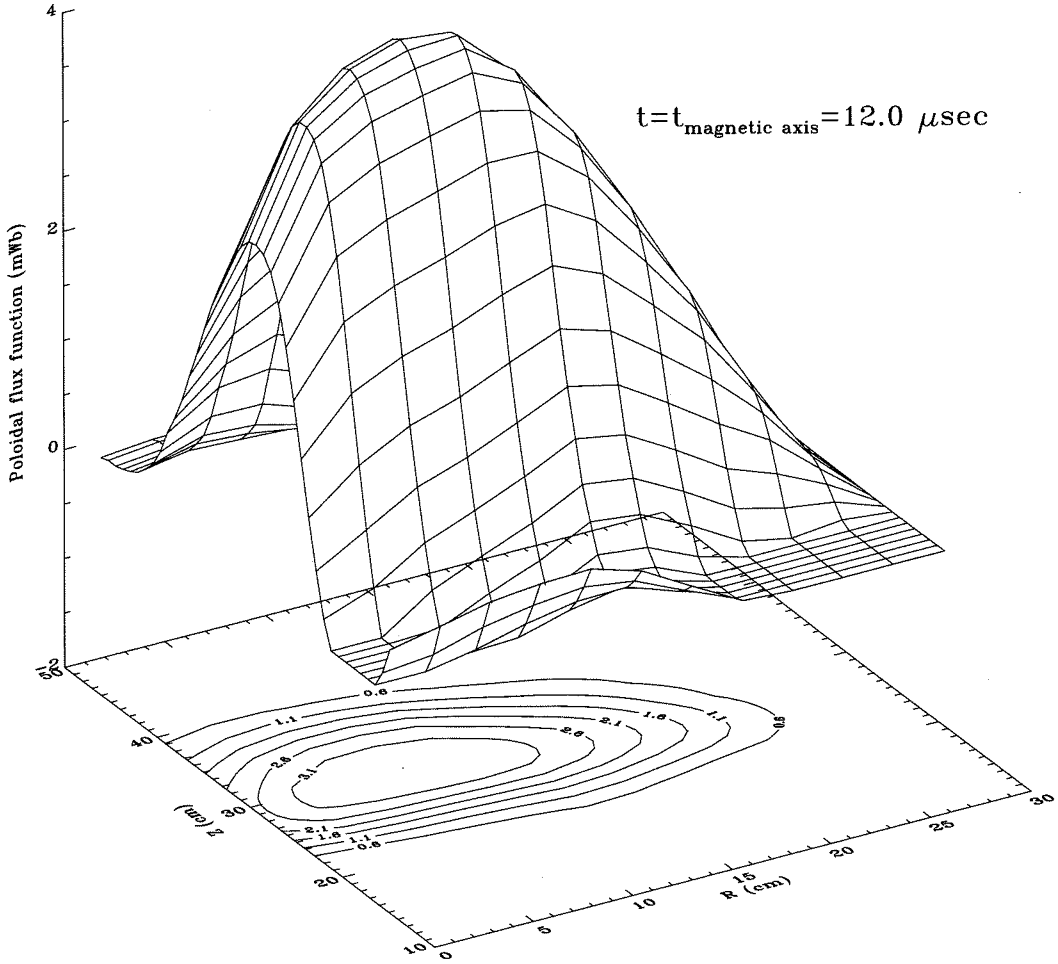

Figure 9.1: Calculated poloidal flux surface.

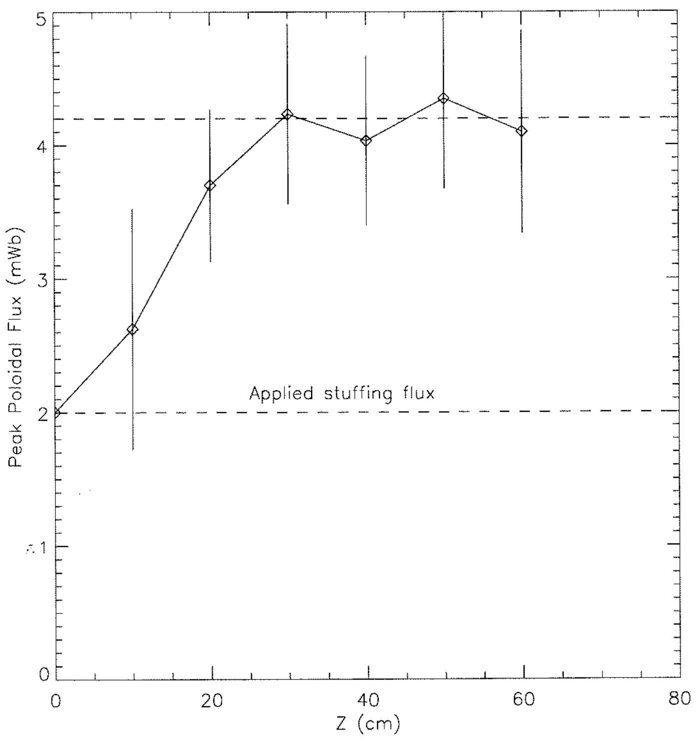

Figure 9.2: Maximum poloidal flux measured at various probe positions.

also comprises the interval in which X-point reconnection is taking place. The obvious interpretation is that poloidal flux amplification continues to occur during the reconnection/detachment process and terminates when the detachment is completed. Poloidal flux then achieves an equilibrium value and is thereafter conserved.

9.3 Toroidal flux calculation

The net toroidal flux contained within the spheromak can be defined as

$$\Phi_{tor} = \int_0^{z_{\max}} dz \int_0^{r_{\max}} dr \cdot B_\phi .$$

Calculation of this quantity presents some difficulty in the present situation because the field is only accurately known over a limited axial range in the vicinity of the probe. It is therefore necessary to restrict the integration area to a region encompassing the

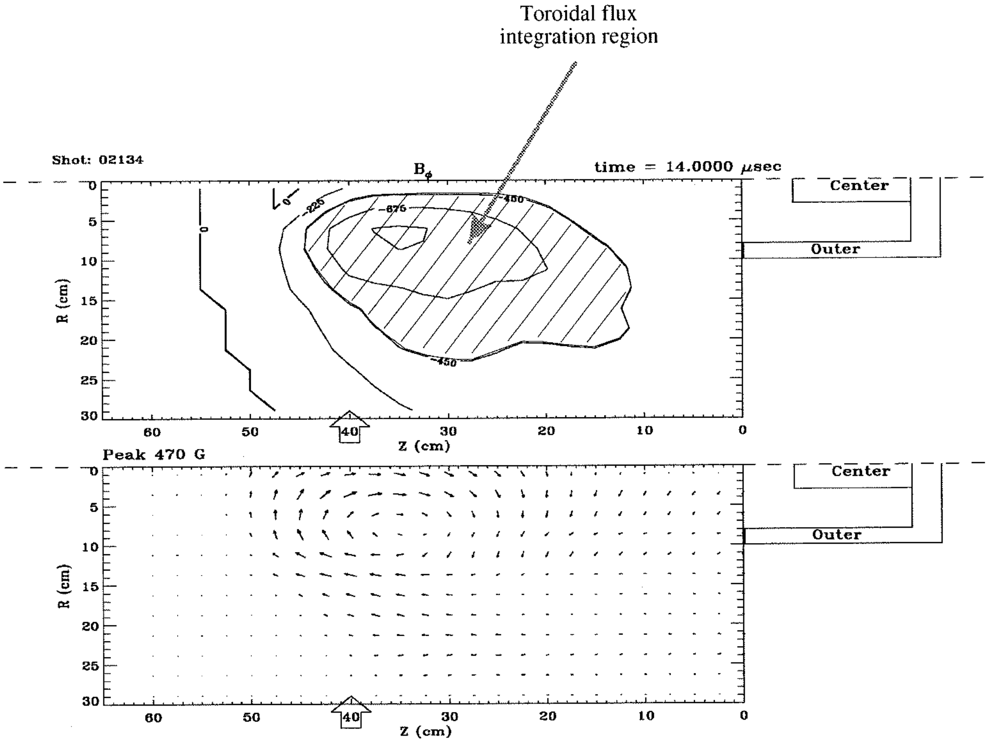

Figure 9.3: Full Width at Half Max (FWHM) poloidal area in which toroidal flux is integrated.

spheromak itself. For this reason, the integration area is defined as locations on the (r, z) plane at which the toroidal magnetic field is greater than one-half of its maximum value. This definition is essentially a Full Width at Half Max (FWHM) in two dimensions and, as an example, the resultant region is highlighted in Figure 9.3. From this plot, it is apparent that the area is roughly equivalent to the area qualitatively encompassed by the vortex structure in the poloidal directions. However, the FWHM area appears to lag somewhat behind the vortex.

The result of this calculation at various probe positions is presented in Figure 9.4. Again, each point corresponds to 3-5 plasma shots, and the error bars indicate the magnitude of their standard deviation. The toroidal flux decays from approximately 11 mWb down to 8 mWb at $z = 30$ cm, where it plateaus until a possible further dip

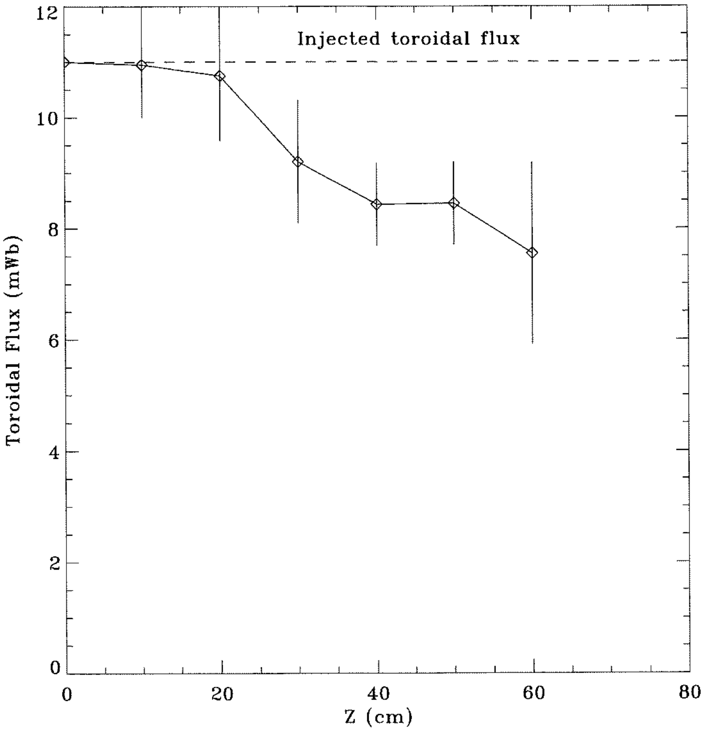

Figure 9.4: Calculated toroidal flux (integrated within FWHM area) at varying probe positions.

at $z = 60$ cm. Note that the reduction in toroidal flux occurs in the same interval over which the poloidal flux was observed to rise earlier. This behavior is consistent with the notion of flux conversion during the relaxation process.

In most spheromaks, the ratio of poloidal flux to toroidal flux is of order unity. This can be shown explicitly for analytically describable spheromaks such as the classical and cylindrical spheromak. In the present case, a ratio of 1:2 is observed in the plateau region: $30 < z < 60$ cm.

9.4 Discussion

In Chapter 7, it was shown from camera images that plasma discharges could be categorized into four classes based on gun parameters and differentiated by distinct plasma dynamics. The results from the present chapter, in conjunction with those from the previous chapter, provide compelling evidence that plasma in the class designated as Regime II is in a spheromak configuration quasiequilibrium.

Calculations of the poloidal and toroidal flux lend credence to the hypothesis of spheromak creation. A significant (2×) poloidal flux amplification effect has been observed, indicating that (i) Taylor relaxation is at work and (ii) closed flux surfaces have been produced. The poloidal flux amplification roughly coincides with a corresponding drop in toroidal flux, as would be expected from the flux conversion principle.

The magnitude of amplification is somewhat less than the roughly five-fold typically observed in earlier experiments; e.g., Ref [34]. However, the latter experiments involved flux-conserver boundaries, which may play a role in the process. Furthermore, as mentioned in Chapter 8, reconnection is observed at probe positions as far out as $z = 30$ cm, indicating that when the spheromak reaches this point, some closed field lines continue to be present. However, during this period the gun voltage is negative, and helicity may be robbed from the spheromak, thereby reducing the magnitude of the amplification. Also, gun parameters have not been optimized for flux amplification. Thus, higher flux amplification may be achievable through different settings.

The bulk of the amplification effect occurs within 3 gun radii (30 cm) from the mouth of the gun, corresponding to $3.5 - 4$ μsec of propagation time. An interesting point here is that a closed flux surface topology is observed through most of this propagation distance. This, coupled with the fact that the gun is no longer injecting helicity during this period, indicates that the flux amplification must be produced entirely by relaxation (and not, e.g., helicity injection). Thus, it is natural to associate this interval in time with the relaxation time, i.e., $\tau_{relax} \approx 3.5{-}4$ μsec. To the author's knowledge, this latter measurement constitutes the first observation of a relaxation time in an unbounded plasma.

As a final note, although non-axisymmetric relaxation mechanisms are generally necessary to drive the observed toroidal current (c.f. Section 9.1), these are not evident in camera or magnetic data, which remain essentially $m = 0$. In particular, neither plasma structures with higher modal components [48] nor relaxation oscillation activity [51][52] were observed. Instead, the relaxation process appears to be taking place on smaller spatial scales; this is suggestive of possible turbulent reconnection at work.

Chapter 10 Regime II: Measurement of Lambda

10.1 Introduction

As discussed in Chapter 2, Taylor's theory predicts that an isolated plasma with finite helicity contained within flux conserving walls will relax into a force free state $\nabla \times \mathbf{B} = \lambda \mathbf{B}$. This plasma configuration has the distinguishing characteristic that the eigenvalue λ is a spatial constant throughout the volume and is designated a Taylor state. When the equilibrium is attained, the plasma is in a true minimum energy state (given the helicity constraint).

The basic theory has been applied with considerable success in a wide variety of applications. However, it must be stressed that the idealized situation embodied in the Taylor solution assumes a fully relaxed plasma and an essentially static environment. In any practical system of interest, the plasma may be influenced by the boundary conditions, impurities can result in inhomogeneous helicity dissipation, and external voltage sources may produce helicity injection. Any of these factors would compete with the mechanisms of Taylor relaxation and tend to drive the plasma away from the minimum energy state.

In the previous two chapters, the plasma generated by the spheromak gun in this experiment was shown to be in a spheromak-like state. This chapter examines the extent to which the magnetic field structure departs from a true Taylor state, as evidenced by non-uniform λ distributions within. Section 10.2 describes previous experimental and theoretical results concerning λ. Section 10.3 details the process of computing the current density, which is required to determine λ. Section 10.4 presents various λ distribution measurement results. Section 10.5 discusses the significance of these results and proposes a self-similarity model. Section 10.6 examines the possible connection with magnetic clouds. A summary of this material is given in Section 10.7.

10.2 Gradients in λ and helicity flow

In analyzing magnetic configurations which differ from the minimum energy state, it is useful to consider the general class of plasmas which are force-free and thus in equilibrium, but are *not* Taylor states. Taking the divergence of the force free relation $\nabla\times\mathbf{B}=\lambda\mathbf{B}$ shows that all force-free plasmas must satisfy the condition $(\mathbf{B}\cdot\boldsymbol{\nabla})\,\lambda=0$; i.e., λ must remain constant within each magnetic flux surface. Thus, for the general force-free plasma, λ may be written as $\lambda=\lambda(\psi)$, where ψ is the poloidal flux function.

Information about the λ profile in a spheromak was first obtained in the CTX experiment by Knox et al. [48]. In that experiment, λ was approximated by a function with linear dependence on ψ,

$$\lambda(\psi)=\overline{\lambda}\left[1+\alpha\left(2\psi-1\right)\right],$$

where ψ is the normalized poloidal flux function. λ is then characterized by a mean value $\overline{\lambda}$, and a parameter α which determines whether the profile is centrally peaked or hollow. Since $\psi=1$ (for a normalized flux function) at the magnetic axis and $\psi=0$ at the outermost flux surfaces, positive α corresponds to a λ distribution with a central peak and negative α signifies a distribution with a central depression (i.e., hollow). Using a numerical solver for the pressure-free Grad-Shafranov equation, values of α were determined as a function of time, based upon measurements of surface currents on the flux-conserver.

During the course of the discharge, the spheromak gun progressed from a sustainment phase to a decay phase. In the sustainment phase, the gun is injecting helicity into the spheromak, and produces flux amplification in the manner described in Chapter 9. α was found to be negative in this case. In the decay phase, the gun is short-circuited, and the spheromak helicity and magnetic energy are expected to resistively decay. In this phase, λ became centrally peaked (i.e., positive α). This type of behavior has also been verified numerically by Kitson and Browning [49] and experimentally by Martin et al. [50] for the SPHEX device.

The results of Knox can be qualitatively summarized with the help of a simply stated principle: *helicity tends to flow from regions of high λ to regions of low λ* (i.e., downhill). The hollow profile in the sustainment phase is thus a result of helicity injection from the outermost flux surfaces (open field lines connected to the gun) toward the magnetic axis. Conversely, during the decay phase, helicity flows from the magnetic axis to replenish increased resistive loss at the plasma edge. This principle was first stated by Jarboe in reference to the Kinked Z-pinch experiment [58], but its theoretical justification is a subject of current research. For instance, dynamo models involving time-averaged fluctuations in the electric and magnetic fields hold promise in this regard [54]. Nevertheless, the rule has been empirically found to be valid and provides a powerful framework for understanding non-uniform λ situations.

In the Kinked Z-pinch experiment, the downhill λ principle was employed in the design of the apparatus. Spheromaks generated by the $m = 1$ mode gun needed to be guided into an axisymmetric flux-conserver. In order to ensure that this took place, the plasma proceeds along a series of increasingly large subvolumes. Since helicity flows to regions of lower λ, the plasma prefers to reside within the subvolume with the lowest characteristic eigenvalue λ_{geom}, corresponding to the largest such subvolume. In practice, the spheromak was in fact found to adhere to this principle [57].

Another application of the λ gradient is relevant to spheromak gun formation theory. In order for a spheromak to be formed, helicity must be transported from the gun into the region bounded by the flux-conserver. As the flux-conserver possesses a characteristic $\lambda = \lambda_{geom}$ determined by geometric considerations, the following requirement is established. The plasma at the mouth of the gun, which has $\lambda = \lambda_{gun}$, must be greater than λ_{geom} so that the correct direction of helicity flow takes place. Note, however, that this is simply a restatement of the stuffing threshold described in Chapter 7.

Finally, λ has one additional interpretation. By integrating the magnetic energy density over the volume V of an isolated spheromak $\frac{1}{2\mu_0}\int_V \mathbf{B}\cdot\boldsymbol{\nabla}\times\mathbf{A}\,d^3r$, it can be shown that $\lambda = 2\mu_0 W/K$ where W and K are the spheromak's net helicity and magnetic energy, respectively (e.g., see Bellan [59]).

From the preceding discussion it is clear that the plasma λ plays an important role in plasma dynamics. To summarize, the significance of λ is fourfold. First, the sign of its gradient is indicative of the direction of helicity flow. Secondly, plasma generally exhibits a preference for regions with lower characteristic λ_{geom}, corresponding to larger length scales. Third, the spheromak formation stuffing flux limit can be stated more simply as $\lambda_{gun} > \lambda_{geom}$, where λ_{geom} is the characteristic eigenvalue of the flux-conserver into which the spheromak is to be injected. Lastly, λ is proportional to the ratio between the magnetic energy and total helicity for an isolated spheromak.

10.3 Current density calculation

Several difficulties are encountered in attempting to numerically evaluate the curl $(\boldsymbol{\nabla}\times)$ operator on the acquired magnetic data. First, the operator is a form of spatial differentiation, and thus requires detailed knowledge of the spatial variation of $\mathbf{B}$. Differentiation, in particular, is notorious for being sensitive to the quality of the input data[60], so it is important from the present experiment's perspective to operate on data from a single plasma discharge due to reproducibility concerns. The three components of the curl operator in cylindrical coordinates are:

$$\begin{aligned}
(\nabla\times\mathbf{B})_r &= \frac{1}{r}\frac{\partial B_z}{\partial\phi} - \frac{\partial B_\phi}{\partial z} \\
(\nabla\times\mathbf{B})_\phi &= \frac{\partial B_r}{\partial z} - \frac{\partial B_z}{\partial r} \\
(\nabla\times\mathbf{B})_z &= \frac{1}{r}\left(\frac{\partial}{\partial r}(rB_\phi) - \frac{\partial B_r}{\partial\phi}\right).
\end{aligned}$$

Thus each vector component of the operator involves taking spatial derivatives in two directions. Taking advantage of the Single Shot Propagation Inference (SSPI) method described in Chapter 8, the variation of $\mathbf{B}$ in two directions (r and z) can be obtained in a poloidal plane, allowing the toroidal component of the current density to be calculated from a single plasma discharge. This will be the technique employed below to derive values for λ, and requires calculation of the axial derivative of B_r and the radial derivative of B_z.

A second concern which must be addressed involves the discrete nature of the grid of points in the poloidal plane. The grid spacing in the axial direction δz is computed by multiplying the digitization interval (0.1 μsec) by the propagation speed (8 cm/μsec) to arrive at a value of 0.8 cm. This spacing generally results in smooth variation in the value of the B_r, and can be differentiated straightforwardly. However, the grid spacing interval in the radial direction $\delta r = 2.5$ cm is considerably coarser and often leads to somewhat jagged B_z variation, making numerical differentiation problematic.

In order to facilitate calculation of the spatial derivative in the radial direction, the value of B_z is interpolated at several intermediate positions using a cubic spline algorithm. With the spline method, the function is approximated by a set of piecewise-continuous polynomials (in this case cubic), which have matched first derivatives at the data points. The important property of continuous differentiability is thus established. A sample calculation using spline interpolation is shown in Figure 10.1. Asterisks denote the locations of the actual measured values for B_z. Values are interpolated at three intermediate points (equally spaced) between each pair of adjacent data points, and is shown as X's.

10.4 Results

10.4.1 Spatial variation in λ

Figure 10.2a shows a contour plot of $J_\phi(= \frac{1}{\mu_0}\widehat{\phi} \cdot \nabla \times B)$ in a poloidal cross section, calculated as described in the previous section. For this shot, the gun was operated using the nominal Regime II parameters used in the previous two chapters. The magnetic probe lay in the natural poloidal plane ($\phi = 0$) and was positioned at axial

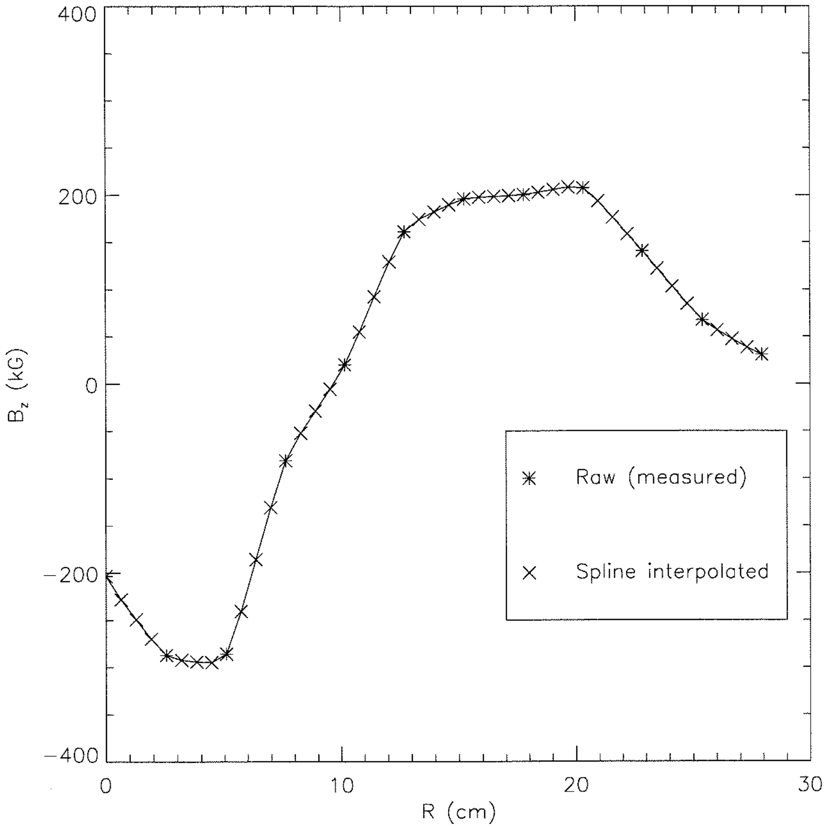

Figure 10.1: Sample calculation using cubic spline interpolation for B_z(r).

location $z = 40$ cm, as indicated by the arrow in the horizontal axis. For reference, Figure 10.3 displays the magnetic field corresponding to the same shot. Note that the contour plot of the toroidal magnetic field is roughly similar in appearance to the contour plot of the toroidal current density, as would be expected in a force-free configuration.

Based on the current density calculation, and assuming a near force-free state, λ can thus be quantitatively determined using the relation $\lambda = \mu_0 J_\phi / B_\phi$. (Note that using this relation to determine λ is similar in principle to calculations of λ which have been made from magnetograms of the solar surface [61].) The results of the computation are shown in the contour plot in Figure 10.2b. In this calculation, it is important to consider error uncertainties. In particular, as the value of B_ϕ approaches

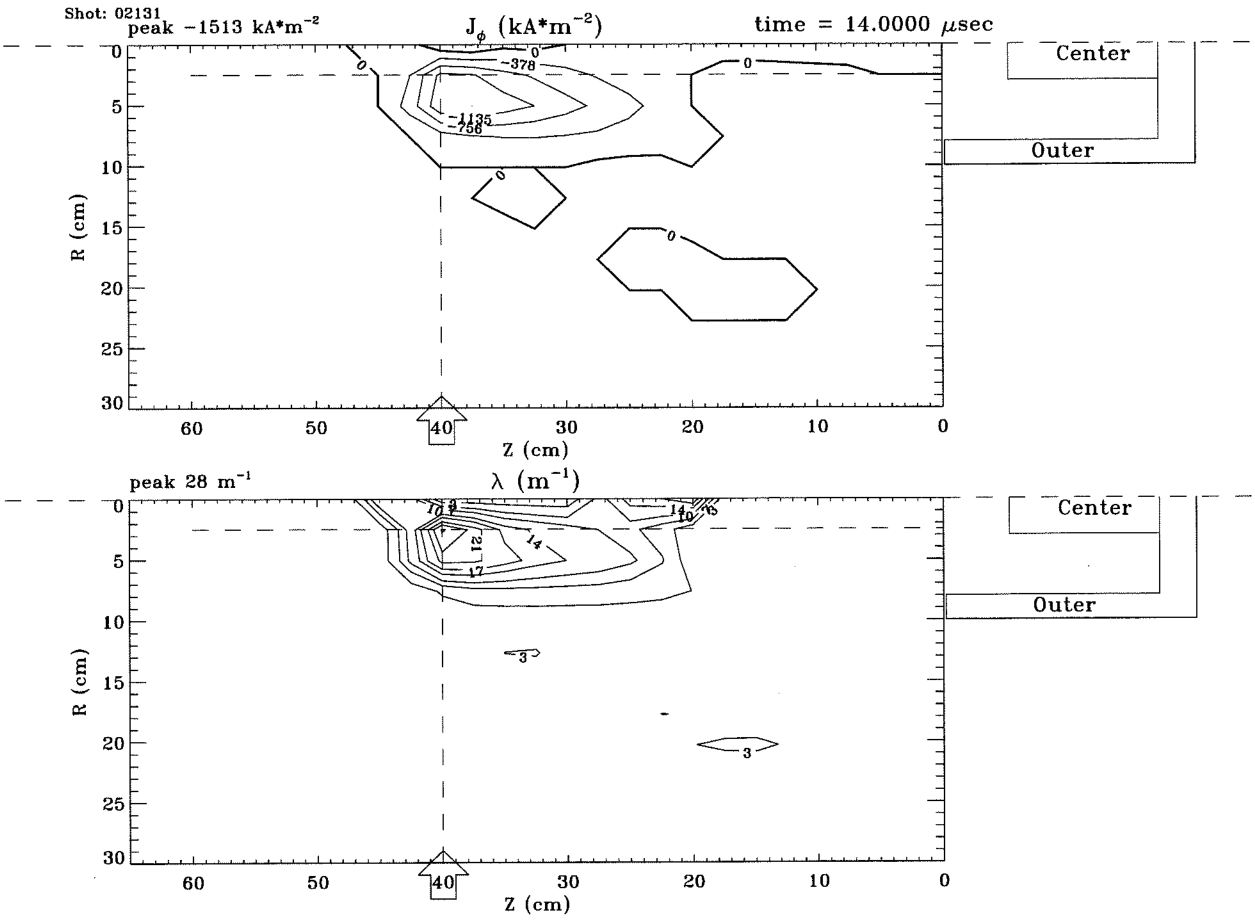

Figure 10.2: Contour plots of calculated (a) toroidal current density and (b) λ. In both computations, SSPI method is used with magnetic probe located at z=40 cm and t=14 μsec.

zero, uncertainties in λ grow without bound. It is for this reason λ is set to zero at points where B_ϕ is small (where small is defined as less than 3% of its maximum value). Typically, J_ϕ is also small in magnitude at these locations, so this caveat should not significantly affect the results.

The dashed lines (z = 40 cm, r = 2.5 cm) intersect at the peak value of λ of 28 m^{-1}. λ is concentrated near this peak location. Figure 10.4 shows an enlarged view near this region, as well as the linear dependence at z = 40 cm and r = 2.5 cm (along the dashed lines). From this data, it is apparent that λ assumes a centrally peaked distribution with FWHM of approximately 5 cm. This type of distribution is

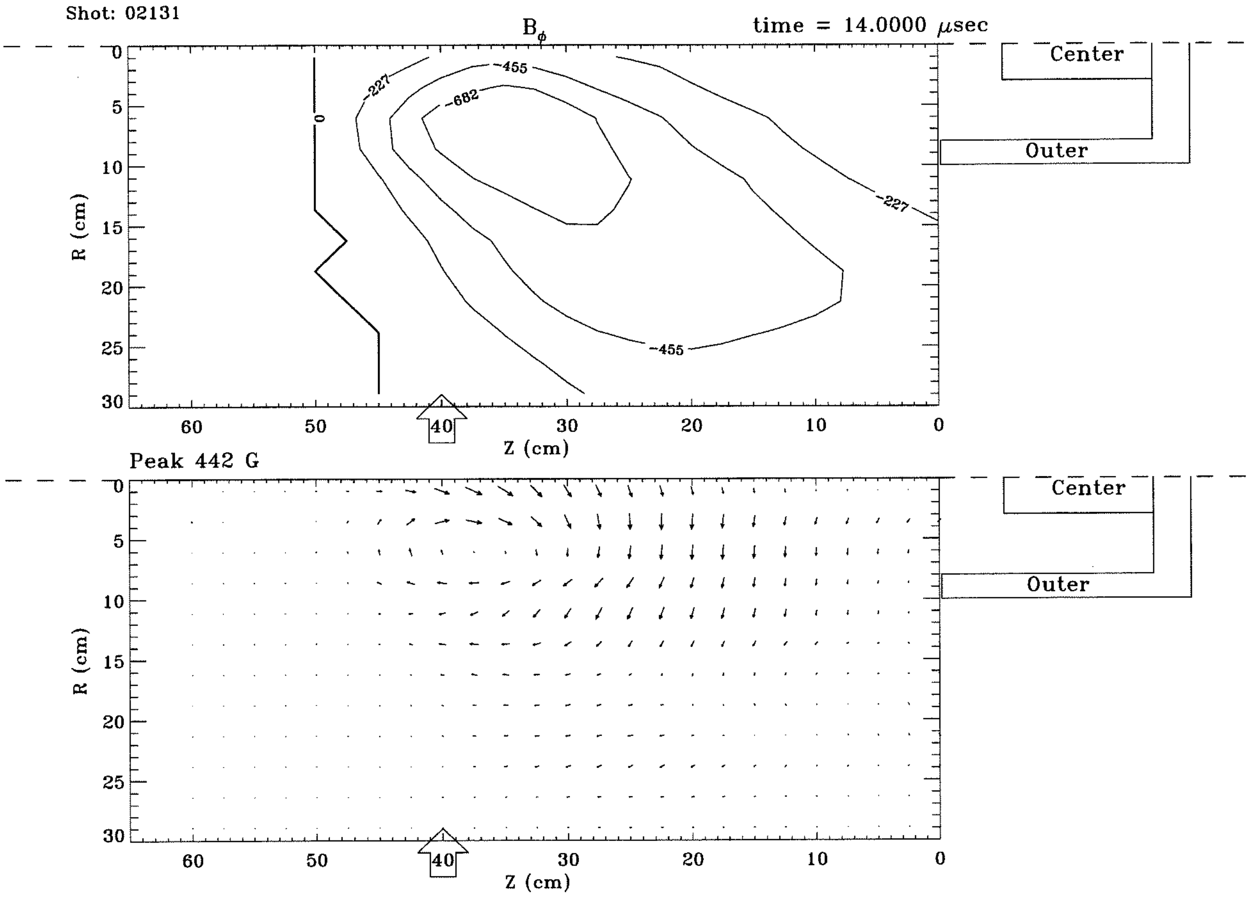

Figure 10.3: Magnetic field plot using SSPI method.

consistent with a decaying spheromak, using the arguments of Section 10.2.

10.4.2 Time evolution of λ

Using the SSPI propagation assumption, the z dependence of the plasma can be inferred from the time variation of the magnetic probe signal. Thus, the time dependence of the plasma λ profile can be obtained by analyzing a set of data taken varying the magnetic probe axial location. The data from such a scan is shown in Figure 10.5. Each trace corresponds to the radial distribution of λ at the magnetic axis (defined as the z location with maximum λ). Note that the spatial resolution of the calculation is limited by the magnetic probe array spacing; i.e., 2.5 cm.

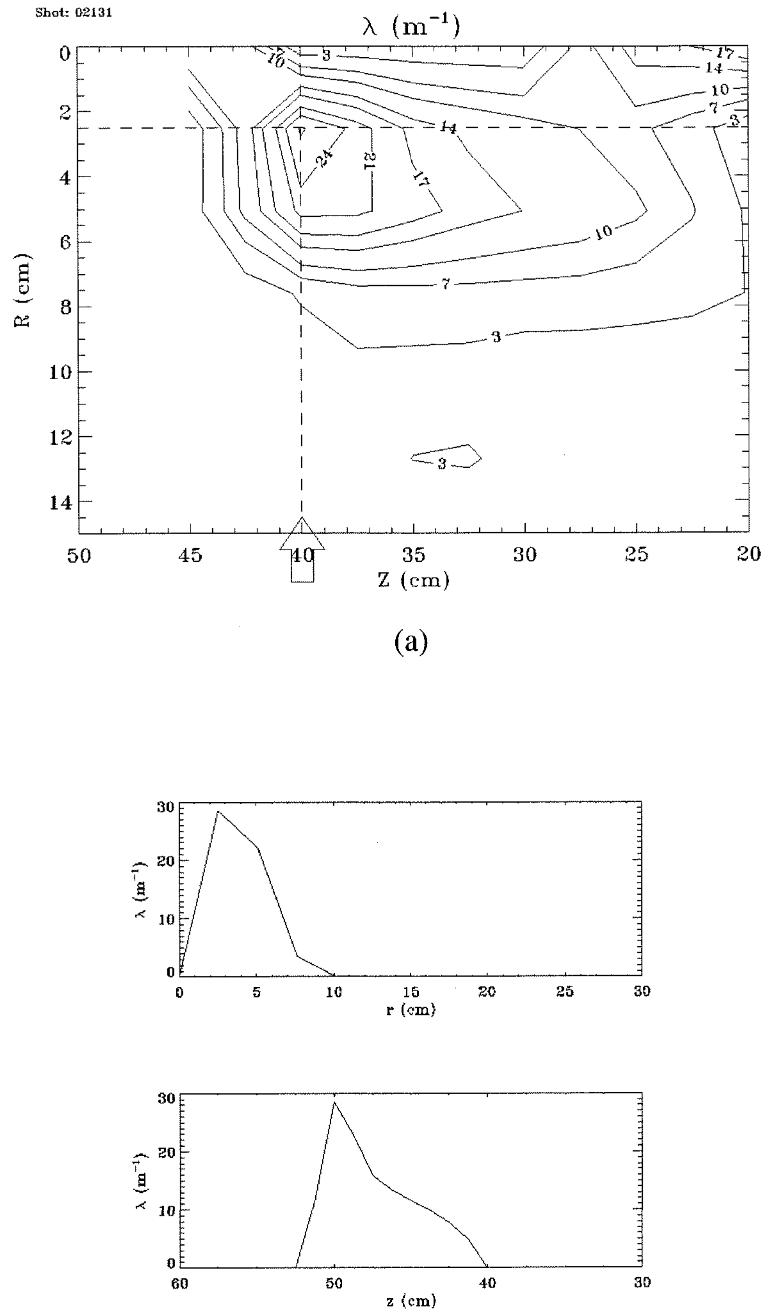

(a)

(b)

Figure 10.4: (a) Closeup view of contour plot of λ. Dashed lines at $z = 40$ cm and $r = 2.5$ cm intersect at the peak value. (b) Radial and axial profiles of λ, at $z = 40$ cm and $r = 2.5$ cm, respectively.

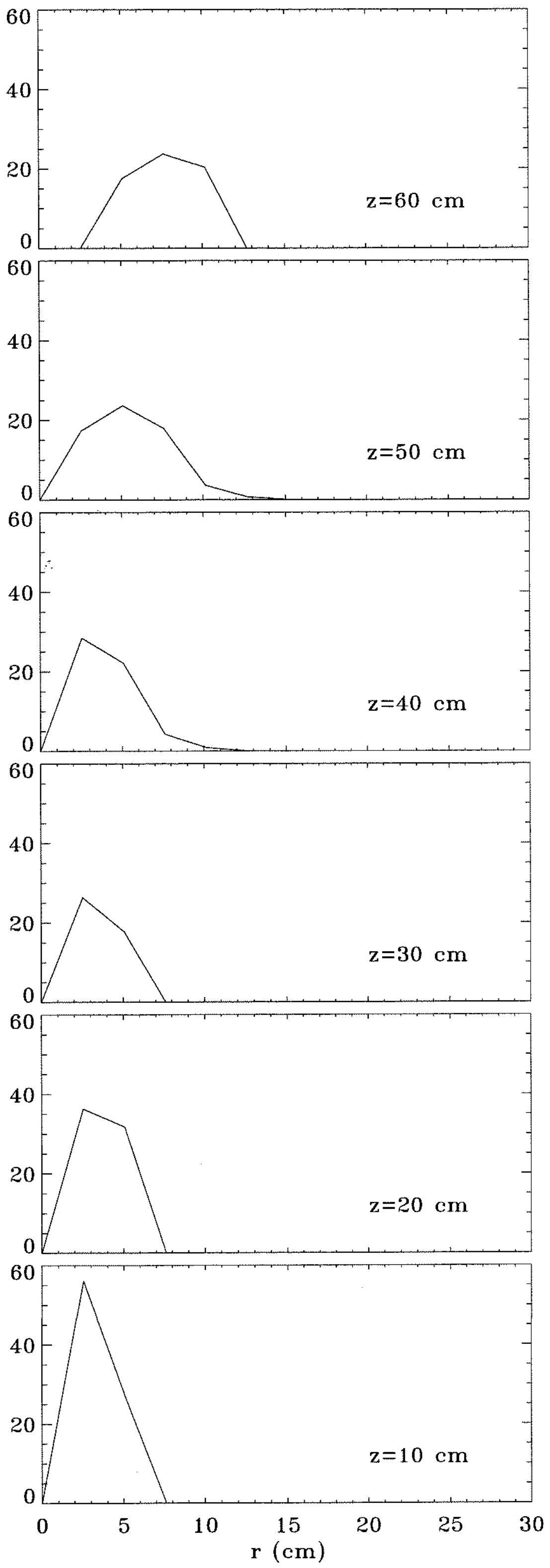

Figure 10.5: Radial lambda profiles measured at a sequence of probe locations.

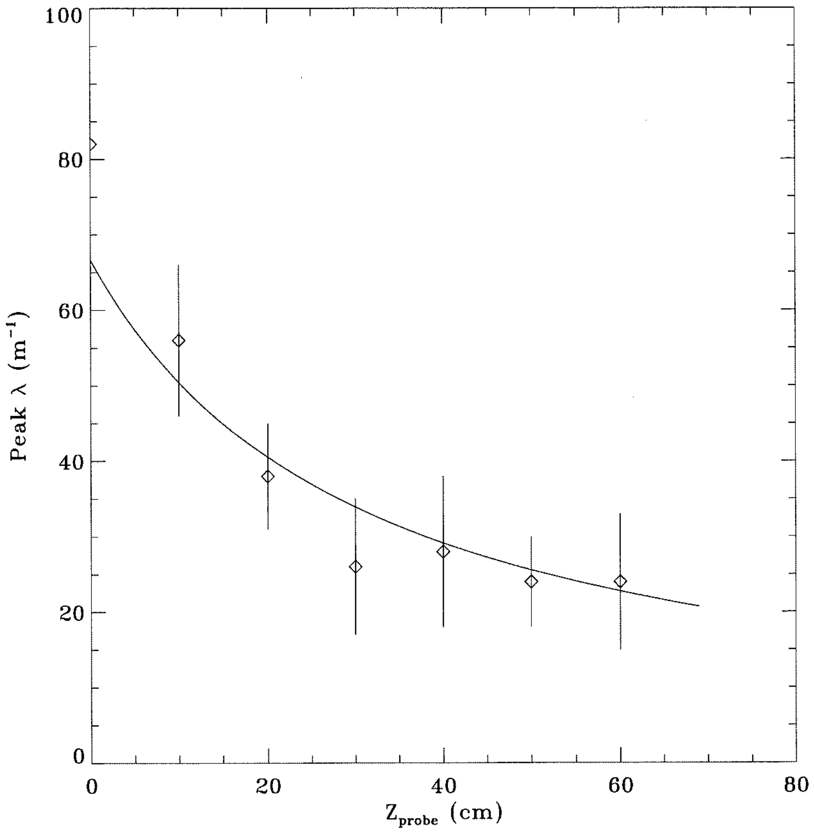

Figure 10.6: Peak values of lambda as a function of probe position. Each point represents an average over 3-5 plasma discharges. Error bars indicate standard deviation. The solid curve represents a fit of the data to a self-similar expansion model. See text.

Two features are immediately evident in comparing the distributions shown. First, there is a definite broadening effect at increasing distances from the gun. The FWHM increases from about 4 cm at $z = 10$ cm to about 8 cm at $z = 60$ cm. (This range in axial positions corresponds to a time interval of about 6 μsec.)

Secondly, the peak values of λ decrease with increasing z. This behavior is depicted in greater detail in Figure 10.6. Each data point is obtained by averaging 3-5 shots at that axial location, and the variation in the values is indicated by the error bars. Clearly, λ decays from approximately 55 m^{-1} to 25 m^{-1} as the plasma propagates away from the gun.

10.5 Discussion

It is evident from the plots in Figure 10.5 that the spheromak exhibits roughly the same qualitative λ profile irrespective of the probe location. In each case, λ is peaked near the magnetic axis and decreases monotonically away from the axis. This positive-α type of λ gradient is consistent with that observed by Knox during the decaying portion of the CTX spheromak.

Notably absent from any of these plots is an example of negative-α λ gradient, which would be expected during spheromak sustainment. In the present experiment, this lack of hollow λ profiles is likely due to early detachment from the gun. With the magnetic probe situated at maximal proximity to the gun ($z = 10$ cm), the spheromak magnetic axis arrives at the probe at $t = 10$ μsec (c.f. Figure 8.10). This is after the end of the sustainment (i.e., helicity injection) phase of the discharge (c.f. Figure 8.2) at 9.5 μsec. Thus, in order to determine whether a negative-α region does develop early in the shot, it would be necessary either to make magnetic probe measurements in the inaccessible region, $0 < z < 10$ cm, or to extend the length of the helicity injection phase. Unfortunately, neither of these options is currently feasible.

Another issue of considerable interest is the magnitude of λ which is observed. For the sake of comparison, it is helpful to consider the situation found in the majority of current spheromak experiments, in which the plasma is injected into a flux-conserver and allowed to relax. In these experiments, during the formation phase λ decreases from λ_{gun} to the eigenvalue of the ultimate minimum energy Taylor state, over the course of the relaxation time. This equilibrium configuration is determined by the boundary conditions, and thus λ is prescribed by the geometry of the apparatus; i.e., $\lambda = \lambda_{geom}$. Using dimensional arguments, λ_{geom} should be roughly proportional to the inverse of the system scale length. During the sustainment phase, λ is maintained at λ_{geom} while helicity and energy are injected. Likewise, in the decay phase, λ will continue to be locked to the λ_{geom} value.

The distinguishing feature in the present free expansion spheromak experiment is that the plasma never attains the true minimum energy state since this would entail filling the entire vacuum chamber. Thus, there is no predetermined λ_{geom} value and the system scale length may simply be the size of the expanding plasma, which is dynamically changing. The results presented in the previous section indicate that the plasma λ falls quickly from the gun value $\lambda_{gun} = \mu_0 I_{gun}/\Phi_{stuff} = 82$ m^{-1} down to $\lambda = 55$ m^{-1} at $z = 10$ cm.

However, it is interesting to note that this dropoff is not necessarily a result of rapid helicity dissipation. An alternative explanation is that the reduction in λ can be associated with expansion considerations. In the most basic model of an unbounded spheromak, one might expect that the plasma (and its embedded magnetic field) would expand in a purely self-similar manner. In this simple prescription, the plasma would remain in a force-free state throughout the expansion. However, the λ of the plasma would decrease in proportion to the inverse of the system scale length; i.e., if the system doubles in size, λ would fall to one-half of its initial value. In order to test whether this phenomenon is occurring in the current experiment, it is first necessary to determine the spheromak size.

Figure 10.7 shows a linear regression analysis of the plasma major radius, as estimated from the location of the magnetic axis; i.e., the peak of the radial lambda profile (c.f. Figure 10.5). Each point represents an average over 4-7 shots. The data suggests a clear uniform expansion rate. Inserting these values into a self-similar expansion model

$$\lambda = \frac{k}{r_{major}},$$

with k an undetermined parameter, and performing a least-squares fit to the data in Figure 10.6 gives $k = 1.3$. With this value for k, the self-similar expansion model's predictions for λ values are represented in Figure 10.6 by the solid curve. For comparison, the same data is presented in Figure 10.8 with λ as a function of r_{major}^{-1}. The prediction of the model is shown as the solid line.

The fit is rather good, and suggests that the decay in λ may be fully accounted for by plasma expansion, rather than helicity decay. Based on this argument, no

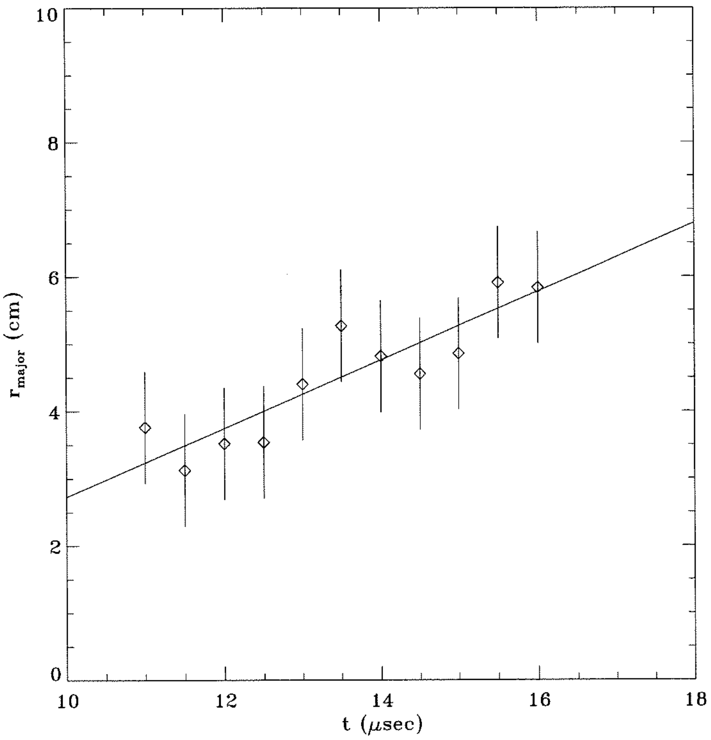

Figure 10.7: Major radius of spheromak, as estimated from radial lambda profiles.

significant helicity decay occurs during the time scale of these measurements, which is approximately 7 μsec. This would imply that $\tau_{res} \gg 7$ μsec, since helicity (like the toroidal and poloidal fluxes of the previous chapter) should decay on a resistive time scale.

10.6 Magnetic clouds

Magnetic clouds are regions within the solar wind with enhanced magnetic field strength and a distinctly helical magnetic field topology. The self-similar expansion ideas presented in the preceding discussion bear a striking resemblance to recent models of magnetic clouds [16]. The possible connection between the experimental results and these space plasmas is addressed in this section.

Magnetic probe measurements by spacecraft [11] have verified that these bodies

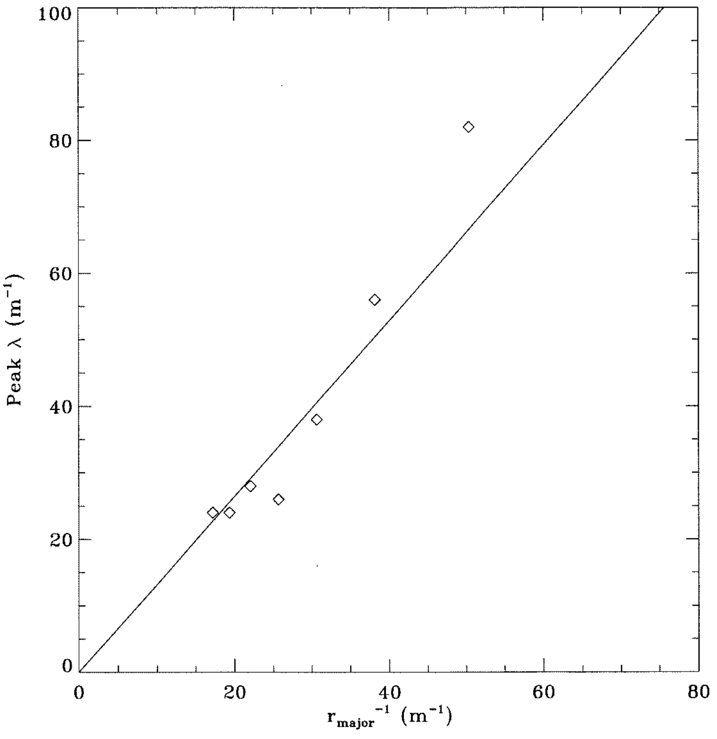

Figure 10.8: Peak λ values as a function of inverse major radius. The self-similar expansion model predicts a linear relationship between the two. The solid line represents $\lambda = 1.3/r_{major}$.

possess a force-free helical magnetic field structure reasonably well described by a Lundquist [45] model. Rust and Kumar [62] have proposed that magnetic clouds are associated with erupting solar prominences, which themselves have been shown to contain magnetic helicity and exhibit force-free properties [44],[63]. Thus, the analysis of magnetic clouds often involves many of the same helicity and relaxation ideas used in spheromak physics.

In the magnetic cloud model of Kumar and Rust [16], the magnetic cloud is modeled as a large aspect ratio torus which is assumed to be in a constant λ force-free state. Specifically, the field is described by the Lundquist [45] solution within the plasma and the dipolar field of a current-carrying ring outside. Because of the toroidal current, a hoop force is generated in the radially outward direction, causing the structure to expand self-similarly. The model predicts a constant (rather than accelerating) rate of growth in both major and minor radii of the cloud. This behavior is borne out in observations [64]. Using an argument similar to that presented above, this expansion is accompanied by a reduction in plasma λ. Since the total magnetic helicity K is conserved, and λ is proportional to the ratio W/K, the net magnetic energy W must decay at the same rate as λ; i.e., Taylor relaxation in this case requires magnetic energy dissipation as a result of the expansion. Most of this magnetic energy depletion will generate heating in the magnetic cloud, a result in agreement with observations of high cloud temperatures. This prediction is rather surprising, as it appears to conflict with the more intuitive thermodynamic idea of adiabatic cooling. In fact, both processes, magnetic heating and adiabatic cooling, are expected to occur in this model, but the heating dominates for low β plasmas. As heating proceeds, the β increases until the two mechanisms balance.

Magnetic heating has previously been observed by Jarboe [65] on the CTX spheromak. This effect was found to heat the plasma up to 100 eV. However, the phenomenon producing the heating in that experiment was simple resistive decay. Thus, both W and K decayed in amplitude while λ remained constant. No enhancement was generated by the self-similar expansion of the plasma and resultant reduction in λ.

It is appropriate to consider here how magnetic clouds may relate to the spheromaks produced in the present experiment. As described by Kumar and Rust's model, magnetic clouds exhibit many of the characteristics we have documented in the expanding spheromak. Self-similar expansion of the plasma proceeds at a constant rate. Helicity is conserved while λ decays in proportion to the inverse of the system size. It appears that the expanding spheromak experiment closely resembles the magnetic cloud model of Kumar and Rust, and may provide a laboratory testbed for their ideas. In particular, it would be intriguing to test the magnetic heating prediction, as the model calls for a quite dramatic heating effect for a low β plasma such as this: temperatures may be increased by a factor of 10 or more. It is interesting to note that preliminary data from a triple Langmuir probe was considered suspect because temperatures appeared far too high. With the current theoretical predictions in mind, the Langmuir findings must be revisited and the probe parameters may need to be altered (e.g., bias voltages increased), in order to accommodate possible increased temperatures.

10.7 Summary

Employing the SSPI method, λ was calculated throughout the spheromak. Centrally peaked profiles were observed, indicating that helicity flows from the magnetic axis; i.e., the spheromak is decaying. A broadening of the λ profile with time reflects expansion in the minor radius. Analysis of the time dependence of the peak values of λ suggests that a self-similar expansion model provides a good explanation for the decay in λ over time and is in accordance with the expected invariant total helicity. The general characteristics of the expanding spheromak appear to be well described by observations and models of magnetic clouds. These models also predict a curious and striking phenomenon that has been observed in clouds: magnetic heating of the plasma. Verification of the dramatic temperature increases in the present experiment would provide strong support for the self-similar expansion magnetic heating effect postulated. This is an important subject for further work.

Chapter 11 Regime III: Helical flux tubes in a stuffed spheromak plasma

11.1 Introduction

In Chapter 7, it was shown that plasma evolution could be categorized into four regimes of behavior which were principally dependent on the ratio λ_{gun} between gun current and applied bias field. Regime III, in particular, was unique in that a great deal of structure and dynamics is visible in the Side View image sequence, as shown in Figure 11.1. The observed behavior is somewhat complex, and we will find it useful to divide plasma evolution into three stages which have distinct qualitative appearance, summarized in Figure 11.3. These stages are described below. For reference, Figure 11.2 reviews the gun current and voltage traces during a discharge with the three stages noted.

Stage A (6-11 μsec): Distension of stuffing flux field lines

This stage begins at 6 μsec, when the plasma initially emerges from the gun with numerous filaments of material visibly joining the end of the inner electrode with the outer electrode. At this point, the current is peaking and the voltage is falling toward zero.

As the plasma continues to be pushed out of the gun, a coherent global structure begins to take form. The connection between inner and outer electrodes evolves into a bright central column, with a fainter return path to the outer electrode. This culminates in a somewhat mushroom-like plasma with a basically spherical outline. The plasma proceeds to expand in a roughly self-similar fashion outside the mouth of the gun.

By 11 μsec, the end of this stage, the current has fallen to roughly half of its peak

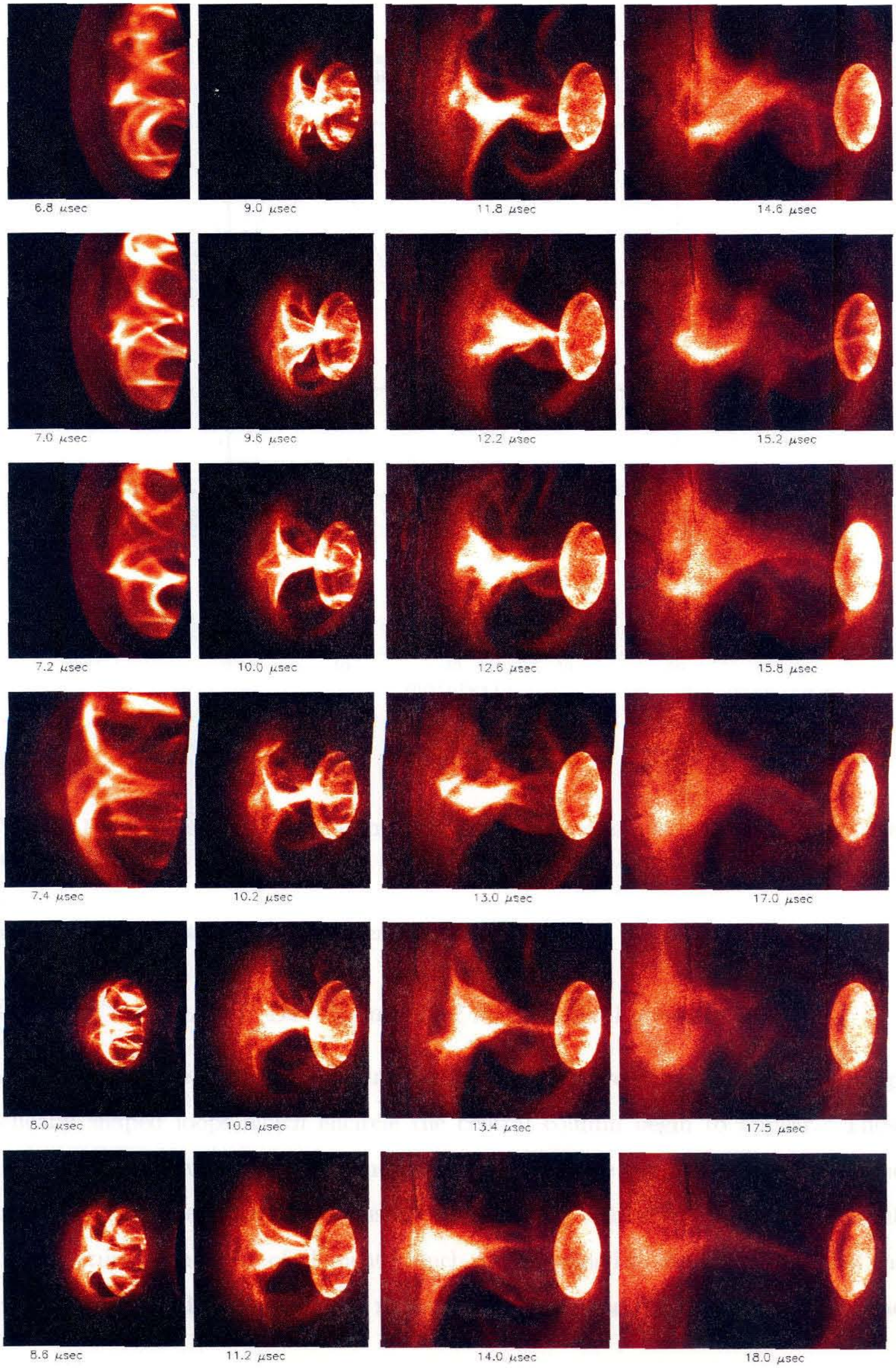

6.8 μsec 9.0 μsec 11.8 μsec 14.6 μsec

7.0 μsec 9.6 μsec 12.2 μsec 15.2 μsec

7.2 μsec 10.0 μsec 12.6 μsec 15.8 μsec

7.4 μsec 10.2 μsec 13.0 μsec 17.0 μsec

8.0 μsec 10.8 μsec 13.4 μsec 17.5 μsec

8.6 μsec 11.2 μsec 14.0 μsec 18.0 μsec

Figure 11.1: Side View image sequence in Regime III.

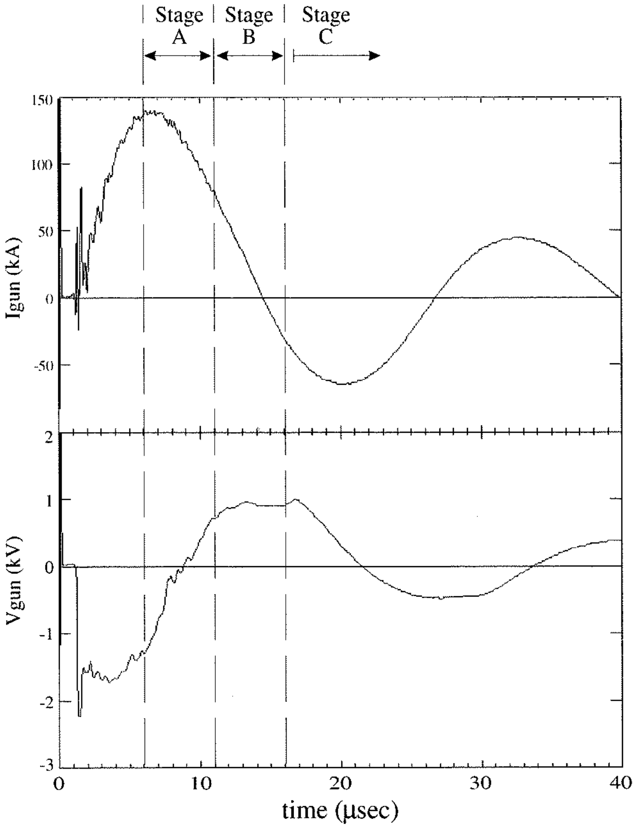

Figure 11.2: Current and voltage measurements with the gun operated at nominal values ($I_{gun} = 130$ kA and $\Phi_{stuff} = 6$ mWb) in Regime III.

value and the voltage has fully reversed.

Stage B (11-16 μsec): Development of large helical structures

As the head of the mushroom continues to gradually move away from the gun, large helically shaped loops which encircle the central column begin to appear. These loops, which appear to be simple and untwisted, originate at the outer electrode and connect to the outer edge of the mushroom head. The central column contains much fine structure in the form of filaments which remain joined to the gun. Note that the brightest part of the plasma is the region where the central column meets the head

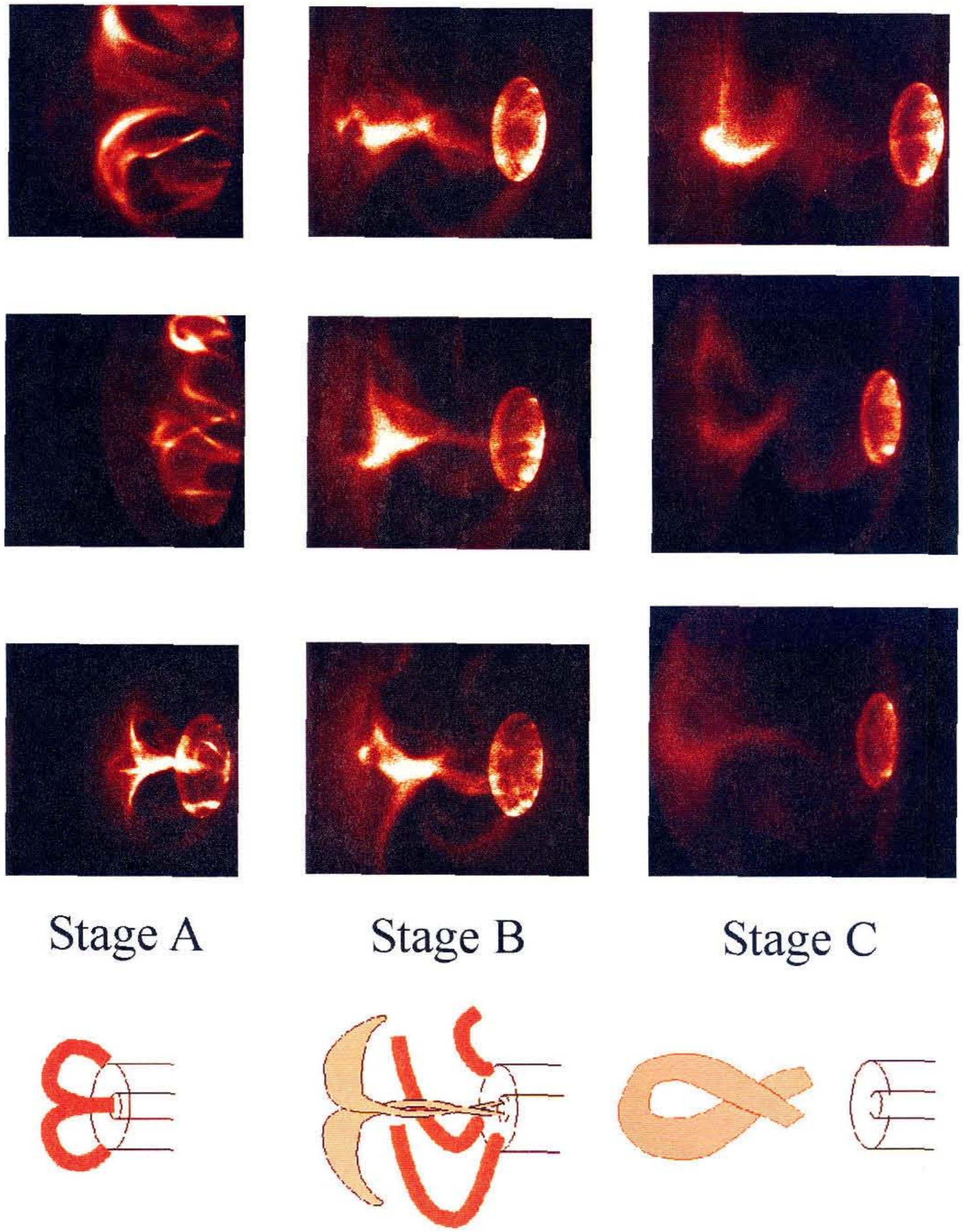

Figure 11.3: Summary of Stages A, B, and C in Regime III. The bottom row shows representative sketches of plasma behavior.

of the mushroom.

During this stage, the voltage remains at a high positive (reversed) value, while the current falls through zero at 14 μsec.

Stage C (16-25+ μsec): Decay

During this final stage, as the large helical loops increase in diameter and decay in intensity, the central column evolves into a single half-turn twist. The connection to the gun becomes quite tenuous although complete detachment does not appear to occur. The brightest portion of the plasma is the former head of the mushroom at this stage, and continues to propagate away from the gun. The current is negative throughout Stage C while the voltage returns to a negative polarity; i.e., negative helicity injection.

11.2 Relationship between bright filaments and flux tubes

Reviewing the images presented above reveals that most of the major features appearing in the pictures consist of filaments; i.e., lines of material which are brighter than the background plasma. In trying to understand the camera data, it is thus important for us to determine the origin of these filaments and how the structure of these filaments reflect properties of the underlying plasma.

Simple experiments with notch filters indicate that the vast majority of the light detected by the camera is in the H_α wavelength. This result has also been corroborated by an optical multichannel analyzer. Therefore, each image consists of radiation from the de-excitation of neutral hydrogen and the intensity of each parcel of plasma is thus a function of the local population of the excited neutrals. The details of the balance between competing processes of electron-neutral and ion-neutral collisions and recombination which determine the excited neutral population are highly complex and require knowledge of plasma parameters which are not readily available.

Fortunately, a basic property of magnetized plasmas may help us to avoid these complexities. In a highly ionized plasma, transport of many plasma quantities, including thermal energy and particles, is much higher along magnetic field lines than in the transverse direction [67]. Thus, it is a reasonable assumption that filaments of material emitting relatively more intense H_α radiation reflect the presence of a magnetic flux tube, which remains relatively isolated from the surrounding plasma. For example, it may be that fast electrons travel along field lines and occasionally collide with neutrals along their path. In fact, these are precisely the types of assumptions which have been commonly used by solar astronomers in interpreting H_α filaments in images of solar prominences [66][68] as magnetic field related.

In this section, data will be presented which provides direct evidence for the unique correspondence between filaments and magnetic field lines and flux tubes.

11.2.1 Chirality

In the Regime III pictures, there are several examples of structures which contain filaments that are twisted and helical in nature, characteristics which are suggestive of magnetic helicity. As a preliminary step in establishing whether or not the visible plasma morphology is indeed linked to the underlying magnetic topology, it is useful to determine the handedness of these structures. In the space and solar plasma literature, this property is referred to as *chirality* (e.g., see Ref. [62]). Right handed helices have positive chirality, whereas left handed structures have negative chirality.

If these helical structures are in fact associated with the magnetic helicity of the plasma, one would expect that their chirality would be affected when the polarity of λ_{gun} is changed. In particular, reversal of the stuffing flux field should result in reversal of the plasma magnetic helicity and hence the structures' chirality. This hypothesis is tested in this section.

End-On images

Stage B is characterized by the development of large helical filaments of plasma. However, it is difficult to ascertain the handedness of these loops simply by examining the Side View pictures shown thus far. In order to help determine the direction of the helical loops, it was found to be helpful to simultaneously view the plasma from a different vantage point. By positioning a second camera at the end viewport (see Figure 6.1), the End-On view could be obtained. Sample images taken using this camera configuration are shown in Figure 11.4a.

In these pictures, the spiral nature of the loops become evident (and is somewhat reminiscent of astronomical images of whirlpool galaxies). Viewed End-On, there are several loops which encircle the geometric axis in the clockwise direction. Thus, these loops possess a left-handed chirality. This direction is consistent for all loops and does not change through Stages B and C, although the size of the loops does increase over time. Pictures also indicate that there is a slow azimuthal rotation in the clockwise direction.

Pictures with the polarity of the applied stuffing flux field reversed are shown in Figure 11.4b. As expected, the direction of spiralling became reversed and spiralled counter-clockwise. Thus, we have shown that the helical loops are left-handed objects for the case of positive helicity injection and right-handed for negative helicity injection. The origin of this counter-intuitive relationship is discussed below.

Stereoscopic imaging

Beginning in Stage B, it was also found that a large degree of twist was apparent in the central column. However, the sense of the twist is not immediately apparent. Fortunately, in this case, the necessary information can be readily obtained through the use of stereoscopic imaging, which was described in Section 6.3.2.

Three-dimensional pictures taken using this method are shown in Figures 11.5 and 11.6, for Stages B and C, respectively. Viewed through the appropriate red-green glasses, the sense of the twist can be seen to be right-handed in both cases. (Note

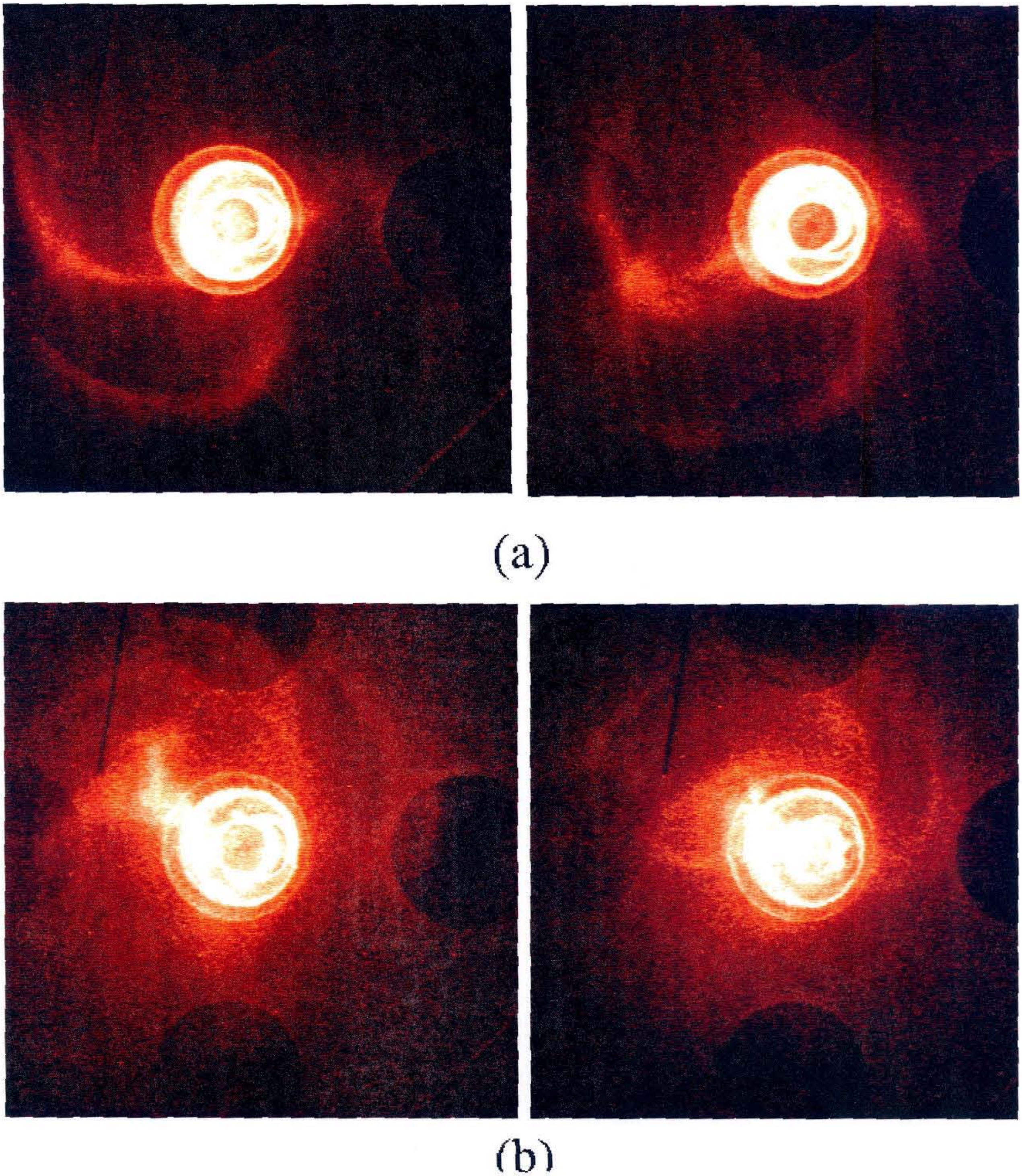

Figure 11.4: Sample images of the plasma from the End-On perspective.

that for technical reasons, the cameras were mounted one atop the other, so that in these pictures as the plasma is propagating away from the gun, it travels across the field of view from bottom to top.) The helical loop is also visible in Figure 11.5 and the direction of twist is consistent with the End-On view discussed above.

Identical experiments with the stuffing flux field reversed verified that the central column twist became left-handed. To summarize, when operated using positive helicity injection, the gun produces a plasma structure with positive chirality in the central column and negative chirality in the surrounding helical arms. With negative helicity injection, the chirality of these two structures are reversed.

Polarity of chirality vs. polarity of helicity

Above, it was shown that a positive helicity object, i.e., the helical loops, can have a negative chirality associated with it. At this point, a short discussion on the significance of this somewhat surprising finding are in order. As a concrete example, consider the simple Lundquist solution [45], given by

$$\begin{aligned} B_\phi &= B_0 J_1(\lambda r) \\ B_z &= B_0 J_0(\lambda r) \end{aligned}$$

in cylindrical coordinates.

This is the simplest constant-λ Taylor state solution, as it assumes both axisymmetry and no axial dependence. The radial dependence is sketched in Figure 11.7. Assuming that λ is positive, this structure clearly has positive helicity. However, the helical field lines prescribed by this configuration are not solely right-handed in nature. For example, near the axis, both B_ϕ and B_z are positive, so the field line trajectories would generate a right-handed corkscrew pattern. But as one proceeds out to slightly larger radii, an annular region is reached where $B_z < 0$ and $B_\phi > 0$, indicating that field lines have negative chirality.

The origin of this confusion can be traced to the following argument. If $\mathbf{B}$ satisfies $\nabla \times \mathbf{B} = \lambda \mathbf{B}$, then $\hat{\mathbf{z}} \cdot \nabla \times \mathbf{B} = \lambda B_z$; i.e., looking down on the z plane, if λ and B_z are

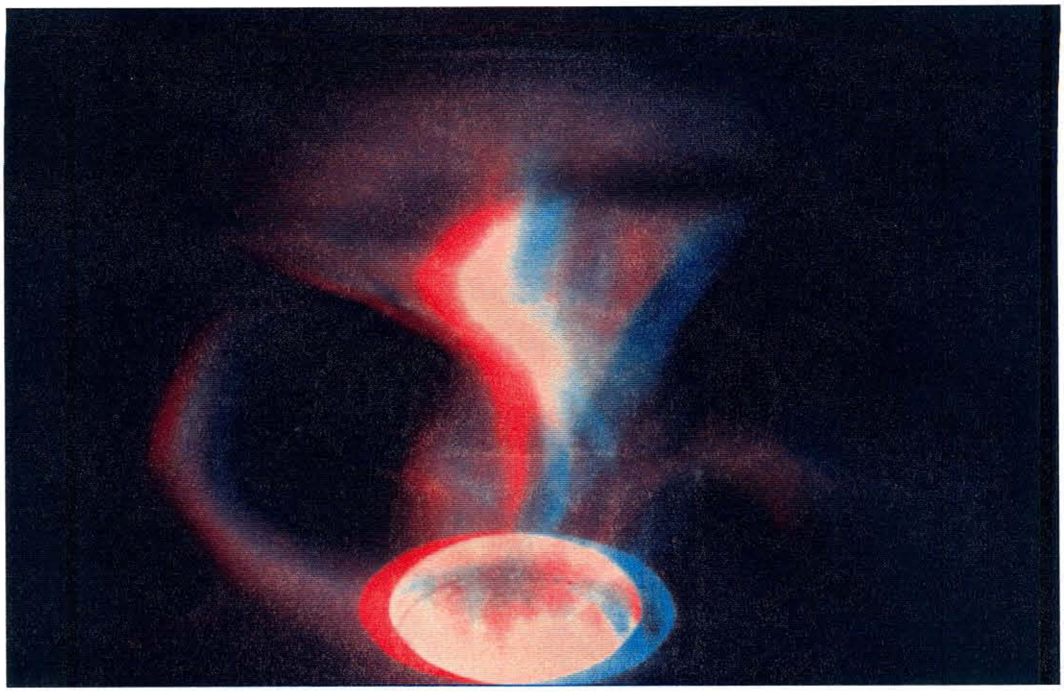

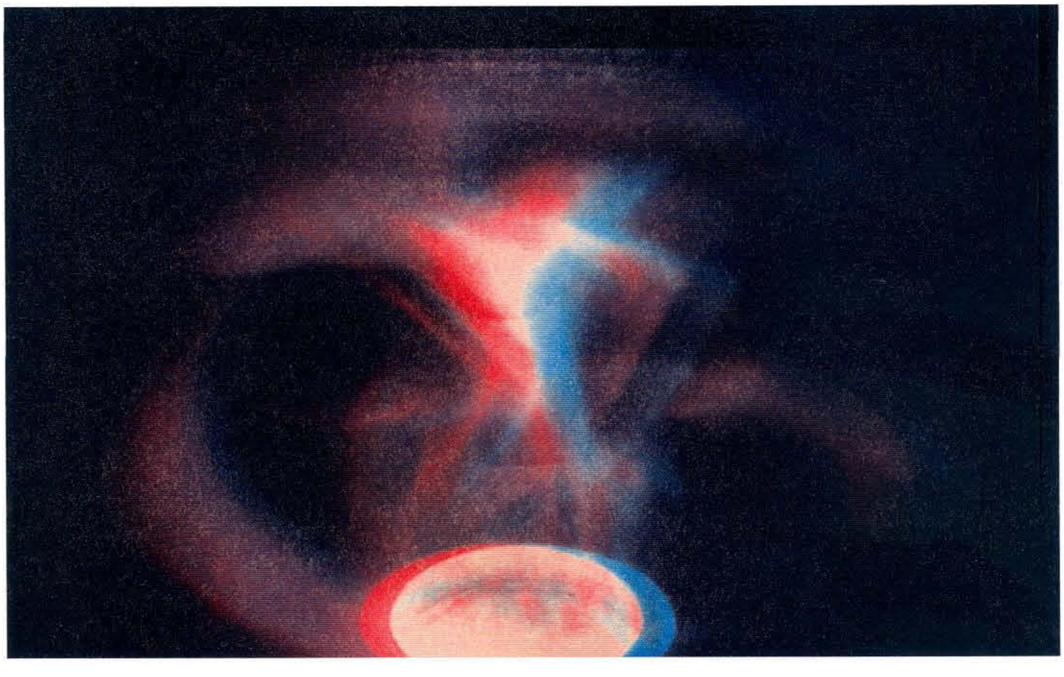

Figure 11.5: Stereographic images of plasma in Regime III, Stage B. (The glasses should be worn with the red filter over the right eye, and the green filter over the left.)

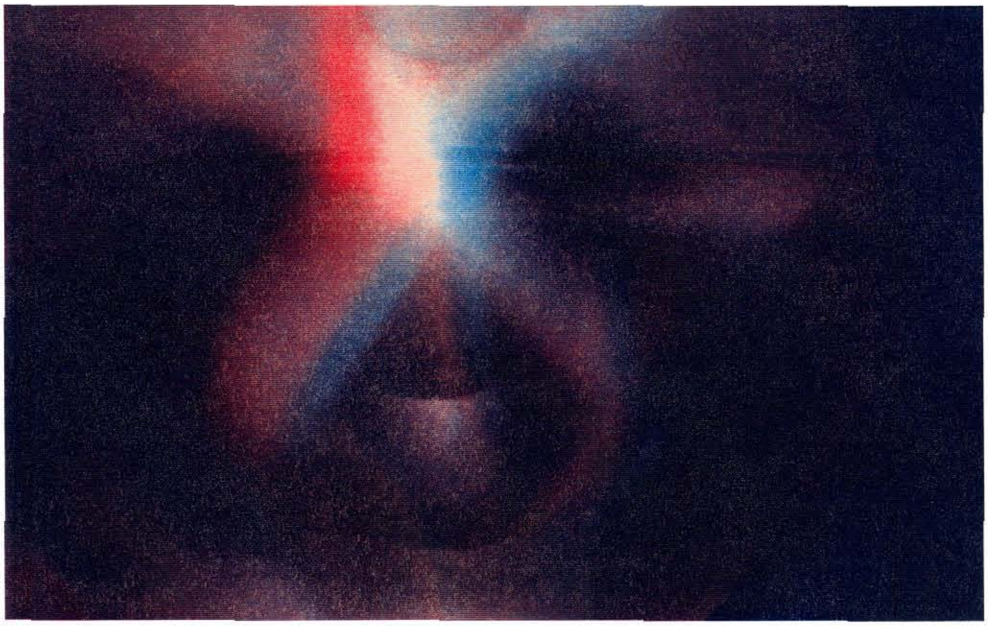

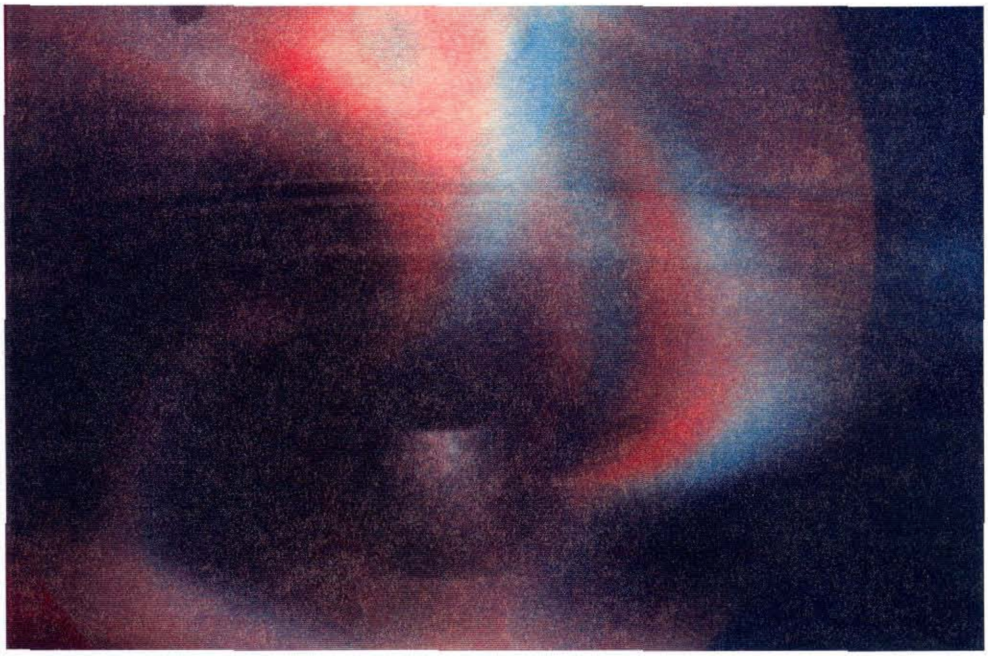

Figure 11.6: Stereographic images of plasma in Regime III, Stage C. (The glasses should be worn with the red filter over the right eye, and the green filter over the left.)

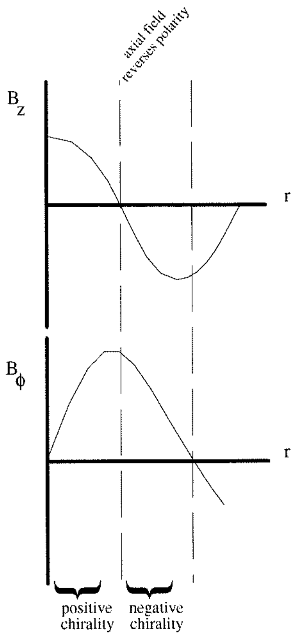

Figure 11.7: Sketch of Lundquist Taylor state solution. The radial component of **B** is zero.

positive, then the z component of the curl must be positive. Thus, we might imagine that the projection of **B** field onto the z plane will consist of vortices swirling in the counter-clockwise direction (again, looking down at the z plane). Together with the positive B_z, the associated 3D field lines would then be right-handed. The fault in this argument lies in the simplistic interpretation of the curl operator. In the Lundquist case above, the region with negative B_z implies that the z component of the curl of **B** must be similarly negative. However, looking down at the z plane, instead of the expected clockwise vortex, the vector field consists of a counter-clockwise vortex as well! The conclusion we can draw from this discussion is that it is not always possible to associate the polarity of helicity with the polarity of chirality, and care must be taken in doing so.

It should be noted, however, that the case presented here is unusual in that a region of one polarity of B_z is enclosed within a region of the opposite polarity, as is the case in the present experiment, and this situation can generally lead to the peculiarities described above. In the simpler (and perhaps more common) situation of a unipolar B_z, it can be shown that the chirality will be consistent with the helicity.

11.2.2 Magnetic probe data

A more direct means of verifying the magnetic nature of the filaments is obtainable using the magnetic probe array. An extensive scan was performed with the probe positioned in the ranges 10 cm $< z <$ 60 cm and $-30^o < \phi^1 < 30^o$ (in probe and not gun coordinates), with increments of $\delta z = 5$ cm, $\delta\phi = 6^o$. It was found that, unlike in Regime II, a high degree of reproducibility was achieved using the methods described in Section 6.4.1. Thus, the SSPI method described in Chapter 8 was not needed in this Regime.

Sample magnetic data from this scan are presented in the form of vector field plots in Figures 11.9,11.10, and 11.11, for times in Stages A, B, and C, respectively. Figure 11.8 sketches the layout and coordinate planes useful for understanding the data presented in the latter three figures. At each time, toroidal slices at various z planes are shown, as well as a poloidal slice in the natural poloidal plane ($\phi = 0$ or $y = 0$). From the magnetic data scan, essentially half the z plane is diagnosed, as shown by the shaded region in Figure 11.8. For convenience, these points are then fit onto a rectangular (x, y) grid through linear interpolation; essentially, a change of coordinates systems is performed, from the probe coordinates (r^1,ϕ^1) to the gun coordinates (x, y). In the gun coordinates, $x = 0$ and $y = 0$ corresponds to the geometric axis. $y = 0$ (or, alternatively, $\phi = 0$) defines the natural poloidal plane. In the figures, the toroidal slices are presented with the horizontal axis as $\widehat{\mathbf{x}}$, the vertical axis as $\widehat{\mathbf{y}}$, and $\widehat{\mathbf{z}}$ pointing out of the page.

The toroidal plots generally fall into one of two categories: vortical or convergent. In Stage A (Figure 11.9), the field is entirely directed radially inward; i.e., convergent. This reflects the magnetic field line return path converging towards the central column and inner electrode. The pattern is essentially axisymmetric about the geometric axis ($x = y = 0$), but the axis appears to drift down a few centimeters in the negative $\widehat{\mathbf{y}}$ direction at greater distances from the gun ($z = 17$ cm). In Stage B (Figure 11.10), the toroidal field has a whirlpool pattern in z planes near the gun, associated with the azimuthal field produced by current flowing in the central column. At increasing distances from the gun, the field pattern becomes progressively more convergent and the axis again seems to drift downward in the negative $\widehat{\mathbf{y}}$ direction. The transition from vortical to convergent patterns is associated with the location of the mushroom head; i.e., current sheath return path. Due to the propagation of the mushroom head, the z location at which the toroidal field transitions from vortical to convergent increases with time during this Stage. The poloidal field slices corroborate this picture, showing magnetic field emerging from the outer electrode and returning through a central column to the inner electrode.

In Stage C (Figure 11.11) the whirlpool pattern is again visible in z planes near the gun. However, the circular pattern becomes elongated vertically, suggesting a loss of axisymmetry. At greater distances from the gun (near the mushroom head) the field cannot be classified in either of the two aforementioned categories, and in fact, has lost its axisymmetric character. The field line structure is somewhat unclear in this region.

Overall, however, this data is consistent with the picture of magnetic structure obtained from the camera images. In Stage A, the poloidal slice shows field lines just beginning to be seen in the $z > 10$ cm region. In Stages B and C, the central column appears in the poloidal slice as a region of strong field near $r = 0$ directed in the negative $\widehat{\mathbf{z}}$ direction. Note that in Stage C, the column becomes kinked, which, when interpreted in conjunction with the toroidal data, shows that it has a helical form (with the correct chirality).

It is evident that the magnetic data presented here is dramatically different from those obtained in Regime II, both quantitatively and qualitatively. Field magnitudes are smaller in magnitude in this Regime and fall off rapidly away from the gun. In poloidal slices, there is no evidence of the vortical high field region characteristic of the closed field structure of a spheromak which was noted in Regime II.

A surprising feature worth addressing here is the lack of toroidal field reversal when the gun current reverses at $t = 14$ μsec, towards the latter half of Stage B (c.f. 11.2). If, as suspected, the gun is stuffed and all field lines are open, connecting the inner and outer electrodes, one would expect that current flow (e.g., within the central column) to change polarity along with the gun current. This would result in polarity reversal in B_ϕ, and consequently, change the chirality of all helical structures mentioned above. This is not observed. The probable reason behind this surprising behavior is that residual plasma within the gun effectively provides a short-circuit (i.e., it is crowbarred). Thus, there may be closed current paths despite the lack of closed field lines.

Flux tube reconstruction

Unlike the central column, the helical loops at the plasma periphery are somewhat more difficult to observe in the magnetic data. These features are associated with regions of the plasma in Stages B and C with positive B_z, and these areas are generally less axisymmetric than the central column, as well as fairly small in amplitude. It is helpful in this case to undertake direct flux tube reconstruction. This technique involves tracing individual magnetic field lines through numerical integration of the measured field. By tracing several lines which are in close proximity to each other, a complete flux tube surface can be obtained.

An example of flux tubes rendered using this method is shown in Figure 11.12a. In this case, the flux tubes are computed using the magnetic probe data from the scan at $t = 13$ μsec. For comparison, a camera image taken at that point in time is shown in Figure 11.12b. Note that, due to constraints in the available volume of space which can be diagnosed by the magnetic probe, data could only be obtained in the range $x > 0$ (i.e., $-\pi < \phi < \pi$). However, field lines generally follow paths helically encircling the geometric axis. Therefore, it was necessary to analytically continue the available data into the inaccessible region by including only $m = 0$ and $m = 1$ Fourier modes. This approximation assumes that these two modes are dominant.

The rendered flux tubes may now be qualitatively compared with the picture data for consistency. The twisted central column in the reconstruction matches the images fairly well. Also visible is one of the helical loops. One feature which does not seem to be well reproduced is the mushroom head. The rendered flux tubes appear to become poorly behaved at this point. This is likely due to insufficient grid resolution, reproducibility-induced measurement uncertainties, or the presence of higher ($m \geq 2$) Fourier modes.

11.3 Verification of stuffed gun operation

Strong evidence was presented in Chapters 8-10 which indicates that force-free spheromaks are produced when the gun is operated in Regime II. It is interesting to test the plasma produced in Regime III in a similar manner to determine whether spheromaks are also generated. Based on the qualitatively different camera images in the two Regimes, and the presence of a λ_{gun} threshold dividing parameter space, it is natural to suspect that, in Regime III, a stuffed spheromak is produced; i.e., no closed flux surfaces are formed and all field lines in the plasma therefore both begin and end at the gun electrodes. Indeed, this is precisely the behavior often exhibited by the filaments in the images. In Stage A, numerous flux tubes clearly link the inner and outer electrodes. In Stage B, flux tubes emerge from the outer electrode in the form of helical loops, meet with the mushroom head feature, and return to the inner electrode in the twisted central column structure. The topology in Stage C is less clear, however. The helical loops have faded in luminosity and the images are dominated by the brighter central column. In this case, the magnetic data can be used to help clarify the situation, and indicates that detachment does not, in fact, occur; the central column remains of negative B_z polarity throughout its cross-section, and no closed flux surfaces are visible in poloidal slices.

Additional confirmation that a discrete spheromak is not formed is provided by calculations of poloidal and toroidal fluxes. Computation of the poloidal flux must be performed in a manner different than that described in Chapter 9 because there is no magnetic axis to define the plane of integration. Instead, the net poloidal flux through an arbitrary $z = const$ plane is found by numerically calculating the surface integral

$$\Psi_{pol}(z_0) = \int_{z=z_0} B_z \cdot dA_-,$$

where dA_- indicates that only negative polarity B_z regions are included. (In principle, either positive or negative polarities can be counted, but not both. Negative polarity corresponds to the central column region.) Because only half the plane is diagnosed in the magnetic probe scan ($x > 0$), approximate bilateral symmetry is assumed and the computed half-plane surface integral is doubled. This constitutes a somewhat less restrictive assumption than the axisymmetry assumed in Chapter 9.

Figure 11.13 shows a plot of the time dependence of the maximum value of the poloidal flux; i.e., the flux is computed for all values of z and the maximum is shown. This maximum value is typically assumed near the gun ($z = 10$ cm). The curve peaks at 2 mWb at 16 μsec. Comparison with the applied bias flux of 6 mWb clearly shows that no flux amplification is taking place. This indicates that most of the poloidal flux does not distend out of the gun sufficiently so that it penetrates the plane defined by $z = 10$ cm; i.e., one gun radius away.

A plot of the time dependence of the total toroidal flux is shown in Figure 11.14. In this case, the flux is computed by integrating B_ϕ over the entire surface of the natural poloidal plane ($\phi = 0$). This curve exhibits a similar time dependence to the poloidal flux and peaks at about 2.7 mWb. Comparison with the toroidal flux measured in Regime II suggests that most of the poloidal current (which generates the toroidal flux) is trapped within the gun as well.

Finally, a calculation of λ is useful in determining the direction and magnitude of helicity flow. Figure 11.15 shows a contour plot of λ in the natural poloidal plane at $t = 13$ μsec. The figure shows that, unlike in Regime II, there is no local maximum of this quantity which propagates away from the gun. Rather, λ is essentially monotonically decreasing away from the gun. At $t = 13$ μsec, its maximum magnitude is 36 m^{-1}, in comparison to $\lambda_{gun} = 245$ m^{-1}. Thus, there is an extreme gradient in λ at the mouth of the gun, providing confirmation that the majority of the helicity must be locked up within the gun.

11.4 Symmetry

In the images above, one particular property of the plasma morphology which seems to be conspicuously absent is axisymmetry. The $m = 0$ nature of the electrode structure and stuffing flux magnetic field might lead one to expect the generated plasma to retain this type of symmetry. Instead, the plasma exhibits numerous features which are manifestly not azimuthally symmetric, most notably including the helical loops at the periphery and the half-twist in the central column. It is worthwhile to address here the possible sources of asymmetry.

Numerous factors may break the symmetry of the formation process. These include subtle geometrical asymmetries such as, for example, the lack of perfectly concentric electrodes. The stuffing flux magnetic field is also clearly not purely $m = 0$ because the iron yoke in the magnetic circuit consists of individual bars instead of an annular ring of material. Another source of asymmetry is the initial gas distribution, which is produced by two gas valves and may therefore introduce an $m = 1$ mode. Finally, even if the device were perfectly symmetric, the plasma breakdown process is not generally homogeneous. For example, in plasma arc experiments, hot spots have been observed on the electrodes and are associated with particularly high current density concentrations [69]. (One may also speculate that these latter inhomogeneities may play a role in the filamentation of the current and generation of plasma filaments.)

It is perhaps not surprising that in the present experiment, although Taylor relaxation processes have been observed, the situation has a more dynamical aspect than in experiments injecting spheromaks into flux conservers. In the latter cases, the axisymmetric flux conserver continuously steers relaxation into an ultimately $m = 0$ mode. In contrast, the unconfined plasma here is largely unaffected by boundary conditions and is thus likely much more highly dependent on initial formation conditions.

11.5 Summary

In this chapter, plasma generated by the gun in Regime III was diagnosed using high speed cameras and the magnetic probe array. The pictures exhibit interesting features including helical loops, a twisted central column, and a mushroom shape. The general evolution of the features was documented. The helical and twisted nature of some of these features were found to correlate well with the underlying magnetic structure, suggesting a close connection between bright filaments of plasma and magnetic flux tubes.

Both in the pictures and the magnetic field measurements, no evidence was found for detachment of a plasmoid body with closed magnetic topology. Analysis of poloidal flux, toroidal flux, and λ distributions indicate that the bulk of the magnetic flux and helicity do not emerge from the gun. This behavior is taken as evidence that the spheromak is stuffed in this regime.

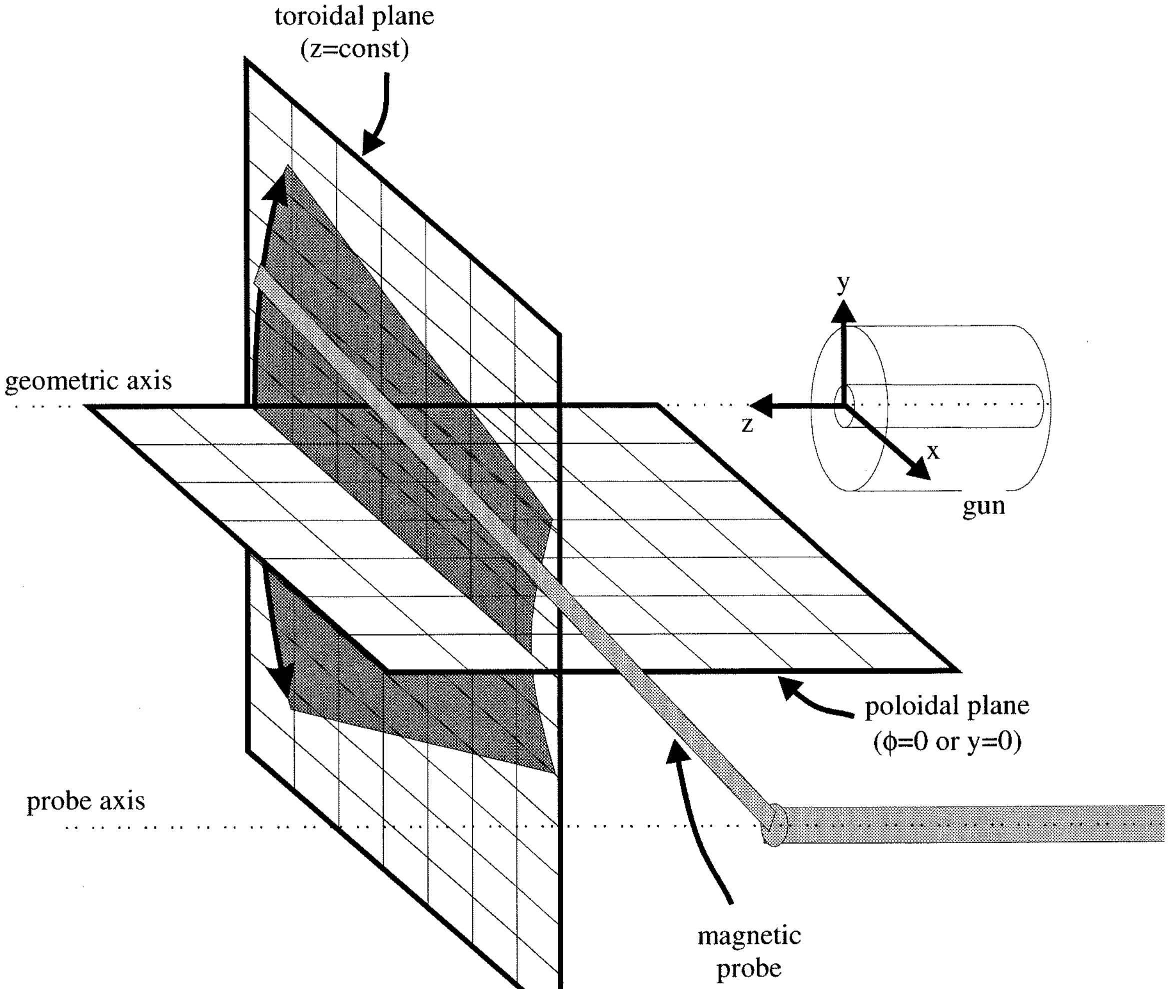

Figure 11.8: Sketch showing the various coordinates planes relevant to the analysis and presentation of data from the B-probe scan. The shaded area represents the range over which the plasma is diagnosed as the probe is swept over a range of ϕ^1 at constant z.

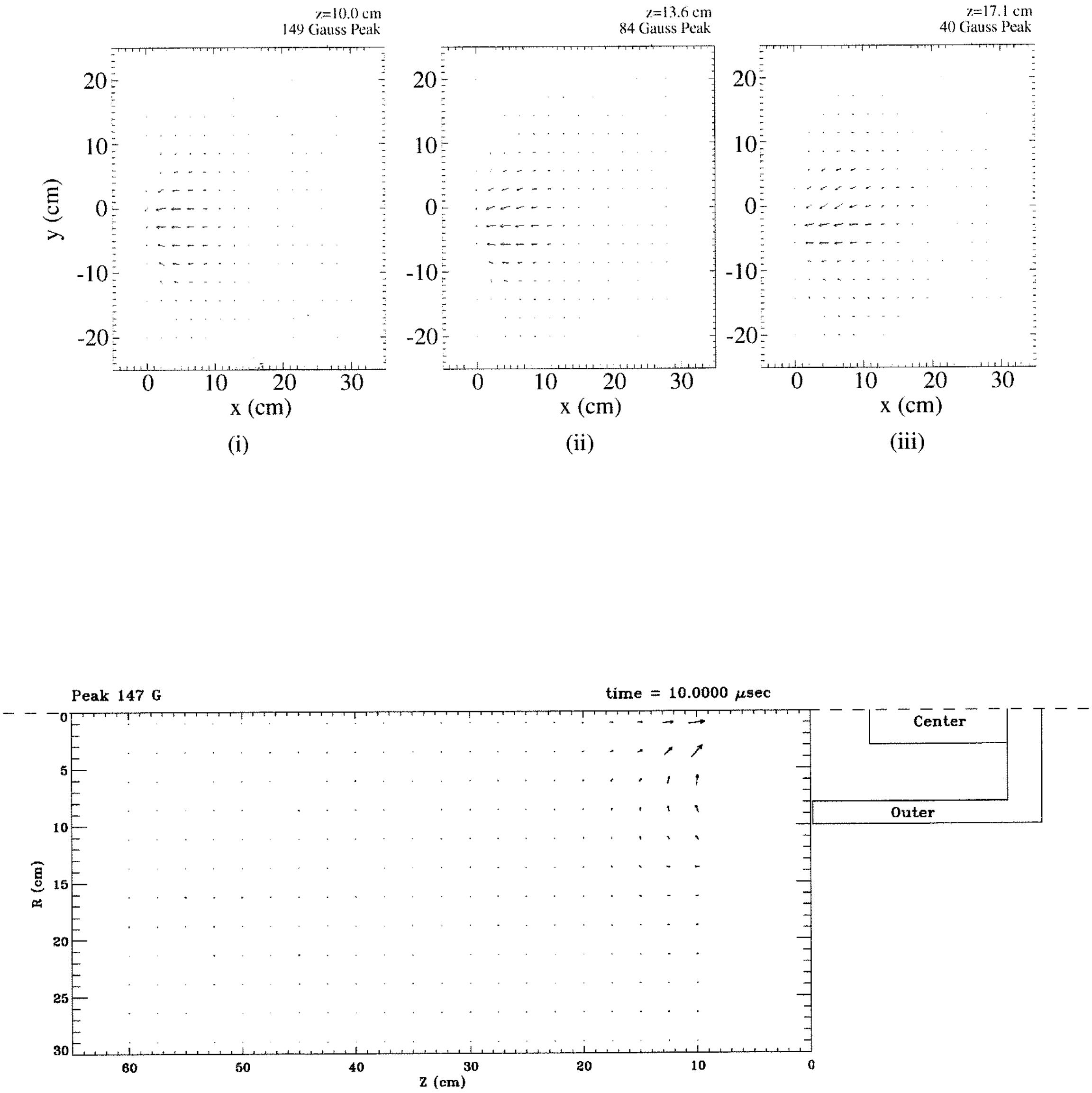

(i) (ii) (iii)

(iv)

Figure 11.9: Toroidal (i,ii,iii) and Poloidal (iv) field vector plots in Regime III, t=10 μsec. This time correponds to Stage A.

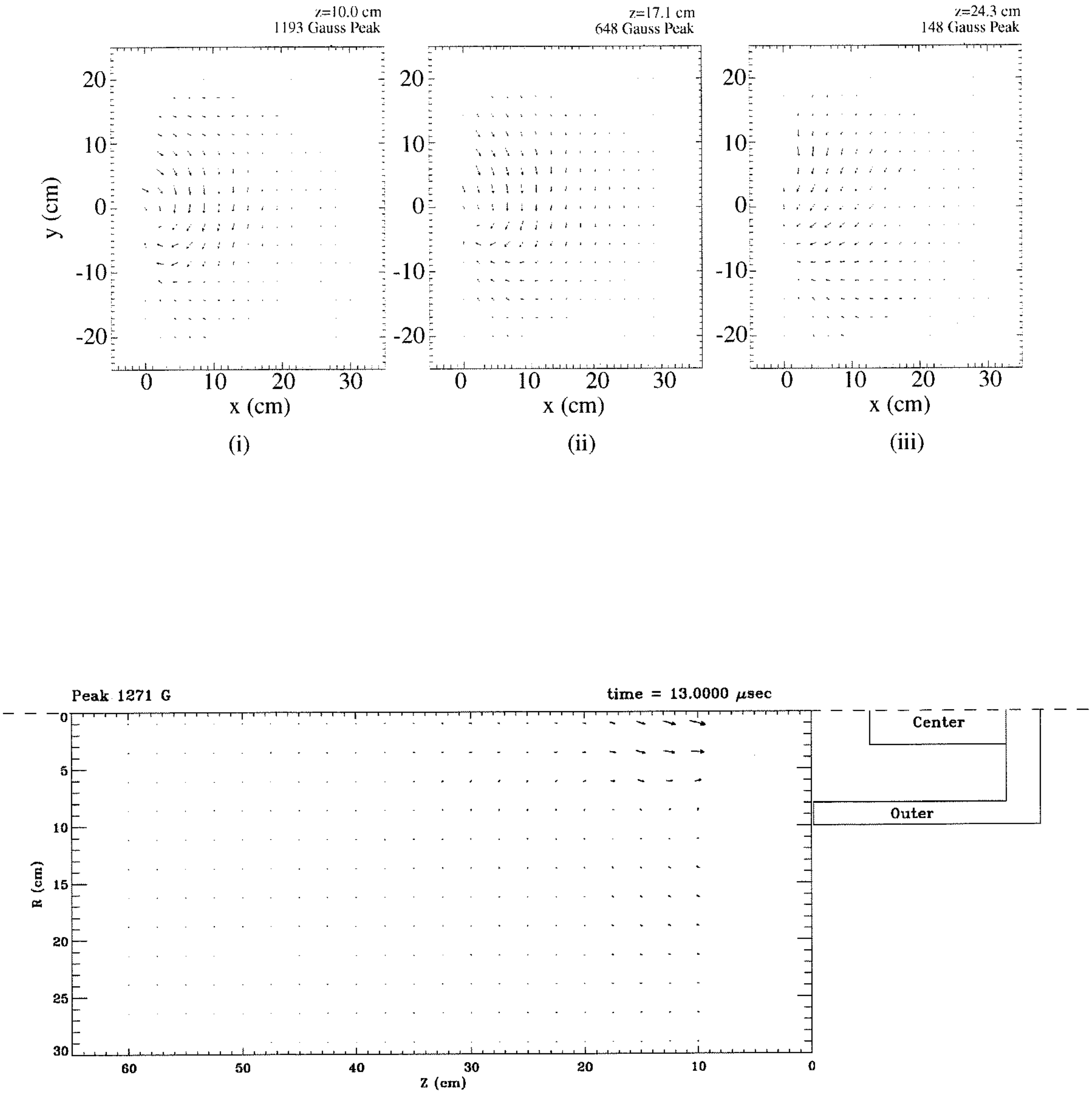

(i) (ii) (iii)

(iv)

Figure 11.10: Toroidal (i,ii,iii) and Poloidal (iv) field vector plots in Regime III, t=13 μsec. This time corresponds to Stage B.

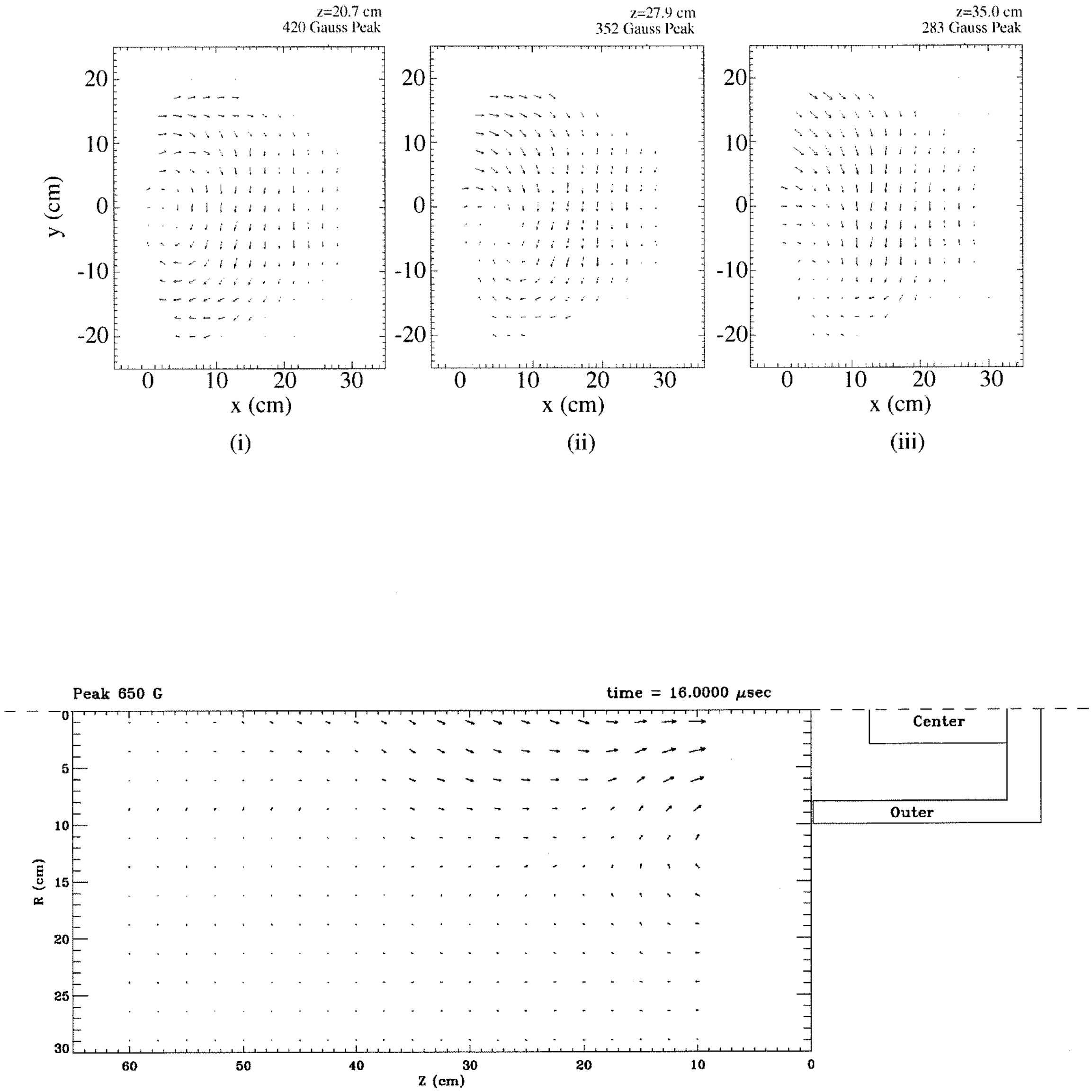

(i) (ii) (iii)

(iv)

Figure 11.11: Toroidal (i,ii,iii) and Poloidal (iv) field vector plots in Regime III, t=16 μsec. This time corresponds to the beginning of Stage C.

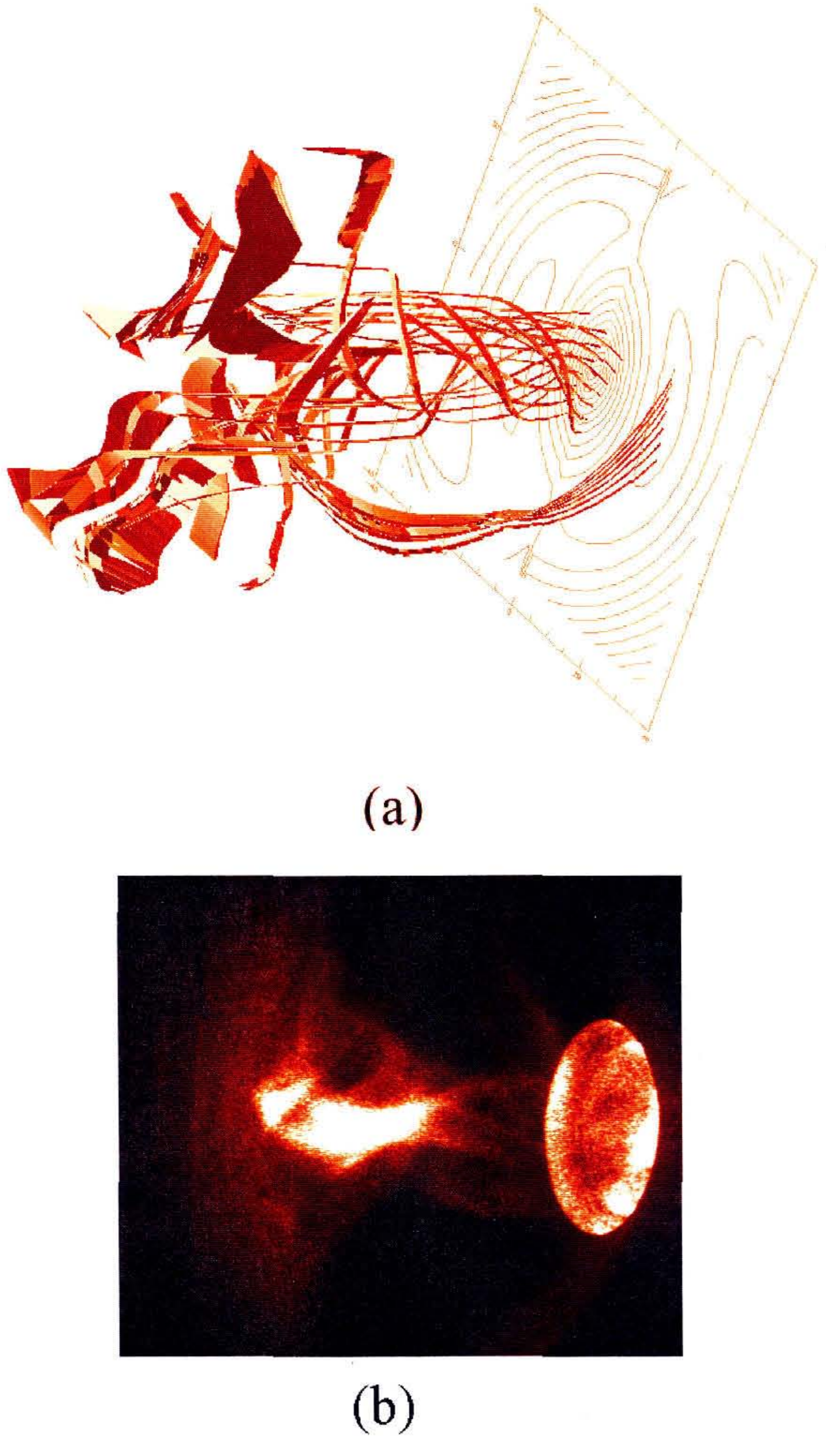

Figure 11.12: (a) Flux tube reconstruction using field line tracing of magnetic probe data. (b) Comparable Side View camera image at same time (t=13 μsec).

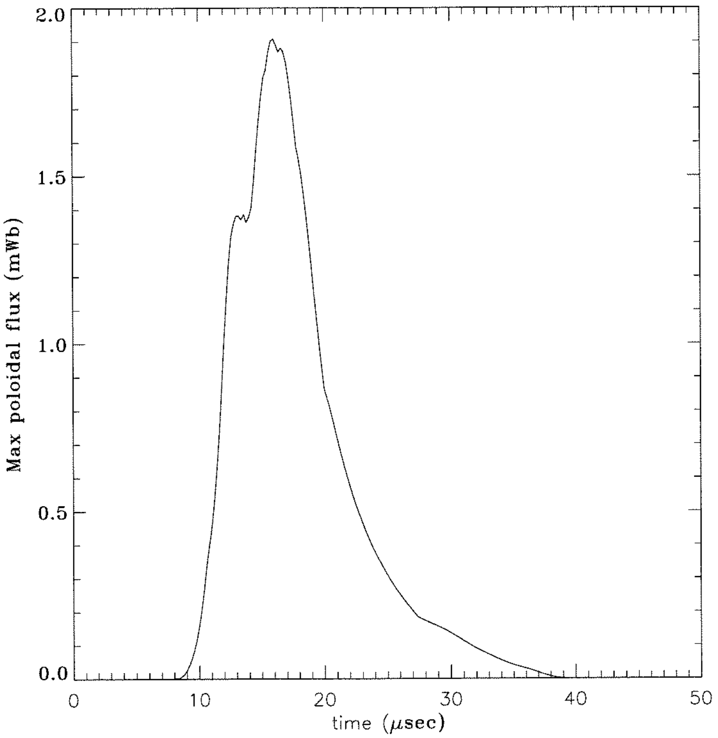

Figure 11.13: Maximum value of the poloidal flux in Regime III. The poloidal flux is computed from volumetric magnetic probe scan data over all z-planes and the maximum value is shown.

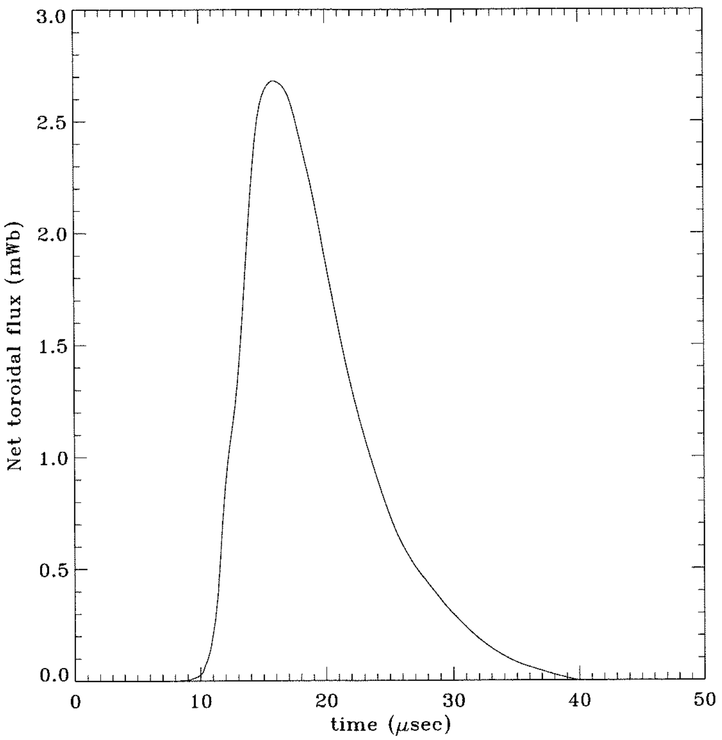

Figure 11.14: Net toroidal flux versus time, as computed using the magnetic probe scan data, from the surface integral of B_ϕ over the poloidal plane $\phi = 0$.

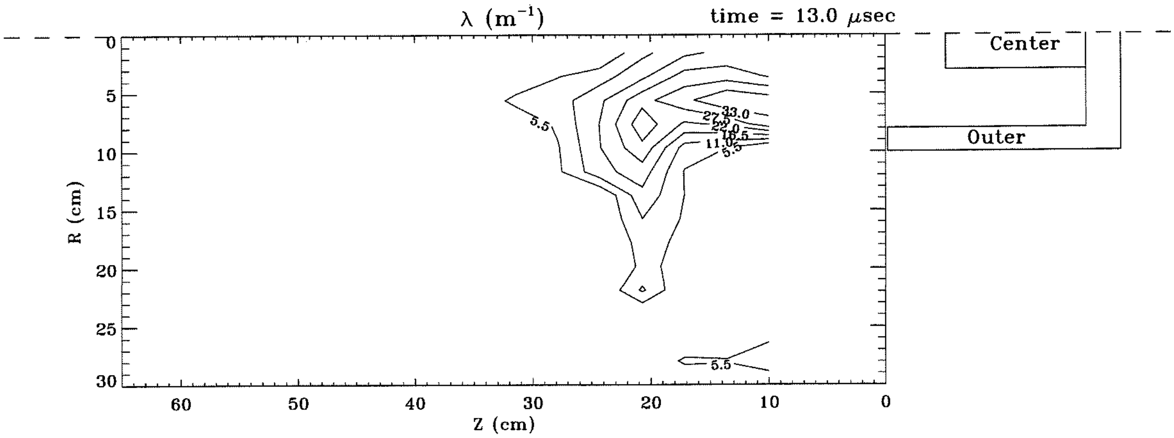

Figure 11.15: A contour plot of λ at t=13 μsec, in the poloidal plane $\phi = 0$, as computed from the magnetic probe scan data.

Bibliography

[1] L. Woltjer, "A theorem on force-free magnetic field," *Proc. Nat. Acad. Sci.*, **44**, 489 (1958).

[2] J.B. Taylor, "Relaxation of toroidal plasma and generation of reverse magnetic fields," *Phys. Rev. Lett.*, **33**, 1139 (1974).

[3] H. Alfven, L. Lindberg, and P. Mitlid, "Experiments with plasma rings," *J. Nucl. Energy Part C: Plasma Physics*, **1**, 116 (1960).

[4] M.R. Brown and P.M. Bellan, "Current drive by spheromak injection into a tokamak," *Phys. Rev. Lett.*, **64**, 2144 (1990).

[5] J.H. Hammer, *et al.*, "Experimental demonstration of acceleration and focusing of magnetically confined plasma rings," *Phys. Rev. Lett.,* **61**, 2843 (1988).

[6] R. Raman, *et al.*, "Experimental demonstration of non-disruptive, central fueling of a tokamak by compact toroid injection," *Phys. Rev. Lett.*, **73**, 3101 (1994).

[7] M.R. Brown, P.K. Loewenhardt, and P.M. Bellan, "The role of impurities in accelerated spheromaks," *Bull. Am. Phys. Soc.*, **38**, Paper 7R25 (1993).

[8] P.K. Loewenhardt, M.R. Brown, J. Yee, and P.M. Bellan, "Performance characterization of the Caltech compact torus injector," *Rev. Sci. Inst.*, **66**, 1050 (1995).

[9] L.J. Perkins, S.K. Ho, and J.H. Hammer, "Deep penetration fueling of reactor-grade tokamak plasmas with accelerated compact toroids," *Nucl. Fusion,* **28**, 1365 (1988).

[10] J.Yee and P.M. Bellan, "Effects of CT injector acceleration electrode configuration on tokamak penetration," *Nucl. Fusion*, **38:(5)**, 711 (1998).

[11] L.F. Burlaga, "Force-free magnetic clouds," *J. Geophys. Res*, **93**, 7217 (1988).

[12] Y. Nakagawa, M.A. Raadu, D.E. Billings, and D. McNamara, "On the topology of filaments and chromospheric fibrils near sunspots," *Solar Phys.*, **19**, 72 (1971).

[13] M.B. Moldwin and W.J. Hughes, "The magnetospheric lobe at geosynchronous orbit," *J. Geophys. Res.*, **99**, 183 (1994).

[14] J. Heyvaerts and E.R. Priest, "Coronal heating by reconnection in D.C. current systems: A theory based on Taylor's hypothesis," *Astron. Astrophys.*, **137**, 163 (1984).

[15] A. Konigl and A.R. Choudhuri, "Force-free equilibria of magnetized jets," *Astrophys J.*, **289**, 173 (1985).

[16] A. Kumar and D.M. Rust, "Interplanetary magnetic clouds, helicity conservation, and current-core flux-ropes," *J. Geophys. Res.*, **101**, 15667 (1996).

[17] W.M. Elsasser, "Hydromagnetic dynamo theory," *Rev. Mod. Phys.*, **28**, 135 (1956).

[18] T.H. Jensen and M.S. Chu, "Current drive and helicity injection," *Phys. Fluids*, **27**, 2881 (1984).

[19] J.M. Finn, W.M. Manheimer and E. Ott, "Spheromak tilting instability in cylindrical geometry," *Phys. Fluids*, **24**, 1336 (1981).

[20] M.A. Berger and G.B. Field, "The topological properties of magnetic helicity," *J. Fluid Mech.*, **147**, 133 (1984).

[21] H.K. Moffatt, *Magnetic Field Generation in Electrically Conducting Fluids*, (Cambridge University Press, 1978).

[22] H.K. Moffatt, "The degree of knottedness of tangled vortex lines," *J. Fluid Mech.*, **35**, 117 (1969).

[23] C.F. Gauss, Zur mathematischen theorie der electrodynamischen Wirkungen, Werke," *Koniglichen Gesellschaft der Wissinchaften zu Gottingen*, **5**, 602 (1877).

[24] J. Mathews an R.L. Walker, *Mathematical Methods of Physics* (Addison-Wesley Publishing Company, Redwood City, CA, 1970).

[25] M.N. Rosenbluth and M.N. Bussac, "MHD stability of spheromak," *Nucl. Fusion*, **19**, 489 (1979).

[26] C.W. Barnes, *et al.*, "Experimental determination of the conservation of magnetic helicity from the balance between source and spheromak," *Phys. Fluids*, **29**, 3415 (1986).

[27] B.A. Nelson, T.R. Jarboe, A.K. Martin, and C.L. Painter, "Tokamak formation and sustainment by coaxial helicity injection current drive," *Nucl. Fusion*, **34:(8)**, 1111 (1994).

[28] P.B. Parks, "Refueling tokamaks by injection of compact toroids," *Phys. Rev. Lett.*, **61**, 1364 (1988).

[29] J. Marshall, "Performance of a hydromagnetic plasma gun," *Phys. Fluids*, **3**, 134 (1960).

[30] M.J. Schaffer, "Exponential Taylor states in circular cylinders," *Phys. Fluids*, **30**, 160 (1987).

[31] J.C. Thomas, D.Q. Hwang, R.D. Horton, J.H. Rogers, and R. Raman, "A simple fast pulse gas valve using a dynamic pressure differential as the primary closing mechanism," *Rev. Sci. Instrum.*, **64**, 1410 (1993).

[32] C.J. Buchenauer and A.R. Jacobson, "Quadrature interferometer for plasma density measurements," *Rev. Sci. Inst.*, **48**, 769 (1977).

[33] B.B. Kadomstev, *Tokamak Plasma: A Complex Physical System* (Institute of Physics Pub., Philadelphia, PA, 1992).

[34] W.C. Turner, *et al.*, "Investigations of the magnetic structure and the decay of a plasma-gun-generated compact torus," *Phys. Fluids*, **26**, 1965 (1983).

[35] W.A. Newcomb, "Magnetohydrodynamic wave drag," *Phys. Fluids B*, **3**, 1818 (1991).

[36] R. Raman, Canadian Fusion Fuels Technology Project, Mississaugaa, Ontario, Canada (private communication, 1997).

[37] J.B. Taylor, "Relaxation and magnetic reconnection in plasmas," *Rev. Mod. Phys.*, **58**, 741 (1986).

[38] T.R. Detman, *et al.*, "A time-dependent, 3-dimensional MHD numerical study of interplanetary magnetic draping around plasmoids in the solar-wind," *J. Geophys. Res.*, **96**, 9531 (1991).

[39] M. Yamada, *et al.*, "Study of driven magnetic reconnection in a laboratory plasma," *Phys. Plasmas*, **4**, 1936 (1997).

[40] G.W. Hart, A. Janos, D.D. Meyerhofer, and M. Yamada, "Verification of the Taylor (minimum energy) state in a spheromak," *Phys. Fluids*, **29**, 1994 (1986).

[41] T.R. Jarboe, I. Henins, H.W. Hoida, R.K. Linford, J. Marshall, D.A. Platts, and A.R. Sherwood, "Motion of a compact toroid inside a cylindrical flux conserver," *Phys. Rev. Let.*, **45**, 1264 (1980).

[42] J.D. Jackson, *Classical Electrodynamics* (John Wiley & Sons, New York, NY, 1975), p298.

[43] M.G. Rusbridge, *et al.*, "The design and operation of the SPHEX spheromak," *Plasma Phys. Control. Fusion*, **39**, 683 (1997).

[44] H. Zirin and A.B. Severny, *Observatory*, **81**, 155 (1961).

[45] S. Lundquist, "Magnetohydrostatic fields", *Arkiv för Fysik*, **2**, 361 (1950).

[46] T.R. Jarboe, "Review of spheromak research," *Plasma Phys. Control. Fusion*, **36**, 945 (1994).

[47] T.G. Cowling, *Monthly Notices Roy. Astron. Soc.*, **94**, 39 (1934).

[48] S.O. Knox, *et al.*, "Observations of spheromak equilibria which differ from the minimum-energy state and have internal kink distortions," *Phys. Rev. Lett.*, **56**, 842 (1986).

[49] D.A. Kitson and P.K. Browning, "Partially relaxed magnetic field equilibria in a gun-injected spheromak," *Plasma Phys. Control. Fusion*, **32**, 1265 (1990).

[50] R. Martin, S.J. Gee, P.K. Browning, and M.G. Rusbridge, "The direct determination of the current density and μ profiles of a spheromak", *Plasma Phys. Control. Fusion*, **35**, 269 (1993).

[51] A. Janos, G.W. Hart, and M. Yamada, "Relaxation of spheromak plasmas toward a minimum-energy state and global magnetic fluctuations," *Phys. Rev. Let.*, **55**, 2868 (1985).

[52] M. Nagata, *et al.*, "Relaxation oscillations and toroidal-current regeneration in a helicity-driven spheromak," *Phys. Rev. Let.*, **71**, 4342 (1993).

[53] A. al-Karkhy, P.K. Browning, G. Cunningham, S.J. Gee, and M.G. Rusbridge, "Observations of the magnetohydrodynamic dynamo effect in a spheromak plasma," *Phys. Rev. Let.*, **70**, 1814 (1993).

[54] A.H. Boozer, "Magnetic helicity and dynamos," *Phys. Fluids B*, **5**, 2271 (1993).

[55] L. Lindberg and C. Jacobsen, "On the amplification of the poloidal magnetic flux in a plasma," *Astrophys. J.*, **133**, 1043 (1961).

[56] A.G. Sgro, A.A. Mirin, and G. Marklin, "The evolution of a decaying spheromak," *Phys. Fluids*, **30**, 3219 (1987).

[57] J.C. Fernández, B.L. Wright, G.J. Marklin, D.A. Platts, and T.R. Jarboe, "The m=1 helicity source spheromak experiment," *Phys. Fluids B*, **1**, 1254 (1989).

[58] T.R. Jarboe, C.W. Barnes, D.A. Platts, and B.L. Wright, "A kinked Z-pinch as the helicity source for spheromak generation and sustainment," *Comm. Plasma Phys. Control. Fusion*, **9**, 161 (1985).

[59] P.M. Bellan, *Spheromaks* (Imperial College Press, London, 1999).

[60] Atkinson, K.E., *An Introduction to Numerical Analysis*, 2nd Edition, (John Wiley and Sons, N.Y., 1989).

[61] A.I. Pevtsov, R.C. Canfield, and T.R. Metcalf, "Patterns of helicity in solar active regions," *Astrophys. J.*, **425**, l117 (1994).

[62] D.M. Rust and A. Kumar, "Helical magnetic fields in filaments," *Sol. Phys.*, **155**, 69 (1994).

[63] P.M. Bellan and J.F. Hansen, "Laboratory simulations of solar prominence eruptions," *Phys. Plasmas*, **5**, 1991 (1998).

[64] V. Bothmer and R. Schwenn, "Eruptive prominences as sources of magnetic clouds in the solar wind," *Space Sci. Rev.*, **70**, 215 (1994).

[65] T.R. Jarboe, *et al.*, "The ohmic heating of a spheromak to 100 eV," *Phys. Fluids*, **27**, 13 (1984).

[66] S.F. Smith, "Structure and development of solar active regions," *IAU Symp.*, **35**, 267 (1968).

[67] N.A. Krall and A.W. Trivelpiece, *Principles of Plasma Physics* (San Francisco Press, Inc., San Francisco, CA, 1986), p308.

[68] N. Seehafer, "Electric current density in the solar atmosphere," *Sol. Physics*, **125**, 219 (1990).

[69] G.R. Jones, *High pressure arcs in industrial devices* (Cambridge Univ. Press, Cambridge, 1988).